

THESE DE DOCTORAT DE

L'UNIVERSITE DU SUD-EST, NANJING, CHINE

ET DE
L'UNIVERSITE DE RENNES 1
COMUE UNIVERSITE BRETAGNE LOIRE

ECOLE DOCTORALE N° 601
*Mathématiques et Sciences et Technologies
de l'Information et de la Communication*
Spécialité : Electronique

Par
Zhi TAO

Photodetection dans une large gamme de longueur d'onde:

- Phototransistor CdSe QDs/RGO sur des Nanofils de ZnO dans la gamme UV-Vis,
- PbS QDs avec un transistor organique C₆₀ de type N imprimé dans la gamme proche IR

Thèse présentée et soutenue à Nanjing, le 22 Mai 2019

Unités de recherche : IETR UMR-CNRS 6164, UFR Informatique-Electronique et Display Center, School of Electronic Science and Engineering, Southeast University

Thèse N° : (8)

Rapporteurs avant soutenance :

Olivier Durand (Professeur INSA Rennes)
YI Zhang Professeur, Nanjing University of Science and Technology, Chine

Composition du Jury :

Président :	Prénom Nom	Fonction et établissement d'exercice (9)	(à préciser après la soutenance)
Examineurs :	Qing Li	Professeur, Université du Sud-Est, Nanjing	
	Jamal Benhlal	Maître de Conférences, INSA Rennes	
	Chaogang Lou	Professeur, Université du Sud-Est, Nanjing	
Exam et Co-Dir:	Emmanuel Jacques	Maître de Conférences, Université de Rennes 1	
Dir. de thèse 1:	Tayeb Mohammed-Brahim,	Professeur Université de Rennes 1	
Dir. de thèse 2:	Wei Lei	Professeur Université du Sud-Est, Nanjing	
Invité et Co-Dir:	Maxime Harnois	Ingénieur de Recherches CNRS	

CONTENT

Abstract	1
General Introduction	4
1 Research status of the photo-detectors	5
1.1 The Photo-detectors	5
<i>1.1.1 The classification of the photo-detectors</i>	<i>5</i>
<i>1.1.2 The research status of the near infrared photodetector</i>	<i>9</i>
1.2 The research status of Quantum Dots	18
1.3 The research status of the Quantum Dots photodetectors	23
<i>1.3.1 UV-Vis photodetectors</i>	<i>23</i>
<i>1.3.2 NIR photodetectors</i>	<i>25</i>
1.4 The Characteristics of the Photo-detector	29
2 The Organic Semiconductor Thin-Film Transistor	32
2.1 Development of the Organic Electronics	32
2.2 Research status of OTFT	34
<i>2.2.1 Development of OTFT</i>	<i>34</i>
<i>2.2.2 The basic points of OTFT</i>	<i>36</i>
<i>2.2.3 Electrical characteristics of OTFT</i>	<i>38</i>
2.3 Organic Semiconductor Material: Fullerene (C60)	44
3 Printing Electronics	47
3.1 Development of the inkjet printing	48
<i>3.1.1 Continuous Printing</i>	<i>49</i>
<i>3.1.2 Drop-on-demand (DoD) Printing</i>	<i>50</i>
3.2 Process of the DoD inkjet printing	52
<i>3.2.1 Droplet formation</i>	<i>53</i>
<i>3.2.2 Droplet collision and spreading on the substrate</i>	<i>54</i>
<i>3.2.3 Droplet drying to form a film</i>	<i>54</i>
Summary	56
References	57
Part A: UV-Visible Photodetectors	68
1.Introduction	69
2.Experiment Sections	70

2.1 Fabrication of ZnO Nanowires	70
2.2 Synthesis of CdSe QDs/RGO Fragments	71
2.3 Manufacture of the Device	72
3.Results and Discussion	73
3.1 Photo-sensitive mechanism of the Quantum Dots	73
3.2 Results and Discussion	73
Summary	81
References	82

Part B: NIR organic phototransistors	86
1.Introduction	87
2.Inkjet Printing	88
2.1 The key steps of inkjet printing pattern formation: Spreading, Wetting and Drying	88
• <i>Spreading</i>	88
• <i>Wetting</i>	90
• <i>Drying</i>	92
2.2 The research of spreading and drying impact on inkjet printing Pattern Accuracy	94
2.2.1 <i>The material and methods of experiment</i>	95
2.2.2 <i>Results and discussion</i>	97
• <i>Droplet spreading</i>	97
• <i>Line formation</i>	106
• <i>Square shaped behaviors</i>	111
Conclusion	120
References	122
3.Printed N-type C60 Organic Semiconductor Thin-film Transistor	125
3.1 Research states of the C60 Organic Thin-film Transistor	125
3.2 Experimental Section	129
3.2.1 <i>Transistor fabrication</i>	129
3.2.2 <i>Transistor Characterization</i>	132
• <i>The discussion of the annealing process</i>	132
• <i>The discussion of annealing temperature</i>	137
• <i>The research of the thickness influence</i>	149
3.2.3 <i>Dynamic behavior of the optimized printed C₆₀ based OFET</i>	153
Conclusion	157

References	159
4. The near infrared photodetector system based on the PbS quantum dots and Organic Thin-film Transistor	165
4.1 PbS Quantum Dots	165
4.2 Printed C60 & PbS Photo-transistor	170
<i>4.2.1 Mixed PbS QDs / SU8 layer as gate insulator of the photo-OTFT</i>	<i>170</i>
<i>4.2.2 Sandwich of mixed PbS QDs / SU8 layer and SU8 layer as gate insulator of the photo-OTFT</i>	<i>172</i>
<i>4.2.3 PbS QDs at the interface between SU8 layer as gate insulator and C60 active layer of the photo-OTFT</i>	<i>174</i>
<i>4.2.4 Photo-sensitive circuit (Inverter)</i>	<i>175</i>
<i>4.2.5 Photo-Inverter using OTFT with cross-finger drain and source electrodes (Large Channel area)</i>	<i>178</i>
Conclusion	181
References	183
General Conclusion	185

Abstract

In our daily life, various wavelength electromagnetic waves play important roles. Various colors can be captured by our naked eyes, massive information is being received by all kinds of terminal and an X-ray photograph can provide the health information. With the advantages of electromagnetic waves, the photo-detectors are very crucial to obtain the signals such as remote sensing, spectrum measurement and Infrared imaging and so on. The traditional photo-detectors fabrication processes are based on molecular beam epitaxy and metal organic chemical vapor deposition and micro-nano processing technology for the photo-sensitive layer and readout circuit. With the developing of the informatization, the requirement of flexible, large area and simplified fabrication process photodetectors is increasing. Thus, new photo-sensitive material and preparation technology are essential for the new devices.

Due to high light absorption rate, photo-electric efficiency and fast response of quantum dots, the photo-detectors with quantum dots attached many attentions in the scientific field. In addition, compared with the traditional photo-detectors such as photodiodes and photo-conductive device, photo-modulated transistor exhibits tripolar modulating, self-amplification ability to improve the photo-electric properties. With the purpose of decreasing the cost of the fabrication and matching the large area devices, inkjet printing process and organic electronics are utilized in this thesis.

Based on the achievements of IETR in thin film transistors, especially the work focus on the organic thin film transistors, inkjet printing and quantum dots photo-detectors, this thesis combines the achievements and expands the application in the field of the low cost and low temperature process near infrared photo-detectors.

The thesis can be divided into two parts. In the part A, the work focuses on the UV-Visible wavelength photodetectors with the CdSe Quantum Dots. Due to expanding the

detecting wavelength and decreasing cost, the near infrared photodetectors is investigated in the Part B. The part B is organized in 4 chapters.

In the first chapter, the research status of the photodetectors is introduced, including the classification of photo-detectors, quantum dots and photo-detectors with quantum dots. Then, due to the organic transistor structure, the general introduction of the organic semiconductor is provided. At the end, as the fabrication process, the development of the printing electronics and the process of the DoD (drop-on-demand) are presented.

For obtaining the good performance of the transistor, the fabrication process of the near infrared photo-modulated transistor should be studied in details. Especially for the pattern formation of the electrodes, the connection of the printing patterns and printing parameters is investigated in chapter 2. Moreover, this work will help to fully understand the phase separation that occurs during inkjet printing of colloids droplets.

Normally, the performance of the near infrared photo-modulated transistor will be influenced by the performance of the organic thin-film transistor. With the novel fabrication process in organic thin-film transistor, the method to improve the performance of the organic thin-film transistor is illustrated in chapter 3. In this chapter, the direct correlation between the structure of the C60 film (grain size, surface roughness) from AFM measurement and electrical parameters of the organic thin-film transistor is highlighted. Besides, considering the potential application in electronic circuits, the response of the transistor is measured. With the 13ms switching time, the application frequency of the transistor could be approximately 10Hz.

In the fourth chapter, integrating the achievements in inkjet printing process, organic thin-film transistor and the PbS quantum dots, the near infrared photo-modulated transistor is synthesized and researched. In order to observe the obviously photo-response phenomenon, four quantum dots distribution modes are studied. Based

on the best distribution mode, the simple photo-detecting circuits are designed. From the first circuit, we obtain approximately 3V voltage difference with the switching of the 1050nm incident light. As measured from the second structure, 110nA photo-current can be gained from the circuits.

Finally, based on the previous work of the laboratory, the thesis expands it in new field.

General Introduction

With the research of the photo-detector developing, the researchers focused on the various parameters of the photo-detector such as high responsivity, obvious photo-signal, flexibility and so on. In my work, the main idea is the detection of the light in large range of wavelength. For this purpose, the unique properties of quantum dots and the possibilities of large gain given by field effect devices were utilized in my photo-detector. In addition, part of these devices were fabricated by using organic electronics technology in the goal to decrease the cost of the fabrication and to use large area substrates in the future. Besides, Drop on Demand printing technique was utilized for this purpose. In the following, I will define and describe the quantum dots photodetectors, the organic electronics and the way to fabricate these organic electronics using printing technology.

1 Research status of the photo-detectors

1.1 The Photo-detectors

1.1.1 The classification of the photo-detectors

The photodetector is a device that measures electromagnetic waves of a specific wavelength or wavelength band by using a photoelectric effect or other physical mechanism. The photodetectors can be easily found in our daily life such as camera, photoelectric sensor and so on.

Normally, photodetectors can be divided into internal photodetectors and external photodetectors by the physical mechanism as shown in Fig1-1. External photodetectors are based on the External Photoelectric Effect. It means that the incident photon energy is greater than the work function of the photosensitive material, and the electrons of the material escape and are detected by the external circuit [1]. For example, the photomultiplier tube converts the incident light into weak electrons by the photoelectric effect, and the secondary electron emission phenomenon occurs multiple times under the action of the high voltage between the dynodes. Therefore, only at the photocathode,

photoelectric conversion effect occurs, so the photomultiplier tube is a current amplifier.

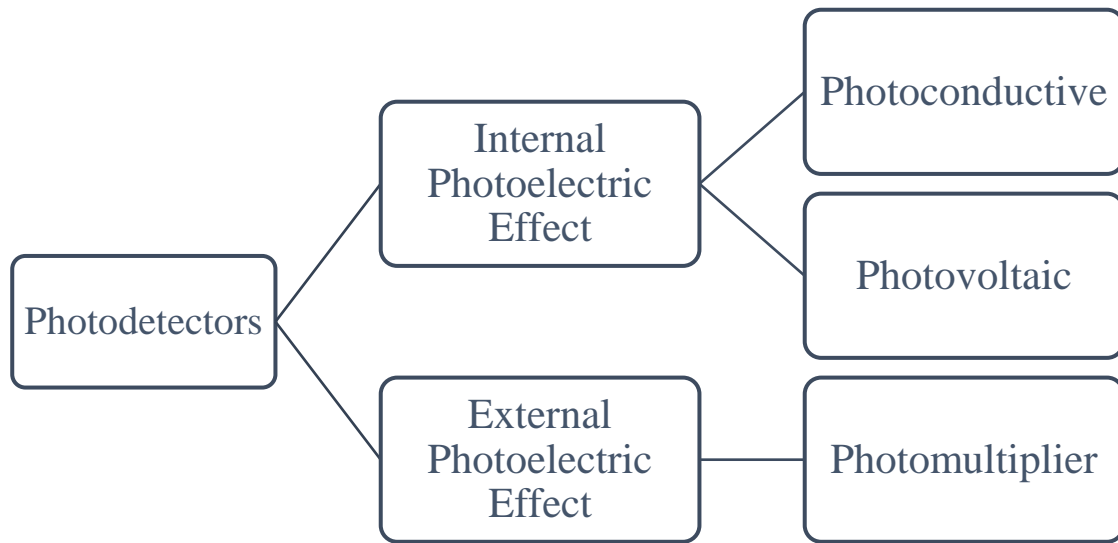


Figure 1-1 the classification of the photodetectors

The internal photodetector refers to the change in the properties of the material under electromagnetic wave irradiation. The most common device is the photoresistor. This kind of resistive photodetector can change the material carrier concentration under different light intensity and directly affect the resistance of the material, so it can be used for detection. The internal photodetectors can also be subdivided into photoconductive detectors and photovoltaic detectors depending on the detection mechanism. Photosensitive resistors belong to photoconductive photodetectors. The main advantage of photoconductive devices is that the photoelectric effect of the device is independent of the positive and negative polarities of the applied electric field. The other advantage is its high sensitivity to the light. However, its sensitivity depends on the light power and the applied voltage. However, the performance of the photoconductive device is greatly affected by external temperature. Then, it is mainly used as light detector and not in the measurement of the light power. At the same time, the detection speed of the photoconductive device is very slow [2].

For example (Fig1-2), *Gerasimous et al.* reported the modification of the graphene surface with PbS Quantum Dots. With the photo-response of the PbS QDs, the responsivity of the device is 10^7A/W [3].

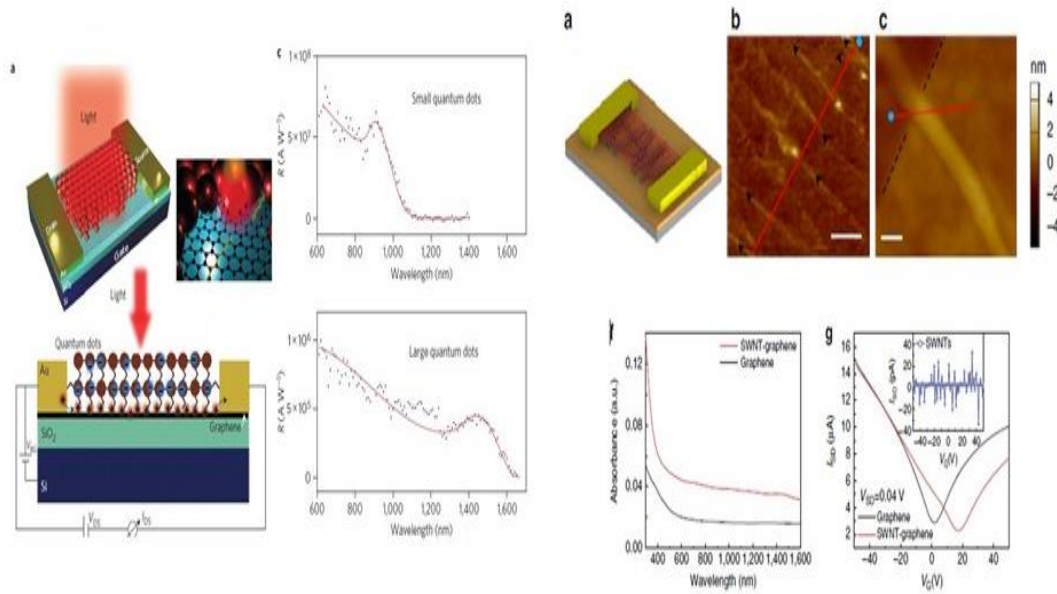


Figure 1-2 the photoconductive photodetector based on the graphene [3,4]

Photovoltaic detectors usually have a homostructure composed of 2 opposite doped parts of the same semiconductor or a heterostructure composed of two different types of semiconductors, which is known as the PN junction. At the interface of the junction, a built-in electric field is formed due to majority carrier drift and minority carrier diffusion. Under lighting, the photogenerated electrons and holes are separated by the electrical field and diffuse to the two ends. As the most common photovoltaic device, the structure of the photodiode device is similar to that of a conventional semiconductor diode device, except that the photodiode device has a photosensitive region capable of detecting an optical signal under illumination and converting it into an electrical signal. Common photodiode devices are Schottky type photodiodes, metal-oxide-semiconductor (MOS) type photodiodes, p-i-n photodiodes and avalanche photodiode

devices.

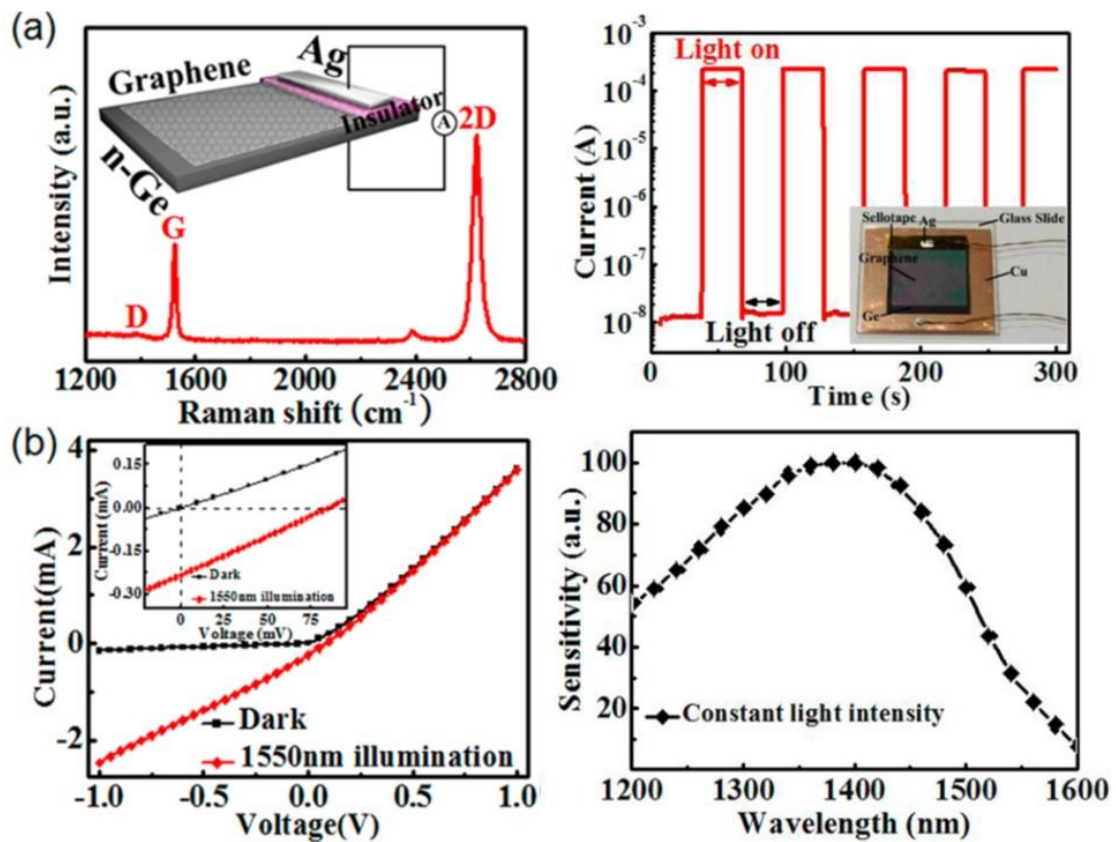


Figure 1-3 the photodiode made with Graphene/Germanium Schottky Junction [5]

As illustrated in Fig1-3, based on the Graphene/Germanium Schottky Junction, the near-infrared photodiode was reported by the Zeng *et.al.* With the incident light, the Schottky Junction will disappear. By this way, the photoelectric response of the device is significantly improved compared to the photoconductive device under reverse bias conditions. In addition, the photodiode has a wide detection range of 1.5 μm communication band, and the detection speed is high [5]. Therefore, the unidirectional conductivity of the photodiode and the operating characteristics under reverse bias make the device widely used in the field of photodetection and have been extensively studied by the scientific community. Advantages of photodiode devices include good linearity, high speed photocurrent response, wideband detection, low cost and long working life. However, photodiode devices have some fatal defects, such as fast

quenching of excitons, low photoelectric response, and no photocurrent amplification. In order to solve these problems, triode structure is utilized to design the photodetectors. Photo-modulated transistors have been focused on by the researchers.

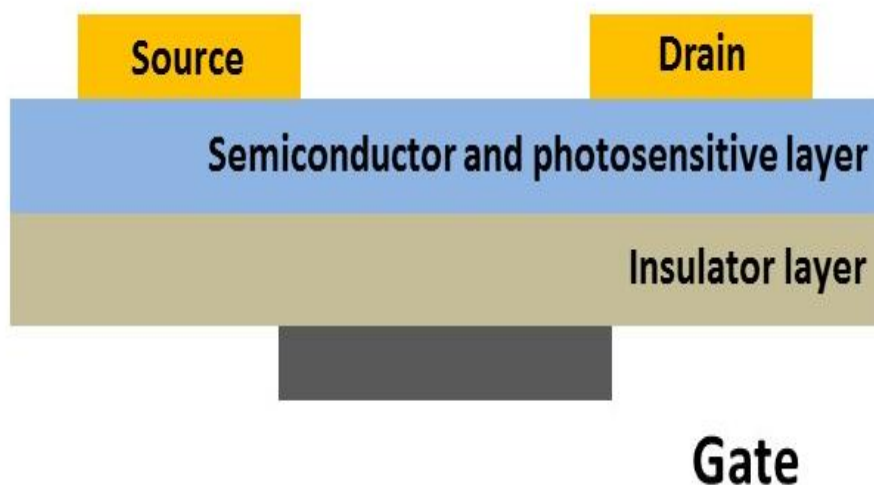


Figure 1-4 the structure of photo-modulated transistor

With the structure in Fig1-4, the photo-modulated transistor has the similar structure with the traditional field-effect transistor. Based on the field effect modulation amplification of gate electrode bias, the photo-modulated transistor exhibits the high efficiency to transfer the photo-signal to the electrical signal. Normally, the photo-sensitivity of the triode structure photo-modulated transistor is higher than photodiode. According to the above reasons, the triode structure is utilized as the photodetector structure.

1.1.2 The research status of the near infrared photodetector

As the core component of the photoelectric system, the photodetector can convert the optical signal into a storable electrical signal [6,7]. After special treatment of electrical signals according to different needs, photodetectors can be widely used in missile guidance [8,9], night vision systems [10,11], environmental testing [12,13], biomedical imaging [14-16], etc. Infrared photodetectors in photodetectors have very

important applications in the military and civilian markets. In the military field, infrared photodetectors are widely used in infrared detection, infrared guidance, and airborne warning, in order to improve the night combat efficiency and the target's precise strike rate, and reduce the casualty rate [17]. In the civilian field, infrared photodetectors are widely used in forest fire alarms, weather forecasts, etc. to improve the ability to monitor the external environment [18].

According to the optical response range, infrared photodetectors can be divided into three categories: near, medium and far infrared photodetectors [19]. Compared with medium and far infrared photodetectors, near-infrared photodetectors have great market prospects due to their low cooling requirements, simple process and excellent performance. At present, the mainstream product of near-infrared photodetectors is indium gallium arsenide (InGaAs) photodiodes. The need for higher lattice matching, greater material consumption, and complex array interconnect technology greatly increases the cost of device fabrication. The price of the InGaAs-based night vision camera has reached 40000 US dollars [20]. Exploring the development of new material systems and device structures, while pursuing high performance, reducing costs, reducing weight and reducing environmental pollution, is of great significance for promoting the research and market application of infrared photodetectors.

At present, infrared detectors have mainly experienced the following three generations of development:

The first generation is dominated by single and multiple infrared focal plane arrays. It has a light machine string and scan imaging and represents the time delay integration function. But the cumbersome one, two-dimensional scanning system and relatively low light and dark current ratio limit its application and promotion.

The second generation is dominated by medium and small gaze focal plane arrays. The devices in this period were focal plane arrays developed on the basis of the US

Lada I, Lada II and Lada III arrays, with an array size of $10^3 \sim 10^6$ pixels.

The third generation is dominated by a gaze-type focal plane array. The array size is above 10^6 pixels. With the features such as large area array, miniaturization, low cost, two-color and multi-color, intelligent system, smart chips and so on, the photo-detective array is integrated with high-performance digital signal processing, single-chip multi-band fusion high-resolution detection and recognition.

There are many materials suitable for infrared photodetection, but it is really suitable for the development of three generations of infrared photodetectors, that is, the materials of the two-color and multi-color infrared focal plane array devices with flexible response bands are few. Now, the main structures and materials of the near infrared photodetectors includes traditional HgCdTe[21], Quantum Well Photodetectors[22], type II strained-layer superlattices[23] and Quantum Dot photodetectors[24,25].

•*HgCdTe Near Infrared Photodetector*

The cross-sectional schematic of the back-illuminated HgCdTe double color near infrared detector structures is illustrated in Fig 1-5[21]. HgCdTe is the direct band gap semiconductor consisted by the CdTe and HgTe. The material include three advantages[26]:(1) By adjusting the content of Cd in the alloy, the absorption range can be adjusted in $1 \sim 30 \mu\text{m}$; (2) Intrinsic absorption results in a detector with high quantum efficiency; (3) a high carrier lifetime and operating temperature. Normally, vacuum epitaxy is used to fabricate high quality HgCdTe near infrared film. MBE (molecular beam epitaxy) and MOCVD (Metal organic chemical vapor deposition) are relatively mature high vacuum forging film technologies. Using these vacuum techniques, multilayer or more complex device structures can be fabricated, and multilayer heterojunction materials suitable for three generations of two-color, multi-color infrared

pupil detectors can be obtained.

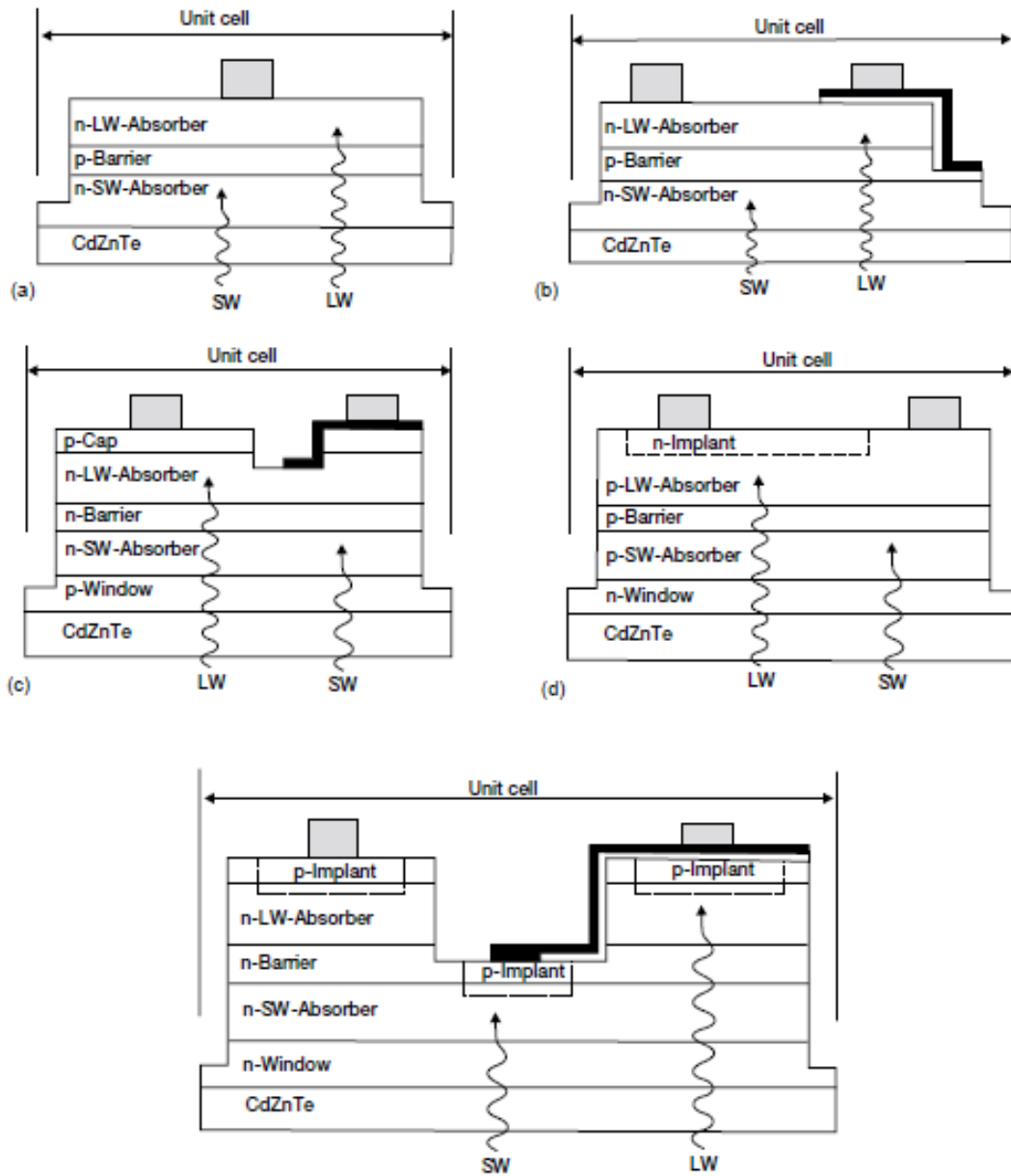


Figure 1-5 Cross-section views of unit cells for various back-illuminated dual-band HgCdTe detector approaches: (a) bias-selectable n-p-n structure reported by Raytheon, (b) simultaneous n-p-n design reported by Raytheon, (c) simultaneous p-n-p-n-p reported by BAE Systems, (d) simultaneous n-p-p-p-n design reported by Leti, and (e) simultaneous structure based on p-on-n junctions reported by Rockwell.[21]

- *Quantum Well Photodetectors*

The potential of electrons or holes with two different semiconductor materials arranged in phase and having a quantum confinement effect is called a quantum well. The infrared ray detection of the target is realized by the electronic hopping principle of the energy level in the quantum well, and the detection wavelength range can cover 1-20 μm .

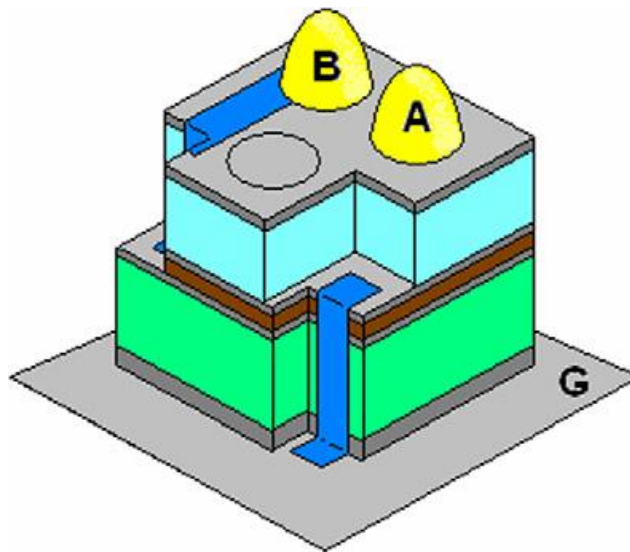


Figure 1-6 3-D view of dual-band Quantum well infrared detectors device structure showing via connects for independent access of middle wavelength infrared and lower wavelength infrared devices. The color code is as follows, orange - isolation layer; green-lower wavelength area; light blue-middle wavelength area; grey-contact layer; dark blue-metal bridges; yellow-indium bumps.[24]

Quantum wells have excellent infrared detection performance, but their shortcoming of zero vertical absorption makes it necessary to fabricate an optical grid to increase the light absorption of the device, thereby increasing the manufacturing difficulty and cost.

- *Type II strained-layer superlattices*

InAs/GaSb energy band has a straddle structure. This infrared photodetector has some unique advantages and has become one of the development directions for third-generation focal plane devices that have received much attention in recent years as illustrated in Fig 1-7.

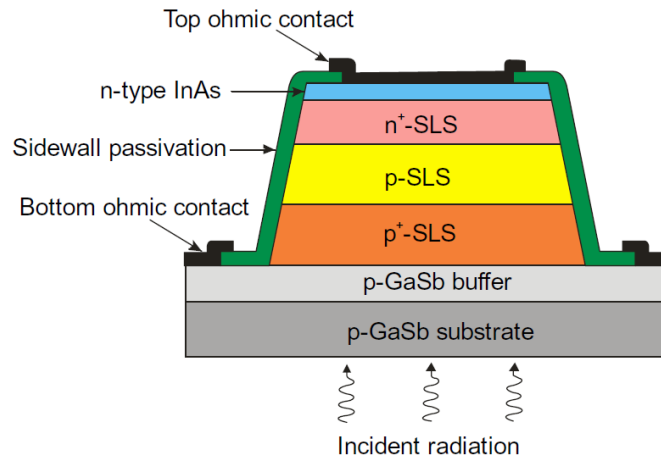


Figure 1-7 Cross section schematic of p - i - n InAs/GaSb superlattice photodiode[24]

Type II strained-layer superlattices have excellent infrared photosensitivity, but high-quality film growth and superior film passivation are difficult to achieve, the biggest challenge in pre-study research.

- *Quantum Dot NIR photodetectors*

The third-generation photodetectors based on HgCdTe, Type II strained-layer superlattices and Quantum Well photodetectors have relatively good infrared photosensitivity, but the deficiency is also obvious. And the use of large high vacuum equipment such as MBE and MOCVD increases the manufacturing cost of the device. Quantum dot photodetectors have the advantages of sensitivity to normal incident light, high photoconductivity, high detection ratio, continuous detection wavelength and low temperature preparation. The Quantum Dot detectors have been extensively studied in recent years.

At present, the research of quantum dot infrared photodetectors mainly focuses on the heterostructure embedded in quantum dots Dwell (Dot in a well) in quantum well. Dwell heterostructure infrared detector combines the characteristics of quantum speaking infrared photodetector and quantum dot infrared photodetector, suitable for the development of the third generation and future generation of infrared photodetectors. However, due to the limitation of fine processing, this preparation method is difficult to obtain a quantum dot material with adjustable size and controllable morphology. At the same time, due to the need for large equipment such as MBE and MOCVD, it is difficult to achieve low-cost, large-area preparation and other requirements, so that the large-scale application of quantum dot infrared detectors is limited to a certain extent.

Compared to vacuum technology, chemically prepared quantum dots can avoid some of the disadvantages of vacuum methods. There are many types of chemical synthesis methods, and various synthesis techniques have been widely used to control quantum dot size, chemical composition and morphology. The prepared quantum dots have the characteristics of high quality, narrow size distribution, and uniform appearance[27], and can be used for preparing large-area films on various substrates by using dip coating, thermal spraying, spin coating, etc. Development and production of low cost, high performance and flexible electronic and optoelectronic devices.

At present, the research of glue mass sub-point photodetectors mainly focuses on photoconductors, photodiodes and phototransistors. These optoelectronic devices make full use of the advantages that the rubber mass point can separately prepare a photovoltaic film or combine with other materials to prepare a photoelectric composite film.

In 2006, *Gerasimos Konstantatos* from the *Prof. Edward H. Sargent* research group reported the work that change the ligand of PbS QDs (Quantum Dots) [28]. And the three processes of post-crosslinking oxidation, post-crossover oxidation, and post-

oxidation transfer are used to enhance the adhesion of carriers between quantum dots, as shown in Fig 1-8. It was found that the device with moderate oxidation treatment after the transfer has the best photo-responsive performance with a responsivity of 2700A/W. And the detectivity is 10^{13} Jones which is higher than the imaging requirement of 10^{12} Jones. Although the device has a modulation frequency of 30Hz, its overall performance has surpassed that of commercial photodiodes.

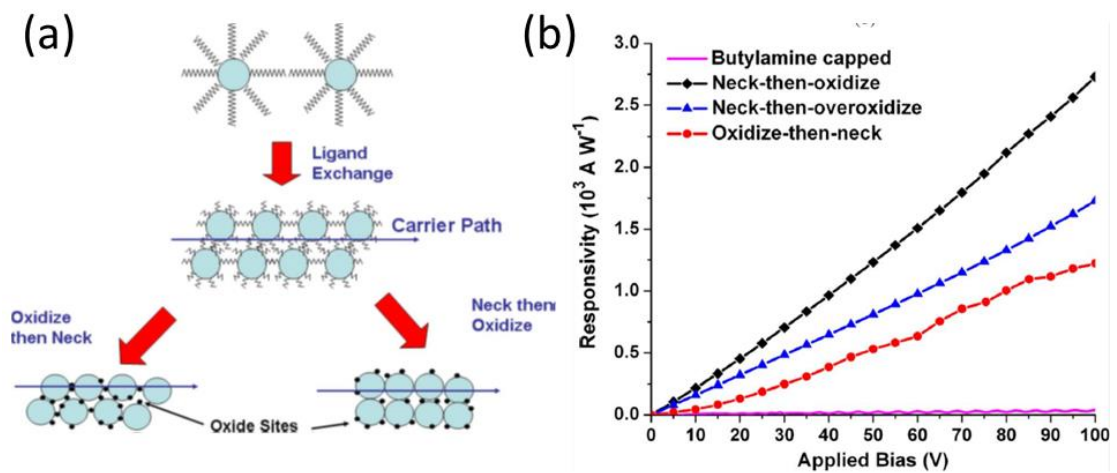


Figure 1-8 the photoconductive detector based on the PbS QDs. (a) Material processing diagram for the development of QDs photoconductive photodetectors; (b) Responsivity as a function of applied bias of photoconductive devices measured at a wavelength of 975 nm and light intensity of 300 nW/cm^2 . [28]

One year later, the research group synthesized the PbS QDs with practical size 2nm [29], and successfully decreased the absorption wavelength to 850nm~900nm. And then they combined the 2nm particle size 2nm with particle size 4nm QDs to fabricate the double color photodetector as illustrated in Fig 1-9.

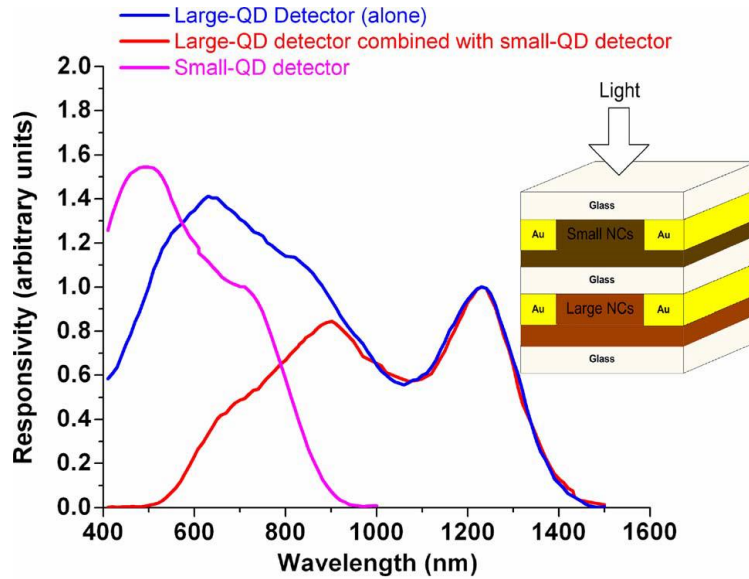


Figure 1-9 Spectral responsivity of the stacked device shown in the inset for dual-spectral detection. The small quantum dot (QD) layer detects effectively the short wavelength light, whereas the longer wavelengths are detected from the large QD layer. The responsivity of the large QD device before the stacking is also shown for comparison.[29]

In 2012, *Mengyu Chen* from the City University of Hong Kong succeed in fabricating the high response speed HgTe QDs photoconductive detector with the thermal inkjet printing[30]. With response frequency of 1MHz and 3dB bandwidth, the response band width is better than the other photoconductive detector, as illustrated in Fig 1-10.

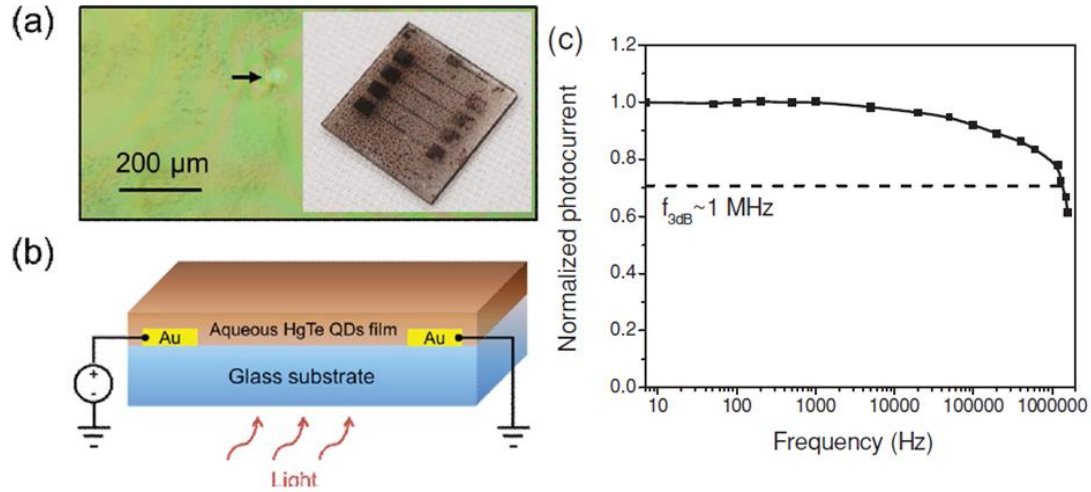


Figure 1-10 a) Optical image of the HgTe QD film after a few passes of spray-coating. The arrow highlights some of the substrate regions that are uncovered with QDs, which can be filled up in the following spray passes. Inset: image of four spray-coated photoconductors with different W/L ratios on one chip. b) Device structure. c) Frequency dependence of the photocurrent illuminated by a square-wave modulated 8 mW, 635 nm laser (295 K, bias=5 V, $I = 800 \text{ mW/cm}^2$).[30]

Based on the above analysis, for photodetectors, responsiveness, response speed, light-dark current ratio and noise are important performance parameters of photodetectors. The response speed of the detector determines how fast the device turns on and off, which can reduce serious problems such as smear; the dark-light current ratio affects the strength of the device to capture the object signal; the noise level determines the strength of the minimum detectable signal. In addition to performance, the problems in the practical process are also important factors affecting the development of photodetectors. Low cost, portability, and good environmental adaptability are increasingly important.

1.2 The research status of Quantum Dots

Recently, the interest of scholars has been occasioned because of the ability to reduce the gap between the material volume and molecular size of the nano-scale

materials. Its unique properties can be applied in many fields, especially in electronics, optoelectronics and biology [31,32]. With a unique change in optical and electronic properties and a particle size of less than 100nm, the structure may be referred to a nanostructure. And the structure can be classified into (1) two-dimensional, such as a quantum well;(2) one-dimensional, such as a quantum wire; (3) zero-dimensional, such as a quantum dot. As a zero-dimensional nanomaterial, quantum dots consist of a finite number of atoms. Due to the limited number of electrons, the energy levels change from quasi-continuous to discrete [33]. The low density of quantum dot states leads to quantum confinement effects on electron-hole pairs, so the optical and electrical properties of quantum dots are distinctly different from bulk semiconductors. As early as the 1980s, two physicists at the Bell Labs in the United States, Daniel and David [34], first proposed the concept of quantum dots. As an emerging research field, the research on quantum dots has been developed into one of the hot topics in research around the world. Quantum dots have the advantages of wide absorption, narrow emission, large quantum yield, etc. Their unique optical and electrical properties provide a good basis for the application of quantum dots. At present, quantum dots are widely used in the field of optoelectronics such as light-emitting diodes [35], transistors [36], and solar cells [37], as well as in biological imaging [38] and biological probes [39]. With the deepening of research, the achievement of the Quantum Dots devices has achieved rapid development in various fields, and their potential application prospects are immeasurable.

In addition, the unique properties of quantum dots, such as quantum size effect, surface effect and small size effect, have led to the unique physicochemical properties, which provide a broad space and opportunity for the development of quantum dots in the field of optoelectronic devices. The quantum size effect refers to the phenomenon that the electron energy level near the Fermi level changes from quasi-continuous to discrete energy level or the energy gap becomes wider when the size of the nanoparticle

decreases to a certain value. Common materials contain nearly infinite numbers of atoms, so the energy level spacing of common materials is approximately zero, and the electronic energy level is quasi-continuous. For nanomaterials, discrete energy levels are formed due to the limited number of atoms involved. When the energy level spacing is greater than the condensing energy of thermal energy, magnetic energy, photon energy or superconducting state, the quantum size effect must be considered. This effect will lead to the optical, thermal, magnetic, acoustic, electrical and other characteristics of the nano-material and conventional materials. There are significant differences.

As the particle size becomes smaller, the ratio of the surface area to the volume, that is, the specific surface area, increases remarkably. Thereby the surface atoms on the nanoparticles are highly active. In turn this causes changes in the properties of the nanoparticles. And this is the surface effect. At the same time, as the particle size of the nanomaterial decreases, the number of surface atoms increases rapidly. For example, when the particle diameter is 10 nm, the number of surface atoms is 20% of the total number of complete crystal atoms; and when the particle diameter is 1 nm, the surface atomic percentage is increased to 99%. Since the surface of the nanoparticles exhibits high chemical activity, it is rapidly oxidized in the air. In order to improve the surface stability, a dense oxide protective layer can be formed on the surface.

When the size of the nanoparticles is equal to or smaller than the physical wavelength of the light wave, the de Broglie wavelength of the conduction electrons, and the coherence or transmission depth of the superconducting state, the periodic boundary conditions are destroyed, along with the particles. As the size is reduced, many properties of the nanoparticle such as light, thermal, electricity and the like will change significantly. This change in the properties of the nanoparticles due to the reduction in size is called the small size effect, also called the volume effect.

- *Fabrication of the Quantum Dots*

In order to limit the particle size of the prepared material to the nano-scale in three dimensions, some specific processes are required to prepare the quantum dots. There are usually three typical quantum dot preparation processes: nanolithography, epitaxial growth and chemical wet synthesis. The earliest research related process is the use of electron beam lithography, directly using photolithography and etching to form the desired quantum dot material. As early as 1986, Bell Communications Laboratory A. Scherer and H. G. Craighead utilize high voltage electron beam lithography. A nanopattern is lithographically patterned on a porous quantum well substrate. A nano-column of approximately 40 nm diameter and 230 nm height close to the quantum dot material was etched by ion reaction [40]. In this research work, quantum well heterojunctions provide a one-dimensional confinement as a traditional two-dimensional nanostructure, while nanoscale lithography is used to achieve nanoscale in the other two dimensions. The quantum dot material prepared by the process has good uniformity, and the Nano-column structure can also be accurately ordered. However, its inherent series of defects, such as slow preparation process, high pollution, high cost, high defect density of the prepared quantum dot material is very low. Therefore, although the process has been extensively researched, it is still difficult to put into practical use.

The other two preparation processes are still quantum dot epitaxial growth processes prepared by physical preparation methods, including a patterned epitaxial growth process and a self-assembled quantum dot growth process. For example, as reported by T. Fukui and S. Ando in 1991, metal oxide chemical vapor deposition (MOCVD) was utilized to fabricate GaAs island-shaped quantum dot on the optional region of GaAs substrate [41]. In 2001, P. Petroff and A. Lorke exploited the self-assembly island-shaped quantum dot with MOCVD and MBE (molecular beam epitaxy)

[42]. However, the uniformity of this quantum dot growth process is very poor, and the shape and size of the quantum dots cannot be controlled, and the lithography patterning process is required to be assisted, so that it is difficult to be practically applied in electronic devices.

The biggest problem of the aforementioned quantum dot physical synthesis process is that the synthesis temperature is high, the cost is high, and it cannot be prepared in a large area and large size in the microelectronic device. It is even more incompatible with flexible substrates that require a room temperature and pressure process. In recent years, the preparation of quantum dot materials by chemical solution method has become a new breakthrough. Scientists used cadmium oxide (CdO) and selenium (Se) elements to synthesize quantum dot materials at low temperatures (225°C) in solution [43]. This quantum dot synthesis process is simple, environmentally friendly, and synthesized at low temperatures. More importantly, the quantum dot material is tunable in size, controllable in the band, and can be sprayed or spin coated onto any substrate device in a simple manner after being synthesized in solution as illustrated in Fig1-11.

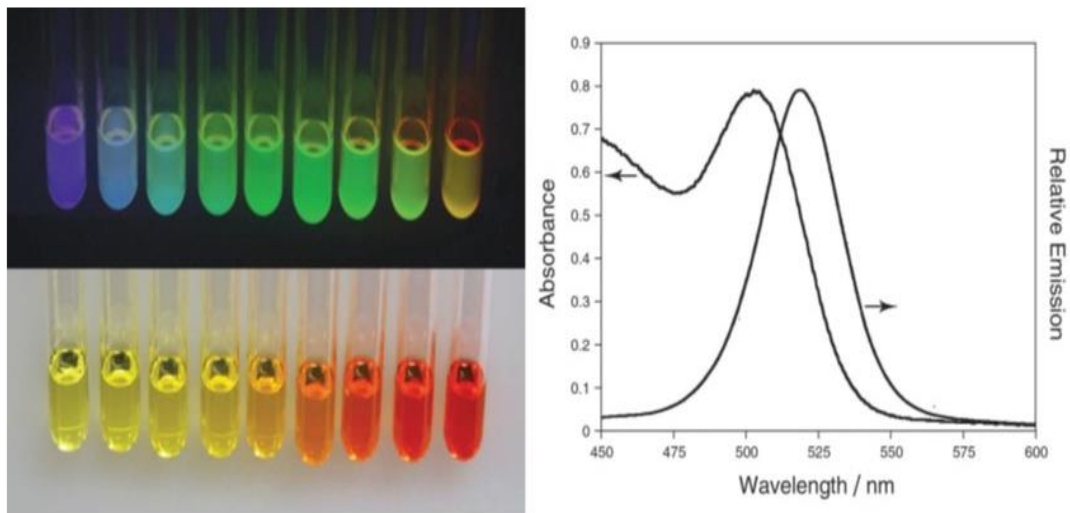


Figure 1-11 Solution process of the CdSe Quantum Dots fabrication [43]

Depending on the application environment and type, the researcher can use a

suitable chemical synthesis method to prepare quantum dots with different chemical compositions, different wavelength bands and different sizes, including Cu₂S and PbS material [44-47].

1.3 The research status of the Quantum Dots photodetectors

1.3.1 UV-Vis photodetectors

Ultraviolet (UV) light wavelengths range from 10 nm to 400 nm, while 1 nm to 10 nm are now also referred to as the extreme ultraviolet spectral range. Ultraviolet light has very few components in the solar spectrum, and most of it is absorbed by the ozone layer, and it is even weaker on the surface of the earth. This band has a wide range of applications in the military. For example, the flame emitted by a missile aircraft generates a large amount of ultraviolet radiation. The flame burning in our daily life also emits ultraviolet light, so the UV detector is widely used in national security, fire alarm and other aspects.

In research field, the study of the UV photo-detectors focused on the wide bandgap semiconductor material ZnO. As a versatile semiconductor material, ZnO has a band gap of 3.37 eV and absorbable photon energy in the ultraviolet range. It is an ideal semiconductor material for UV detectors.

In 2007, C.Soci and A.Zhang et.al. report the UV photo-detectors with single ZnO nanowire, the work was reported in Nano letters. With 390nm incident light, the photoconductive gain of the device is 10⁸. [48]

In 2013, Biao Nie and Ji-Gang Hu et.al. report the detectors based on the ZnO nanorod array for high performance. With 365nm Ultraviolet light, the response frequency achieves 2250Hz. [49]

Recently, due to the research of the Quantum Dots(QDs), the UV photodetectors with QDs has been the research hotspot. In 2017, Ludong Li and Leilei Gu et.al reported

the UV image sensors based on the ZnO Quantum dots decorated Zn₂SnO₄ nanowire, which provide light-to-dark current ratio (6.8×10^4), specific detectivity (9×10^{17} Jones), photoconductive gain (1.1×10^7), fast response and excellent stability with 300nm incident light. [50]

The waveband from 400nm to 800nm is the visible light band. This band is the most familiar range. From colorful scenery to colorful neon, it is in the range of visible light. The application of detectors in the band is also very extensive. Optical measurement based on visible light wavelength has been widely used because of its high precision, high speed, and no damage to the sample. Therefore, efficient photodetector components have become a research hotspot and have an important role in daily life and industrial production. The most common is the imaging system, the digital CMOS (Complementary Metal Oxide Semiconductor) system has been successfully used in the field of consumer electronics, and the CCD (Charge-coupled Device) detection system is also widely used in high-end consumer electronics and special fields. They also have many advantages such as fast imaging speed and rich optical signals.

With the development of the nano-scale material, more and more researcher focus on the new materials visible photodetectors for low cost, flexible and simple fabrication process.

In 2009, Jason P. Clifford reported the work which focused on the tuneable colloidal-quantum-dot photodetectors with the various advantages such as fast response, sensitive and spectrally. The wide photo-sensitive waveband (from 400 to 1800nm), the detectivity is approximately 1×10^{13} Jones. [51]

Then, in 2015, Seung Won Shin et.al. reported the work of the highly transparent, visible-light photodetector based on oxide semiconductors and QDs. The device showed a responsivity of 1.35×10^4 A/W and an external quantum efficiency of 2.59×10^4 under illumination by a 635nm incident light. [52]

In this thesis, we focused on the combination of the QDs and low demission materials for design the UV-visible photodetectors in Part A.

1.3.2 NIR photodetectors

In 2000, the Leatherdale's group first reported the CdSe Quantum Dots photoconductive photodetectors. The group successfully measure the core-shell structure shielding effect. The correlation between quantum dot particles spacing and photoionization efficiency was also studied [53].

In 2005, as reported by S.A. McDonald, PbS Quantum dots were utilized in the photoconductive photodetector. With 975nm incident light, the photodetector exhibits the internal quantum efficiency as 3%, the $I_{\text{light}}/I_{\text{dark}}$ as 630, and the largest photo-current response as $3.1 \times 10^{-3} A/W$ [54].

In 2006, G.Konstantatos et.al reported the solution process of the PbS Quantum Dots photodetectors. The photo-gain of the detectors is more than 100. And the photo-detectivity is higher than $5 \times 10^{12} Jones$, with the 800nm incident light. [55].

In 2012, Jae Woong Lee et.al fabricated the high-performance near-infrared photodiode based on the solution process and PbS Quantum Dots. With 1500nm incident light, the photodiode exhibits the photo-detectivity as $7 \times 10^{13} Jones$.. More importantly, this photo-detectivity is higher than the commercial InGaAs photodiode [56].

In 2015, Valerio Adinolfi's group reported a device which utilize the PbS Quantum Dots as the photo-sensitive layer and the MoO₃ as the top gate for photo heterojunction field effect transistors. The device exhibits a fast photo-response which decreases to 10 μ s [57]. Meanwhile, Lyudmila Turyanska et.al reported the triode photo-transistor with PbS Quantum Dots and monolayer graphene. With the modification of the ligand, the photo-responsivity increases to 10⁹A/W with the 532nm incident. [58].

Colloidal quantum dot photodetectors mainly include three types of structures: photoconductors, photodiodes and field effect phototransistors [59-61]. Colloidal quantum dots can be used to prepare photosensitive films separately or in combination with other materials to prepare photoelectric composite films for different types of photodetectors. Photoconductive quantum dot photodetectors are typically composed of a quantum dot semiconductor material and two ohmic metal contacts to form a dual port electronic device as illustrated in Fig1-12(a). With the incident light, the conductivity of the material changes due to the change in carrier density. Due to the generation of electron-hole pairs during illumination, the carrier density increases and the electrical conductivity of the material increases. Photoconductive gain is produced when the number of circulating charge carriers generated by each photon absorbed by the photoconductor is greater than one. The physical mechanism of the photoconductive gain is derived from the photosensitive defect state, also known as the photosensitive center. It is possible to bind one type of carrier (such as an electron) and not to bind another type of carrier (such as a hole). The electrons are bound by the defect state in the conduction band, and the holes circulate in the channel as illustrated in Fig1-12(b). The photoconductive gain is equal to the ratio of carrier lifetime to carrier transit time. If the lifetime of the holes exceeds the transit time, the long lifetime of the bound electrons ensures that the holes can be circulated multiple times in the outer circuit, resulting in a gain.

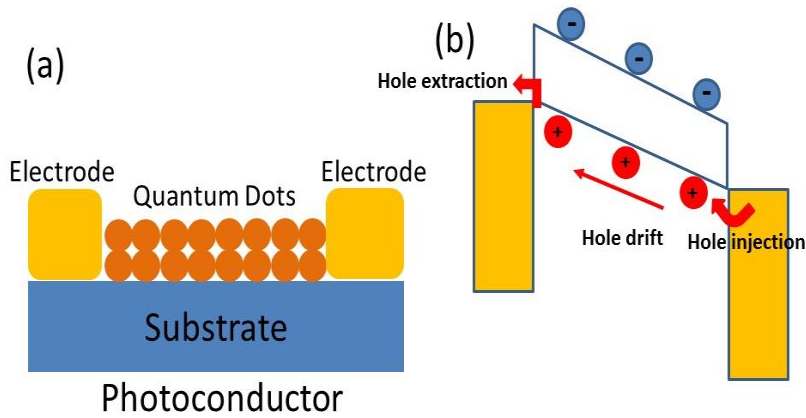


Figure 1-12 (a) Quantum Dots Photoconductive Photodetector structure (b) the energy band of the Quantum Dots Photoconductive Photodetector

As illustrated in Fig1-13(a), the quantum dot photodiode is formed by a quantum dot sheet connected to two electrodes of different work functions. The built-in electric field is generated due to the difference in material band structure. As the Fermi level of the material in the heterojunction reaches equilibrium, a built-in electric field is generated in the depletion region near the quantum dot heterojunction. The built-in electric field pushes electrons and holes in opposite directions.

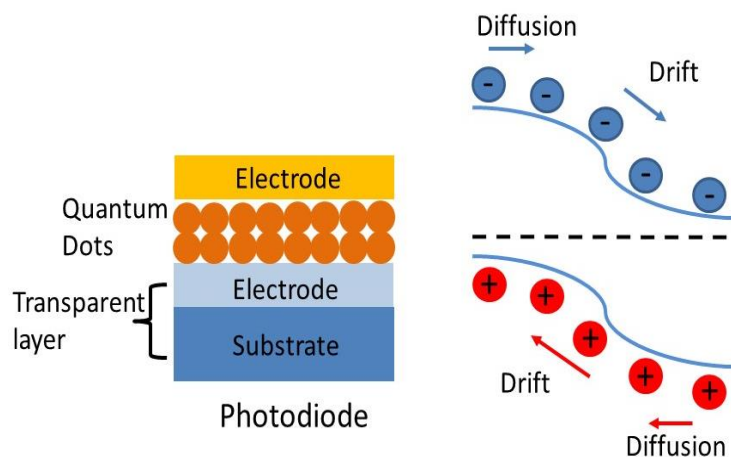


Figure 1-13(a) the Quantum Dots Photodiode detector structure (b) the energy band of the Quantum Dots Photodiode Photodetector

The principle of the photodiode is that the light is irradiated on the heterojunction to generate photogenerated electron-hole pairs. Under the action of the built-in electric field, the photogenerated electron-hole pairs are rapidly separated, and the photogenerated carriers are transported to the metal electrode. Each time a photon is absorbed to generate a carrier, the principle ensures that the quantum efficiency of the photodiode is not more than one. At the same time, since the response time of the photodiode is determined by the transit time of the carrier, rather than by the carrier lifetime, the photodiode is generally faster than the photoconductor. The electron-hole pairs in the photodiode are separated by the built-in electric field, and then the electrons and holes flow to the electrode under the action of the electric field. As explained in Fig1-13(b), after absorbing light, the energy of the photons is transferred to the electrons in the semiconductor, and the electrons are excited to the conduction band, leaving a hole in the valence band. The energy band diagram shows the junction region when p-type (more holes) and n-type (more electrons) semiconductors are close to equilibrium. In the p-n junction diode, the dotted line indicates the Fermi level.

The field effect phototransistor type photodetector can achieve low dark current and high gain at the same time, and has a high application prospect [61]. The field effect phototransistor structure is similar to the lateral photoconductivity of a metal-semiconductor-metal structure having a source and a drain, but the third electrode (the gate electrode in which the semiconductor channel is contacted by the insulating layer) can be used to modulate the channel conductivity (as shown in Fig1-14a). The applied gate voltage V_{GS} controls the carrier density by field effect modulation, allowing the device to operate in a depleted state to turn off the dark current of the device. The incident light generates photo-generated carriers in the channel, changes the conductivity of the device channel, and then uses the photoconductive gain mechanism to analyze the photoelectric characteristics of the device. In order to achieve high performance field effect phototransistors, the ideal channel material should have high

carrier mobility to achieve a high gain bandwidth product, and a moderately sized direct bandgap for current modulation and light absorption in the channel.

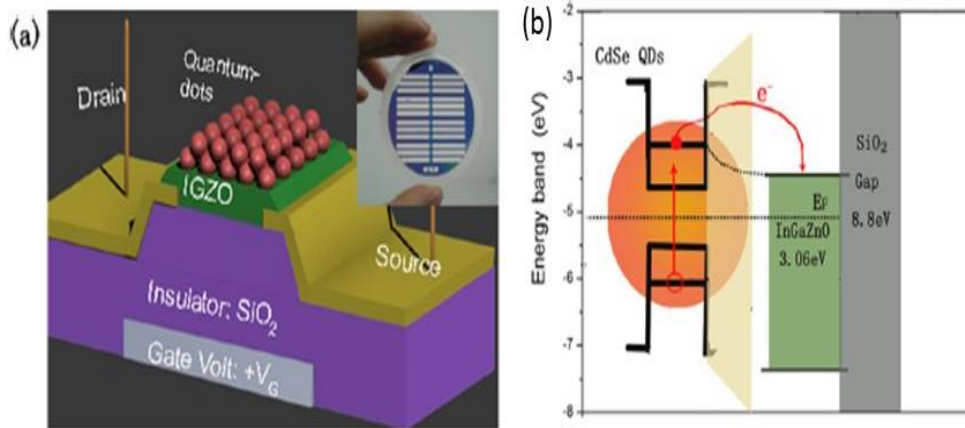


Figure 1-14 (a) Quantum Dots photo-transistor structure. (b) the energy band of the Quantum Dots Photo-transistor

In the device structure, the source and drain are used to inject and discharge charge carriers. The insulating layer separates the gate from the semiconductor. A gate electric field is generated by applying a voltage to the gate to control the current in the channel. A charge transport channel is formed at the interface between the insulating layer and the semiconductor layer, and the width of the charge transport channel is controlled by the gate electric field. With the electric field effect, the photo-generated carriers inject the semiconductor (as shown in Fig1-14b).

1.4 The Characteristics of the Photo-detector

There are four main indicators for evaluating the performance of photodetector devices: 1. Responsivity; 2. External quantum efficiency (EQE); 3. Sensitivity; 4. Detectivity.

- *Responsivity:*

The introduction of responsiveness is to quantitatively study the relationship

between the electrical signal output by the detector and the optical signal. This is the main parameter to measure the response performance of the device. Responsivity is defined as the ratio of photocurrent to illumination area in A/W.

The photo responsivity could be calculated from Eq.1-1 with the transfer characteristic:

$$R = \frac{I_{total} - I_{dark}}{P} = \frac{I_{ph}}{\rho \cdot S} \quad 1-1$$

Herein, P represents optical power, I_{total} denotes total current, I_{dark} is dark current, I_{ph} is the photocurrent, ρ indicates optical incident power density, and S is the effective area of the photoelectric reaction.

Responsivity describes the results of changes in electrical signals caused by certain illumination intensities. Therefore, it can only reflect one aspect of detector sensitivity.

External Quantum Efficiency (EQE)

The external quantum efficiency is described as the ratio of the number of charge carriers collected by the device to the number of incident photons under illumination of incident light. The device performance can be expressed by this parameter, and external quantum efficiency (EQE) can be calculated for the Eq.1-2

$$EQE = \frac{I_{ph}/q}{\rho/h\nu} \times 100\% \quad 1-2$$

In Eq2, I_{ph} is the photo current, q the quantity of one electron, ρ the incident optical power density, h the Plank constant, and $h\nu$ the incident photon energy.

Sensitivity

The photo-sensitivity is the amount to which an object reacts upon receiving photons. Normally, the photo-sensitivity could be calculated in Eq.1-3,

$$S = \frac{I_{\text{total}} - I_{\text{dark}}}{I_{\text{dark}}} \quad 1-3$$

As previously, I_{total} denotes total current, I_{dark} is dark current. These parameters can be obtained from static transfer characteristics to calculate the photo-sensitivity.

Detectivity

Detectivity can evaluate the performance of detectors of different geometries, and it can evaluate the sensitivity of photoconductive materials relative to detectors of a specific size. Besides, detectivity (D) is an important parameter that indicates the ability of phototransistor to measure weak optical signals. D is given by Eq 1-4,

$$D = \frac{R}{\sqrt{2qI_{\text{Dark}}}} \quad 1-4$$

Where R is the photo-responsivity, I_{Dark} is the dark current, and q is the elementary charge.

2 The Organic Semiconductor Thin-Film Transistor

2.1 Development of the Organic Electronics

Organic semiconductor materials are used in many fields, such as organic field effect transistors, organic solar cells, organic electroluminescent diodes, organic sensors and memories. A simple introduction to devices using organic semiconductor materials is presented as follow [52-64].

Organic solar battery

The main advantage of the organic solar cell prepared by using the organic material compared to the single crystal and amorphous Si solar cell is that the manufacturing cost is greatly reduced and the preparation process is simple. Its working principle is to use organic semiconductor materials to generate electron hole pairs by absorption of sunlight, further dissociation, and transport to the electrodes to be collected. The basic structure of an organic solar cell mainly has a double-layer heterojunction structure and a bulk heterojunction structure.

Organic Light Emitting Diode

There are two main applications in Organic Light Emitting Diode (OLED). One is information display and the other is solid-state lighting. Under the action of the applied voltage, holes/electrons are injected into the highest occupied molecular orbital (HOMO) and lowest unoccupied molecular orbital (LUMO) of the organic functional layer through the anode/cathode respectively. The excitons are transported to the luminescent layer through the carrier transport layer, and excitons with a certain lifetime are diffused. A part of the excitons are radiated, and part of the exciton energy is consumed by non-radiative recombination as illustrated in Fig 1-15.

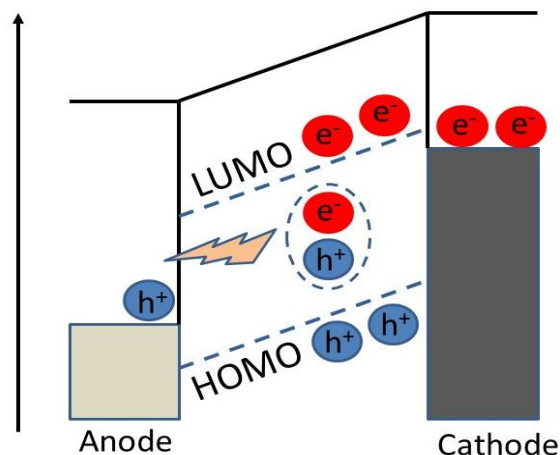


Figure 1-15 the mechanism of the OLED

Organic Thin-Film Transistor

Organic Thin-Film Transistor (OTFT) is a field effect transistor with an organic small molecule or polymer film as an active layer and deposited on an insulating layer substrate with logic switching characteristics. Thin film transistors play an important role in microelectronics as the main driving components. The specific working principle of OTFT will also be described in detail in the following sections.

Organic Sensor and Memory

In electronic information technology, the collection, exchange, storage and processing of information is also very important. Sensors can collect information, detect and identify changes in physical/chemical states within a specific range. Organic sensors have good biocompatibility and are easy to prepare on different kinds of substrates. According to the different characteristics of organic materials, sensors of various types such as photosensitive, heat sensitive, force sensitive, gas sensitive and humidity sensitive can be developed separately. The memory can exchange, store and process information. The requirement for the memory is that the reaction time is fast, the stability is good, and the device size and storage density are as low as possible.

2.2 Research status of OTFT

2.2.1 Development of OTFT

Although in 1964, scientists observed field effect characteristics on organic semiconductor material copper phthalocyanine (CuPc) films [65]. However, the polythiophene-based organic field effect transistors, which were recognized as the first organic thin film transistor devices, were successfully developed until 1986 [66]. And the performance standard that can work effectively on the organic circuit is achieved, the field effect mobility μ reaches $10^{-5}\text{cm}^2/\text{Vs}$, the threshold voltage V_{TH} reaches -12V , and the switching current ratio $I_{\text{Don/Doff}}$ reaches the order of 10^2 . Looking back at the entire history of organic thin film field-effect transistors, there are countless milestones.

In 1986, Tsumura et al. synthesized polythiophene by electrochemical polymerization and used it as an active layer to prepare the first organic thin film transistor device that can be used in organic circuits [66].

In 1989, small organic molecules were used as field effect materials for the first time on the historical stage. Horowitz et al. prepared an OTFT device based on oligothiophene [67].

In 1994, Gamier et al. tried new techniques and successfully developed all-organic OTFT devices by printing [68].

In 1996, Katz et al. through several experiments and comparative analysis, the research proves that the morphology of pentacene film is closely related to the performance of the device [69]. One year later, Y. Y. Lin et al. modified the insulating layer by using a finishing layer, thereby controlling the surface morphology of the pentacene film. The device performance has been greatly optimized with a switching current ratio of up to 10^8 orders of magnitude and a mobility of $1\text{cm}^2/\text{Vs}$. Compared to amorphous silicon transistor devices, such device performance has reached a standard that can be applied to a wide range of applications in flat panel display [70].

In 2004, Jurchescu chose to use the excellent semiconductor material of pentacene to prepare an OTFT device with an active layer of pentacene single crystal film. With the use of polymers as an insulating layer, its mobility has reached a historic height. With the room temperature 295K the carrier mobility has arrived up to 35 and 58 cm^2/Vs [71].

In 2006, Ichikawa et al. significantly improved the mobility of OTFT devices by vacuum annealing[72]. Itaka et al. [73] and Anthopoulos et al. [74] respectively made the mobility of the prepared C60 thin film transistor to $4.9\text{cm}^2/\text{Vs}$ and $6\text{cm}^2/\text{Vs}$ by using Mg as the source-drain electrode and the substrate during the deposition process of the active layer.

In 2012, Ting Lei et al. [75] used a polymer semiconductor material to prepare a P-type OTFTs device with a mobility of $3.62 \text{ cm}^2/\text{Vs}$).

In 2015, Wu et al. prepared a thermally stable, biocompatible, flexible organic thin film transistor and realized its application in artificial skin temperature sensing arrays [76].

Although existing organic thin film transistors have disadvantages such as low mobility, low switching current, and high threshold voltage, organic thin film transistors have the following advantages.

- (1) Organic semiconductor materials have many kinds and can obtain more ideal semiconductor materials through molecular design and synthesis, and prepare organic thin film transistor devices with better performance;
- (2) Organic semiconductor materials have good flexibility characteristics, and can realize fully flexible devices and circuits that do not significantly change electrical properties even after bending and twisting [77].
- (3) Organic semiconductor materials can be prepared by a variety of chemical

methods, greatly reducing the cost of the device equipment, simplifying the preparation process, and achieving large-area processing.

- (4) With more and newer organic film forming technology, the device size is getting smaller and smaller, the weight is getting lighter, the integration is getting higher and higher, the operating power is getting lower and lower, and the computing speed is getting faster and faster.

All of the above advantages make organic thin film field effect transistors have broad market prospects.

2.2.2 The basic points of OTFT

The basic structure of the OTFT is as shown in the following figure, and is usually composed of five parts of a substrate, a gate electrode, an insulating layer, an active layer, and source/drain electrodes. The four different structures shown in the figure are the bottom gate top contact and the bottom gate bottom contact, respectively.

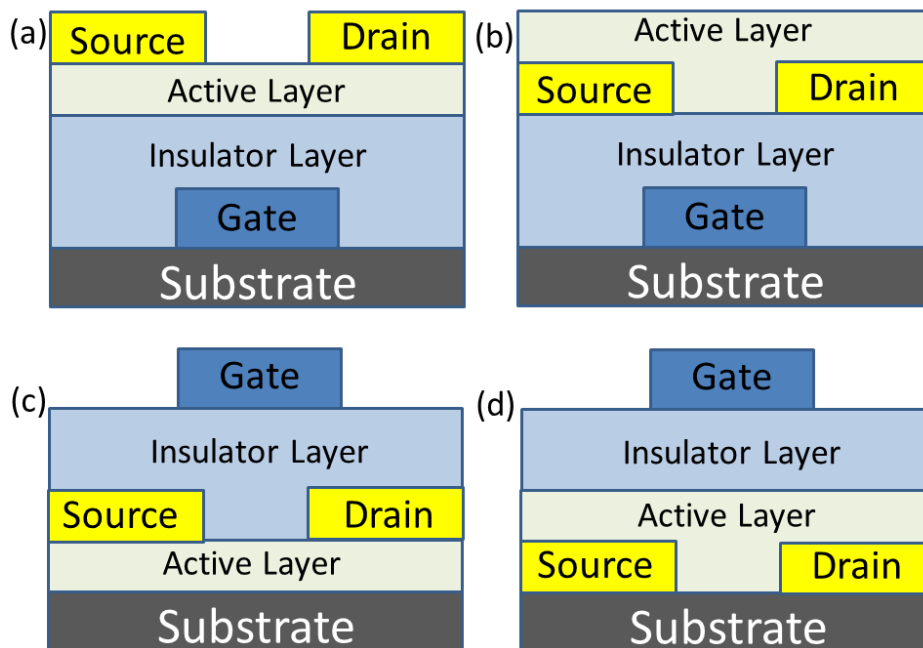


Figure 1-16 (a) bottom gate top contact structure. (b) bottom gate bottom contact structure. (c) top gate top contact structure. (d) top gate bottom contact structure

Due to the processing characteristics of the organic material and its own properties, the device with the top gate structure may damage the active layer during the preparation process, thereby affecting device performance. In addition, the preparation process of the bottom gate structure is simpler. Therefore, the bottom gate structure is currently a relatively common structure. However, since the transmission path of the charge carriers is different, and the difference in the contact area and the contact quality between the source and the drain electrode and the organic semiconductor layer, the performance difference between the top contact structure and the bottom contact structure is relatively large. In the top contact structure, the semiconductor layer is synthesized at first. And then, the source-drain contact electrodes are fabricated. The molecular packing and structural quality of the semiconductor are better for the interface between semiconductor and electrodes more smoothness. In the bottom contact structure, since the source and drain electrodes are prepared first, and the semiconductor layer is deposited later, the patterning method of the electrodes is more convenient. Precise patterning techniques such as photolithography and electron beam etching can be applied, which is more useful to the practical application of the device. However, due to the inkjet printing methods, bottom gate bottom contact structure is more convenient for fabrication.

During operation of the organic thin film transistor, a voltage is usually applied to the gate electrode and the drain electrode, and the source electrode is kept grounded. The potential difference between the source electrode and the gate electrode is commonly defined as the gate voltage (V_{GS}). The potential difference between the source and drain electrodes is often defined as the source-drain voltage (V_{DS}). The source electrode is an injection electrode of charge carriers. When a positive voltage is applied to the gate, electron injection is performed, and a hole is injected when a negative voltage is applied to the gate. When the OTFT device is in operation, a certain voltage is applied to the gate, causing charge carriers (electrons or holes) to be induced

in the organic semiconductor layer near the insulating layer. Under a certain source-drain voltage, the induced charge can form a conductive channel and participate in conduction, resulting in an order of magnitude decrease in the resistivity of the semiconductor. By adjusting the magnitude of the gate voltage, it is possible to change the amount of induced charges in the organic semiconductor layer. The width and narrowness of the conductive channel between the source and drain electrodes are changed and then the source-drain current is changed. That is to say, in the organic thin film transistor, the effect of controlling the source leakage current can be achieved by adjusting the gate voltage.

2.2.3 Electrical characteristics of OTFT

- *Transfer Characteristics*

With a constant drain-source voltage V_{DS} , the transfer characteristics corresponds to the measurement of drain current I_D as a function of the gate-source voltage V_{GS} . As presented in Figure 1-17, a typical transfer characteristic of a N-type OTFT can be defined by 3 operation zones.

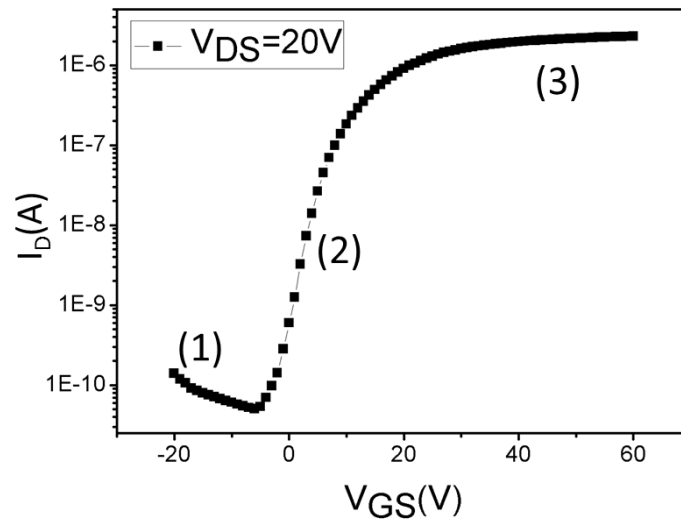


Figure 1-17: Typical transfer characteristic of N-type OTFT

The first area shows the OTFT behavior in off state with a current ($I_D=I_{OFF}$). The

low value of current is primarily due to the electrical conductivity of the active layer, which should be as low as possible in order to decrease this current. An increase of this current under a reverse gate voltage can be observed sometimes, is due to the activation of the carriers by the inverse electric field.

The second area shows that the formation of the channel and the drain current increases rapidly with the gate voltage.

The third area shows the on state of OTFT ($I_D=I_{ON}$).

- *Output characteristics*

The output characteristics correspond to the measurement of current I_D as a function of the drain-source voltage V_{DS} for a constant gate-source voltage. As showed in Fig1-18, a typical output characteristics of a N-type OTFT show clearly the linear regime under a weak drain-source voltage and the saturation regime occurs when V_{DS} becomes larger than $|V_{GS}-V_{TH}|$. This figure also shows the drain current variation with different gate voltages.

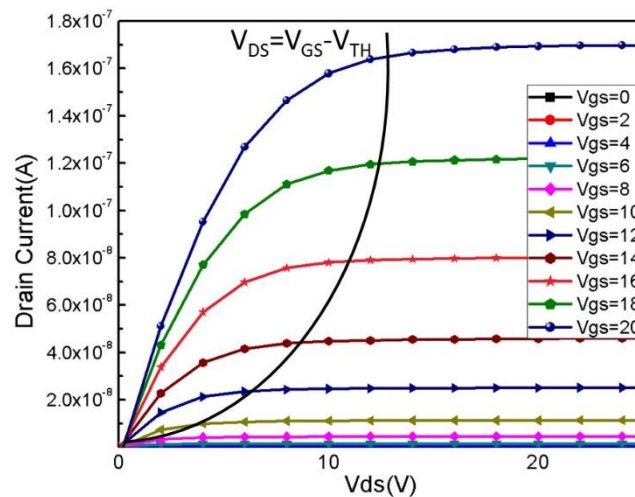


Figure 1-18 Output characteristics of a N-type OTFT

- *Carrier mobility*

Carrier mobility is one of the most important characteristics of the OTFT. It refers to the drift velocity of charge carriers under the action of a unit electric field. The mobility in a thin film transistor is divided into a mobility of a linear region and a mobility of a saturated region. When the device is operating in the linear region, the device channel conductivity varies linearly with the density of the electric field induced charge and can be calculated with the equation 1-5 and 1-6.

$$I_D = \frac{W}{L} \mu C_i (V_G - V_T) V_{DS} \quad (1-5)$$

$$\mu_{eff} = \frac{L}{WC_i V_{DS}} \frac{\partial I_{DS}}{\partial V_G} \quad (1-6)$$

Here, L is the distance between source and drain electrodes (called length of the conductive channel under the gate) and W is the length of these electrodes in front (called the width of the conductive channel under the gate). μ_{eff} is the field effect mobility; C_i is the insulator capacitance per unit area. V_{GS} , V_{TH} , V_{DS} are the gate-source voltage, the threshold voltage and the drain-source voltage.

When the device is operating in the saturation region, the field effect mobility of the device can be obtained by Equations 1-7 and 1-8.

$$I_D = \frac{W}{2L} \mu C_i (V_G - V_T)^2 \quad (1-7)$$

$$\mu = \frac{2L}{WC_i} \left(\frac{\partial \sqrt{I_{DS}}}{\partial V_G} \right)^2 \quad (1-8)$$

Typically, the field effect mobility calculated in the saturation region is greater than the field effect mobility calculated in the linear region. If the field effect mobility of the saturation region is closer to the field effect mobility of the linear region, it can reflect that the contact resistance of the device is smaller. That is, the contact quality between the source and drain electrodes and the organic semiconductor layer is good. At this

time, the contact resistance has a smaller influence on the device performance of the organic thin film transistor.

In organic thin film transistors, there are many factors affecting the field effect mobility, such as the type and purity of semiconductors, the size of semiconductor grains, the difference in crystal quality, the difference in device configuration, the contact between electrodes and semiconductors, and the trench of devices, length to width ratio and so on.

- *Threshold Voltage V_{TH}*

The threshold voltage (V_{TH}) is the lowest value of the gate-source voltage when the organic thin film transistor device is in operation.

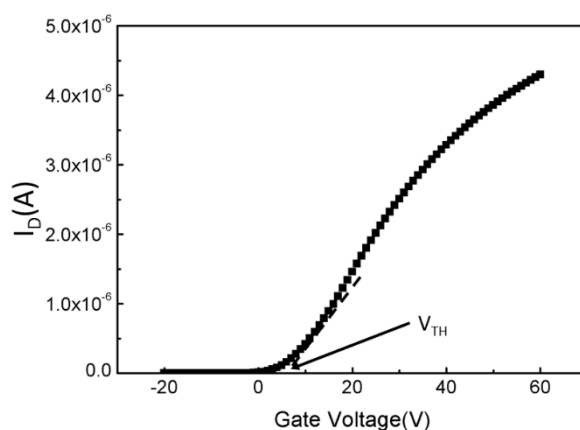


Figure 1-19 the threshold voltage of a N-type OTFT

In organic thin film transistors, the threshold voltage is mainly affected by the interfacial properties between the insulating layer and the organic semiconductor layer, the generation of dipoles in the interface, the impureness of the semiconductor layer, the interface state and the charge trap density. In practical applications, it is generally advantageous that the absolute value of the threshold voltage is smaller.

- The current on/off ratio I_{DON}/I_{DOFF}

Generally, the ratio of the maximum value of the on-state current to the minimum value of the off-state current in the transfer characteristic curve of the organic thin film transistor is defined as "current on/off ratio".

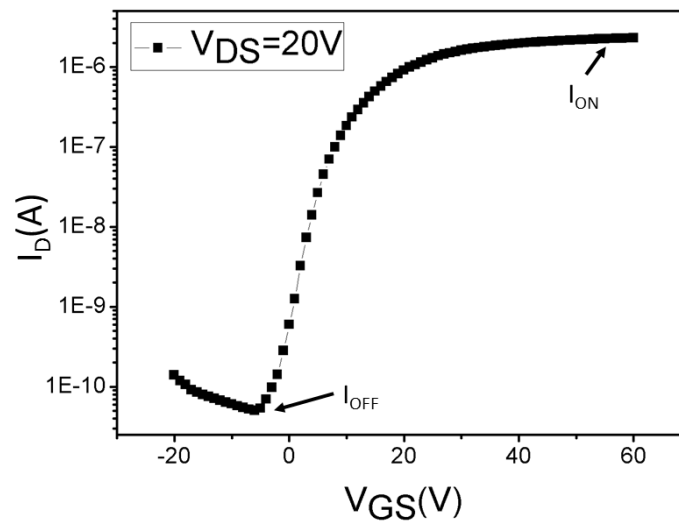


Figure 1-20 the on/off ratio of a N-type OTFT

In practical applications, it will be more useful in the active matrix display and logic circuit with the larger the value of the current switching ratio. To achieve better stability, immunity to interference, and greater load drive capability, higher current switching ratios are required. In the case where the contact resistance between the source, drain electrode and the semiconductor layer is negligible; the highest on-state current depends on the intrinsic mobility of the organic semiconductor and the capacitance per unit area of the insulating layer. The magnitude of the off-state current is determined by the gate leakage current, the conduction path of the interface of the insulating layer, and the body conductance of the organic semiconductor. Usually, the unintentional miscellaneous organic semiconductor, or oblique incidence during the evaporation of the source and drain electrodes, causes the value of the off-state current to become large.

- *Subthreshold Slope SS*

The subthreshold Slope is one of the important characteristics, it can be calculated by the equation 1-9:

$$SS = dV_G/d(\log_{10} I_{SD}) \quad 1-9$$

The subthreshold slope reflects the rapidity of the source-drain current switching from the off state to the on state during the operation of the organic thin film transistor. The smaller the SS, the faster the transition from the off state to the on state and the smaller the change in gate voltage. The subthreshold slope is related to the capacitance per unit area of the insulating layer and the performance of the interface between the organic semiconductor layer and the insulating layer.

- *Hysteresis characteristics*

The hysteresis characteristics corresponds to the measurement of current I_D as a function of the gate voltage V_{GS} for a constant drain voltage V_{DS} . The measurement of the transfer characteristic is performed when gate-source voltages increases then when it decreases. The difference between these two curves is called hysteresis. As shown in fig 1-21, a typical N-type hysteresis characteristic exhibits the difference between these two curves.

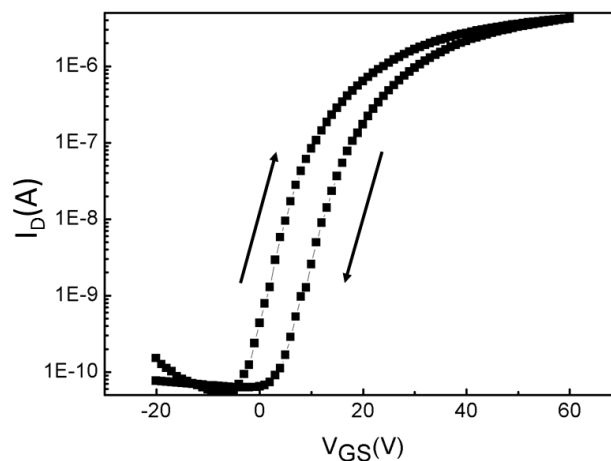


Figure 1-21 hysteresis characteristic of a N-type OTFT

The hysteresis may be related to the charge trapping and de-trapping at the interface between the active layer and the insulator layer, or in the insulator layer.

2.3 Organic Semiconductor Material: Fullerene (C60)

Organic semiconductor materials are the core materials of OTFTs. In the preparation process of OTFT, the nature, purity and film quality of the organic semiconductor material directly affect the overall performance of the device. There are three requirements for the nature of the material itself: First, Stable electrochemical properties. Second, the HOMO level or LUMO level facilitates the injection of carriers [78]. Third, it has a π -bond conjugated system that facilitates carrier transport. The organic semiconductor material can be classified into two types: a polymer material and a small molecule material according to the molecular weight of the material. In general, the polymer material can be prepared by LB film, spin coating, inkjet printing, etc., and the process is simple and low in cost, but the field effect mobility is low due to poor adhesion of the material π bond [79-80]. In contrast, organic small molecular materials are easy to purify, and it is easier to prepare polycrystalline or even single crystal films, so the mobility is usually higher [81]. The organic semiconductor material can also be classified into a P-type material in which a majority of carriers are holes and an N-type material in which majority carriers are electrons, depending on carriers to be transported. Pentacene is currently the most widely used P-type material in OTFT [82]. The active layer material C60 selected in this work is one of the most common N-type materials[83-84].

C60, also called fullerene, has an HOMO level of 6.2 e V, a LUMO level of 3.6 eV, and a forbidden energy band gap of 2.6 eV [85]. The molecular structure is shown in Figure 1-22.

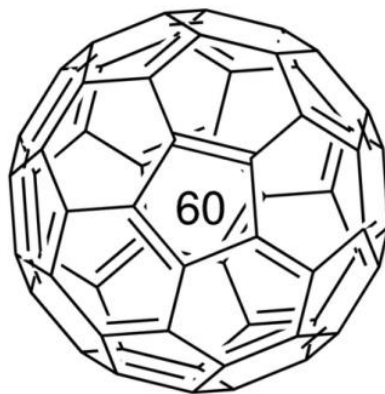


Figure 1-22 the molecular structure of the C60

When the C60 was bombarded with graphite by Kroto et al. in 1985 [86], it was found to be the third allotrope of carbon after diamond and graphite. C60 is a symmetrical football-like molecule composed of 60 carbon atoms with a molecular weight of 720 and a molecular diameter of about 0.7 nm. As a large fused aromatic hydrocarbon, C60 has the property of electron-deficient olefin and the ability to supply electrons. It is an excellent electron transport material. The disadvantages of C60 is its poor stability and the instable conductivity that is easily affected by water and oxygen in the air. Therefore, the electrical performance of the C60-based OTFT prepared in this work is carried out in a glove box under a low oxygen and low moisture environment (<1ppm).

The performance of OTFT is closely related to the film formation quality of the active layer film, and the highly crystalline film is more favorable for carrier transport [87]. The implementation of some high performance C60-based OTFTs also relies on a highly crystalline C60 active layer film. In general, there are two main ways to increase the crystallinity of C60. The first method is to increase the crystallinity of the film by introducing a special layer of modification. Itaka et al. [88] prepared a thin film of pentacene on an Al₂O₃ substrate and then prepared a C60 film. The devices with a maximum mobility of 4.9 cm²/Vs. The effect of the pentacene modified layer on the

device performance was compared. It was found that the electron mobility of the device directly grown on the insulating layer was $0.25\text{-}1\text{ cm}^2/\text{Vs}$, and the mobility of the device after the introduction of the pentacene modified layer reached $2\text{-}4.9\text{ cm}^2/\text{Vs}$. Through characterization, it was found that the surface morphology of C60 film grown on the pentacene modified layer was significantly improved, and obvious hexagonal grains could be directly observed. The second method is to heat treat the C60 film. The device with a mobility of $6\text{ cm}^2/\text{Vs}$ prepared by Anthopoulos et al. [89] is a C60 film prepared by HWE technology at a high temperature of $250\text{ }^\circ\text{C}$. Singh et al. [90] studied the relationship between the crystallinity of C60 film and the deposition temperature more systematically in the subsequent work. In the experiment, the morphology of C60 film at $25\text{ }^\circ\text{C}$, $120\text{ }^\circ\text{C}$ and $250\text{ }^\circ\text{C}$ was compared by using AFM and XRD. It was found that the crystallinity of the film was enhanced significantly under high temperature conditions, and the field effect mobility of the corresponding device was improved. From $0.6\text{ cm}^2/\text{Vs}$ at $25\text{ }^\circ\text{C}$ film formation to $6\text{ cm}^2/\text{Vs}$ at $250\text{ }^\circ\text{C}$ film formation. In our work, the C60 film is thermally evaporated at ambient temperature and then the effect of the post thermal annealing is analyzed.

3 Printing Electronics

Printing electronics benefits from techniques already developed in the field of graphic arts last centuries. The past few years, a growing interest has gained for additive printing technologies. Such technologies offer an alternative to others based on conventional lithography processing using silicon derivative materials, for instance. Printing electronics offers many advantages such as: 1) unconventional substrates processing (flexible, stretchable, wearable...), 2) large area processing, 3) fast processing, 4) environmentally friendly processing, 5) low capital investment, 6) low time lapse from idea to the fabrication. Consequently, printing electronics has gained a growing interest throughout the past decades and many applications can be envisaged.

Printing electronics, benefiting from previously mentioned advantages, has become the most suitable technology for realizing large area applications such as printed RFID tags, sensors and flexible display. As shown in Fig 1-17, the roadmap for organic and printed electronics applications is published by the Organic Electronics Association.



Figure 1-23: roadmap for organic and printed electronics applications [91]

3.1 Development of the inkjet printing

As a kind of meaningful patterning technology for converting electronic data onto substrates such as paper or glass, inkjet printing technology has been widely used in people's daily life and work [92]. Especially in recent years, inkjet printing technology has been applied more to the spraying of tiny amounts of materials, such as welding glue for spraying microelectronic devices, lubricants between mechanical parts, and the like. With the development of inkjet printing equipment, inkjet printing technology enables tiny droplets to be accurately positioned at the desired position. And it can effectively save materials and reduce costs and environmental friendliness. Inkjet printing technology has gradually become a solution process microelectronic device in the field of organic semiconductors, such as organic electroluminescent devices [93] (especially organic full color display), color filters in LCD [94], organic field effect transistors [95]. Inkjet printing is not a independent technology, but an integration with

different technologies. These techniques have similar functions to accurately produce free-moving droplets. The volume of the droplets, the time the droplets are produced, the speed at which the droplets move, and the trajectory of the movement can all be precisely controlled by the application of specific techniques. The material is only deposited in the desired location, which is more environmentally friendly. In general, inkjet printing is one or more layers used to deposit device structures. Different from the traditional deposition method, the material utilization rate of inkjet printing is over 90%, and the deposition profile can be fairly uniform on the substrate, resulting in a high-quality film. Compared to other printing processes, inkjet printing is readily adaptable to pattern writing/no mask processing deposition process.

Inkjet printing technology can use two modes of continuous injection and Drop-on-demand injection [96]. Continuous inkjet refers to the continuous ejection of nozzles during the operation of the device and the deflection of ink droplets that do not participate in imaging. Drop-on-demand inkjet nozzles only eject ink when needed for imaging, so there is no need to install deflection, recovery, etc. on the nozzles, and the range of use is wider.

3.1.1 Continuous Printing

The working principle of continuous inkjet printing is shown in Fig 1-18. The droplets are continuously ejected at the same size and spacing. The key to controlling the printing pattern generation is the ink droplet migration system that comes with the nozzle. Under the control of the computer, the nozzle charges a part of the ink droplets, and the injected charged ink droplets are divided into droplets of the same size according to the amount of charge under the action of the applied electric field. At the same time, the ink droplets participating in the imaging smoothly reach the specified position of the substrate, and the ink droplets that are not involved in the imaging are deflected into the recycling system. The continuous inkjet printing method is the earliest

inkjet printing method, and it is more advantageous in terms of printing speed than the drop-on-demand inkjet printing that appears later. However, based on continuous inkjet technology, it is necessary to additionally provide an ink droplet charging device, a deflection device, and an ink recycling cycle system, and the equipment cost is high, and the lower material utilization rate further increases the production cost. The method is currently largely replaced by drop-on-demand printing.

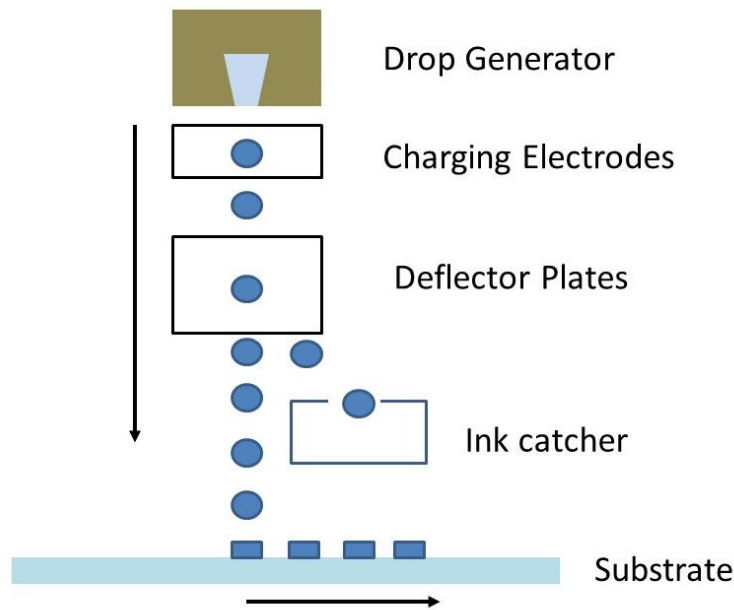


Figure 1-24 the working principle of continuous inkjet printing [97]

3.1.2 Drop-on-demand (DoD) Printing

DoD inkjet printing only ejects ink droplets when needed for imaging. Since the generation and ejection of ink droplets are generally controlled by electric pulse signals, it is also called pulse inkjet, and its working principle is shown in Fig 1-25.

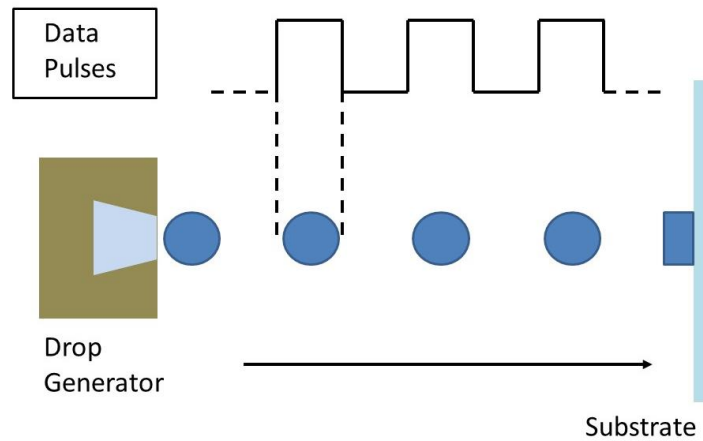


Figure 1-25 The working principle of drop-on-demand inkjet printing [97]

The nozzle structure of the DoD inkjet principle is greatly simplified, and the inherent unreliability of the nozzle structure of the continuous inkjet principle is eliminated. The size and spacing of the ejected ink droplets are controllable, and the utilization of the material is also significantly improved. At present, the principle of ink drop generation of DoD inkjet technology mainly includes thermal inkjet, piezoelectric inkjet, electrostatic inkjet and acoustic inkjet. Among them, the inkjet printing technology used in the preparation of printed electronics is basically in the category of piezoelectric inkjet.

The principle of the operation of the piezoelectric ink-jet system is to deform by applying a voltage to the piezoelectric material, and the volume of the ink chamber changes to squeeze the ink droplets and eject them from the nozzles. When the applied voltage is zero, the piezoelectric material returns to its original shape and the ink chamber is refilled [98], as shown in Fig 1-26.

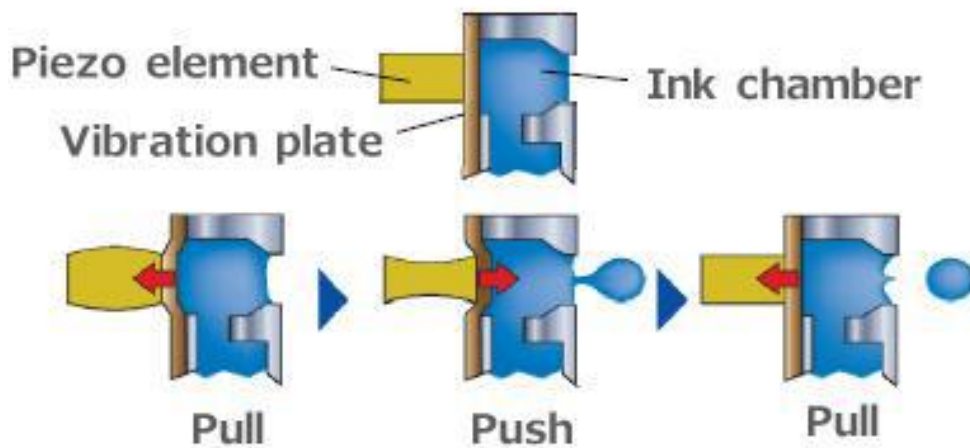


Figure 1-26 Schematic diagram of a piezoelectric DoD inkjet printing process [98]

Compared to thermal inkjet technology, the droplets are smaller, have higher resolution, and have substantially no side effects on electronic ink. Therefore, most of the current printing electronics are produced by piezoelectric inkjet. The research in this work also uses DoD piezoelectric inkjet printing.

3.2 Process of the DoD inkjet printing

The inkjet printing process is divided into three stages (Fig. 1-27): (1) droplet formation; (2) droplet collision and spreading on the substrate; (3) droplet drying to form a film.

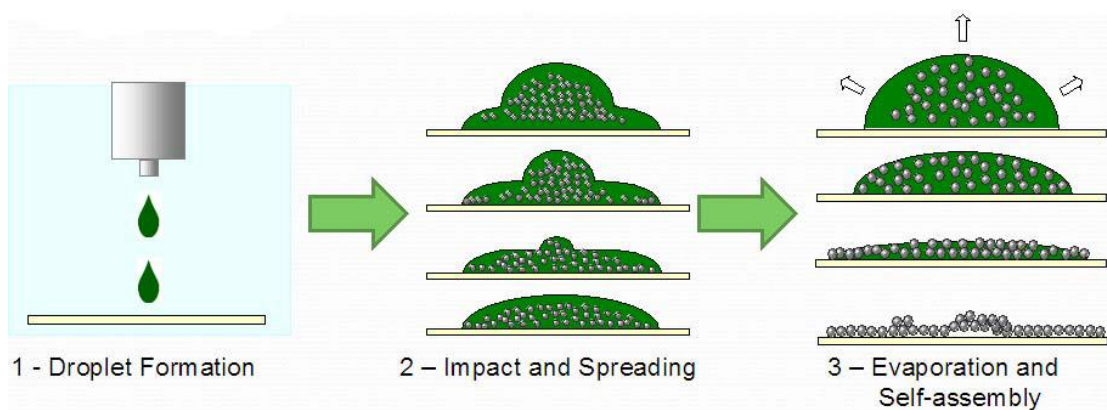


Figure 1-27 Physical stages of inkjet printing

3.2.1 Droplet formation

During inkjet printing, the solution is ejected by an external pulse to form droplets. Fig1-28 shows the most commonly used pulse signals. Fig 1.29 shows the process of droplet formation driven by the pulse signal in Fig 1.28.

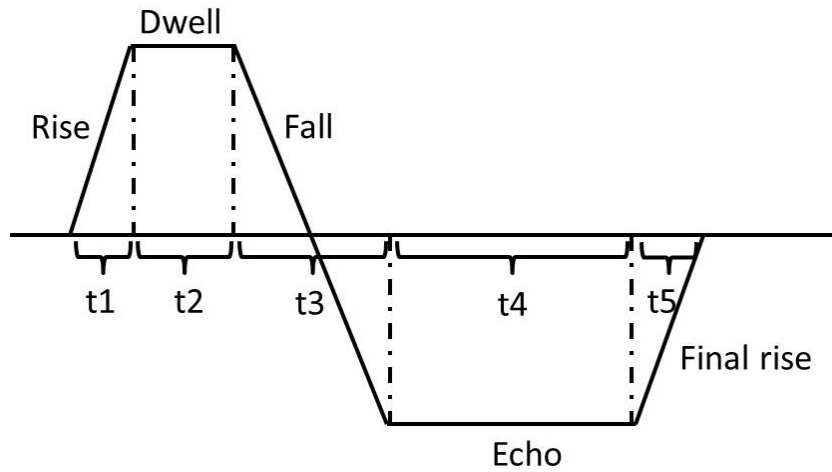


Figure 1-28 Driving Pulse used to fire jetting devices

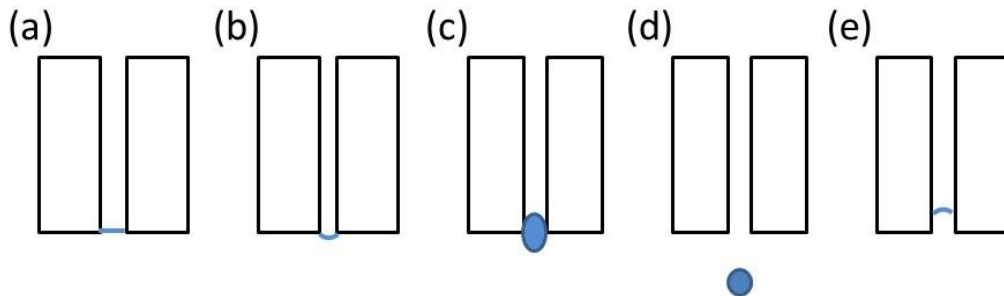


Figure 1-29 Schematic illustration of the drop formation process steps in sequence

[99]

In the absence of an applied pulse, the droplets in the nozzle are in equilibrium (Fig1-29a). When a certain positive pulse is applied, the nozzle deforms the solution and is squeezed out of the nozzle (Fig1-29b). As the deformation of the nozzle continues, the kinetic energy of the nozzle continues to accumulate (Fig1-29c). When the kinetic energy of the solution from the nozzle reaches a certain threshold, the

solution leaves the nozzle and the droplets form (Fig1-29d). The previously accumulated kinetic energy is converted into the kinetic energy and surface energy of the newly generated droplets. The newly formed droplets fly toward the substrate, and the remaining solution of the nozzle returns to the nozzle under the action of a negative pulse voltage (Fig1-29e).

3.2.2 Droplet collision and spreading on the substrate

The collision and spreading behavior of the formed droplets flying toward the substrate is controlled by the inertial force of the droplets, capillary flow force and gravity. The diameter of the film obtained by drying the droplets after equilibrium is determined by the initial diameter d_0 of the droplets and the contact angle θ_{eqm} at equilibrium. For printing droplets, gravity can be ignored, and the spread droplet can be regarded as a hemisphere, which can simulate the diameter of the dry droplet d_{con} :

$$d_{con} = d_0^3 \sqrt{\frac{8}{\tan \frac{\theta_{eqm}}{2} [3 + \left(\tan \frac{\theta_{eqm}}{2}\right)^2]}}$$

The diameter d_{con} at which the droplet reaches equilibrium determines the resolution of the printed image. The resolution of the pattern is determined mainly by the size of the ejected droplets at the time of printing and the contact angle of the ink droplets on the substrate. Its size is linear with the initial diameter d_0 of the droplet and increases with decreasing contact angle.

3.2.3 Droplet drying to form a film

The droplets that reach the dynamic equilibrium are dried to form a film as the solvent evaporates. Deegan et al. were the first to study the morphology of films after droplet drying [100]. Generally, droplet drying is divided into two modes, one is constant contact angle mode, that is, the contact line of the droplet is not pinned, and the solvent is uniformly volatilized to form a uniform film, as shown in Fig. 1-30a.

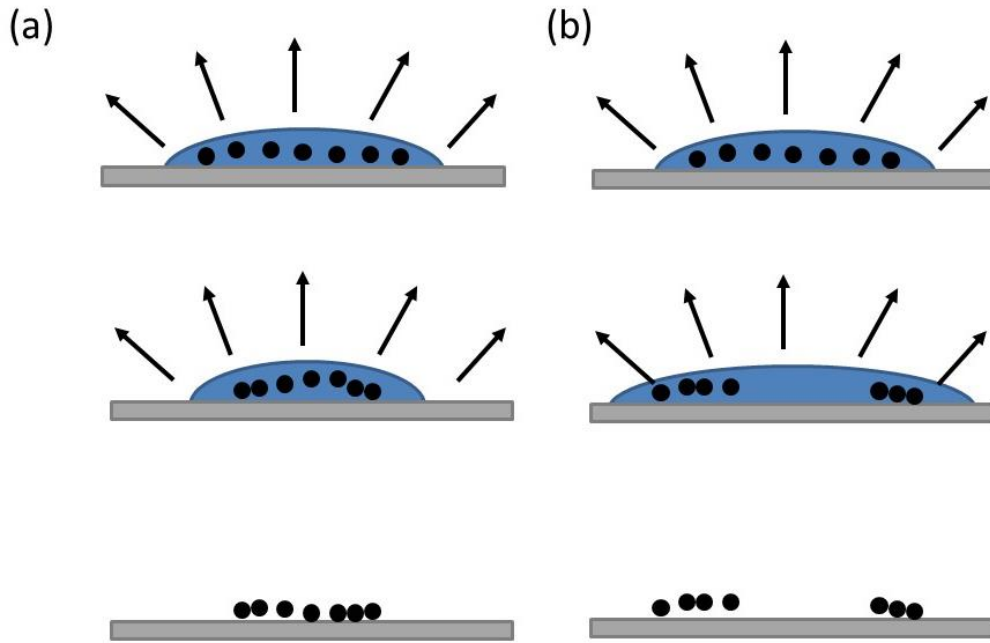


Figure 1-30 Drop evaporation and deposition process. a) Uniform drop evaporation and deposition. b) pinned contact line drops evaporation and deposition

The other is the constant diameter mode, in which the droplet contact line is pinned and the rate of solvent evaporation at the edge of the droplet is greater than at the center. To compensate for the volatilization of the edge solvent, capillary flow from the center to the edge is formed within the solution. This capillary flow moves the solute in the solution to the edge of the droplet, forming a ring-shaped top with a thin intermediate edge, as shown in Fig. 1-30b, the coffee ring phenomenon. In this work, we have further discussed the parameters that affect the print pattern.

Summary

In this chapter, the general introduction of the photo-detectors, organic electronics and inkjet printing are provided. In order to expand the range of the detection wavelength, quantum dots are utilized for the size tunable and the quantum effect. Meanwhile, based on the thin-film transistor structure, the possibilities of large gain can be obtained. With the organic electronics technology, the cost of the photo-transistor fabrication can be decreased. Finally, due to the inkjet printing properties, large area devices and circuit design could achieve. In the following, I will define and describe the quantum dots photodetectors, the organic electronics and the way to fabricate this organic electronics by printing technology.

References:

[1] Dakin, John, and Robert GW Brown, eds. Handbook of optoelectronics. Vol. 1. New York: Taylor & Francis, 2006.

[2] Kasap S, Frey J B, Belev G, et al. Amorphous and polycrystalline photoconductors for direct conversion flat panel X-ray image sensors[J]. Sensors, 2011, 11(5): 5112-5157.

[3] Konstantatos G, Badioli M, Gaudreau L, et al. Hybrid graphene–quantum dot phototransistors with ultrahigh gain[J]. Nature nanotechnology, 2012, 7(6): 363.

[4] Liu Y, Wang F, Wang X, et al. Planar carbon nanotube–graphene hybrid films for high-performance broadband photodetectors[J]. Nature communications, 2015, 6: 8589.

[5] Zeng L H, Wang M Z, Hu H, et al. Monolayer graphene/germanium Schottky junction as high-performance self-driven infrared light photodetector[J]. ACS applied materials & interfaces, 2013, 5(19): 9362-9366.

[6] Sze S M, Ng K K. Physics of semiconductor devices[M]. John wiley & sons, 2006.

[7] Neamen D A. Semiconductor physics and devices[M]. New York: McGraw-Hill, 1997.

[8] Liu K, Sakurai M, Aono M. ZnO-based ultraviolet photodetectors[J]. Sensors, 2010, 10(9): 8604-8634.

[9] Adivarahan V, Simin G, Tamulaitis G, et al. Indium–silicon co-doping of high-aluminum-content AlGaIn for solar blind photodetectors[J]. Applied Physics Letters, 2001, 79(12): 1903-1905.

[10] LoVecchio P, Jasper M, Cox J T, et al. planar $\text{Pb}_{0.8}\text{Sn}_{0.2}\text{Te}$ photodiode

array development at the night vision laboratory[M]//Infrared Detectors. 1976: 295-301.

[11] Böberl M, Kovalenko M V, Gamerith S, et al. Inkjet - Printed Nanocrystal Photodetectors Operating up to 3 μm Wavelengths[J]. *Advanced materials*, 2007, 19(21): 3574-3578.

[12] Gao H H, Krier A, Sherstnev V V. Room-temperature InAs 0.89 Sb 0.11 photodetectors for CO detection at 4.6 μm [J]. *Applied Physics Letters*, 2000, 77(6): 872-874.

[13] Herrmann W, Blake M, Doyle M, et al. Short wavelength infrared (SWIR) spectral analysis of hydrothermal alteration zones associated with base metal sulfide deposits at Rosebery and Western Tharsis, Tasmania, and Highway-Reward, Queensland[J]. *Economic Geology*, 2001, 96(5): 939-955.

[14] Gao X, Cui Y, Levenson R M, et al. In vivo cancer targeting and imaging with semiconductor quantum dots[J]. *Nature biotechnology*, 2004, 22(8): 969.

[15] Lim Y T, Kim S, Nakayama A, et al. Selection of quantum dot wavelengths for biomedical assays and imaging[J]. *Molecular imaging*, 2003, 2(1): 15353500200302163.

[16] Kim S, Lim Y T, Soltesz E G, et al. Near-infrared fluorescent type II quantum dots for sentinel lymph node mapping[J]. *Nature biotechnology*, 2004, 22(1): 93.

[17] Driggers R G, Jacobs E L, Vollmerhausen R H, et al. Current infrared target acquisition approach for military sensor design and wargaming[C]//Infrared Imaging Systems: Design, Analysis, Modeling, and Testing XVII. International Society for Optics and Photonics, 2006, 6207: 620709.

[18] Ferrari M, Quaresima V. A brief review on the history of human functional near-infrared spectroscopy (fNIRS) development and fields of application[J]. *Neuroimage*, 2012, 63(2): 921-935.

[19] Rogalski A. *Infrared detectors*[M]. CRC press, 2010.

[20] Konstantatos G. *Sensitive Solution-processed Quantum Dot Photodetectors*[D]. , 2009.

[21] Rogalski A. Toward third generation HgCdTe infrared detectors[J]. *Journal of alloys and compounds*, 2004, 371(1-2): 53-57.

[22] Sarusi G. QWIP or other alternative for third generation infrared systems[J]. *Infrared physics & technology*, 2003, 44(5-6): 439-444.

[23] Rogalski A, Martyniuk P. InAs/GaInSb superlattices as a promising material system for third generation infrared detectors[J]. *Infrared Physics & Technology*, 2006, 48(1): 39-52.

[24] Rogalski A. Recent progress in infrared detector technologies[J]. *Infrared Physics & Technology*, 2011, 54(3): 136-154.

[25] Martyniuk P, Rogalski A. Quantum-dot infrared photodetectors: Status and outlook[J]. *Progress in Quantum Electronics*, 2008, 32(3-4): 89-120.

[26] Norton P. HgCdTe infrared detectors[J]. *Optoelectronics review*, 2002 (3): 159-174.

[27] Talapin D V, Lee J S, Kovalenko M V, et al. Prospects of colloidal nanocrystals for electronic and optoelectronic applications[J]. *Chemical reviews*, 2009, 110(1): 389-458.

[28] Konstantatos G, Howard I, Fischer A, et al. Ultrasensitive solution-cast quantum dot photodetectors[J]. *Nature*, 2006, 442(7099): 180.

[29] Konstantatos G, Sargent E H. Solution-processed quantum dot photodetectors[J]. Proceedings of the IEEE, 2009, 97(10): 1666-1683.

[30] Chen M, Yu H, Kershaw S V, et al. Fast, air - stable infrared photodetectors based on spray - deposited aqueous HgTe quantum dots[J]. Advanced Functional Materials, 2014, 24(1): 53-59.

[31] Trindade T, O'Brien P, Pickett N L. Nanocrystalline semiconductors: synthesis, properties, and perspectives[J]. Chemistry of Materials, 2001, 13(11): 3843-3858.

[32] Kuchibhatla S V N T, Karakoti A S, Bera D, et al. One dimensional nanostructured materials[J]. Progress in materials science, 2007, 52(5): 699-913.

[33] Alivisatos A P. Perspectives on the physical chemistry of semiconductor nanocrystals[J]. The Journal of Physical Chemistry, 1996, 100(31): 13226-13239.

[34] Chemla D S, Miller D A B, Schmitt-Rink S. Quantum wells to quantum dots: physics and prospects[C]//Conference on Lasers and Electro-Optics. Optical Society of America, 1988: TUR1.[10] Cho K S, Lee E K, Joo W J, et al. High-performance crosslinked colloidal quantum-dot light-emitting diodes[J]. Nature Photonics, 2009, 3(6): 341.

[35] Bae W K, Kwak J, Park J W, et al. Highly efficient green - light - emitting diodes based on CdSe@ ZnS quantum dots with a chemical - composition gradient[J]. Advanced Materials, 2009, 21(17): 1690-1694.

[36] Kagan C R, Murray C B. Charge transport in strongly coupled quantum dot solids[J]. Nature nanotechnology, 2015, 10(12): 1013.

[37] Niitsoo O, Sarkar S K, Pejoux C, et al. Chemical bath deposited CdS/CdSe-sensitized porous TiO₂ solar cells[J]. Journal of Photochemistry and Photobiology A: Chemistry, 2006, 181(2-3): 306-313.

[38] Hu X, An X, Li L. Easy synthesis of highly fluorescent carbon dots from albumin and their photoluminescent mechanism and biological imaging applications[J]. *Materials Science and Engineering: C*, 2016, 58: 730-736.

[39] Liu T C, Huang Z L, Wang H Q, et al. Temperature-dependent photoluminescence of water-soluble quantum dots for a bioprobe[J]. *Analytica Chimica Acta*, 2006, 559(1): 120-123.

[40] Scherer A, Craighead H G. Fabrication of small laterally patterned multiple quantum wells[J]. *Applied Physics Letters*, 1986, 49(19): 1284-1286.

[41] Fukui T, Ando S, Tokura Y, et al. GaAs tetrahedral quantum dot structures fabricated using selective area metalorganic chemical vapor deposition[J]. *Applied physics letters*, 1991, 58(18): 2018-2020.

[42] Petroff P M, Lorke A, Imamoglu A. Epitaxially self-assembled quantum dots[J]. *Physics Today*, 2001, 54(5): 46-52.

[43] Nordell K J, Boatman E M, Lisensky G C. A safer, easier, faster synthesis for CdSe quantum dot nanocrystals[J]. *Journal of chemical education*, 2005, 82(11): 1697.

[44] Tang L, Deng Y, Zeng G, et al. CdS/Cu₂S co-sensitized TiO₂ branched nanorod arrays of enhanced photoelectrochemical properties by forming nanoscale heterostructure[J]. *Journal of Alloys and Compounds*, 2016, 662: 516-527.

[45] Jun H K, Careem M A, Arof A K. Quantum dot-sensitized solar cells—perspective and recent developments: a review of Cd chalcogenide quantum dots as sensitizers[J]. *Renewable and Sustainable Energy Reviews*, 2013, 22: 148-167.

[46] Tian J, Shen T, Liu X, et al. Enhanced performance of PbS-quantum-dot-sensitized solar cells via optimizing precursor solution and electrolytes[J]. *Scientific reports*, 2016, 6: 23094.

[47] Kurpiers J, Balazs D M, Paulke A, et al. Free carrier generation and recombination in PbS quantum dot solar cells[J]. *Applied Physics Letters*, 2016, 108(10): 103102.

[48] Soci C, Zhang A, Xiang B, et al. ZnO nanowire UV photodetectors with high internal gain[J]. *Nano letters*, 2007, 7(4): 1003-1009.

[49] Nie B, Hu J G, Luo L B, et al. Monolayer Graphene Film on ZnO Nanorod Array for High - Performance Schottky Junction Ultraviolet Photodetectors[J]. *Small*, 2013, 9(17): 2872-2879.

[50] Li L, Gu L, Lou Z, et al. ZnO quantum dot decorated Zn₂SnO₄ nanowire heterojunction photodetectors with drastic performance enhancement and flexible ultraviolet image sensors[J]. *ACS nano*, 2017, 11(4): 4067-4076.

[51] Clifford J P, Konstantatos G, Johnston K W, et al. Fast, sensitive and spectrally tuneable colloidal-quantum-dot photodetectors[J]. *Nature nanotechnology*, 2009, 4(1): 40.

[52] Shin S W, Lee K H, Park J S, et al. Highly transparent, visible-light photodetector based on oxide semiconductors and quantum dots[J]. *ACS applied materials & interfaces*, 2015, 7(35): 19666-19671.

[53] Leatherdale C A, Kagan C R, Morgan N Y, et al. Photoconductivity in CdSe quantum dot solids[J]. *Physical Review B*, 2000, 62(4): 2669.

[54] McDonald S A, Cyr P W, Levina L, et al. Photoconductivity from PbS-nanocrystal/ semiconducting polymer composites for solution-processible, quantum-size tunableinfrared photodetectors[J]. *Applied physics letters*, 2004, 85(11): 2089-2091.

- [55] Konstantatos G, Clifford J, Levina L, et al. Sensitive solution-processed visible-wavelength photodetectors[J]. *Nature photonics*, 2007, 1(9): 531.
- [56] Lee J W, Kim D Y, So F. Unraveling the Gain Mechanism in High Performance Solution - Processed PbS Infrared PIN Photodiodes[J]. *Advanced Functional Materials*, 2015, 25(8): 1233-1238.
- [57] Adinolfi V, Kramer I J, Labelle A J, et al. Photojunction field-effect transistor based on a colloidal quantum dot absorber channel layer[J]. *ACS nano*, 2015, 9(1): 356-362.
- [58] Turyanska L, Makarovskiy O, Svatek S A, et al. Ligand - Induced Control of Photoconductive Gain and Doping in a Hybrid Graphene–Quantum Dot Transistor[J]. *Advanced Electronic Materials*, 2015, 1(7): 1500062.
- [59] Kufer D, Lasanta T, Bernechea M, et al. Interface engineering in hybrid quantum dot–2D phototransistors[J]. *ACS Photonics*, 2016, 3(7): 1324-1330.
- [60] de Arquer F P G, Armin A, Meredith P, et al. Solution-processed semiconductors for next-generation photodetectors [J]. *Nature Reviews Materials*, 2017, 2(3): 16100.
- [61] Liu X, Yang X, Liu M, et al. Photo-modulated thin film transistor based on dynamic charge transfer within quantum-dots-InGaZnO interface[J]. *Applied Physics Letters*, 2014, 104(11): 113501.
- [62] Sun Y, Giebink N C, Kanno H, et al. Management of singlet and triplet excitons for efficient white organic light-emitting devices[J]. *Nature*, 2006, 440(7086): 908.
- [63] D'Andrade B W, Thompson M E, Forrest S R. Controlling exciton diffusion in multilayer white phosphorescent organic light emitting devices[J]. *Advanced Materials*, 2002, 14(2): 147-151.

- [64] Physics of organic semiconductors[M]. John Wiley & Sons, 2006.
- [65] G.H.Heilmeier, L.A.Zanoni, Surface studies of phthalocyanine-copper films, J.Phys.Chem.Solids,(1964)25,603-611.
- [66] Tsumura A, Koezuka H, Ando T. Macromolecular electronic device: Field - effect transistor with a polythiophene thin film[J]. Applied Physics Letters, 1986, 49(18): 1210-1212.
- [67] Horowitz G, Fichou D, Peng X, et al. A field-effect transistor based on conjugated alpha-sexithienyl[J]. Solid State Communications, 1989, 72(4): 381-384.
- [68] Garnier F, Hajlaoui R, Yassar A, et al. All-polymer field-effect transistor realized by printing techniques[J]. Science, 1994, 265(5179): 1684-1686.
- [69] Laquindanum J G, Katz H E, Lovinger A J, et al. Morphological origin of high mobility in pentacene thin-film transistors[J]. Chemistry of materials, 1996, 8(11): 2542-2544.
- [70] Lin Y Y, Gundlach D J, Nelson S F, et al. Stacked pentacene layer organic thin-film transistors with improved characteristics[J]. IEEE Electron Device Letters, 1997, 18(12): 606-608.
- [71] Jurchescu O D, Baas J, Palstra T T M. Effect of impurities on the mobility of single crystal pentacene[J]. Applied Physics Letters, 2004, 84(16): 3061-3063.
- [72] Tatemichi S, Ichikawa M, Koyama T, et al. High mobility n-type thin-film transistors based on N, N'-ditridecyl perylene diimide with thermal treatments[J]. Applied physics letters, 2006, 89(11): 112108.
- [73] Itaka K, Yamashiro M, Yamaguchi J, et al. High - mobility C60 field - effect transistors fabricated on molecular - wetting controlled substrates[J]. Advanced Materials, 2006, 18(13): 1713-1716.

[74] Anthopoulos T D, Singh B, Marjanovic N, et al. High performance n-channel organic field-effect transistors and ring oscillators based on C 60 fullerene films[J]. Applied Physics Letters, 2006, 89(21): 213504.

[75] Lei T, Dou J H, Pei J. Influence of Alkyl Chain Branching Positions on the Hole Mobilities of Polymer Thin - Film Transistors[J]. Advanced Materials, 2012, 24(48): 6457-6461.

[76] Wu X, Ma Y, Zhang G, et al. Thermally stable, biocompatible, and flexible organic field - effect transistors and their application in temperature sensing arrays for artificial skin[J]. Advanced Functional Materials, 2015, 25(14): 2138-2146.

[77] Scenev V, Cosseddu P, Bonfiglio A, et al. Origin of mechanical strain sensitivity of pentacene thin-film transistors[J]. Organic Electronics, 2013, 14(5): 1323-1329.

[78] Hill I G, Rajagopal A, Kahn A, et al. Molecular level alignment at organic semiconductor-metal interfaces[J]. Applied Physics Letters, 1998, 73(5): 662-664.

[79] Bao Z, Dodabalapur A, Lovinger A J. Soluble and processable regioregular poly (3 - hexylthiophene) for thin film field - effect transistor applications with high mobility[J]. Applied Physics Letters, 1996, 69(26): 4108-4110.

[80] Xu Y, Baeg K J, Park W T, et al. Regulating charge injection in ambipolar organic field-effect transistors by mixed self-assembled monolayers[J]. ACS applied materials & interfaces, 2014, 6(16): 14493-14499.

[81] Van Mullekom H A M, Vekemans J, Havinga E E, et al. Developments in the chemistry and band gap engineering of donor-acceptor substituted conjugated polymers[J]. Materials Science and Engineering: R: Reports, 2001, 32(1): 1-40.

[82] Horowitz G, Fichou D, Peng X, et al. Thin-film transistors based on alpha-conjugated oligomers[J]. *Synthetic Metals*, 1991, 41(3): 1127-1130.

[83] Kobayashi S, Takenobu T, Mori S, et al. Fabrication and characterization of C₆₀ thin-film transistors with high field-effect mobility[J]. *Applied physics letters*, 2003, 82(25): 4581-4583.

[84] Zhang X H, Kippelen B. High-performance C₆₀ n-channel organic field-effect transistors through optimization of interfaces[J]. *Journal of Applied Physics*, 2008, 104(10): 104504.

[85] Benning P J, Poirier D M, Ohno T R, et al. C₆₀ and C₇₀ fullerenes and potassium fullerides[J]. *Physical Review B*, 1992, 45(12): 6899.

[86] Kroto H W, Heath J R, O'Brien S C, et al. C₆₀: Buckminsterfullerene[J]. *Nature*, 1985, 318(6042): 162.

[87] Dinelli F, Murgia M, Levy P, et al. Spatially correlated charge transport in organic thin film transistors[J]. *Physical Review Letters*, 2004, 92(11): 116802.

[88] Itaka K, Yamashiro M, Yamaguchi J, et al. High - mobility C₆₀ field - effect transistors fabricated on molecular - wetting controlled substrates[J]. *Advanced Materials*, 2006, 18(13): 1713-1716.

[89] Anthopoulos T D, Singh B, Marjanovic N, et al. High performance n-channel organic field-effect transistors and ring oscillators based on C₆₀ fullerene films[J]. *Applied Physics Letters*, 2006, 89(21): 213504.

[90] Singh T B, Sariciftci N S, Yang H, et al. Correlation of crystalline and structural properties of C₆₀ thin films grown at various temperature with charge carrier mobility[J]. *Applied Physics Letters*, 2007, 90(21): 213512.

[91] Hecker, Klaus. "Roadmap for Organic and Printed Electronics." NIP & Digital Fabrication Conference. Vol. 2010. No. 2. Society for Imaging Science and Technology, 2010.

[92] Adachi, Chihaya, et al. "Nearly 100% internal phosphorescence efficiency in an organic light-emitting device." *Journal of Applied Physics* 90.10 (2001): 5048-5051.

[93] Kalinowski, Jan. "Electroluminescence in organics." *Journal of Physics D: Applied Physics* 32.24 (1999): R179.

[94] Burrows, P. E., and S. R. Forrest. "Electroluminescence from trap - limited current transport in vacuum deposited organic light emitting devices." *Applied Physics Letters* 64.17 (1994): 2285-2287.

[95] Meier, M., S. Karg, and W. Riess. "Light-emitting diodes based on poly-p-phenylene-vinylene: II. Impedance spectroscopy." *Journal of Applied Physics* 82.4 (1997): 1961-1966.

[96] Sheats, James R., et al. "Organic electroluminescent devices." *Science* 273.5277 (1996): 884-888.

[97] Le, Hue P. "Progress and trends in ink-jet printing technology." *Journal of Imaging Science and Technology* 42.1 (1998): 49-62.

[98] "Secrets Behind the Development of Epson's Micro Piezo Technology (Part 2)" ,http://global.epson.com/innovation/topics/201306_03.html

[99] Dijkstra J F, Pierik A. Dynamics of Piezoelectric Print - Heads[J]. *Inkjet Technology for Digital Fabrication*, 2012: 45-86.

[100] Deegan R D, Bakajin O, Dupont T F, et al. Capillary flow as the cause of ring stains from dried liquid drops[J]. *Nature*, 1997, 389(6653): 827.

Part A: UV-Visible Photodetectors

1. Introduction

In last few years, photo-modulated thin-film transistors (TFTs) have been drawn widespread applications using photo sensitive materials [1-3] as the electronic and electro-optic components. For applications of integrated circuit [4, 5], amorphous metal oxide semiconductors (AMOS) based TFTs have been utilized in phototransistors and photo-sensors due to their high sensitivity, electron mobility and on/off ratio. With properties of wide-band gap (~ 3.3 eV) and a large exciton binding energy (60 meV), ZnO not only can be considered as a promising candidate for ultraviolet (UV) photo-sensors and but also it can be used as an active layer for photo-modulated TFTs [6-8].

In the meanwhile, the rapid development of tunable semiconductor quantum dots (QDs) have been focused on applications in optoelectronics devices, such as light emitting devices and photodetectors [9-12]. By taking into consideration of the recent progress in optoelectronics devices, the size-tunability of the QDs can be useful in overlapping more regions of optical spectrum [13]. Conventional visible-band cadmium selenide CdSe quantum dot materials have been widely used in electro-optical conversion devices such as organic light-emitting tubes and sensitized solar cells. Benefiting from its high light absorption rate and electron-hole pair generation efficiency, quantum dot materials can improve the photocurrent conversion performance of optoelectronic devices, and have the prospect of large-scale application in photodetector devices.

Compared with traditional photo-modulated transistor, as reported by *Yuyu Bu* [14], properties of photo-sensitive waveband and fast response can be improved by using hybrid materials of ZnO nanowires and QDs. However, due to the mechanism of carrier transfer, low photo responsivity was still a challenge in photo-modulated TFTs

application [15]. In order to improve the performance of the hybrid materials of ZnO nanowires and QDs, graphene was exploited. Graphene as an atomic layer with remarkable electric and optical properties was considered as a highly desired material in applications in photodetectors, biological imaging, and telecommunication system [16-18]. Based on the graphene linear electronic dispersion and the electrons transferred along the surface, graphene can be used as an efficient intermediary material for injected electrons. In addition, the high drift velocity of the charge in graphene also provides a more efficient separation of electron from the site of injection [19-22]. Compared with monolayer graphene, reduced graphene oxide (RGO) with similar electric properties can be utilized to provide defect energy states [23, 24]. In addition, due to the existence of the narrow photosensitive waveband and discontinuity distribution, hybrid materials of ZnO nanowires/RGO fragments and QDs/RGO fragments were not recommended to use in photo-modulated transistors [25].

In this chapter, a photo modulated transistor with TFTs structure is demonstrated using CdSe QDs/RGO fragments decorated on the surface of ZnO nanowires as the active layer [16]. CdSe QDs, as an electron donor, was attached to the RGO fragments to expand the photo-sensitive waveband. RGO fragments were exploited to provide a favorable photo-responsivity. Eventually, the performances of this device such as photocurrent, responsivity and rectifying capability were also measured and analyzed.

2. Experiment Sections

2.1 Fabrication of ZnO Nanowires

The CdSe QDs/RGO fragments decorated on the surface of ZnO nanowires was utilized as the active layer and photo-sensitive layer (Fig. 1a). The fabrication process of ZnO nanowires was illustrated in the following. First, a piece of silicon (001) wafer was washed sequentially with acetone, ethanol and deionized water for 10 mins, respectively. The quartz boat filled with 0.2g zinc powder was covered by the silicon

wafer before transferring to the chamber. With a flow rate of 20 sccm (Ar:O₂=3:1), a pressure of chamber under 7.5×10^{-3} torr and 800°C controlled temperature of the substrate, high quality ZnO nanowires with a length of 25 μm and a diameter of 150 nm were deposited by RF sputtering. The aspect ratio is higher than 150 as shown in Fig. 1b.

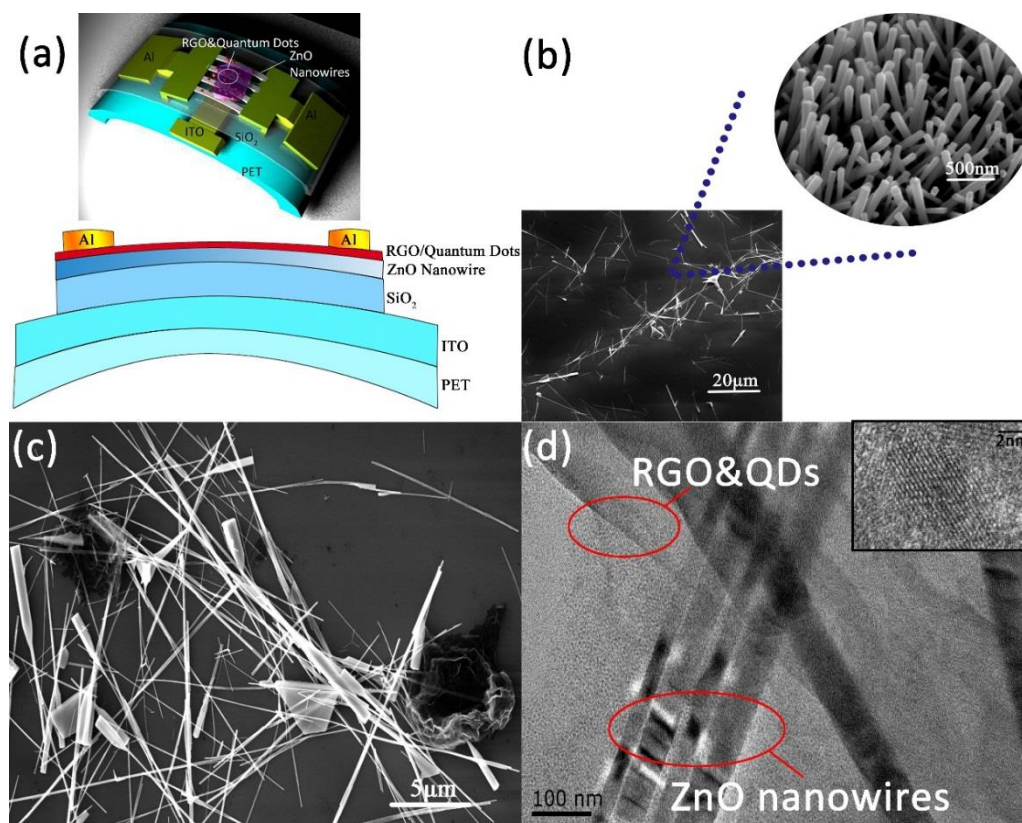


Figure1. Characterization of flexible photo-modulated transistors. (a) The structure of the CdSe QDs/RGO decorated on the surface of ZnO nanowires photo-modulated transistor. (b) SEM image of ZnO nanowires. (c) SEM image of hybrid materials. (d) TEM image of the CdSe QDs/RGO/ZnO nanowires and CdSe QDs inset.

2.2 Synthesis of CdSe QDs/RGO Fragments

Graphene oxide (GO) was purchased from Hengqiu Graphene Technology (Suzhou Co. Ltd.). It was reacted to produce the RGO fragments in ~5 μm diameter by

adding oxidation-reductant of NaBH_4 . N-type CdSe QDs modified with tri-n-octylphosphine oxide (TOPO) in ~ 7 nm diameter was utilized as the photosensitive material (purchased from Mesolight Inc (Suzhou Co. Ltd)). The hybrid CdSe QDs/RGO fragments solution is composed of equal micro litre of 5 mg mL^{-1} CdSe QDs and 1 mg mL^{-1} RGO solution. And then, in order to obtain CdSe QDs-decorated RGO fragments, hybrid solution was oscillated in ultrasonic bath before it was filtered by membrane materials.

2.3 Manufacture of the Device

The three terminal gated photo-modulated transistor was fabricated on the substrate of polyethylene terephthalate (PET). The PET coating with ITO layer and SiO_2 insulating layer were deposited by magnetron sputtering process. After ZnO nanowires dispersed in ethanol, the dispersion solution was spin-coated on the SiO_2 substrate with a speed of 2000 r min^{-1} . Next, the hybrid solution of CdSe QDs/RGO fragments was spin-coated on ZnO nanowire film with the speed of 1000 r min^{-1} . Finally, the thermal annealing was processed at the temperature of $180 \text{ }^\circ\text{C}$ for promoting uniformity of hybrid material layer and removing the solvent before the electroplating process with the mask (W:L=100 μm :20 μm) for the electrodes. The channel of the device was characterized by scanning electron microscope (SEM, FEI Quanta 200, Holland) and the hybrid material samples were characterized by transmission electron microscope (TEM, JEM-2100, Japan). The morphology of hybrid composed of RGO and ZnO nanowires is shown in Fig. 1c. It can be seen ZnO nanowires in diameter of ~ 150 nm and length of $\sim 25 \mu\text{m}$ are covered by RGO fragments so that ZnO nanowires are able to present the proper contact with the RGO fragments. In the inset of Fig. 1d, the diameter of CdSe QDs with clear crystal lattices is ~ 7 nm. In addition, the crystallization of CdSe QDs can be indicated by clear crystal lattices.

3. Results and Discussion

3.1 Photo-sensitive mechanism of the Quantum Dots

When the ionic crystal or molecular crystal is irradiated with light, if the frequency ν of the light is less than a certain threshold ($h\nu_0 < E_g$), the material does not absorb light, and it's a light transmissive material. When $h\nu_0 > E_g$, light absorption occurs and the material will no longer transmit light. At this time, electrons enter the conduction band in the valence band, leaving a number of holes in the phase, they will become free carriers, increase the conductance, and the increased conductance becomes a photoconductor. This effect is generally called the internal photoelectric effect. When $h\nu_0 = E_g$, electron holes cannot be separated, but are bound together to form a system, and such electron hole pairs are usually called excitons.

Exciton light absorption is an important mode of light absorption for new low-dimensional nanomaterials. After photoexcitation, QDs materials with photosensitive properties will generate excitons (ie, electron-hole pairs). For most photoelectric conversion devices, it is necessary to extract photocarriers (electrons or holes) from the quantum dot material before the excitons are bound or recombined in the quantum dots. But in most quantum dot materials, exciton binding and recombination are done in a very fast time. In this work, we try to find a solution of this problem.

3.2 Results and Discussion

In Fig. 1d, it can be seen that the size of RGO fragments is much larger than that of CdSe QDs. The CdSe QDs were only distributed on the surface of RGO fragments. This confirms that CdSe QDs were blended with RGO fragments and the contact is constructed between RGO fragments and ZnO nanowires.

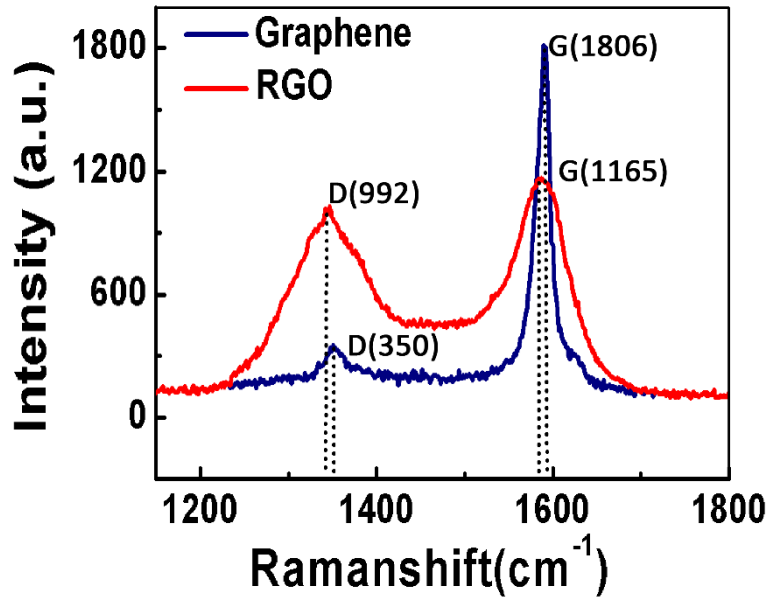


Figure 2. The Raman spectrum for Graphene and RGO.

Fig. 2 shows the Raman spectrum (carried on Renishaw, England) of the graphene and RGO, where the peak intensity of D band and G band are respectively located at 1350 and 1580 cm^{-1} for RGO. It is clear evident that defect states of RGO are existed because the peak intensity of D band and G band are shifted [26, 27].

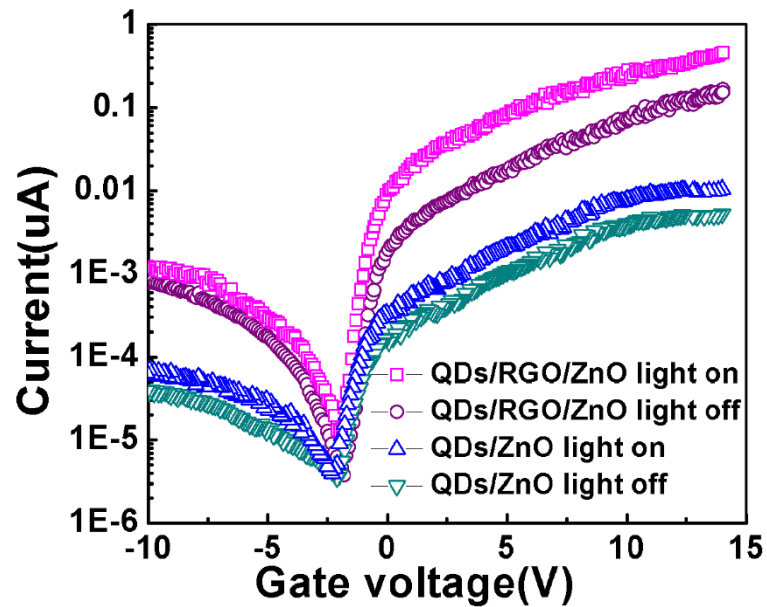


Figure 3 Photocurrent variation of two different devices with and without incident light ($V_{DS}=5\text{V}$, $\lambda=580\text{nm}$).

The dimension of channel area is $100 \times 20 \mu\text{m}^2$. When incident power intensity is applied as $10 \mu\text{W cm}^{-2}$, the photo responsivity can be calculated from the Eqs. (1) [25] and the transfer characteristic curve is shown in Fig. 3.

$$R = \frac{I_{total} - I_{dark}}{P} = \frac{I_{ph}}{\rho S} \quad (1)$$

Where P represents optical power, I_{total} denotes total current, I_{dark} is dark current, I_{ph} implies photocurrent, ρ indicates optical incident power density, and S is effective area for photo-electric reaction, respectively. When the drain-source voltage is applied as a value of 5 V and the wavelength of incident light is 580 nm. The responsivity of the CdSe QDs/RGO/ZnO nanowires can be calculated of $\sim 2000 \text{ A W}^{-1}$, which is approximately 2 orders of magnitude larger than that of CdSe QDs/ZnO nanowires.

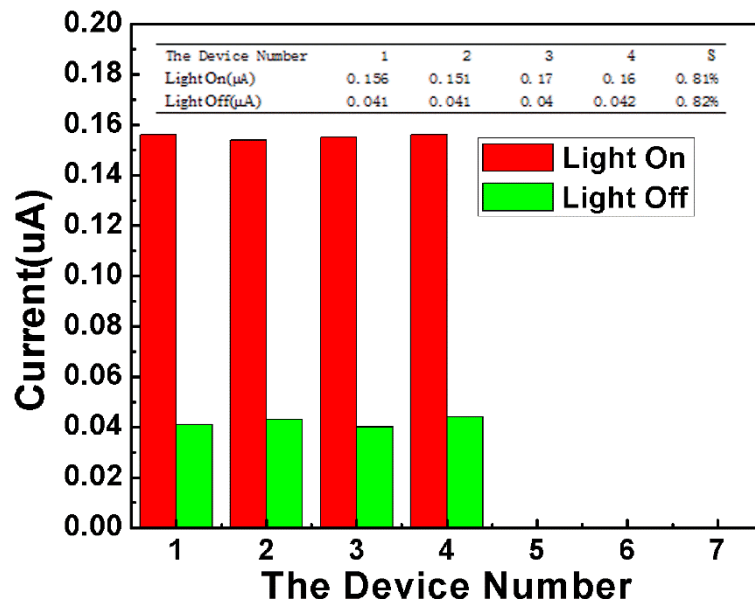


Figure 4 the reproducibility test of different ($V_{DS}=5\text{V}$, $V_{GS}=8\text{V}$, $\lambda=580\text{nm}$).

In order to find the reproducibility of the devices, four devices have been assembled and measured at same conditions when the voltage of drain-source is 5 V and the voltage of back gate is 8 V, respectively. The standard deviation of the photocurrent shown in Fig. 4 is below 1 % when incident wavelength is at 580 nm.

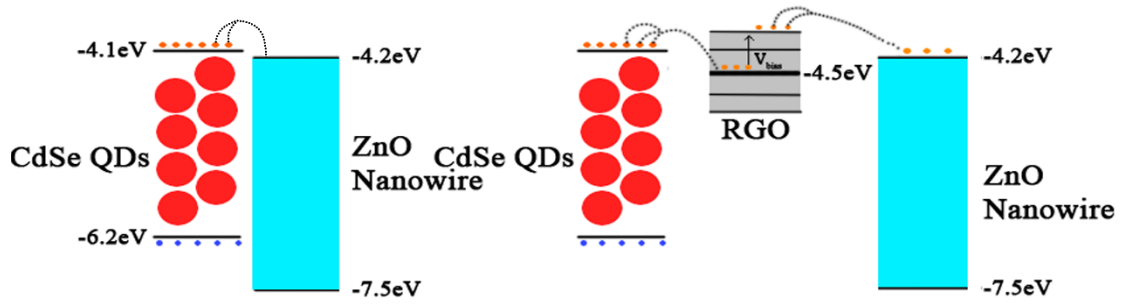


Figure 5 Energy band schematic of the device with and without using RGO.

The energy band schematics of the two kinds of devices are illustrated in Fig. 5. The charge transfer takes place among the interfaces of CdSe QDs/RGO/ZnO nanowires. For the CdSe QDs/ZnO nanowires hybrid materials, CdSe QDs are regarded as optical origins, where carriers can be generated and transferred from ligand capped CdSe QDs to the ZnO nanowires. Before the recombination of the electron-hole pairs in CdSe QDs happens, the charge can be injected into ZnO nanowire ($E_{CB} = -4.2$ eV, $E_{VB} = -7.7$ eV) and then drifted to the source electrode under the bias. In the meanwhile, an equal number of carriers can be provided by the drain electrode to satisfy the conversation of charge in the channel (Fig. 5 left). Since vacuum energy level is considered as the reference of potential energy, valence band (E_{VB}) and conduction band (E_{CB}) of CdSe QDs can be also measured as a value of -4.1 and -6.2 eV. The Fermi level of graphene was reported to be -4.5 eV [19], which is much lower compared with the conduction band of CdSe QDs (Fig. 5 right). Therefore, after incorporating with RGO, electrons can be transferred more efficiently from the conduction band of CdSe QDs to graphene due to the more favorable energy barrier between the interface of CdSe QDs and RGO. Furthermore, the electrons can jump more efficiently from the Fermi level of the graphene to the defect level and transfer to the ZnO nanowires when the electrical field is constructed by the positive back gate voltage directed to source electrode. Consequently, due to the more favorable energy of CdSe QDs/RGO/ZnO hybrid, it can be effectively promoting the charge transferring from CdSe QDs to ZnO nanowire. Moreover, fewer traps are existed at the interfaces among CdSe QDs/RGO

fragments/ZnO nanowires hybrid. As the result, electron annihilation is decreased and the carrier separation in hybrid material is benefited. Based on the Fig. 3, due to the enrichment of the interface and heterostructure by the RGO fragments, the improvement of photocurrent has been improved approximately 100 folds. According to the Eq. (1), corresponding photo responsivity of the transistor with RGO fragments is promoted approximately 100 folds.

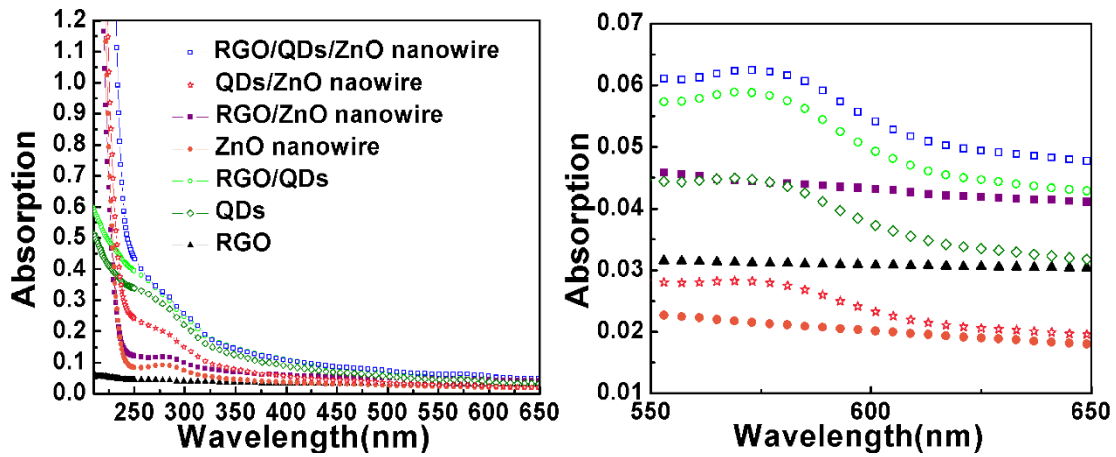


Figure 6. The absorption spectra of CdSe QDs, RGO, ZnO nanowires respectively and the hybrid materials.

To investigate the optical absorption characteristics of CdSe QDs, RGO fragments, ZnO nanowires, and CdSe QDs/RGO/ZnO nanowires hybrids, absorption spectra were respectively characterized in Fig. 6. Compared with the optical absorption spectra of CdSe QDs/ZnO nanowires hybrid, optical absorption intensity is enhanced for CdSe QDs/RGO/ZnO nanowires during the wavelength from 200 to 650 nm. Meanwhile, it can be proved that the optical absorption can be increased for the visible light photo-modulated TFTs based on CdSe QDs/RGO/ZnO nanowires with excitonic transition peak at wavelength of 580 nm (Fig. 6).

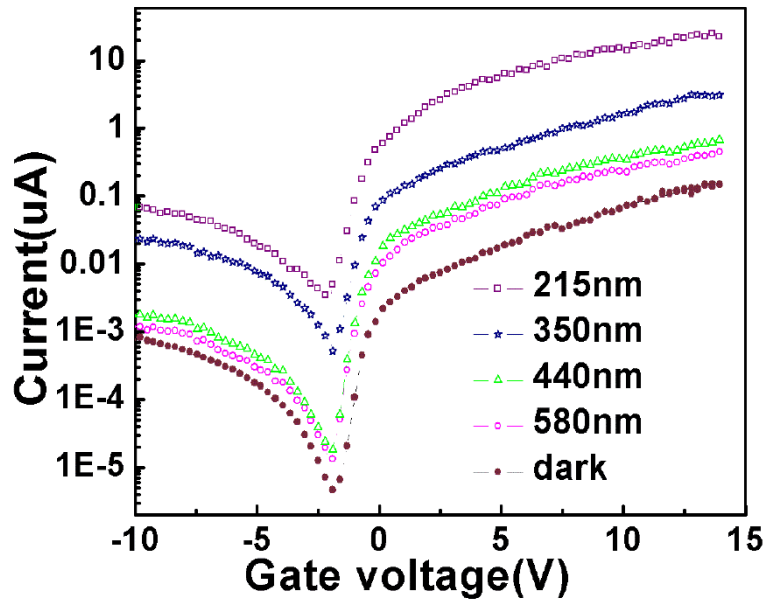


Figure 7 Transfer character curves for CdSe QDs/RGO/ZnO nanowire exposed to different wave incident light.

Fig. 7 it illustrates the transfer characteristic curves of CdSe QDs/RGO/ZnO nanowires device from the wavelength ranging from 215 to 580 nm. The result indicates a fluctuated decrease of current occurred from ultraviolet to red. Traditionally, the number of the electron and hole achieve balance and the material presents electric neutrality with the minimum current when gate voltage equals to 0 V. However, the electrons are injected to the RGO/ZnO nanowires by the built-in field when N-type CdSe QDs are utilized as the electron donor. In order to achieve the electric neutrality, a certain number of holes are ought to be provided from when N-type QDs are being doped. Therefore, the negative back gate voltage is playing a role for the contribution to attract holes and achieve the balance between the electrons and holes where the current is the minimum. Additionally, photogenerated carriers are consistent with results shown as the absorption spectra in Fig. 6, where the photocurrent has a relatively high value near the wavelength of excitonic transition peak.

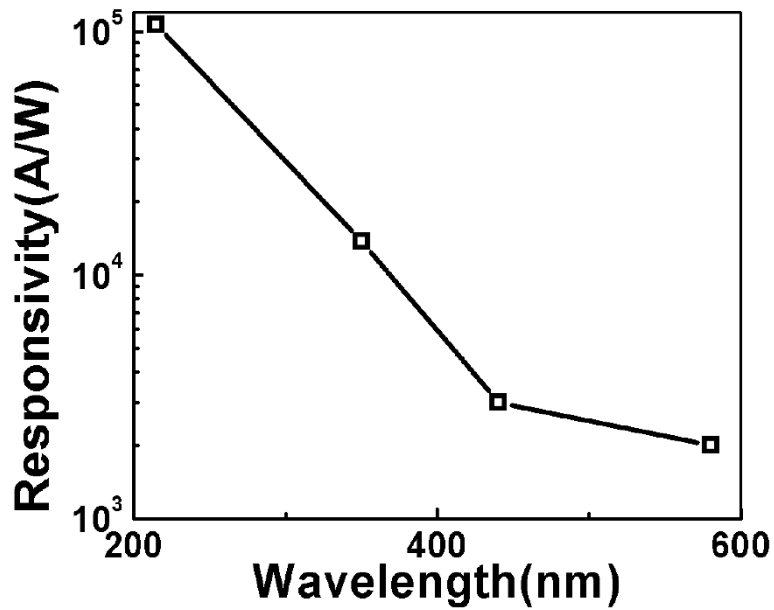


Figure 8 The responsivity curve for different devices in incident light ($\lambda=215\text{nm}$, 350nm , 440nm , 580nm).

As illustrated in Fig. 8, the photoresponse waveband of the hybrid material can be expanded and the opportunity for the exciton separation can be improved. This contributes to the enhanced photo-current and photo-responsivity gain.

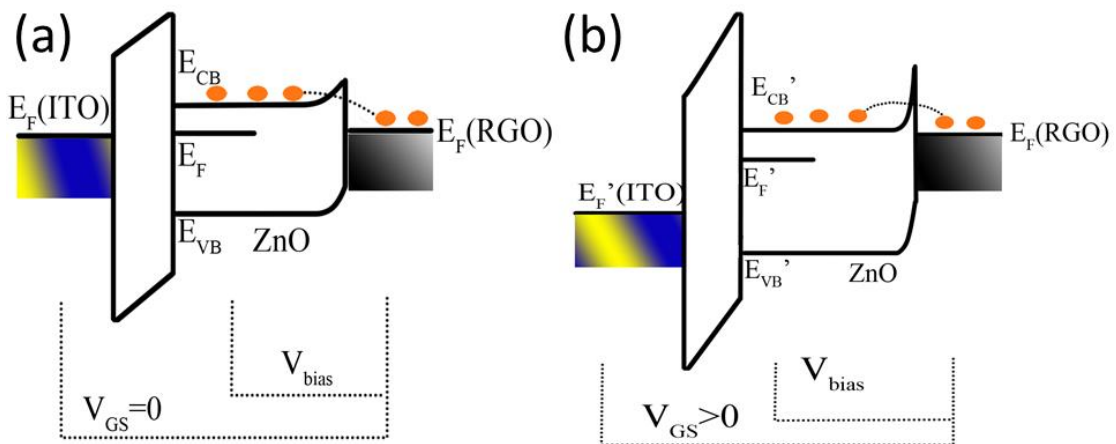


Figure 9. Bias mechanism schematic diagram of the device with positive back gate voltage on and off.

The photo-responsivity can be enhanced by modulating the back-gate voltage due

to the existence of carrier transport mechanism [28-30] (in Fig. 9 left). It shows the energy band distribution with adjusting the diverse voltages of V_{GS} . For the interface of RGO/ZnO nanowires near the source electrode, a Schottky barrier is formed between ZnO nanowires and RGO fragments. When V_{bias} is applied in the ZnO nanowires and RGO fragments near the source electrode, electrons in RGO fragments can be transferred into the ZnO nanowires. Thus, I_S increases as the bias voltage is increased. In addition, $E_{F(RGO)}$ and $E_{F(ZnO)}$ levels are shifted upwards as V_{GS} is above zero. In the meanwhile, the width of Schottky barrier is reduced simultaneously (Fig. 9 right).

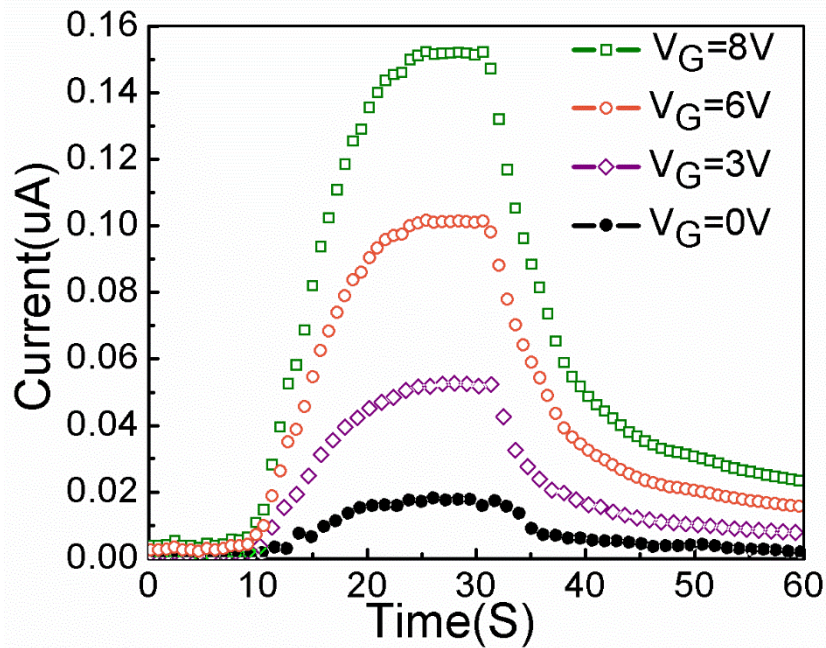


Figure 10 Time-dependent photo current response measurement with different gate-voltage ($V_{DS}=5V$) under illumination (580nm).

When the photo-modulated transistor is excited by the incident light ($\lambda=580$ nm), the improvement of the photocurrent can be measured by applying the back-gate voltage demonstrated in Fig. 10. In this measurement, the value of applied back gate voltage is proportional to the photocurrent. For instance, the photocurrent was measured as a value of $0.15 \mu A$ when back gate voltage was applied of 8 V. And the

photocurrent values of 0.015, 0.05, and 0.10 μA were measured when the back-gate voltages were 0, 3, and 6 V, respectively. Consequently, the electrons tunneling from RGO fragments to ZnO nanowires is easily obtained by applying the positive back gate voltage and it leads to the 10 folds improvement of the photo responsivity.

Summary

To summarize, a novel photo-modulated transistor based on the TFT structure was fabricated by using hybrid material of CdSe QDs/RGO fragments and ZnO nanowires. By incorporating the RGO fragment, the interface and heterostructure in this hybrid material can be properly improved and the photo responsivity of this transistor was improved by $\sim 10^2$ times. This can be more advanced than that of based on CdSe QDs/ZnO nanowires in the visible wavelength of incident light. In addition, the photocurrent of this device was improved by 10 times by manipulating the back-gate voltages. The photo responsivity (2000 A W^{-1}) was also enhanced and the photo-response waveband was upgraded. Since the process of our work was operated in room temperature, achievements of using hybrid materials in photo-modulated transistor can be a potential candidate for applications in the large-area transparent flexible photo electronics.

References

- [1] C.H. Wu, K.M. Chang, S.H. Huang, I.C. Deng, C.J. Wu, W.H. Chiang, C.C. Chang, Characteristics of IGZO TFT prepared by atmospheric pressure plasma jet using PE-ALD Al₂O₃ gate dielectric. *IEEE Electr. Device Lett.* **33**(4), 552-554 (2012). doi:[10.1109/LED.2012.2185774](https://doi.org/10.1109/LED.2012.2185774)
- [2] S. Jeon, S.E. Ahn, I. Song, C.J. Kim, U.I. Chung, E. Lee, I. Yoo, A. Nathan, S. Lee, J. Robertson, K. Kim, Gated three-terminal device architecture to eliminate persistent photoconductivity in oxide semiconductor photosensor arrays. *Nat. Mater.* **11**(4), 301-305 (2012). doi:[10.1038/nmat3256](https://doi.org/10.1038/nmat3256)
- [3] E. Fortunato, P. Barquinha, R. Martins, Oxide semiconductor thin-film transistors: a review of recent advances. *Adv. Mater.* **24**(22), 2945-2986 (2012). doi:[10.1002/adma.201103228](https://doi.org/10.1002/adma.201103228).
- [4] K. Ghaffarzadeh, A. Nathan, J. Robertson, S. Kim, S. Jeon, C. Kim, U.I. Chung, J.-H. Lee, Persistent photoconductivity in Hf-In-Zn-O thin film transistors. *Appl. Phys. Lett.* **97**, 143510 (2010). doi:[10.1063/1.3496029](https://doi.org/10.1063/1.3496029)
- [5] K. Ghaffarzadeh, A. Nathan, J. Robertson, S. Kim, S. Jeon, C. Kim, U. I. Chung, J.-H. Lee, Instability in threshold voltage and subthreshold behavior in Hf-In-Zn-O thin film transistors induced by bias-and light-stress. *Appl. Phys. Lett.* **97**, 113504 (2010). doi:[10.1063/1.3480547](https://doi.org/10.1063/1.3480547)
- [6] Y.K. Su, S.M. Peng, L.W. Ji, C.Z. Wu, W.B. Cheng, C.H. Liu, Ultraviolet ZnO nanorod photosensors. *Langmuir* **26**(1), 603-606 (2010). doi:[10.1021/la902171j](https://doi.org/10.1021/la902171j)
- [7] Z. Dai, L. Wei, D. Xu, Y. Zhang, Ultraviolet photoresponse of ZnO nanowire thin-film transistors. *Physica E* **44**(10), 1999-2004 (2012). doi:[10.1016/j.physe.2012.05.033](https://doi.org/10.1016/j.physe.2012.05.033)

- [8] E.S. Ates, S. Kucukyildiz, H.E. Unalan, Zinc oxide nanowire photodetectors with single-walled carbon nanotube thin-film electrodes. *ACS Appl. Mater. Interf.* **4**(10), 5142-5146 (2012). doi:[10.1021/am301402y](https://doi.org/10.1021/am301402y)
- [9] A.J. Nozik, Spectroscopy and hot electron relaxation dynamics in semiconductor quantum wells and quantum dots. *Ann. Rev. Phys. Chem.* **52**, 193-231 (2001). doi:[10.1146/annurev.physchem.52.1.193](https://doi.org/10.1146/annurev.physchem.52.1.193)
- [10] S. Sapra, D.D. Sarma, Evolution of the electronic structure with size in II-VI semiconductor nanocrystals. *Phys. Rev. B* **69**(12), 125304 (2004). doi:[10.1103/PhysRevB.69.125304](https://doi.org/10.1103/PhysRevB.69.125304)
- [11] X. Michalet, F.F. Pinaud, L.A. Bentolila, J.M. Tsay, S. Doose et al., Quantum dots for live cells, in vivo imaging, and diagnostics. *Science* **307**(5709), 538-544 (2005). doi:[10.1126/science.1104274](https://doi.org/10.1126/science.1104274)
- [12] S. Kaniyankandy, S. Rawalekar, S. Verma, D.K. Palit, H.N. Ghosh, Charge carrier dynamics in thiol capped CdTe quantum dots. *Phys. Chem. Chem. Phys.* **12**(16), 4210-4216 (2010). doi:[10.1039/b921130f](https://doi.org/10.1039/b921130f)
- [13] S.A. McDonald, G. Konstantatos, S.G. Zhang, P.W. Cyr, E.J.D. Klem, L. Levina, E.H. Sargent, Solution-processed PbS quantum dot infrared photodetectors and photovoltaics. *Nat. Mater.* **4**(2), 138-142 (2005). doi:[10.1038/nmat1299](https://doi.org/10.1038/nmat1299)
- [14] Y. Bu, Z. Chen, Effect of hydrogen treatment on the photoelectrochemical properties of quantum dots sensitized ZnO nanorod array. *J. Power Sources* **272**, 647-653 (2014). doi:[10.1016/j.jpowsour.2014.08.127](https://doi.org/10.1016/j.jpowsour.2014.08.127)
- [15] H. Kim, K. Yong, Highly efficient photoelectrochemical hydrogen generation using a quantum dot coupled hierarchical ZnO nanowires array. *ACS Appl. Mater. Interfaces* **5**(24), 13258-64 (2013). doi:[10.1021/am404259y](https://doi.org/10.1021/am404259y)

- [16] Q. Bao, K.P. Loh, Graphene photonics, plasmonics, and broadband optoelectronic devices. *ACS Nano* **6**(5), 3677-3694 (2012). doi:[10.1021/nm300989g](https://doi.org/10.1021/nm300989g)
- [17] F. Bonaccorso, Z. Sun, T. Hasan, A.C. Ferrari, Graphene photonics and optoelectronics. *Nat. Photonics* **4**(9), 611-622 (2010). doi:[10.1038/nphoton.2010.186](https://doi.org/10.1038/nphoton.2010.186)
- [18] T.J. Echtermeyer, L. Britnell, P.K. Jasnós, A. Lombardo, R.V. Gorbachev, A.N. Grigorenko, A.K. Geim, A.C. Ferrari, K.S. Novoselov, Strong plasmonic enhancement of photovoltage in graphene. *Nat. Commun.* **2**, **458** (2011). doi:[10.1038/ncomms1464](https://doi.org/10.1038/ncomms1464)
- [19] S. Kaniyankandy, S. Rawalekar, H.N. Ghosh, Ultrafast charge transfer dynamics in photoexcited CdTe quantum dot decorated on graphene. *J. Phys. Chem. C* **116**(30), 16271-16275 (2012). doi:[10.1021/jp303712y](https://doi.org/10.1021/jp303712y)
- [20] J. Li, L. Niu, Z. Zheng, F. Yan, Photosensitive graphene transistors. *Adv. Mater.* **26**(31), 5239-5273 (2014). doi:[10.1002/adma.201400349](https://doi.org/10.1002/adma.201400349)
- [21] S.-H. Cheng, T.-M. Weng, M.-L. Lu, W.-C. Tan, J.-Y. Chen, Y.-F. Chen, All carbon-based photodetectors: An eminent integration of graphite quantum dots and two dimensional graphene. *Sci. Rep.-UK* **3**, 2694 (2013). doi:[10.1038/srep02694](https://doi.org/10.1038/srep02694)
- [22] L.-H. Zeng, M.-Z. Wang, H. Hu, B. Nie, Y.-Q. Yu et al., Monolayer graphene/germanium schottky junction as high-performance self-driven infrared light photodetector. *ACS Appl. Mater. Interfaces* **5**(19), 9362-9366 (2013). doi:[10.1021/am4026505](https://doi.org/10.1021/am4026505)
- [23] M. Zhu, X. Li, Y. Guo, X. Li, P. Sun et al., Vertical junction photodetectors based on reduced graphene oxide/silicon Schottky diodes. *Nanoscale* **6**(9), 4909-4914 (2014). doi:[10.1039/c4nr00056k](https://doi.org/10.1039/c4nr00056k)

- [24] X. Liu, X. Ji, M. Liu, N. Liu, Z. Tao, Q. Dai, L. Wei, C. Li, X. Zhang, B. Wang, High-performance Ge quantum dot decorated graphene/zinc-oxide heterostructure infrared photodetector. *ACS Appl. Mater. Interfaces* **7**(4), 2452-8 (2015). doi:[10.1021/am5072173](https://doi.org/10.1021/am5072173)
- [25] L. Cai, S. Zhang, J. Miao, Q. Wei, C. Wang, Capacitance-voltage characteristics of thin-film transistors fabricated with solution-processed semiconducting carbon nanotube networks. *Nanoscale Res. Lett.* **10**, 291 (2015). doi:[10.1186/s11671-015-0999-8](https://doi.org/10.1186/s11671-015-0999-8)
- [26] L.G. Cancado, A. Jorio, E.H. Martins Ferreira, F. Stavale, C.A. Achete et al., Quantifying defects in graphene via raman spectroscopy at different excitation energies. *Nano Lett.* **11**(8), 3190-3196 (2011). doi:[10.1021/nl201432g](https://doi.org/10.1021/nl201432g)
- [27] H. Chang, Z. Sun, M. Saito, Q. Yuan, H. Zhang et al., Regulating infrared photoresponses in reduced graphene oxide phototransistors by defect and atomic structure control. *ACS Nano* **7**(7), 6310-6320 (2013). doi:[10.1021/nn4023679](https://doi.org/10.1021/nn4023679)
- [28] L.-H. Zeng, M.-Z. Wang, H. Hu, B. Nie, Y.-Q. Yu et al., Monolayer graphene/germanium schottky junction as high-performance self-driven infrared light photodetector. *ACS Appl. Mater. Interfaces* **5**(19), 9362-9366 (2013). doi:[10.1021/am4026505](https://doi.org/10.1021/am4026505)
- [29] X.-W. Fu, Z.-M. Liao, Y.-B. Zhou, H.-C. Wu, Y.-Q. Bie, J. Xu, D.-P. Yu, Graphene/ZnO nanowire/graphene vertical structure based fast-response ultraviolet photodetector. *Appl. Phys. Lett.* **100**, 223114 (2012). doi:[10.1063/1.4724208](https://doi.org/10.1063/1.4724208)
- [30] T. Xin, A. Eric, L. Feng, L. Handong and M. W. Zhiming, "Advances in MoS₂-based Field Effect Transistors (FETs)", *Nano-Micro Letters.* **7** (2)(2015). doi:[10.1007/s40820-015-0034-8](https://doi.org/10.1007/s40820-015-0034-8)

Part B: NIR organic phototransistors

1. Introduction

Although UV-visible waveband plays a very important role in our daily lives, infrared waveband has an irreplaceable and important use in medical examination, military detection and communication. When the wavelength is above 800nm, we can call it the range of infrared light, including the near infrared, mid-infrared and far-infrared regions. Since the infrared band is beyond the visible range, we can't see it with the naked eye. Infrared is mainly thermal radiation, that is, any object that is not absolutely zero will radiate infrared light, so most of the nighttime camera devices we use are based on infrared imaging. In healthcare field, near-infrared is the most important infrared waveband for medical examination.

With the connection between individuals and Internet deepening, portable photo-detectors have been one of the most important sensor terminals. In the near infrared waveband, traditional near infrared photo-detectors can't meet the requirement for the photo-electric mechanism and complicated fabrication process. Large area, low cost, flexible and environmental near-infrared photo-detector has been as the research hotspot. Due to the high efficiency of the photo-electric conversion, solution process and tunable response waveband, Quantum dots have been as the attractive photo-sensitive materials. Meanwhile, organic materials have been widely utilized in the low cost, flexible electronics. Printing technology have been studied in flexible, low cost and large area electronics fabrication. The combination of the Quantum dots and printed organic electronics is the focus of our work.

In Part B, we will conduct an in-depth study of printing pattern formation with modification printing parameters, the connection between the n-type organic semiconductor layer (C60) grain size and electrical performance, and printed organic near infrared photo-sensitive system with PbS Quantum Dots.

2. Inkjet Printing

Although continuous inkjet printing is the earliest inkjet printing method, it is more advantageous in terms of printing speed than the on-demand inkjet printing that appears later. Based on the continuous inkjet technology, it is necessary to additionally equip the ink droplet charging device, the deflection device and the ink recovery circulation system, etc., and the equipment cost is high, and the lower material utilization rate further increases the production cost. The continuous inkjet printing is currently largely replaced by drop-on-demand (DoD) printing. The nozzle structure of the DoD inkjet principle is greatly simplified, and the inherent unreliability of the nozzle structure of the continuous ink jet principle is eliminated, the size and spacing of the jet ink droplets can be controlled, and the utilization rate of the material is also significantly improved. We will present the key steps of the printing techniques. And then our result will explain the connection between the pattern formation and the printing parameters such as surface energy, working frequency, overlap distance.

2.1 The key steps of inkjet printing pattern formation: Spreading, Wetting and Drying

- *Spreading*

With a relatively high jetting velocity (6-10m/s), a droplet impacts on a dry surface and several behaviors can be observed. Indeed, depending on substrates (hydrophobicity, roughness...) and/or fluid (viscosity, elasticity...) properties, different spreading behaviors can be observed as shown in Fig 2-1.

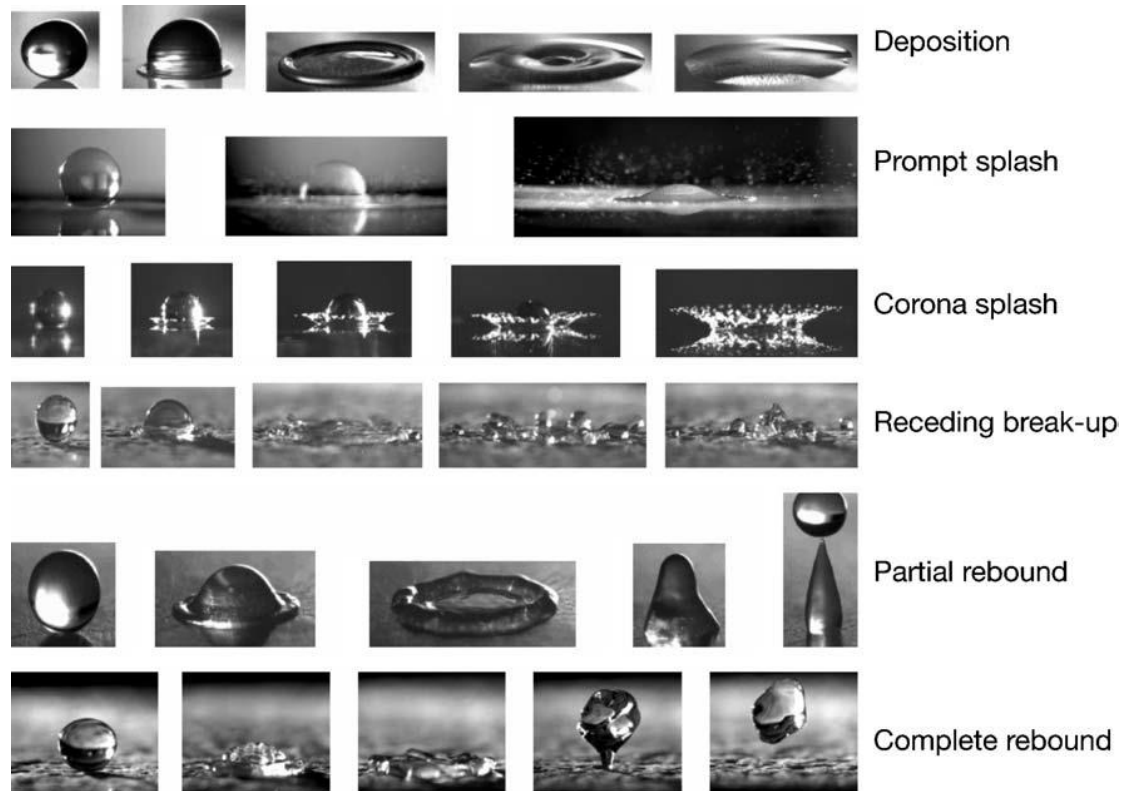


Figure 2-1: Behavior of drop impact on a dry surface [1]

As illustrated in the first line of Fig 2-1, the requisition for inkjet printing techniques impact mechanism is analyzed. The droplet deposition can be divided in two parts: i) Images 1,2 and 3 of the first line show the spreading step (i.e, drop let impact and its diameter increased). This step is mainly affected by fluid viscosity. The lower is the viscosity, the larger is the impact diameter and consequently large printed patterns will be performed. ii) Images 4 and 5 of the first line show the relaxation phase where the droplet minimizes its energy and determines the equilibrium contact angle. Surface wetting properties strongly affect this phase.

The other lines of Fig 2-1 show unwanted spreading effects for inkjet printing technology. For instance, splashing showing in the second and third lines affects the printed pattern accuracy. This behavior can appear when: velocity is too high, surface tension and viscosity is too low or substrate is too rough [2]. The other lines of Fig 2-1

show unwanted phenomenon that can occur on super-hydrophobic surfaces.

- **Wetting**

The wettability of a solid surface is the ability of a liquid to remain in contact with a solid. It is the result of intermolecular interactions between solid and liquid, and depends primarily on the balance between adsorption and adhesion. The adsorption between the solid and liquid molecules promotes the spreading of the droplets on the solid surface, while the internal viscosity of the liquid prevents the droplets from spreading in order to maintain the spherical crown of the droplets. Regardless of the wettability, the droplets are spherically crowned when they are in contact with the substrate, as shown in Fig 2-2. At this time, the contact angle θ of the droplet on the solid surface is the angle between the solid-liquid interface and the tangent to the gas-liquid interface. The contact angle is the result of the interaction between the adsorption force and the viscosity, and is therefore used to judge the wettability of the solid surface. When the droplets tend to spread out on the solid surface, the solid-liquid contact surface increases and the contact angle decreases. Therefore, the value of the contact angle is inversely proportional to the solid infiltration property, and the smaller the contact angle, the better the wettability.

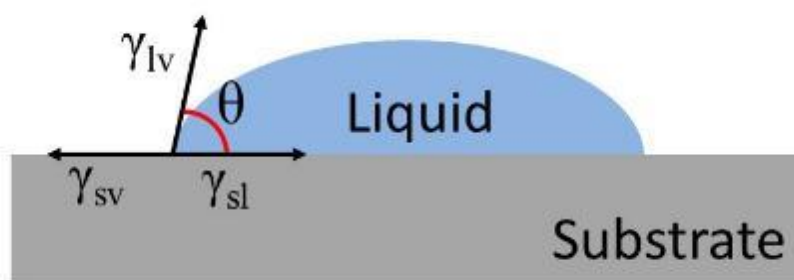


Figure 2-2 Definition of the contact angle between liquid droplets and solid surfaces

The relationship between various wettability and contact angle is shown in Table

2-1.

Contact Angle	Wettability	Solid-liquid interaction	Liquid action
$\theta=0^\circ$	Complete wetting	Strong	Weak
$0^\circ<\theta<90^\circ$	High wetting	Strong	Strong
		Weak	Weak
$90^\circ\leq\theta<180^\circ$	Mild wetting	Weak	Strong
$\theta=180^\circ$	Complete non-wetting	Weak	Strong

Table 2-1 contact angle versus wettability

The quantification of the molecular bonds that are destroyed when creating a surface is called surface energy. In solid physics, the molecular energy of the surface of the material is higher than the molecular energy of the internal material, otherwise there will be a driving force for removing the internal material on the surface of the material. Therefore, from an energy point of view, the solid surface energy can be defined as the portion of the energy of the solid surface that is larger than the solid internal material.

The value of solid surface energy depends mainly on the interaction force between solid constituent molecules. Solids with higher surface energy interact with each other through strong chemical bonds, such as covalent bonds, metal bonds, ionic bonds, etc. The solid molecules with low surface energy are connected by weak molecular forces, such as Van der Waals forces, hydrogen bonds. The high-energy surface has a very strong chemical bond that requires a large amount of energy to be destroyed and is usually easily wetted by the solution. On the low energy surface, the intermolecular interaction is weak, it is easy to be destroyed, and it is generally difficult to be wetted by the solution. Partial or complete infiltration of low energy surfaces can be done with

liquids of different polarity [3-4].

In 1805, T. Young assumed the ideal condition that the solid surface was isotropic and uniform smooth. The condition that the force in the horizontal direction at the three-phase contact point reached equilibrium was obtained, and the Young's equation of the wetting basic equation was obtained [5].

$$\cos \theta = \frac{\gamma_{sv} - \gamma_{sl}}{\gamma_{lv}} \quad (2-1)$$

Here, θ is the static contact angle of the droplet, γ_{sv} , γ_{sl} , γ_{lv} represents "solid-gas", "solid-liquid" and "liquid-gas" interfacial tension, respectively. According to the Young's equation, the ability of a droplet to wet a solid surface depends on the magnitude of the surface tension at various interfaces. Corresponding to the relationship between contact angle and wettability in Table 2-1: when $\gamma_{sv} > \gamma_{sl}$, $\cos \theta > 0$, it means $0^\circ < \theta < 90^\circ$, the liquid can highly wet the solid surface; when $\gamma_{sv} < \gamma_{sl}$, $\cos \theta < 0$, it means $90^\circ < \theta < 180^\circ$, the liquid can mildly wet the solid surface. when $\gamma_{sv} \ll \gamma_{vl}$, $\cos \theta = -\infty$, it means $\theta = 180^\circ$, the liquid completely non-wet the solid surface. when $\gamma_{sv} \gg \gamma_{vl}$, $\cos \theta = +\infty$, it means $\theta = 0^\circ$, the liquid completely wet the solid surface. In summary, it can be understood that the level of solid surface tension (surface energy) determines the wettability of the droplets thereon. The higher the surface energy, the easier it is to be wetted. The lower the surface energy, the more likely it is to be super-sparse.

Usually, the surfaces with contact angle $\theta < 90^\circ$ are classified as hydrophilic, and those with contact angle $\theta > 90^\circ$ as hydrophobic.

- **Drying**

When the droplet is deposited on the substrate, a phase change occurs that is usually induced by solvent evaporation. For instance, a well-known drying behavior, which is reported as a drawback, in most cases, is the coffee ring effect. *R.D.Deegan et al.*

conducted an in-depth study of the "coffee ring" phenomenon in 1997[6]. They believe that the formation of the "coffee ring" is due to the capillary flow caused by the uneven evaporation of the droplets, which causes the suspended solute to be carried to the edge of the droplet and deposited, as shown in Fig 2-3. As reported by *Lim et al.* They proposed that the pinning of the three-phase contact line of the volatile droplets is one of the necessary conditions for the formation of the "coffee ring" effect. When the contact line of the droplet is pinned to the substrate, the rate of evaporation of the solvent at the edge of the droplet is greater than the rate of evaporation at the center. To compensate for the loss of solvent at the edge of the droplet, a capillary flow from the center to the edge is created within the droplet, which causes the solute to carry the solute to the edge and dry to form a "coffee ring."

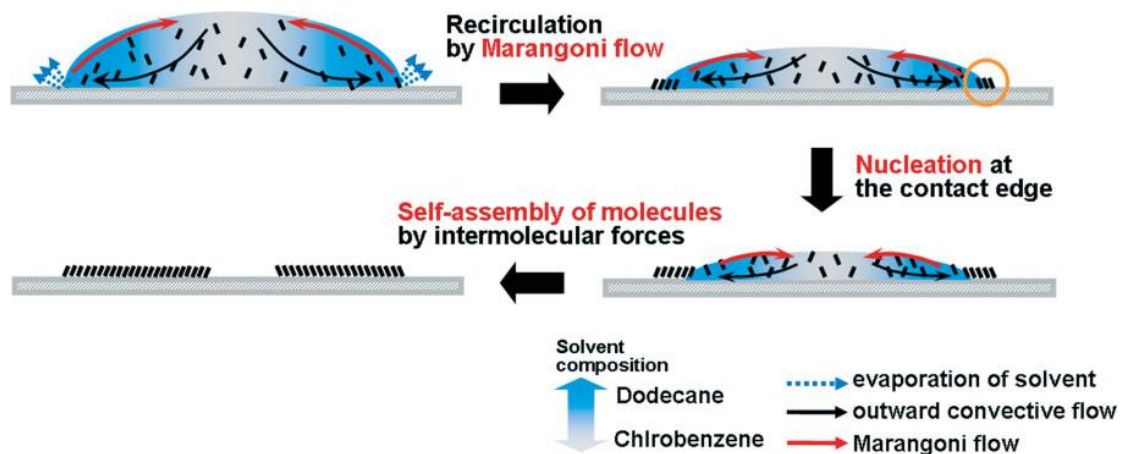


Figure 2-3 the schematic illustration of the coffee ring formation[7]

Many techniques have been utilized in order to decrease such phenomena. For instance, the use of higher substrate temperature during printing can improve the film homogeneity. Heating the substrate increases the surface tension gradient between the edge and the center of the droplet. Such surface tension gradient induces Marangoni flows that carry the solute inward [8]. Consequently, this effect competes with this one observed by Deegan leading to obtain a more uniform profile.

2.2 The research of spreading and drying impact on inkjet printing Pattern Accuracy

According to the foregoing, inkjet printing process is composed of three main steps: i) droplet generation, ii) droplet spreading onto an arbitrary substrate and iii) droplet drying. Each step has to be fully understood in order to fabricate accurate patterns [9]. Concerning droplet generation, recent works have demonstrated the exploitation of a jettable window (i.e., using Ca-We space) to adjust the rheology of nanoparticle ink [10] or polymeric ink [11] to allow the design of a jettable ink. Using such methodology, nozzle clogging, long-lived filament, and satellite droplets can be suppressed improving pattern accuracy [12-14]. However, the patterns generation behavior remains complex to understand because many experimental parameters play a crucial role during ink spreading and drying, due to its interaction with the substrate. For instance, lines can show uniform, bulged, scalloped, stacked or separated patterns as function of jetting frequency and drop spacing [15, 16].

After the drying step, droplets often show non-uniform profile that is frequently attributed to the so-called coffee stain effect, firstly described by Deegan. [6] Moreover, several works proposed strategies to suppress such undesirable behavior. [11, 17, 18] Consequently, patterns profile can be optimized from smooth to periodically wave-shaped film depending on application requirements. [11, 17, 19]

On the one hand, new inks designs are more and more complex and multicomponent mixtures are usually required to obtain jettable inks fitting desired properties (e.g., high conductivity for colloidal ink) [20]. On the other hand, literature dealing with multicomponent mixture reports more complex droplets drying behavior than in the work of Deegan [21-23]. Indeed, these works that mainly dealt with isolated drop-casted microliters droplets, have shown the presence of phase separation during spreading and drying. In our work, this behavior has been verified on picoliters printed droplets as function of substrate wettability. Moreover, in the second part of this work,

ink phase separation impact on patterns formation such as lines or squares is studied. Indeed, in the field of printed electronics, lines or squares are required to fabricate interconnects or electrodes for instance.

2.2.1 The material and methods of experiment

- *Hardware*

The inkjet printer used in this thesis is piezoelectric jet systems, named Ceraprinter X-series. It is an “all-in-one” advanced materials deposition inkjet tool for inkjet processes development in printed electronics and smart 3D printing. It offers the possibility to use different print-head manufacturers. Thanks to its embedded post-process and its innovative software package, Ceraprinter X-series brings new opportunities to a wide range of industrial fields. The optical picture of Ceraprinter X-series is shown in Fig 2-4.



Figure 2-4: Optical picture of Ceraprinter X-series

The Ceraprinter X-series, used in this work, is equipped with one print-head with 256 nozzles (256 nozzles Q-class print-head (Dimatix[®])). It was used to print silver ink as electrodes.

- *Software*

The software is composed of three modules: Ceraslice, Fab-analyser and Drop-analyser.

Drop-analyzer is an advanced droplets jetting analysis software.

Fab-analyzer is used for analyzing printed layers and substrate alignment.

Ceraslice is dedicated to the design (including: a gds files viewing, simulation step allowing the visualization of droplets overlapping).

- *Materials*

400nm thick Su8 2002 films were obtained using spin-coating (Velocity = 3000 rpm; Acceleration = $3000\text{rpm}\cdot\text{s}^{-1}$, time = 60 seconds) on glass substrates. Su8 films were baked at 95°C and exposed to UV before the final baking at 110°C during at 20 minutes. Jetlight equipment (UVO-Cleaner[®] 42) was used for UV ozone exposure. For SEM experiments, Su8 was spin coated following the same process. Silicon substrates was used and 5nm gold was deposited after inkjet printing step (silver-based ink). Such protocol was used in order to reduce charging effect during SEM observations. Silver based ink was purchase from ANP and used as received. Ink reference is: ANP 40LT15C which is composed of Silver nanopowder, <100nm particle size and contains PVP as dispersant (Sigma Aldrich). TGME ($\text{C}_8\text{H}_{18}\text{O}_4$) is used as main solvent. The metal content, the surface tension, the viscosity and the density equal 30.18wt%, 36.8mN/m, 14.16cps, 1.45g/mL respectively.

- *Jetting experiments*

- i) Jetting criteria

The jettable criterion is the ability to obtain a droplet at a distance range from $800\mu\text{m}$ to 1 mm (acceptable working distance for the printer equipment: CERADROP Xseries). Satellite droplets or tail must be reabsorbed by the nozzle and jettability must be stable for a long time with low droplet misalignment on the substrate. The stroboscopic vision system was used to determine droplet volume and velocity of three ink dilutions.

ii) Jetting at low frequency

For all the experiments, results obtained using 20Hz as jetting frequency show deformed printed patterns. In this case, jetting frequency is close to the lowest printing velocity of the printer. Consequently, authors suggest that pattern deformations are only due to the printer.

- *Characterization*

Scanning electron microscope images were obtained using a JEOL 7100 FEG microscope. Water contact angle measurements were obtained using Kruss DSA30 equipment. Data are an average value of 10 measurements. Profilometry measurements were performed using TENCOR KLA P6 equipment. Optical microscope images were obtained using a Leica microscope equipped with a digital camera.

2.2.2 Results and discussion

The inkjet printing parameters such as: velocity, firing voltage, substrate temperature have been kept constant and equal 3m/s, 65V and 50°C, respectively. This crucial step is prerequisite in order to study the accuracy of printed pattern.

- *Droplet spreading*

With the increasing of the UV-ozone exposure time, the effect of the substrate wetting properties on the droplets' drying behavior is illustrated in Fig 2-5. As UV-ozone exposure time increasing from 0min to 10min, the droplet drying pattern has been performed immediately.

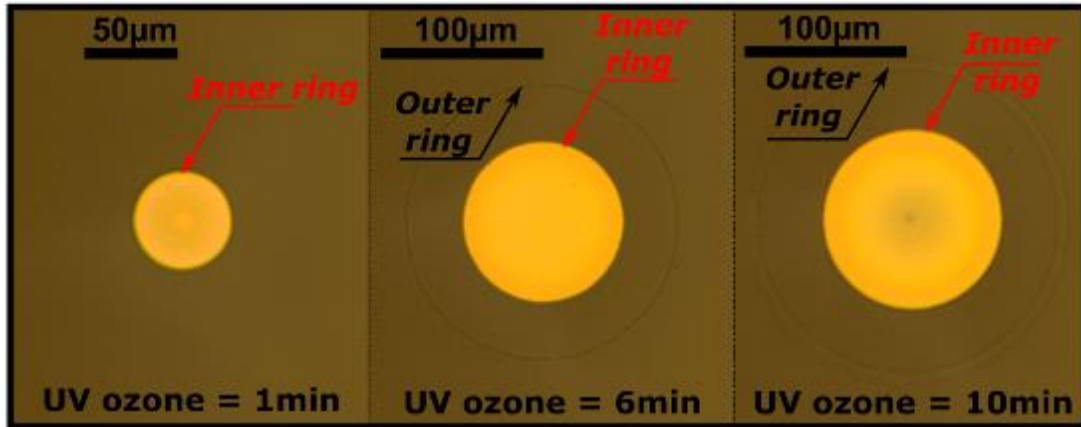


Figure 2-5 top view optical pictures of dried droplet as function of UV ozone time

As illustrated in Fig 2-5, aggregated silver nanoparticles are highlighted by a light-yellow region delimited by the mark: “Inner ring”. It means that the diameter of the inner ring is the boundary of the silver nanoparticles. Normally, the diameter and thickness of the inner ring are easily influenced by the surface character such as hydrophobic and hydrophilic. As expected, UV ozone exposure time has a strong impact on the silver nanoparticles spreading for the surface character changing. The more the surface has been exposed to UV ozone, the more the droplet has spread and consequently the more the region covered with nanoparticles is large. The drop diameter increase and the average thickness decreases. Surprisingly, two different droplet drying behaviors can be distinguished as function of UV ozone exposure time. At low UV exposure time (1 minute), only the inner ring can be observed. At higher UV ozone exposure times (6 and 10 minutes) another ring, marked “outer ring”, was observed. For the inner ring is the boundary of the aggregated silver nanoparticle, the constituent of the outer ring and the influenced factors are discussed.

In order to analyze the phenomena, the height and the diameter of the droplet is shown in Fig 2-6. From the Fig 2-6a, the dried droplets morphologies as function of UV ozone exposure time with the purpose of highlight the evolution is shown. With the 1min UV ozone treatment, the height of the droplet is above 200nm and without any

indication of the outer ring. By increasing the UV ozone time, firstly, the coffee stain effect is more obviously. For 4min UV ozone treatment, the height of the droplet boundary is 180nm, but the height of the central part of the droplet is 90nm. With this condition, the coffee stain effect is the most obvious one. Then, with the UV ozone increasing, the coffee stain effect and the height of the droplet are decreasing. When the UV ozone treatment is above 6min, there is no obviously change of the inner ring and the morphology is similar. Meanwhile, the outer ring phenomenon is more and more obviously.

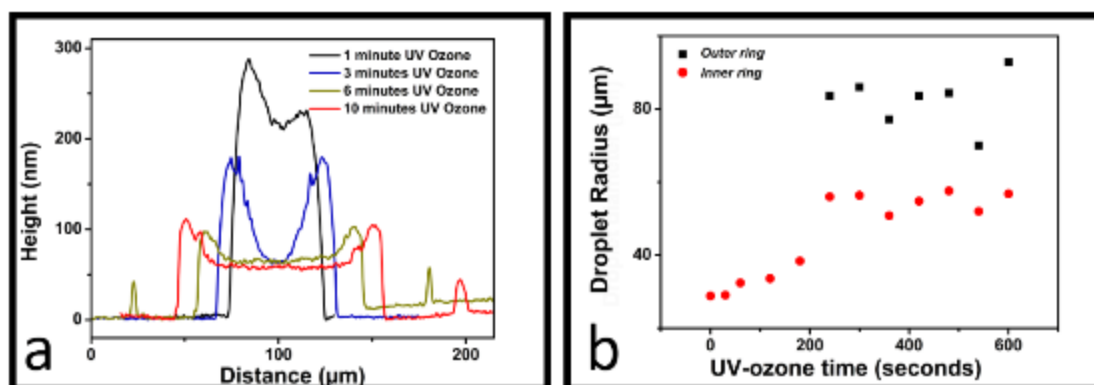


Figure 2.6 (a) two-dimensional profiles extracted along the diameter of a dried droplet as function of UV-ozone exposure time. UV-ozone exposure time equals 1,3,6 and 10min. (b) Inner droplet diameter and outer droplet diameter as function of UV-ozone exposure time.

Meanwhile, the diameter values of droplet are extracted from Fig 2-6b. With the UV ozone treatment time increasing, the inner ring, the diameter increased from 50 μm to 120 μm . Outer ring cannot be observed before 4 minutes UV exposure time whereas inner ring diameter increases. After 4 minutes UV ozone exposure time, both diameters (inner and outer ring) have no significant evolution. The diameter of the outer-ring is around 160 μm and doesn't change so much with the UV ozone treatment time. Meanwhile, UV ozone exposure time have a strong impact on colloids layer thickness

and morphology. Indeed, 10 minutes UV ozone exposure time divides the average thickness by more than 2 and exacerbates the well-known coffee stain effect [6]. Moreover, outer diameter is larger for 10 minutes of UV exposure time than for 6 minutes.

In conclusion, at low UV ozone exposure time (less than 4 minutes) the behavior of colloidal drying can be described, in first approximation, using Deegan's work [6]. This phenomenon, known as "coffee stain", is due to the solvent evaporation rate which is greater at the surroundings of the so-called "triple contact line". Consequently, when the contact line is pinned, solute transport from the center to the edge is induced by replenish flow, leading to inhomogeneous films after complete evaporation. However, as previously described, droplets drying behavior is different when the surface becomes highly hydrophilic (i.e., at higher UV ozone exposure time). In this case, Deegan's theory cannot fully explain the drying behavior.

A relevant study has reported the creation of a hydrophobic layer that surrounds (i.e., outer ring) printed patterns (e.g., isolated droplets) on a hydrophilic substrate [24]. This study showed that upon the impact, the droplet spreads at its maximum value before receding to its equilibrium state. Consequently, during triple contact line receding step, the desorbed stabilizing agent (hexadecylamine, in their case) was deposited leading to a hydrophobic boundary around the printed patterns. Note that, in this study, no observations were performed to confirm this hypothesis. However, this interesting work has shown that the surrounding layer impacts patterns creation.

Meanwhile, as shown in Fig 2-7, surface treatment has increased Su8 surface hydrophilicity. Indeed, water contact angle values have varied over a wide range, from hydrophobic (water contact angle equals at least 90°) to hydrophilic behavior (water contact angle value is less than 40°). Note that, after 60 seconds silver-based ink wets totally the surface and contact angle could not be measured. The silver-based ink

contact angle is close to the zero. Surface free energy as function of UV ozone exposure time is plotted on right axis. Values confirm that the more the Su8 surface is exposed to UV ozone treatment, the more the surface becomes hydrophilic (Fig 2-7a). The normalized radius show that the inner ring is about 2.5 times larger after 600s of exposure to UV ozone. The outer ring radius remains relatively consistent from its appearance (after 240s) to 600s exposure time (Fig 2-7b). Consequently, Su8 film has been chosen to deeply highlight the impact of UV ozone exposure effect. The surface energy increases from 40N/m to 75N/m.

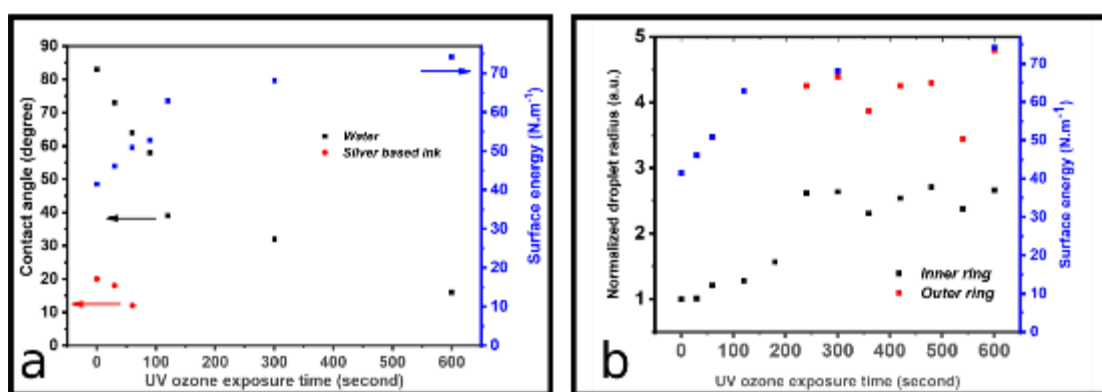


Figure 2-7 Spreading and wetting behavior of the droplets a) Water contact angle and silver-based ink contact angle (left axis) as function of UV ozone exposure time. b) Normalized droplet radii (inner and outer rings) and surface energy as function of UV ozone exposure time.

In our work, three components composed the silver-based ink (see in experimental section: “materials”): i) hard silver nanoparticles, ii) solvent and iii) Polyvinylpyrrolidone (PVP). Indeed, it has ever been demonstrated that the commercial ink (DGP 40LT15C) used in this study, reveals the presence of carbonyl groups (FT-IR experiments), suggesting that a polymer ligand such as PVP, has been used [25,26]. Moreover, it is well-known that PVP is commonly used in nanoparticles-based ink as surface stabilizer, growth modifier, nanoparticle dispersant, and reducing agent. The PVP avoids large sized nanoparticles agglomerations which can occur due to Van Der

Waals or Coulomb's forces [18,21,22]. Indeed, nanoparticles agglomeration is a major drawback for inkjet printing because it drastically increases nozzles clogging and must be avoided [27]. Furthermore, as for the work dealing with hexadecylamine as stabilizing agent, we suggest that an amount of PVP adhered to silver thanks to carbonyl silver bound and another amount is free (desorbed).

Taking into consideration ink composition and the previously mentioned works dealing with multicomponent mixtures drying, a hypothesis can be drawn: during spreading and drying steps, the droplets show a formation of an inner "cap" and an outer "foot" (see in Figure 2-8a), as described in other works [21,23]. A phase separation can occur leading to a colloid rich and a polymer rich region located in the center and at the periphery of the droplet, respectively. We suggest that the polymer rich region is mainly composed of desorbed (free) PVP. In that case, colloidal particles that are confined in the central region, also called "gelation region", form a "solid-like particle gel" which resists to droplet internal flow [21]. Indeed, as the solvent evaporates, concentration of nanoparticles increases and consequently they approach each other until they aggregate due to strong Van Der Waals interactions [21]. Due to phase separation, polymer which are confined in the foot pinned the droplet and is accumulated at the contact line due to internal flow in the foot. Such a behavior leads to the final residue as shown in Fig 1-8. Besides, as shown in Fig 2-8b the 3D schematic of dried droplet, the height of the top is approximately 160nm and the height of the foot is approximately 100nm. But there is no obviously phenomenon in the region between inner ring and outer ring. Based on this, except the coffee stain effect, there are some other parameters influence the morphology. Besides, considering the height of the outer ring, the pattern formation should be care of the foot part.

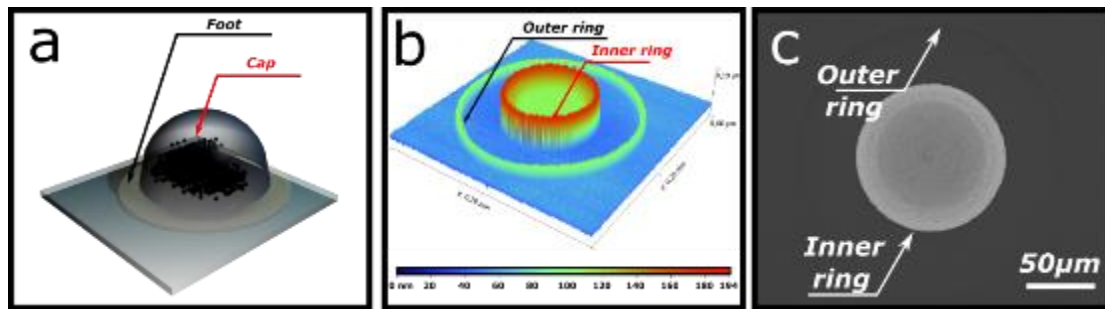


Figure 2-8 Drying behavior of droplet. a) 3D schematic of droplet at the beginning of drying step. A foot and a cap area occur. b) 3D profiles showing outer and inner ring of a dried droplet on polymeric surface exposed to UV ozone (10 minutes). d) SEM picture showing dried droplet.

Furthermore, as illustrated in Fig 2-9, with the SEM image of the dried droplet, the dried droplet can be divided into four part. Except the inner ring and outer ring, for the central part of the dried droplet, there are two zones. For the zone 1, cap is divided in two regions named C and G. foot is the darkest region of the image; Black arrows shows internal flow in the C region during drying. It means that for the process of the droplet drying, the nanoparticles in the zone 1 were constrained in this part. When PVP solution evaporated, the silver nanoparticles shrink to the central zone. However, the nanoparticles in the zone 1 was dried. The nanoparticles flowed back and aggregated around the boundary of the zone 1 and form the highest part of the dried part. In the zone 2, for the internal flow, the dried nanoparticles show the inhomogeneity. In this process, the aggregation of the nanoparticles was influenced by the force from the dried zone 1 and the internal flow from the solvent. The height of this zone was higher than zone 1. Besides, with the shrink of the silver nanoparticles, between the inter-ring and outer-ring, there are some silver colloids left. With this information, the drying behavior inside the cap can be obtained.

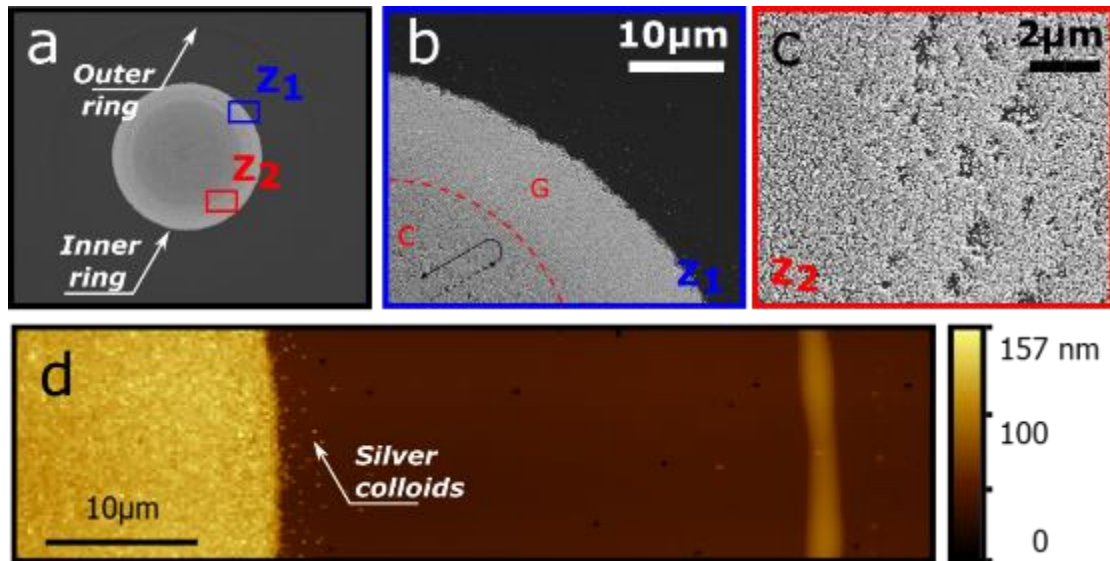


Figure 2-9: SEM pictures showing: a) dried droplet, b) A zoom Z1 showing the border between cap and foot; c) A zoom Z2 showing inhomogeneity of dried nanoparticles in C region. d) AFM scan showing: colloid rich region (yellow region on left side of image) and polymer rich region (right side of the image). AFM image shows the only few amounts of silver colloids can be found at the border of colloid and polymer rich region.

Equipment used to perform inkjet printing experiments does not allow to acquire top view images immediately when droplets land on substrate surface to verify this hypothesis. Moreover, due to the small droplet volume (fast evaporation) it is not possible to take the substrate out of the equipment in order to fully analyze spreading and drying behavior. Consequently, spreading and drying analyze have been performed on 0.1 μL droplet deposited using micropipettes under microscope to mimic the phenomena.

Top view optical pictures acquired as function of time are shown in Fig 2-10. Images in Fig 2-10a to 2-10e show the spreading behavior of the droplet onto Su8 surfaces exposed to 6 minutes of UV-ozone. During droplets spreading, materials are not uniformly distributed and two advancing fronts can be observed: the first one is

relative to the triple contact line and the second one corresponds to the perimeter of the dark area. As analyzed previously, the first front is the PVP solution and the second front is the hard-silver nanoparticles aggregation. It confirms that two phases exist in the droplet. Importantly, this observation highlights that the foot area is formed immediately after the droplet deposition and continually expand until the contact line is pinned (i.e, during the spreading step). Note that the dark area corresponds to a region rich in colloids. Colloids show replenish movement and never go outside this region that can suggest the existence of a gelation region. Iridescent region can be relative to polymer rich thin films. When spreading reaches its maximum, the triple contact line (first front) is pinned before it recedes letting the residue (Fig 2-10f and 2-10e). Colloids rich region that has also been pinned (see Fig 2-10g and 2-10h), dries at last step occurring a classical coffee stain. Consequently, the resulting dried profile (i.e., two rings) is obtained because of a stick-slip motion of the contact line. Indeed, contact line is mainly pinned two times during its receding phase and consequently lets residues of materials where it has been pinned.

Note that the observation of the wetting and the drying behavior highlights that the residue is due to a combination of several physical phenomena mainly due to phase separation occurring during droplet spreading and not only the stick-slip motion of the contact line.

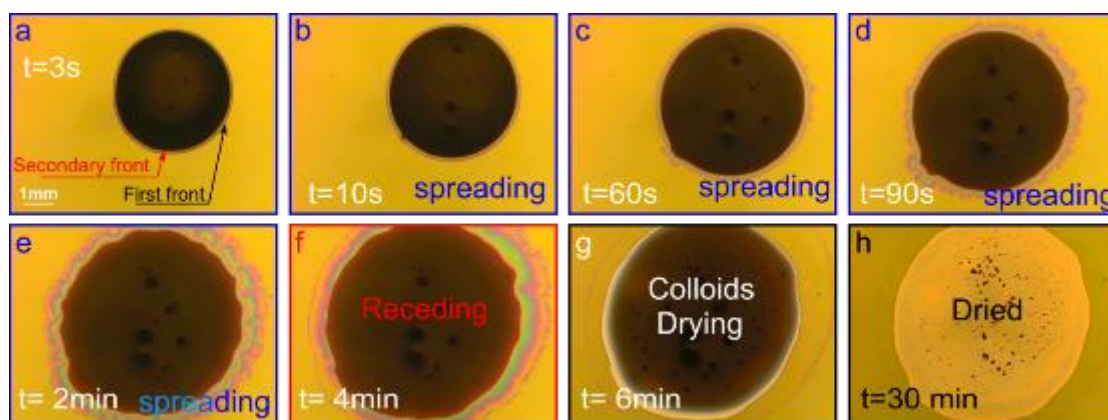


Figure 2-10: Optical images of silver ink drop-casted on Su8 surface exposed to 6 minutes UV-ozone. Images a to d show the drying behavior of the droplet as function of time. Images a) to h) have been captured respectively 3s, 10s, 60s, 90s, 2min, 4min, 6min and 30min, after the droplet deposition. From a) to d), two advancing fronts could be observed showing the separation phase when the droplet spreads. In Figure f) the droplet contact line has been pinned and is beginning to recede. In Figure g) the solvent has evaporated in the foot area and colloids area remains to dry. in Figure h) the droplet is fully dry.

The results presented in this section have shown that due to the presence of PVP molecules a residue remains at the periphery of the droplet triple contact line whereas colloids are confined in the central region. We have demonstrated that the control of the surface wetting properties is an easy way to drastically reduce such unexpected behavior. Note that, other ink composition using another stabilizer agent have also shown the existence of a surrounding layer.

Moreover, it has also been shown that such layer can have a strong impact on the pattern's formation. That's why, in the following, deeper investigations will be performed on more complicated patterns (conductive lines and square shaped patterns) to understand the effect of such residue as function of the substrates wetting and the jetting frequency.

- *Line formation*

In order to understand the effect as function of the substrates wetting and the jetting frequency, firstly, we should analyze the line patterns formation. DoD printing technique relies on the coalescence of adjacent droplets in order to form patterns. However, the substrate wettability control is a key parameter to obtain well-defined patterns. Indeed, when triple contact line is not firmly pinned patterns can split during drying due to fluid instability as shown in Fig 2-11. Thus, it is well-known that surface

treatment (e.g., UV ozone) is necessary to solve this drawback.

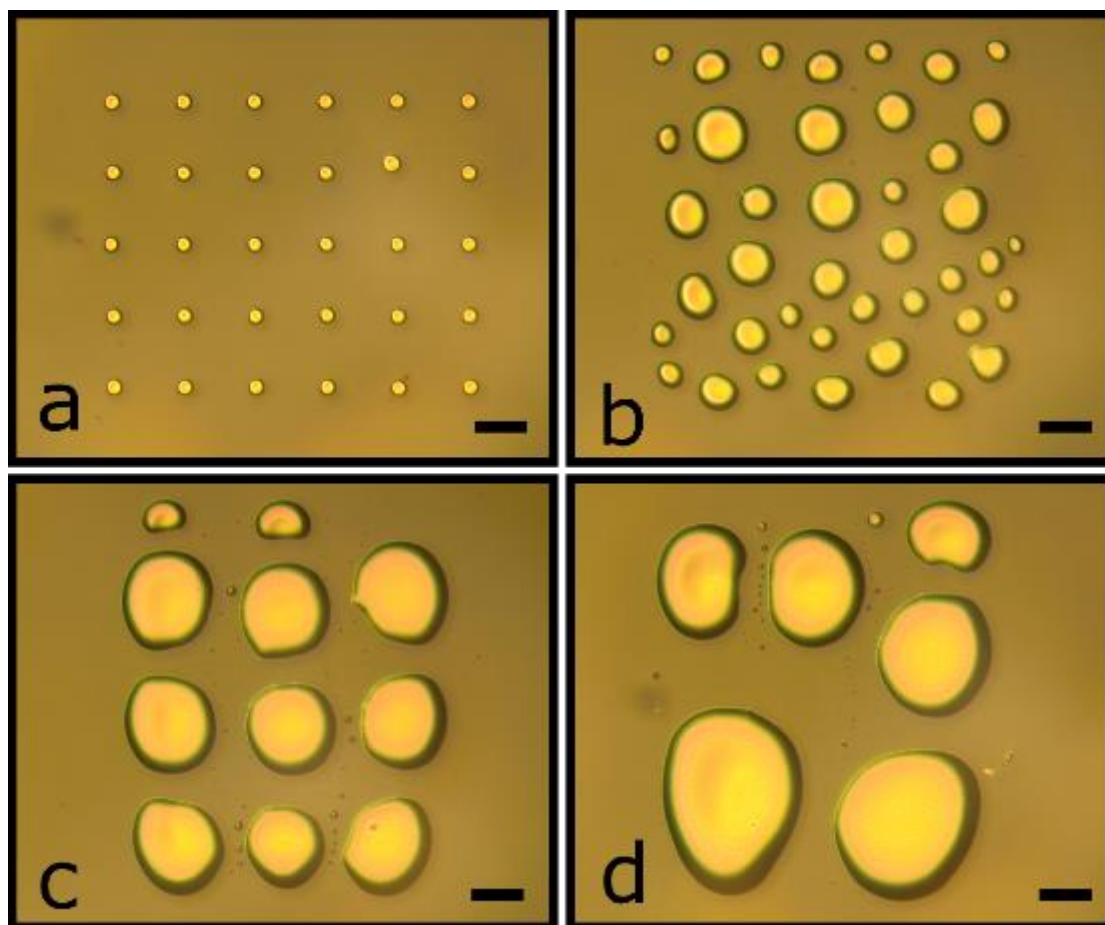


Figure 2-11: Square shaped patterns printed on polymeric surface (Su8 2000.5 MicroChem) without UV ozone treatment. Jetting frequency equals 1KHz and drop spacing equals: a) 100 μm leading to isolated droplets, b) 20 μm , c) 10 μm , d) 5 μm .

Scale bars equal 50 μm .

Matrix of isolated droplet is obtained in Figure a) because drop spacing (I.e., the distance between the centers of two adjacent droplets) is higher than droplet diameter. Fig2-11b, 2-11c and 2-11d shows non-continuous patterns even if drop spacing is lower than droplets diameter. With the droplet space decreasing, the size of the droplets' aggregation is increasing. There are some small droplets' aggregation encircle the big droplets' aggregation.

Such phenomena are due to fluid instability on hydrophobic surfaces when triple contact line is not firmly pinned. As previously highlighted, such a treatment will promote polymeric residue that could have an impact on pattern accuracy. Note that, numerous works report on printed lines drying behaviors.

However, at our knowledge, no works have focused on the printed lines formations when a residue is accumulated at the triple line (outer ring). Fig 2-12 shows the printed lines formation as function of surface wetting behavior and drop spacing (distance between the centers of two adjacent droplets).

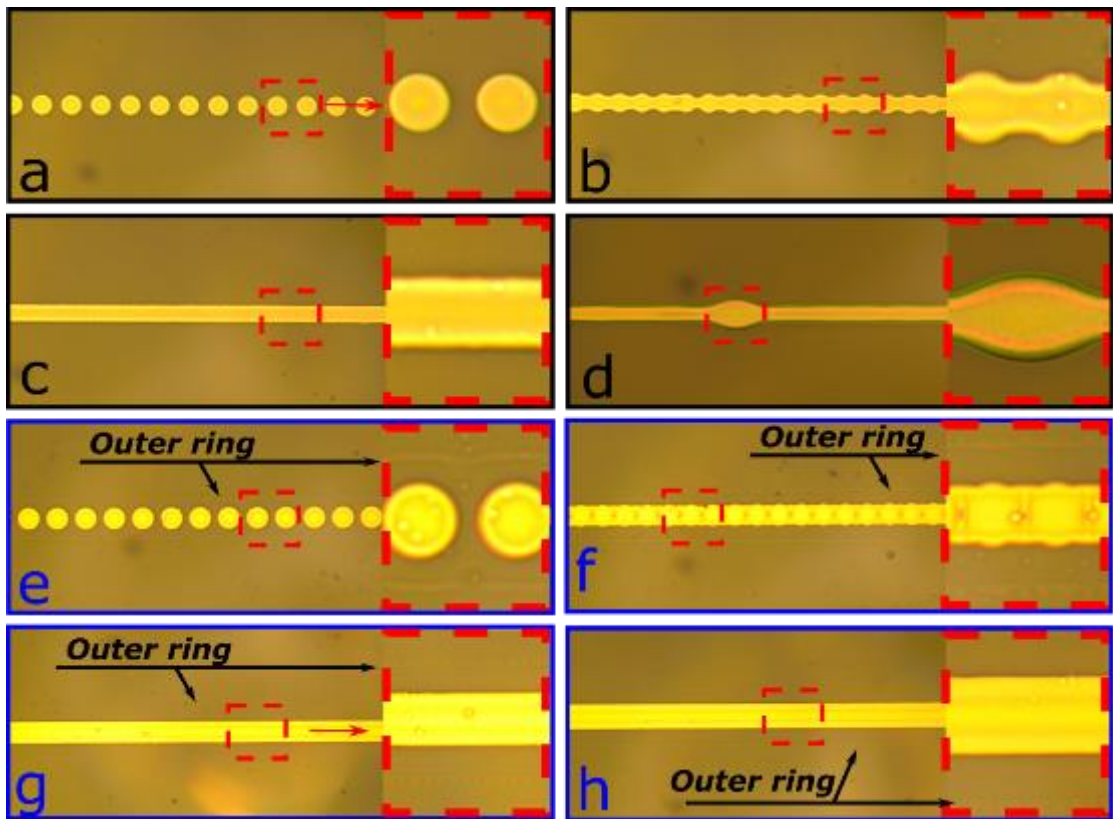


Figure 2-12: Lines formation mechanism as function of drop spacing and UV ozone exposure time. Jetting frequency equals 1 kHz. Hatched marks show zoom on lines. UV ozone time equals 2 minutes and drop spacing equals: a) 80 μ m leading to isolated droplets, b) 60 μ m leading to scalloped line, c) 40 μ m leading to well defined lines, d) 25 μ m leading to bulged line; UV ozone times equals 10 minutes and drop

spacing equals: e) 200 μ m leading to isolated droplets, f) 130 μ m leading to scalloped lines, g) 70 μ m leading to well defined line, h) 60 μ m leading to well defined line.

Figures (2-12a, b, c, and d) show line formation behavior at low UV ozone exposure time (2 minutes). As expected, when the gap between droplets centers (drop spacing) is: higher than the droplets diameters, closed to droplets diameters, well-adjusted or too closed, it leads to isolated droplets, scalloped lines, well-defined lines or bulged lines, respectively. The origin of this phenomenon has ever been reported in literature and will not be detailed here. For UV exposure time equals 10 minutes (Figures 2-12e, f, g, h), the same phenomenon occurs for isolated droplets (Figure 2-12e) and scalloped lines (Figure 2-12f). Well-defined lines can also be printed (Figure 2-12g). However, even if drop spacing is drastically reduced (Figure 2-12h), line does not show bulges. It seems that due to surface hydrophilicity (i.e., low water contact angle), inks spreads and consequently even if drop spacing is reduced, not enough materials are added to obtain bulges instabilities [15,16]. Meanwhile, from the Figure 2-12g and Figure 2-12h, we can find the dark line in the center of the line pattern. With the droplets spacing decreasing, the dark line is more obviously. When the droplets forming the line, the internal flow influences the pattern formation. Due to the droplet's density increasing, the internal flow influences the morphology (Figure 2-13a). Moreover, zoom in red hatched inset shows that outer ring is formed around the line independently of drop spacing value. This phenomenon can be explained as follows: a line is formed when at least two droplets coalesce. Indeed, a droplet falls down and begins to dry. Another one lands and merges with the first one. At high UV exposure time, the separation phase occurs when droplets dry.

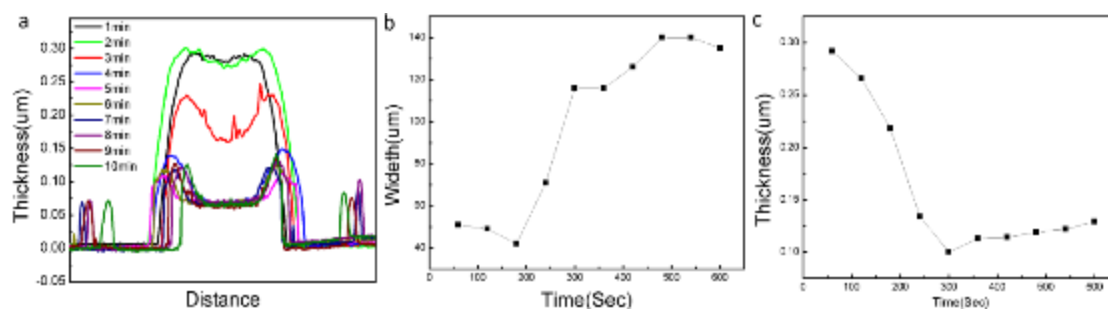


Figure 2-13 (a) the morphology of the one drop line on the Su8 surface. (b) the diameters of the drop line with different UV-ozone time. (c) the thickness of the drop line with different UV-ozone.

With the UV-ozone time increasing, the thickness of the one drop line is decreasing. And after 4min UV-ozone treatment, the performance tends to be stable. The average thickness is approximately 100nm. The width range is from 120μm to 140μm with the droplet spacing close to 40μm. The maximum thickness is from 120μm to 150μm as shown in Fig 2-13b and Fig 2-13c. But, as illustrated in the Fig 2-13a, when the UV-ozone time is more than 7min, there are protuberances at the boundary of the one drop line. By this way, we can find the outer ring of the line pattern in Fig 2-13a.

Consequently, PVP residue that remains at the triple contact when the first droplet is printed can be dissolved when the second one is printed. The same mechanism occurs until the last droplet of the line is printed. The case shown in Figure 2-12f, well describes the phenomena. Indeed, when inter-droplet distance is higher than inner ring diameter but lower than outer ring diameter only the morphology of the outer ring is impacted during drying.

In order to mimic this phenomena, two droplets have been successively drop-casted using micropipette. Top view optical images acquired during droplet spreading and drying confirms the previously mentioned explanations (see in Fig 2-14). Droplet in the bottom left has been deposited at first. Images a to c show that the two droplets spread with same mechanism than for isolated droplet. In image d, the two-contact line

collapse and form the same outer ring than this one observed when droplet is printed. Images e to h show the drying step of polymer rich region. For the polymer rich region, the outer rings connect and dissolve with each other. With the time increasing, the outer rings of the two droplets mixed together, and the big outer ring of the two droplets formed even if there is no connection of the colloid rich region. Based on this phenomena and Figure 2-12, the outer ring of the hole line patterns can be explained.

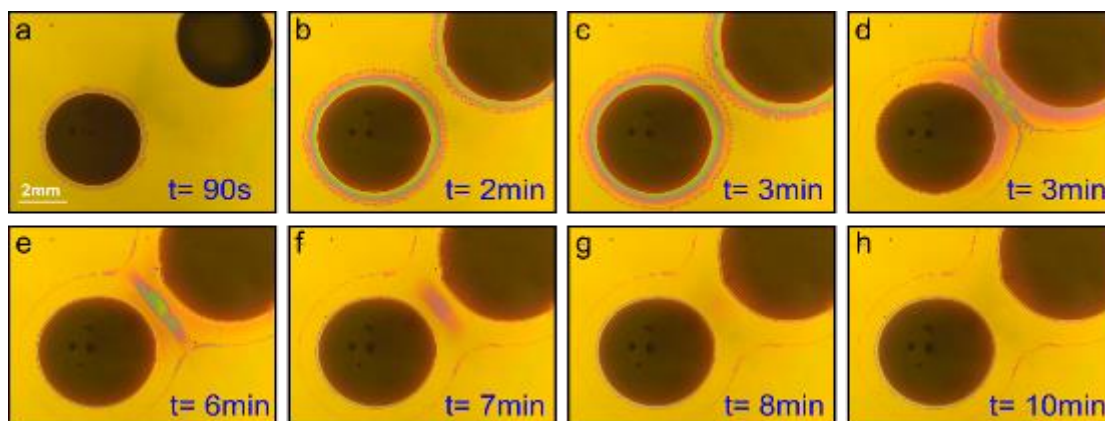


Figure 2-14 Optical images of two droplets successively drop casted on Su8 surface exposed to 6 minutes UV ozone as function of time.

In conclusion, the same drying mechanism observed in the first section at droplet scale, also occurs when line dries. However, it does not drastically impact lines formation but PVP residue remains at periphery of the inner lines. In the next section, deeper investigations will be performed on square shaped patterns to highlight the impact of PVP residue on more complex patterns' formation.

- *Square shaped behaviors*
- ✓ Systematic

Optical pictures in Fig 2-15 show the impact of drop spacing, jetting frequency and UV ozone exposure time on printing accuracy of the printed square patterns. The squares are fabricated as follows: droplets are successively printed along x axis (from left to right) and coalesce to form a line. This printing scenario is repeated when the

printhead has shifted along y axis, toward the top of the pictures. Consequently, lines coalesce and form the squares (for more details, see the 3D scheme in Fig 2-16). Importantly, in this set of experiments each square are printed from the bottom left to the top right. The accuracy criterion is that patterns shape have to be a square (1mm×1mm) fully filled with silver.

This systematic study shows experimental parameters impact on printing accuracy. The jetting frequency, the drop spacing, the UV ozone exposure time have been varied. As shown in Fig 2-15, whatever UV ozone exposure time is, three behaviors can be clearly distinguished: i) isolated droplets, ii) partially collapsed droplets and iii) merged droplets. Note that the drop spacing values have been carefully adjusted to highlight such well-known behaviors.

When UV ozone exposure time increases the patterns, accuracy decreases independently of the jetting frequency or the drop spacing. Nevertheless, whatever UV ozone exposure time was, the patterns could be fully filled with ink (i.e., no fluidic instability). However, patterns are not well-defined even in the wide tested range of drop spacing and jetting frequency. This unexpected behavior needs to be clarified. In order to explain this behavior, deeper investigations on these two parameters influences have been performed.

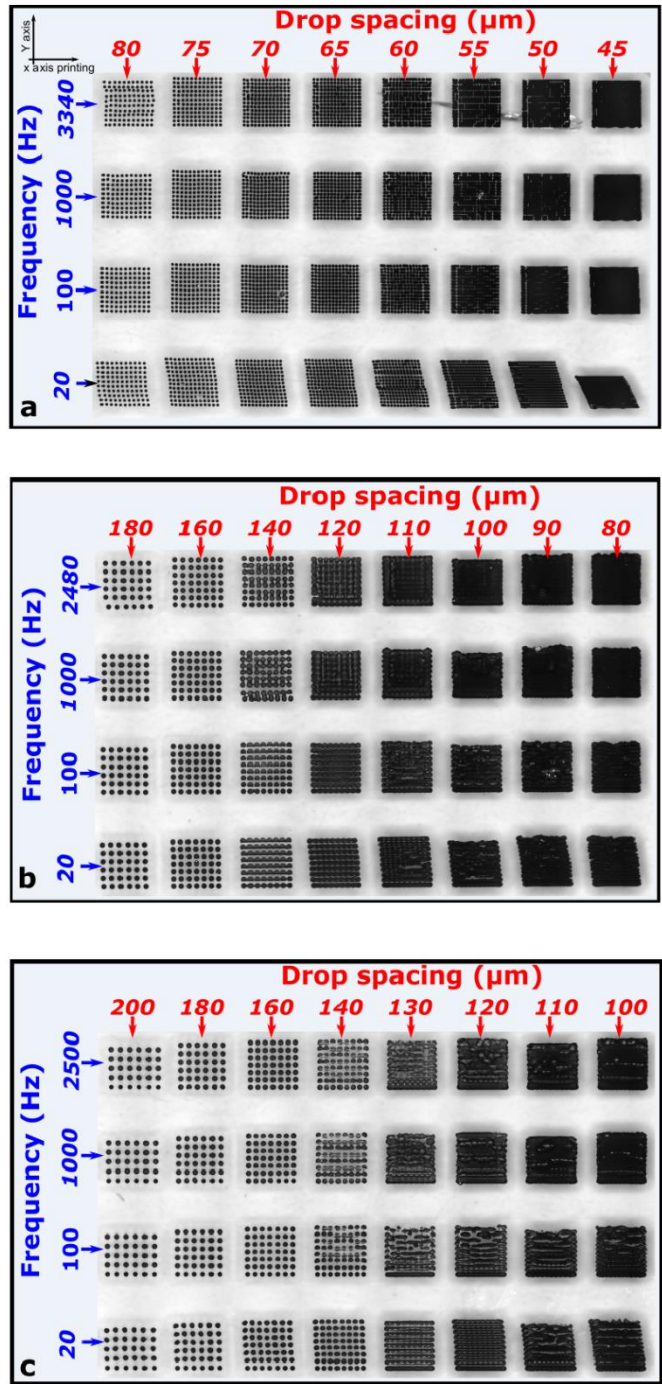


Figure 2-15 Square shaped patterns (approximately 1*1mm) varying drop spacing, jetting frequency and UV ozone exposure time; a) UV ozone exposure time equal 2 minutes; drop spacing varies from 80 to 45 μm and jetting frequency varies from 3340 to 20Hz; b) UV ozone exposure time equals 6 minutes; drop spacing varies from 180 to 80 μm and jetting frequency varies from 2480 to 20Hz; c) UV ozone exposure time

equal 10 minutes; drop spacing varies from 200 to 100 μm and jetting frequency varies from 2500 to 20Hz.

Based on the 2mins UV-Ozone treatment, the square with the same size emerges the rich variation with the frequency and overlap distance respectively as shown in the Fig 2-15a. With not obvious outer ring, the merging distance is based on the diameters of the inner ring. Along with the overlap distance approaching to the 60 μm which is the diameter of the inner ring, the merging phenomenon began apparent. Especially, with the overlap distance less than 65 μm , the drops connected each other and took shape. In addition, compared with overlap distance determining the foundation of the merging, the printing frequency of the pattern determine the level of the merging. With the decreasing of the frequency from 3300Hz to 20Hz, the time of the drop drying was increasing and the time between two drops landing up was increasing. In accompany with the first drop drying, the second drop landed up on the substrate and connected to the first drop. Because of the first drop drying, the influence of the drop's interaction was weaker than the two wet drops.

Compared with the 2min UV-ozone treatment, 6min UV-ozone treatment substrate emerges better hydrophilic. With an obvious outer ring, the interaction of the two drops was based on the approaching distance of the overlap distance and outer ring. As illustrated in Fig 2-15b, with the overlap distance approaching to the 140 μm larger than the inner ring diameters 120 μm , the drops began to merge. And the second line from the bottom of the square was obviously influenced by the outer ring of the first line. Inner ring wasn't the only factor determined the foundation merging. Furthermore, with the working frequency decreasing from 2500Hz to 20Hz, the interaction of the two drops was different with the 2min UV-Ozone treatment. As shown in the column in the Fig 2-15b, the pattern of the low frequency was more uniform than the high frequency, for the interaction of the two drops was between outer ring of the first drop and the

second drop. When the frequency was 2500Hz, the second drop landed up on the substrate was influenced by the wet outer ring of the first drop. Based on the non-uniform interaction between the outer ring and the second drop, the pattern was non-uniform as shown in the overlap distance 140 μ m and 2500Hz. Compared with high frequency, the interaction of the dry outer ring and wet second drop was uniform. Because of the dried outer ring forming a boundary which was in the range of the second drop landed up areas, the hydrophobicity of the area influence the second drop flow up to the inner ring of the first drop. And the overlap distance 140 μ m permits the second drop flowing to the inner ring rather than shrinking in the process of the drying with a larger overlap distance. Besides, because of the boundary shaping up with low frequency, the second line of the printing was more uniform than the high frequency one.

Similarly, the merging phenomenon of the 10min UV-Ozone treatment patterns in Fig 2-15c were influenced by the diameters of the outer ring and the frequency. However, based on a larger outer ring diameter, the drop was dry in the process of flowing from latter line to the previous line as shown in the overlap distance 130 μ m and 20Hz working frequency.

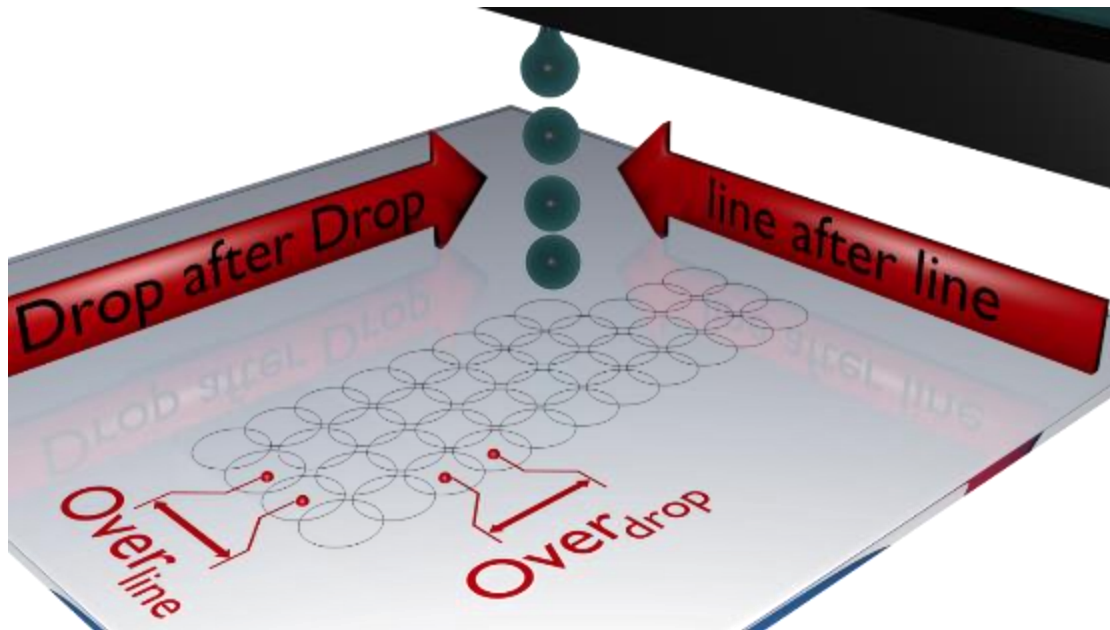


Figure 2-16: 3D scheme showing working principle of DoD inkjet printing for square shaped patterns.

$Over_{drop}$ is relative to droplets spacing that coalesce to form a line. $Over_{line}$ is relative to line spacing parameters in order to form square shaped patterns. Note that “Drop after Drop” and “line after line” are relative to X axis displacement and Y axis displacement, respectively.

✓ Drop spacing study

The first row (Fig 2-17a, b and c) shows independent droplets (i.e., drop spacing is higher than droplet diameter). The second row (Fig 2-17d, 2-17e and 2-17c) shows partially merged droplets (i.e., drop spacing value is closed to droplet diameter). The third row (Fig 2-17g, 2-17h and 2-17i) shows merged droplets (i.e., drop spacing value is lower than droplet diameter). Each column corresponds to a different UV ozone exposure time (2, 6 or 10 minutes from left to right).

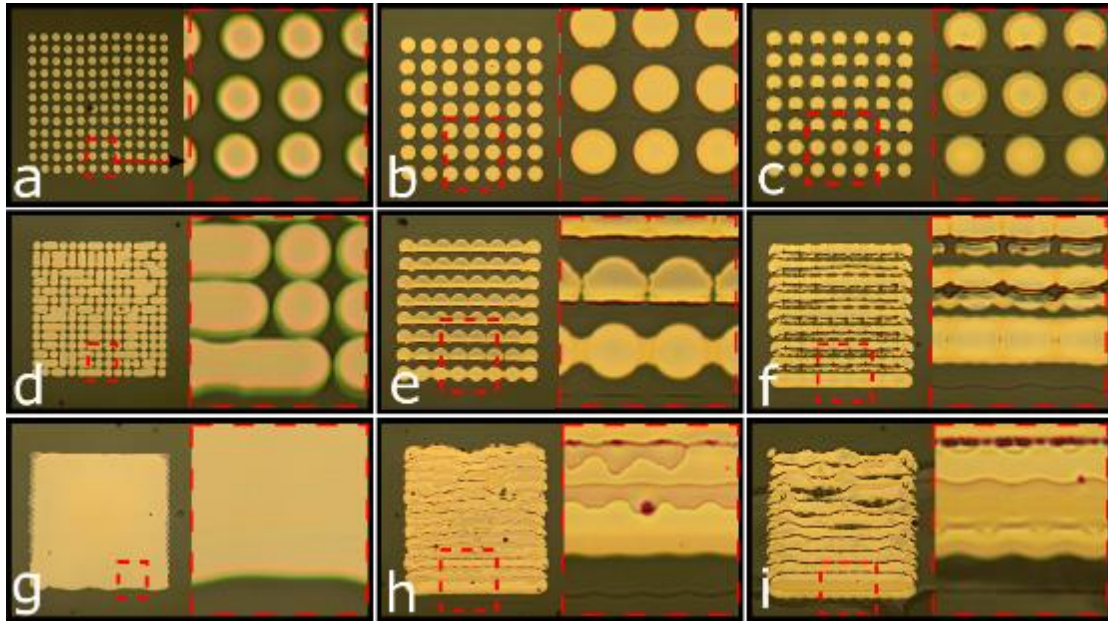


Figure 2-17 optical pictures of square shaped patterns (approximately 1×1 mm) printed at fixed jetting frequency equals 100Hz and varying: i) UV ozone exposure time equals: 2, 6 and 10 minutes shown in column 1, 2 and 3, respectively; ii) drop spacing in order to print: isolated droplets matrix, partially merged droplets, continues patterns shown in row 1, 2 and 3, respectively. Drop spacing experimental values equals: a) $75\mu\text{m}$; b) $160\mu\text{m}$; c) $160\mu\text{m}$; d) $60\mu\text{m}$; e) $140\mu\text{m}$; f) $130\mu\text{m}$; g) $45\mu\text{m}$; h) $80\mu\text{m}$; i) $100\mu\text{m}$.

As previously mentioned, film formation at low UV exposure time (first column) shows different behavior compared to the others columns due to PVP residue (“outer ring”) remaining when surface is highly hydrophilic. However, the first line residue impacts the second printed line. Such a phenomenon is in good agreement with the Figure 2-14 where the phenomena has been observed in real time under microscope. It is exacerbated when the drop spacing value decreases for the following reasons. At high drop spacing (first row), in each case, the three first printed lines show different spreading and drying behavior. In Figure 2-17a, isolated droplets are observed because outer ring does not occur.

In Figure 2-17b and 2-17c, PVP residue is observed but outer ring of each droplet that form a line has collapsed but has no impact on inner ring of each droplet. In this case, PVP residue does not influence droplet shapes for the droplet space big enough. However, squares are not totally filled with ink. Besides, for the outer ring formation, the whole outer ring of the line even with the isolated droplets can be observed. It's the same phenomenon as shown in Figure 2-14.

When the drop spacing is equal or slightly inferior to the droplet diameters (second row), the outer ring of the previously printed droplets has not enough time to dry and to pin before its neighbor droplet has landed (Figure 2-17e). This behavior occurs for all the droplet that form a line. However, when printing the second line, the PVP residue of the first line is firmly pinned and consequently, induces deformation of the second line due to its 2-dimensional profile (see Figures 2-17e and 2-17f). In this case, PVP residue does not influence the first printed lines but the others ones are impacted. Consequently, square is not well-defined. Note that, the printing parameters that have been fixed in Figure 2-17e are optimum to highlight such hypothesis. In the first line, droplets show circular shape partially collapsed, whereas, in the second line, droplets also collapse but show semicircular shape. Note that the flat droplets vertex of the second line faces the first printed line that clearly show the negative impact of PVP residue.

When drop spacing is inferior to droplet diameters (third row), the aforementioned phenomena occur. Indeed, as inner ring of each droplet overlap square is more filled. However, as shown in Fig 2-17h and 2-17i, PVP residue remains leading to square deformation. Such assertion is in good agreement with the optical picture of Fig 2-17g. Indeed, when no PVP residue occurs patterns are well-defined.

As highlighted in this section, the PVP residue influence on patterns formation occurs when such residue has enough time to be pinned. Consequently, the influence of the increase of printing velocity will be discussed in the next section.

✓ Jetting frequency study

Experiments have been performed to highlight the impact of jetting frequency on square patterns formation. Fig 2-18a and b show optical pictures of squares using the following experimental parameters. For both Figures, drop spacing and UV exposure time are fixed and equals 180 μ m and 10 minutes, respectively. Jetting frequencies varied and equal 20Hz and 3340Hz as shown in Fig 2-18a and 2-18b, respectively.

At low jetting frequency (Fig 2-18a), outer ring is formed around each line as usual. Interestingly, when printing frequency increases, as shown in Figure 2-18b, outer ring is observed around the square but cannot be observed around each printed lines. In this case, outer ring formed around each line has not enough time to be pinned. Consequently, the shape of each droplet inner ring is not impacted. Finally, PVP residue remains at the periphery of the square. Obviously, in this drop spacing conditions, square is not fully filled with ink. When the drop spacing is reduced (see Fig 2-18c), the same phenomena occurs. Patterns accuracy are better when printing at high velocity (Fig 2-18d) compare with those printed at lower frequency (Fig 2-17i for instance). However, in these conditions' holes remain. Such a phenomenon could be due to a largest amount of PVP induced when printing at lower drop spacing. A way to solve this problem could be to increase printing velocity, however it was not possible with the printer used in this study.

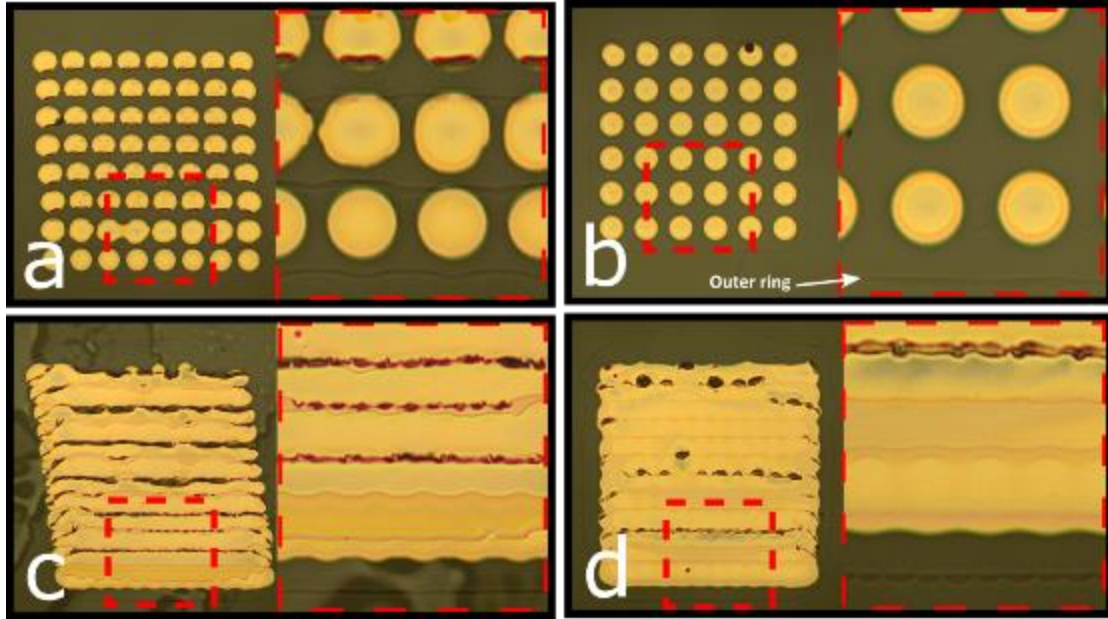


Figure 2-18 optical pictures of square shaped patterns (approximately 1×1 mm) printed at fixed UV ozone exposure time equals 10 minutes and varying: i) Jetting frequency equals: 20Hz and 3340Hz, shown in column 1 and 2, respectively; Note that, these values corresponds to the lowest and highest available printing velocities. ii) drop spacing in order to print: isolated droplets matrix and, continues patterns shown in row 1 and 2, respectively. Drop spacing experimental values equals: a) $180\mu\text{m}$; b) $180\mu\text{m}$; c) $100\mu\text{m}$; d) $100\mu\text{m}$.

Conclusion

On the basis of previously reported works dealing with multicomponent mixture, microliters scale drop can show phase separation when a multicomponent mixture is used. [22, 24] This work highlights that this phenomenon can occur when PVP is used as stabilizer in colloidal based ink. It has been demonstrated that printed picolitres droplets and drop casted microliters drops show the same morphology after drying. Indeed, an inner colloidal rich region and an outer polymer rich region can be distinguished independently of deposition techniques. Moreover, the optical observation of the spreading and drying behavior confirm that a phase separation occurs.

The new results observed in this work gave an alternative explanation of the phenomena already observed for another ink containing another kind of stabilizing agent. [25]

This complementary work gives more information for ink designer and experimenter involved in the field of printed electronics. Indeed, in the second part of this work, it has been demonstrated that PVP residue has a negative impact onto printed pattern accuracy, especially when the substrate became highly hydrophilic. Moreover, this work has highlighted one of the experimental conditions (i.e., substrates wetting behavior) that exacerbates the phase separation of a complex mixture made of colloids and polymer ligand. This study could pave to other dealing with a systematical study of other experimental conditions such as: ligand kind of material, surface materials and or roughness. It should help to fully understand the phase separation that occurs during inkjet printing of colloids droplets.

References:

[1] Yarin A L. Drop impact dynamics: splashing, spreading, receding, bouncing...[J]. *Annu. Rev. Fluid Mech.*, 2006, 38: 159-192.

[2] Hon K K B, Li L, Hutchings I M. Direct writing technology—Advances and developments[J]. *CIRP Annals*, 2008, 57(2): 601-620.

[3] Modern approaches to wettability: theory and applications[M]. Springer Science & Business Media, 2013.

[4] De Gennes P G. Wetting: statics and dynamics[J]. *Reviews of modern physics*, 1985, 57(3): 827.

[5] Young T. III. An essay on the cohesion of fluids[J]. *Philosophical transactions of the royal society of London*, 1805, 95: 65-87.

[6] Deegan R D, Bakajin O, Dupont T F, et al. Capillary flow as the cause of ring stains from dried liquid drops[J]. *Nature*, 1997, 389(6653): 827.

[7] Lim, J. A., Lee, W. H., Lee, H. S., Lee, J. H., Park, Y. D., & Cho, K. (2008). Self - organization of ink - jet - printed triisopropylsilylethynyl pentacene via evaporation - induced flows in a drying droplet. *Advanced functional materials*, 18(2), 229-234.

[8] Yan H, Chen Z, Zheng Y, et al. A high-mobility electron-transporting polymer for printed transistors[J]. *Nature*, 2009, 457(7230): 679.

[9] Rogel R, Borgne B L, Mohammed - Brahim T, et al. Spontaneous Buckling of Multiaxially Flexible and Stretchable Interconnects Using PDMS/Fibrous Composite Substrates[J]. *Advanced Materials Interfaces*, 2017, 4(3): 1600946.

[10] Nallan H C, Sadie J A, Kitsomboonloha R, et al. Systematic design of jettable nanoparticle-based inkjet inks: Rheology, acoustics, and jettability[J]. *Langmuir*, 2014, 30(44): 13470-13477.

[11] Robin M, Kuai W, Amela-Cortes M, et al. Epoxy based ink as versatile material for inkjet-printed devices[J]. *ACS applied materials & interfaces*, 2015, 7(39): 21975-21984.

[12] Calvert P. Inkjet printing for materials and devices[J]. *Chemistry of materials*, 2001, 13(10): 3299-3305.

[13] de Gans B J, Kazancioglu E, Meyer W, et al. Ink - jet printing polymers and polymer libraries using micropipettes[J]. *Macromolecular Rapid Communications*, 2004, 25(1): 292-296.

[14] Jang D, Kim D, Moon J. Influence of fluid physical properties on ink-jet printability[J]. *Langmuir*, 2009, 25(5): 2629-2635.

[15] Stringer J, Derby B. Formation and stability of lines produced by inkjet printing[J]. *Langmuir*, 2010, 26(12): 10365-10372.

[16] Soltman D, Subramanian V. Inkjet-printed line morphologies and temperature control of the coffee ring effect[J]. *Langmuir*, 2008, 24(5): 2224-2231.

[17] Hu H, Larson R G. Marangoni effect reverses coffee-ring depositions[J]. *The Journal of Physical Chemistry B*, 2006, 110(14): 7090-7094.

[18] Duineveld P C. The stability of ink-jet printed lines of liquid with zero receding contact angle on a homogeneous substrate[J]. *Journal of Fluid Mechanics*, 2003, 477: 175-200.

[19] Park J, Moon J. Control of colloidal particle deposit patterns within picoliter droplets ejected by ink-jet printing[J]. *Langmuir*, 2006, 22(8): 3506-3513.

[20] Kamyshny A, Steinke J, Magdassi S. Metal-based inkjet inks for printed electronics[J]. *The Open Applied Physics Journal*, 2011, 4(1).

[21] Haw M D, Gillie M, Poon W C K. Effects of phase behavior on the drying of colloidal suspensions[J]. *Langmuir*, 2002, 18(5): 1626-1633.

[22] Tarasevich Y Y, Pravoslavnova D M. Segregation in desiccated sessile drops of biological fluids[J]. *The European Physical Journal E*, 2007, 22(4): 311-314.

[23] Parisse F, Allain C. Shape changes of colloidal suspension droplets during drying[J]. *Journal de Physique II*, 1996, 6(7): 1111-1119.

[24] Doggart J, Wu Y, Liu P, et al. Facile inkjet-printing self-aligned electrodes for organic thin-film transistor arrays with small and uniform channel length[J]. *ACS Applied Materials & Interfaces*, 2010, 2(8): 2189-2192.

[25] Allen M, Leppäniemi J, Vilkman M, et al. Substrate-facilitated nanoparticle sintering and component interconnection procedure[J]. *Nanotechnology*, 2010, 21(47): 475204.

[26] Andersson H, Manuilskiy A, Lidenmark C, et al. The influence of paper coating content on room temperature sintering of silver nanoparticle ink[J]. *Nanotechnology*, 2013, 24(45): 455203.

[27] Lee H H, Chou K S, Huang K C. Inkjet printing of nanosized silver colloids[J]. *Nanotechnology*, 2005, 16(10): 2436.

3 Printed N-type C60 Organic Semiconductor Thin-film Transistor

Generally, the thin-film transistor characteristic will be influenced by the quality of the semiconducting active layer and by the interface quality between the semiconductor and insulator layer. Besides, the interface between semiconductor layer and electrodes is another important influence factor. Based on the previous printing technique result, the best parameters for printing silver electrodes can be achieved. For the next step, the high performance organic thin-film transistor should be investigated to lay the foundation of the photo-transistor.

3.1 Research states of the C60 Organic Thin-film Transistor

Based on the research result of the printing methods, the characteristics of semiconductor layer are the following object of study for the photo-transistor. Based on the previous PhD. Liu Xiang's work, we succeed in fabricating the photo-transistor in the silicon transistor. However, with the low performance and complicated fabrication process, a new thin-film transistor by means of low cost and easier fabricating process is on required. With the research of the organic semiconductor, organic thin-film transistor was investigated.

Due to the broad application in flexible, low-cost, and light electronic applications such as flat-panel displays [1,2], radio-frequency identification tags [3,4], complementary integrated circuits [5-7] and biological and medical applications [8-13], transparent organic semiconductor thin films with high charge mobility and electrical stability has been an important target. Based on the organic thin films, organic field effect transistors (OFFTs) have been widely used for their facile process-ability in large areas. Until now, more efforts have been made to improve the charge mobility. The performance has developed rapidly in the past two decades. So far, a large number of experiments have focused on the research of P-type devices, but few reported focused on the N-type devices. The most likely cause is that the material is unstable and very

sensitive to oxygen and moisture. Then, in order to realize the practical application of the device in complementary logic circuits and the like, both the type and the type of transistor need to have excellent performance. Therefore, there is still a need for further research-type devices in organic electronics.

As reported, the charge mobility of p-channel OFETs has reached up to $23.2 \text{ cm}^2\text{V}^{-1}\text{s}^{-1}$ [14-18]. Meanwhile, vapor-deposited OFETs exhibit mobility as high as $6 \text{ cm}^2\text{V}^{-1}\text{s}^{-1}$ [19,20] and solution-processed transistors have lower mobility of $\sim 1 \text{ cm}^2\text{V}^{-1}\text{s}^{-1}$ [21,22]. Besides, n-type organic semiconductor thin-film transistor is the most important research field for the design of the logic circuit. Among n-type organic semiconductors, fullerene shows great potential with common mobility close to $1 \text{ cm}^2\text{V}^{-1}\text{s}^{-1}$ [23]. Fullerene FETs present not only interesting charge mobility but also a high electrical stability. Since Haddon et.al first reported field effect transistors in 1995 on journal Applied Physics Letters [24], especially in the past decade, there have been many reports on field effect transistors. Among them, the highest performance is the preparation method using 250°C hot wall epitaxy reported by Anthopoulos et al. [25], which makes the device mobility reach $6 \text{ cm}^2\text{V}^{-1}\text{s}^{-1}$. With the modifying by the pentacene, Itaka et.al reported the fabrication process with the temperature 50°C and high vacuum, the carrier mobility increases to $4.9 \text{ cm}^2\text{V}^{-1}\text{s}^{-1}$. [26]

By changing gate insulator, Zhang et al. [27] succeeded in fabricating C60-OFET with high performance but also with high electrical stability under continuous polarization. Although these reported field effect transistor devices exhibit higher mobility, they all employ special fabrication conditions. Therefore, the most common method of thermal evaporation can be used to provide a technical reference and reference for exploring simple, low-cost preparation processes and preparing high-performance types.

With the combination of the PbS quantum dots, the organic material should be

carefully selected. Because of the bandgap of the PbS quantum dots is approximately 0.91eV, the conduction band is 4.5eV and the valence band is 5.41eV. [28] In order to fix the PbS quantum dots, the C60 was utilized as the semiconductor. Indeed, the energy levels of C60 changes depending of the conducting material it is in contact [29]. However, the mean value of LUMO level can be taken around 5eV when C60 is in contact with conducting material. Same value was taken by Biebersdorf et.al. [30] Therefore, photoexcited electrons in the PbS quantum dots are likely to transfer to C60 semiconductors. On the other hand, the holes are supposed to stay in the PbS quantum dots because the valence band in C60 is around 7.3eV. In addition, the fabrication process of C60 layer is easier than silicon and suitable with the printing methods which we are experienced in the fabrication. By this consideration, the C60 is the most suitable material for the thin-film transistor.

Based on the PhD. Malo Robin's work, our group succeeded in modifying the contact characteristic between the metal electrodes and C60 layer. Improving the C60 semiconductor layer performance is another method to improve the OTFT performance. Especially, for matching the printing technology, the improvement of the C60 layer own characteristic is more useful. Fabrication processes based on printing have a number of advantages over conventional photolithography. Printable processes can dramatically reduce material waste and manufacturing process steps while lowering manufacturing costs. Moreover, they can be readily scaled to large-area production with high throughput [31]. Hence, for commercialization or complex circuit integration, printed OFET should have high performances, high electrical parameters uniformity and should be stable under long-term electrical stress. The operational stability is even more relevant when transistors are used as current source to drive QLED for instance. Indeed, the change in drain current under continuous operating voltage will dictate the device stability and reliability.

For improving the semiconductor layer performance, some research results were investigated and surveyed. Based on the *Jean-Luc Bredas's* report, the carrier mobility of organic film is strongly influenced by the crystallinity, molecular packing structures of the organic semiconductor. Meanwhile, with the study by *Sokolov et.al*, the influence of the charge traps at the gate dielectric/semiconductor interface for modifying the electric stability was investigated. [32,33]

Because of the changes in threshold voltage, contact resistances and in gate dielectric capacitances, the degradation of the OFET performances during bias stress is illustrated by the drain current decay from *D.K. Hwang & T. Richards's* achievements [34,35].

From report of *H.L.Cheng & W.Y.Chou et.al*, the degradation was explained with several mechanisms, for instance, defect creation and charge trapping/tunneling in the organic semiconductor which is supplemented by *Clemens Simgrunner's* group [36,37], in the insulator layer and at the interface dielectric-organic semiconductor [38]. Numerous methods have been utilized to improve the electrical stability such as substitutable organic semiconductor and gate insulator [14,34].

However, few investigations were reported about the modification of the annealing process of the OFET to improve the stability of the devices. With the bottom gate/top contact architecture is used, continuous polarization was found to increase contact resistances which revealed contact degradation from *Rizwan Ahmed's paper*. [39]

In this configuration, changes in threshold voltage and in contact resistance observed during the bias stress were metal dependent. The contact degradation was assumed to be related to charges trapping and space charge built up near the contact interface, preventing more charge to be injected. Up to now, studies about the modification of the thermal annealing process impact on electrical stability in printed bottom gate/bottom contact configuration have never been reported.

Based on the printing methods, the influence factor of the interface between the insulator layer and semiconductor layer should be investigated for improving the printed C60 organic thin-film transistor performance.

In this chapter, the effect of the thermal annealing of this active layer on the process reproducibility and on the electrical stability of the bottom gate/bottom contact geometry C60 transistors is studied. The study included the effects of the organic semiconductor layer thickness and the thermal annealing process. An optimum of thermal annealing process linked to the organic semiconductor layer thickness is found. This optimum led to reproducible process and uniform parameters of OTFTs distributed on the surface of the sample.

3.2 Experimental Section

3.2.1 Transistor fabrication

- *Structure*

Fig.3-1 shows a schematic cross-section of the C₆₀ OFET fabricated following bottom gate and bottom contacts geometry. This figure highlights the problematic of the high aspect ratio between the drain and source contacts and the gate insulator. The thickness of the active layer has to be enough to insure good coverage between the source and drain contacts.

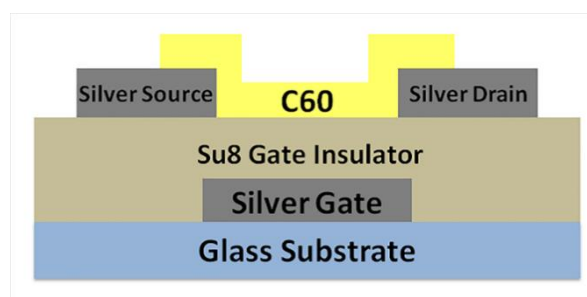


Fig. 3-1: Cross-section of the C₆₀ OFETs using bottom gate and bottom contacts

geometry. The figure highlights the problematic of the high aspect ratio between the drain and source contacts and the gate insulator

- *Materials*

Besides the fullerene (C60) utilized as the semiconductor layer, the materials of the electrodes and insulator are very important.

Due to the requirement of the inkjet printer, the 0.7mm thickness glass was utilized as the substrate of the thin-film transistor. Besides, with the requirement of the printing electronics, the glass should be super smooth. Silver based ink was purchase from ANP and used as received. Ink reference is: ANP 40LT15C which is composed of Silver nanoparticle <100 nm particle size and contains PVP as dispersant (Sigma Aldrich). TGME (C₈H₁₈O₄) is used as main solvent. The metal content, the surface tension, the viscosity and the density equal 30.18wt%, 36.8mN/m, 14.16cps, 1.45g/mL respectively.

The high-polymer Su8 photoresist is a negative, epoxy-based, near-ultraviolet photoresist based on bisphenol A epoxy resin proposed by BIM in 1995. It has excellent physical, mechanical, optical, mechanical, chemical and thermal stability properties. The most important feature of SU8 glue is its high transparency in the UV range. Due to this advantage of Su8, people can use traditional UV lithography equipment to achieve thick glue exposure, which becomes the preferred glue for making high aspect ratio structures. Su8 is a transparent solid epoxy resin with an average of 8 functional epoxy groups to maximize the sensitivity of the photoresist. The ideal chemical structure of Su8 resin is shown in Figure 3-2. Besides, Su8 is suitable for printing electronics with the UV-Ozone treatment as discussed in chapter 2.

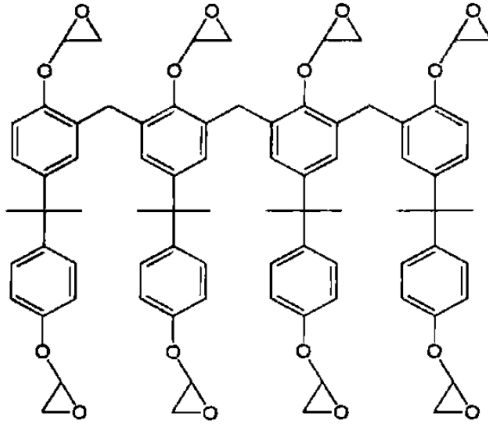


Figure 3-2 The ideal chemical structure of Su8

- *Fabrication Process*

As illustrated in Fig.3-3, after cleaning the glass substrate with acetone, ethanol, and deionized water for 10 mins sequentially, the silver gate electrode was printed on the substrate (kept at 50°C) with a thickness of 200nm using 256 nozzles Q-class printhead (Dimatix[®])(Fig 3-3b). Before spin coating the gate insulator layer, the substrate with silver gate electrodes is baked at 110°C for 30min allowing nanoparticles based ink sintering. Then, 1.2μm thick uncross-linked SU8 2000 series photoresist (Bisphenol A Novolak epoxy; MicroChem) is spin-coated at a speed of 4500r/min during 60 seconds (Fig 3-3c). This layer will be used as polymeric gate insulator. After UV exposure and development (SU8 micro Dev, MicroChem), the SU8 layer was baked at 115°C during 15min. The baked SU8 layer is then submitted to 2mins UV-Ozone treatment to adjust SU8 wetting behavior [10-12] ready for the printing of source and drain contacts. Drain and source electrodes were printed at 50°C using different patterns (width of the electrodes $W=4000\mu\text{m}$, distance between the electrodes $L=150\mu\text{m}$, and the thickness of the electrodes $D=205\text{nm}$ in Fig 3-3d). Finally, C_{60} film is thermally evaporated as the active layer of the transistor at room temperature under vacuum (2×10^{-7} mbar) with a constant deposition rate of 0.15A/s (Fig 2-3e).

The C₆₀ active layer was deposited with four different thicknesses, 60 nm, 90 nm, 125nm and 250 nm in the purpose to study the effect of its thickness. The OFET is then characterized electrically, as deposited and after annealing at 3 different temperatures, 160°C, 200°C and 250°C, during 5 mins. Electrical characterization was performed in dark and under nitrogen atmosphere using a 2636A Keithley (Fig 3-3f).

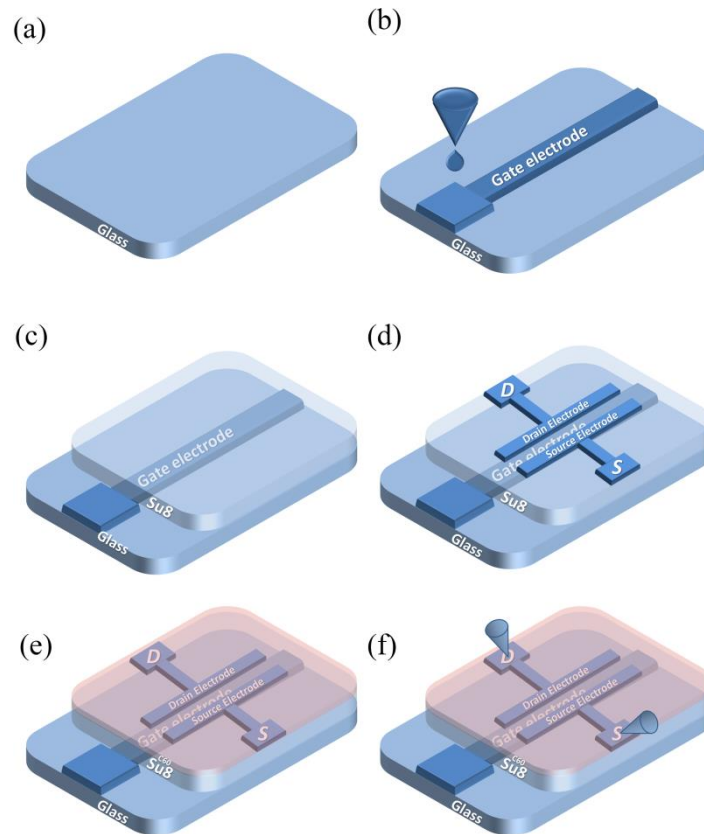


Fig. 3-3: Fabrication process of C₆₀ OFET

3.2.2 Transistor Characterization

- *The discussion of the annealing process*

Based on the suitable thickness of the printed electrodes, the 125nm C₆₀ was utilized for the research of the annealing process. Based on the typical thermal annealing process, the process can be divided into three steps: **A** step is the temperature increasing (increasing from room temperature to 200 °C); **B** step is the temperature duration (with 200 °C for 10mins); **C** step is the temperature decreasing (decreasing

from 200°C to room temperature). With the suitable thickness of the organic semiconductor layer, the transistors were divided into four groups. The first group transistors were under the whole process of the thermal annealing. Then, the second group transistors were under the **A** step and **B** step. The third group was only with the **C** step. Finally, the fourth group was under the **B** and **C** step. With the analyzing of the transfer and output characteristics, the performances and uniformity of the devices were systematically performed. In addition, hysteresis measurements and continuous polarization were done to investigate the electrical stability. With the time increasing and bias stress, transfer and output characteristics were performed to evaluate the defect changes during continuous polarization.

As illustrated in Fig 3-4, the transfer characteristics of four annealing process groups. All the OFETs have the same size (channel width and length equals to 4000 and 150 μm , respectively). From Fig 3-4a, the on-state current is approximately 1~10 μA and from off-state current is less than 1nA. Then, as illustrated in Fig 3-4b, the transfer characteristics are much better than the first annealing process. Even with higher leakage current, the on-state currents are more uniform and higher than the first annealing process. By this comparison, it seems that the step C doesn't obviously influence the performance of the OFETs. Besides, the uniformity of the first annealing process is not as good as the second annealing process.

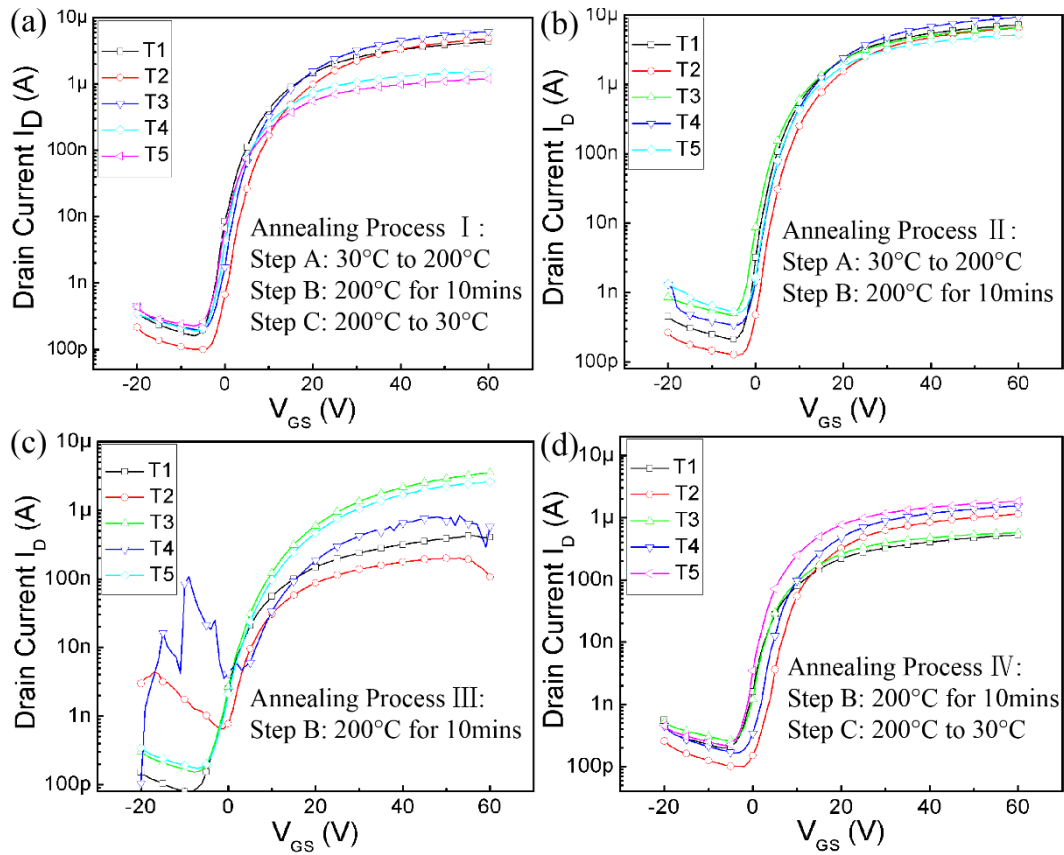


Figure 3-4 transfer characteristics of the four annealing processes OFETs

In Fig 3-4c, with the third annealing process, the leakage currents of the OFETs are much higher than the other annealing process. In addition, from the leakage current, it seems that the third annealing process easily destroy the insulator layer. And the on-state current's uniform is very bad. It doesn't show some uniformity. Finally, for the fourth annealing process, the transfer characteristics of the OFETs are much better than the third annealing process. Even the on-state currents are not as big as the first and second annealing process. But the uniformity of the OFETs is as good as the first and second annealing process. By this way, it seems that the OFETs benefit from the step C, they become more stable. It means that, short time and high temperature annealing will destroy insulator layer. But the slowly temperature increasing and decreasing process will stabilize the performance of the OFETs.

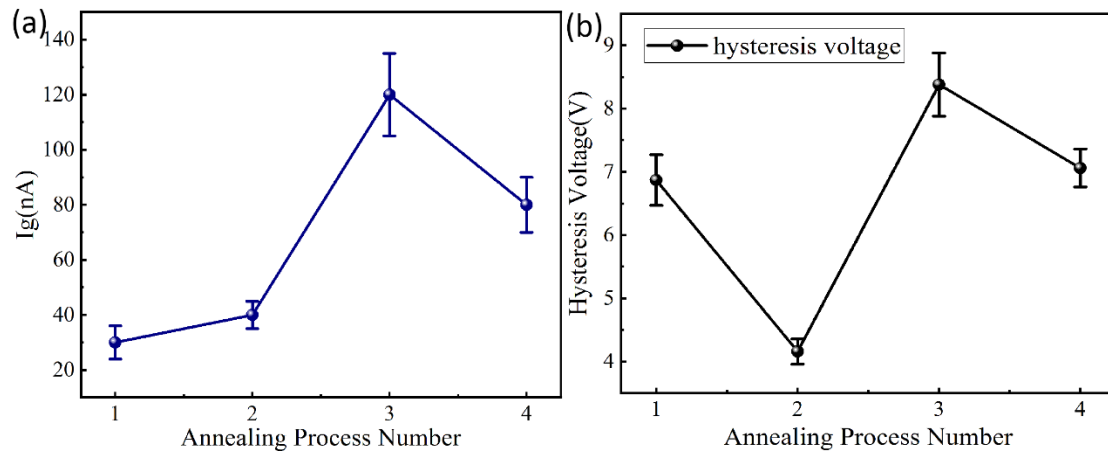


Figure 3-5 the Gate Current and the hysteresis voltage of the four annealing processes OFETs

With the purpose of investigating the performance of the OFETs annealing processes, the gate current and hysteresis of the OFETs are measured. In Fig 3-5a, we can find that the gate current of the third annealing process is much higher than the others. And the performance is not as uniform as the others. Meanwhile, there is no big difference of the first and the second annealing process. From this figure, the first and the second annealing process are much better than the others. And the insulator layer seems that it's not influenced by the annealing process.

As illustrated in Fig 3-5b, from the hysteresis characteristic of the OFETs with different annealing process, the best performance device is the second annealing process. Normally, the hysteresis characteristic connects with the defect density of the semiconductor layer and the interface of the insulator and semiconductor layer. Based on this point, the defect density of the second annealing process is lower than the others. Besides, we can find that the fourth annealing process is much similar in influencing the hysteresis characteristic with the first annealing process. That means the step C modifying the interface of the insulator layer and semiconductor layer and decreasing the defect density which related to the stability of the OFETs.

For OFETs performance, another important parameter is the stability of the OFETs. As illustrated in Fig 3-6, the drain-current of OFETs using 125 nm thick C_{60} active layer and annealed at different processes, was plotted as a function of the time when constant gate voltage V_{GS} and drain voltage V_{DS} are applied. Under $V_{GS}=20V$ and $V_{DS}=20V$, the drain current decreases with the time (Fig. 3-6a). The constant polarization under $V_{GS}=40V$ and $V_{DS}=20V$ is shown in Fig 3-6b.

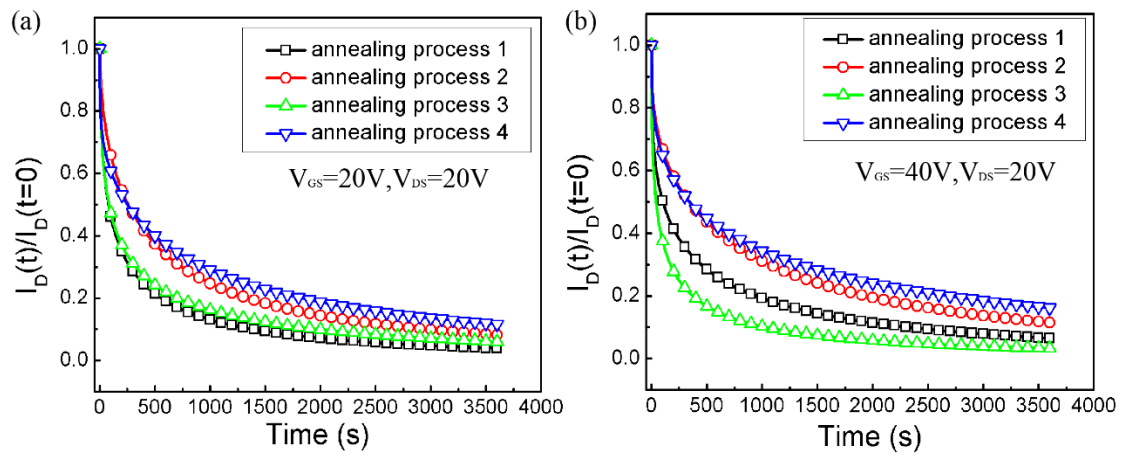


Figure 3-6 Drain-current of OFETs using 90 nm thick C_{60} active layer un-annealed and annealed at different processes under (a) 20V gate-source voltage and 20V drain-source voltage, (b) 40V gate-source voltage and 20V drain-source voltage

With 20V gate voltage and 20V drain voltage, the fourth annealing process is the best one. The first annealing process and third annealing process are similar and their performance decreases quickly. With increasing the gate voltage to 40V, we can find that the third annealing process OFET is not stable. And the fourth annealing process and second annealing process devices' stability are better than others. By this comparison, we can find that the short time and high temperature annealing will generate negative influence of the OFETs. Meanwhile, the moderate temperature decreasing step will improve the stability performance. Based on this analyzation, the second annealing process with the temperature increasing step and temperature duration step is the best choice of the annealing process.

In order to analyzing the performance of the annealing process, for the next step, we use different annealing temperature.

- *The discussion of annealing temperature*

Based on the previous discussion, we find that the influence factor of the annealing process. With the best annealing process (increasing from room temperature to 200°C and then sustain 200 °C for 10mins), there is another parameter which is temperature in view. We choose 4 temperature degrees for experiment that is room temperature (as-fabricated OFET), 160 °C, 200 °C and 250 °C with the thickness of 125nm. First, we analyze the morphology of the device with AFM measurement to compare the performance of the C60 surface.

✓ Morphology

In the purpose to study the effect of the temperature of the final annealing of the OFET, the morphology of the C60 active layer was characterized through Atomic Force Microscopy (AFM) analysis.

An Atomic Force Microscope (AFM VEECO Di Caliber) was utilized in tapping mode on an area of 1x1 μm².

Describing the topography by the Power Spectral Density Function (PSDF), we use its formulation given in [40]:

$$S(f_x, f_y) = \frac{1}{L^2} \left| \sum_{m=1}^N \sum_{n=1}^N h_{nm} e^{2\pi i \Delta L (f_x n + f_y m)} (\Delta L)^2 \right|^2 \quad (1)$$

to calculate the grain size.

Here S is the 2-dimensional PSDF, L² is the scanned surface area, N is the number of data points in both X and Y direction of scanned area, h_{nm} is the surface profile height at position (m,n), f_x and f_y are the spatial frequencies in X and Y directions respectively, ΔL is the sampling interval.

Based on the Senthilkumar et.al. report [41]:

$$\text{PSD}_{\text{total}} = \frac{K}{f^{\nu+1}} + \frac{A}{(1+B^2f^2)^{(C+1)/2}} + \sum_m \pi \sigma_{\text{sh},m}^2 \tau_{\text{sh},m}^2 \exp[-\pi^2 \tau_{\text{sh},m}^2 (f - f_{\text{sh},m})^2] \quad (2)$$

Here, the first part of the equation:

$$\frac{K}{f^{\nu+1}}$$

is with the order to describe the surface roughness over large range of spatial frequencies, f is the spatial frequencies, K is the spectral strength and ν is the spectral indices. Then, for the second part:

$$\frac{A}{(1 + B^2 f^2)^{(C+1)/2}}$$

with the purpose of analyzing the random rough surfaces over large length scales, the correlation length is determined by B ; at small f values, PSD is determined by A , and at high f values, the PSD function is determined by C . However, the equivalent RMS roughness σ and correlation length τ that are depend on these three parameters.

$$\sigma^2 = \frac{2\pi A}{B^2(C-1)}, \quad \tau^2 = \frac{(C-1)^2 B^2}{2\pi^2 C} \quad (3)$$

For the third part:

$$\sum_m \pi \sigma_{\text{sh},m}^2 \tau_{\text{sh},m}^2 \exp[-\pi^2 \tau_{\text{sh},m}^2 (f - f_{\text{sh},m})^2]$$

it corresponds to the periodicity of the superstructures in the surface. The period is translated into the spatial frequency domain as the shift of the PSD maximum to the frequency $f_{\text{sh},m}$. Here, $\tau_{\text{sh},m}$ corresponds to the size and $\sigma_{\text{sh},m}$ to the height of the superstructures of the 1D file of the AFM. (as shown in Figure 2-7)

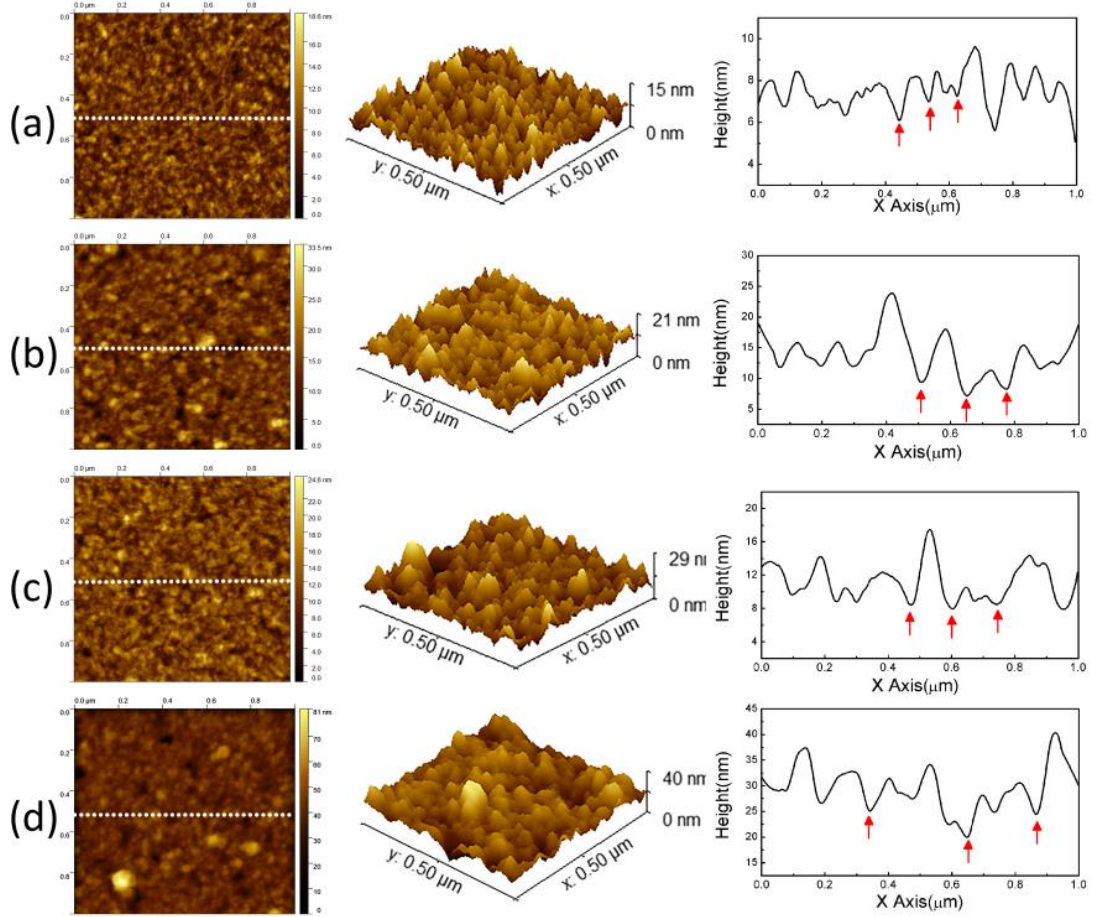


Figure 3-7 2D($1 \times 1 \mu\text{m}^2$) AFM images, corresponding 3D enlarged ($0.5 \times 0.5 \mu\text{m}^2$) and corresponding 1D profile along the dash line of C_{60} thin film with different annealing temperature: (a) room temperature; (b) 160°C ; (c) 200°C ; (d) 250°C

Corresponding 1D profiles on Fig 3-7, the morphological “superstructure” was highlighted different from C_{60} grain and could reveal organization at larger scale. Indeed, the distance between two deeper adjacent gaps marked by red arrow could indicate C_{60} “superstructure” size (τ_s). The average distance between domains for room temperature, 160°C , 200°C , 250°C are respectively 0.09, 0.12, 0.16, $0.22 \mu\text{m}$.

Based on the PSDF data from the 2D AFM images, the equation 2 can be simplified to:

$$\text{PSD}_{\text{total}} = \frac{A}{(1+B^2f^2)^{(C+1)/2}} + \pi\sigma_{\text{sh},m}^2\tau_{\text{sh},m}^2\exp[-\pi^2\tau_{\text{sh},m}^2(f-f_{\text{sh},m})^2] \quad (4)$$

By fitting the PSDF data from the 2D AFM image with the equation 4, the equivalent roughness (σ) and lateral correlation length (τ) can be derived with the equation 3.

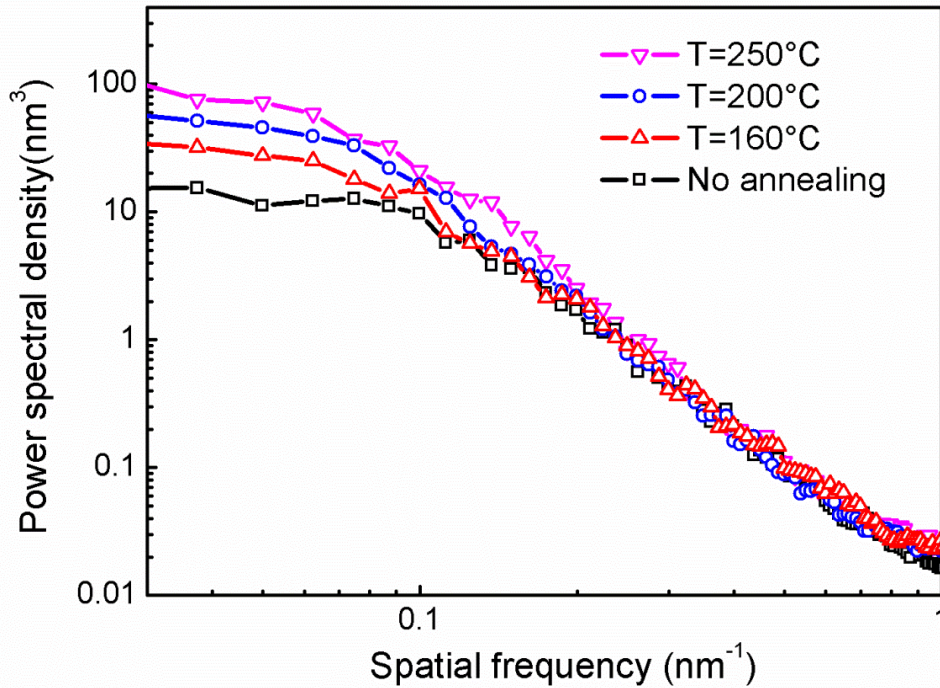


Figure 3-8: Power spectral density versus the spatial frequency extracted from 2D AFM images of C_{60} thin film with no annealing, annealing at 160°C , 200°C , and 250°C .

Based on the AFM images ($1 \times 1 \mu\text{m}^2$), the RMS roughness (σ) and the lateral correlation length (τ) were calculated from these PSDF functions with log-log plot. Besides, the lateral correlation length (τ) is related to the grain size.

With the thickness 125nm , C_{60} thin-films were annealed at 160°C , 200°C and 250°C . In order to study the relationship between C_{60} layer morphology and electrical behavior of the devices, the AFM images were investigated. As illustrated in Fig.3-7, the 2D, 3D and line scan AFM images of C_{60} thin film with room temperature (as-fabricated) and after annealing at 160°C , 200°C and 250°C exhibit that C_{60} morphology

depends on the annealing temperature. Based on the annealing process, large grain size C_{60} molecules crystals were integrated by the interaction of the small grain size C_{60} molecules crystals. First, surface parameters extracted from the PSDF analysis on 2D AFM images show that with the annealing temperature 160°C , the small enhancement of the grain size and RMS roughness were calculated by the formulation(1). The roughness and the grain size are $\sigma = 1.42\text{nm}$, $\tau = 4.72\text{nm}$ for the no annealing devices (a); and $\sigma = 1.75\text{nm}$, $\tau = 7.70\text{nm}$ for 160°C (b). Meanwhile, 200°C (c) and 250°C (d) have different roughness (respectively $\sigma = 1.91\text{nm}$ and $\sigma = 2.72\text{nm}$) and a large improvement of the grain size (respectively $\tau = 13.46\text{nm}$ and $\tau = 14.16\text{nm}$). Corresponding 1D profiles on Fig 3-4, the morphological “superstructure” was highlighted different from C_{60} grain and could reveal organization at larger scale. Indeed, the distance between two deeper adjacent gaps marked by red arrow could indicate C_{60} “superstructure” size (τ_s). The average distance between domains for room temperature, 160°C , 200°C , 250°C are respectively 0.09 , 0.12 , 0.16 , $0.22\mu\text{m}$.

To study only the effect of the final annealing temperature of the OFET, on the morphology of its C_{60} active layer, the thickness of this layer was fixed at 125nm . The morphology was studied as deposited and after annealing at 160°C , 200°C , 250°C .

As illustrated in Fig.3-7, the 2D, 3D and line scan AFM images of C_{60} thin film as deposited and after annealing at 160°C , 200°C , 250°C exhibit that C_{60} morphology depends on the annealing temperature. Obviously from the 2D AFM images, the surface roughness increases and the number of grains decreases in the same area when the annealing temperature increases.

Quantitatively, the RMS roughness σ and grain size τ were calculated using the formulation and reported in Table 3-1.

Annealing Temperature (°C)	Roughness σ (nm)	Grain Size τ (nm)
As-Deposited	1.42	4.72
160	1.75	7.70
200	1.91	13.46
250	2.72	14.16

Table 3-1: RMS roughness and grain size calculated using PSDF formulation

Continuous increase of the morphology parameters is observed after annealing at increasing temperatures. The grain size seems increase more importantly between 160°C and 200°C and nearly saturate between 200°C and 250°C.

Meanwhile, with the PSDF data in Fig 3-5, the trend of the change in grain size and roughness is observed and implies that with the annealing temperature increasing, the grain size of the C₆₀ layer was increasing. Compared with the grain size of the 200°C and the 250°C, the grain sizes are similar.

✓ *Electrical Characteristics*

Fig.3-9 shows the mean transfer and output characteristics of 4 OFETs as-fabricated and after an annealing at 3 different temperatures, 160°C, 200°C and 250°C. All the OFETS have the same size (channel width and length equals to 4000 μm and 150 μm , respectively).

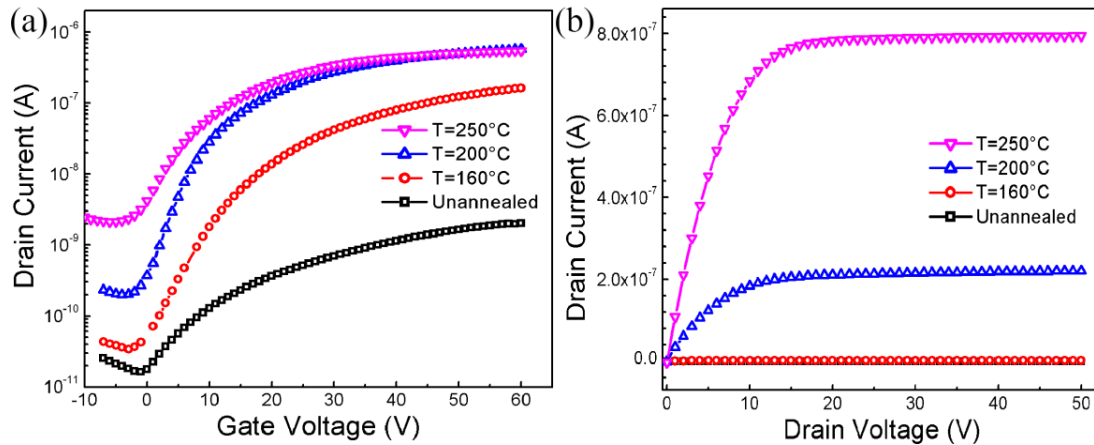


Fig.3-9: (a) Mean transfer characteristics ($V_D=20V$) and (b) output characteristics ($V_G=20V$) of several OFETs having the same channel size (channel width $W=4000 \mu m$, channel length $L=150 \mu m$) and 125 nm thick C_{60} active layer, measured as-fabricated and after annealing at 160°C, 200°C and 250°C.

All the OFET's parameters such as threshold voltage, subthreshold slope, field effect mobility, on-current, improve when the annealing temperature increases. The value of these parameters is reported in Table 3.2 and plotted as a function of the annealing temperature in Fig. 3-10a.

Table 3-2 highlights that the main electrical parameters (i.e., threshold voltage, subthreshold slope, mobility) are strongly impacted by annealing temperature (especially below 200°C). It seems that these electrical parameters are governed by the grain size.

With the annealing temperature increasing, the decreasing threshold voltage refer to the changes in interfacial properties between the insulating layer and the organic semiconductor layer, the generation of dipoles in the interface, the impureness of the semiconductor layer, the interface state and the charge trap density. Normally, in my opinion, for this trend, it's because of the interface state and the charge trap density. Based on this analyze, the trap density decreasing with the annealing temperature

increasing.

Besides, with the annealing temperature increasing, the leakage current is increasing from 1.6×10^{-11} to 2×10^{-9} . And the on/off ratio increases from 125 to 4.7×10^3 , then the ratio decreasing to 270. In general, the leakage current is the lower the better and the on/off ratio is the higher the better for the circuit design. By this comprehensive comparison, we find that the 200°C exhibits the best adaption for circuit design.

T_A (°C)	V_{TH} (V)	SS (V/dec)	μ ($cm^2/V.s$)	R_c (Ω)	μ after R_c ($cm^2/V.s$)	I_{off} (A)	I_{on}/I_{off}
Unannealed	19.3	9.3	5.3×10^{-5}	8×10^6	5.8×10^{-5}	1.6×10^{-11}	125
160°C	20	7	4.2×10^{-3}	2×10^6	4.47×10^{-3}	3.4×10^{-11}	4.7×10^3
200°C	11.2	4	1.44×10^{-2}	1.7×10^6	1.46×10^{-2}	2×10^{-10}	2.85×10^3
250°C	6.2	6.2	1.46×10^{-2}	2×10^6	1.5×10^{-2}	2×10^{-9}	270

Table 3-2 Main mean electrical parameters of several OFETs having the same size (channel width $W=4000 \mu m$, channel length $L=150 \mu m$) and 125 nm thick C_{60} active layer, measured as-fabricated and after annealing at $T_A=160^\circ C$, $200^\circ C$ and $250^\circ C$. V_{TH} is the threshold voltage, SS the subthreshold slope, μ the field effect mobility, R_c the contact resistance, μ after R_c the mobility after correction by R_c , I_{off} is the minimum current and I_{on}/I_{off} is the ratio between the maximum current and the minimum current

The contact resistance decreases after the annealing at 160°C and then stabilizes. Its value stays much lower than the channel resistance and then the corrected mobility by removing the effect of the contact resistance, does not change drastically. This

conclusion was expected due to the starting linear increase of the drain current as can be observed in the output characteristics. Moreover, the off-current increases when the annealing temperature increases. The increase seems to be due to the improvement of the active layer after annealing and then to better conductive layer. Considering these preliminary observations, it seems that the optimum annealing temperature is 200°C. The different parameters after this annealing are similar to the 250°C annealing ones. Moreover, the on-current to off-current ratio is higher than its value after 250°C annealing.

To understand the behavior of the main parameters depending on the annealing temperature, we can try to highlight a relationship between the AFM and the electrical characterizations. The mobility and the grain size present similar behavior as shown in Fig. 3-10b. Both, mobility and grain size strongly increase when temperature increases until 200°C and a little bit when the grain size increases between 200°C and 250°C.

The subthreshold slope SS presents a specific behavior as it increases between 200°C and 250°C. Such behavior can be understood from the usual equation of SS (5) as a function of the defect's density in the channel N_{ep} and at the interface between the channel and the gate insulator N_{SS} [41]

$$SS = \frac{kT \ln(10)}{q} \left(1 + \sqrt{\frac{q^2 \epsilon_0 \epsilon_{sc} N_{ep}}{C_{ins}}} + \frac{q^2 N_{SS}}{C_{ins}} \right) \quad (5)$$

C_{ins} is the capacitance per area unit of the gate insulator and ϵ_{sc} is the relative dielectric constant of the semiconducting active layer.

On the one hand, if the C_{60} active layer is considered as a polycrystalline material, N_{ep} is the defect density concentrated mainly in the grain boundaries. The defect density at the interface N_{SS} depends at least partially on the roughness of the interface between the channel and the active layer. Note that, the grain size was previously determined by

AFM measurements. Meanwhile, Fig.2-10c compares the behavior of SS, the roughness and the grain size determined from AFM measurements. SS decreases whereas the grain size and the roughness increase before 200°C. It seems that this decrease of SS is governed mainly by the decrease of the defect density inside the channel due to the increase of the grain size. Between 200°C and 250°C, SS increases, the grain size increases only a little bit however the roughness increases strongly. In conclusion, as the grain size and then the defect density inside the channel saturates more or less, the increase of SS is mainly attributed to the increase of the roughness.

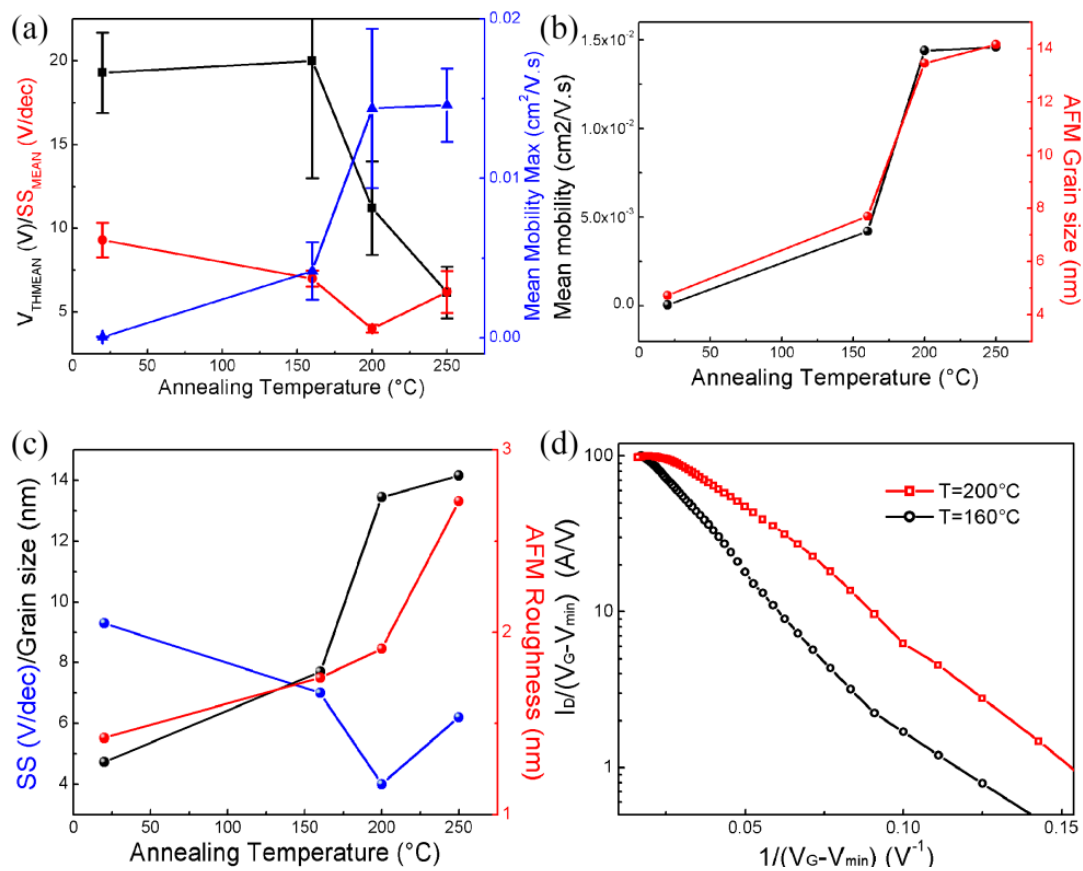


Figure 3-10: (a) Behavior of the mean threshold voltage V_{THMEAN} , subthreshold slope SS_{MEAN} and field effect mobility, when the annealing temperature increases; (b) Similar behavior of the mobility and the grain size as a function of the annealing temperature; (c) Behavior of the subthreshold slope SS, the surface roughness and the grain size as a function of the annealing temperature; (d) Semi-logarithmic plot of

$I_D/(V_G-V_{\min})$ versus $1/(V_G-V_{\min})$ for OFETs annealed at 160°C and 200°C

Coming back to the link between the mobility and the grain size, the conduction models in polycrystalline materials can be apply, particularly the conduction in thin-film transistors with polycrystalline active layer. If we assume that polycrystalline materials are composed by a chain of crystalline regions with superficial discrete traps at the grain boundaries, the drain current, I_D , and the gate voltage, V_G , of these transistors are found [42-43] to be related in the subthreshold regime to:

$$I_D = \frac{W}{L} \mu_0 C_{\text{ins}} (V_G - V_{\min}) V_D \exp\left(-\frac{q^3 N_T^2 t}{8 \epsilon_0 \epsilon_{\text{SC}} k T C_{\text{ins}} (V_G - V_{\min})}\right) \quad (6)$$

W and L are the width and the length of the channel. C_{ins} is the capacitance per area unit of the gate insulator. V_{\min} is the gate voltage at the minimum of I_D from which the channel starts to form and then I_D start to increase. V_D is the drain voltage. q is the electronic charge. t is the thickness of the channel. N_T , is the superficial concentration of defects in the grain boundaries. ϵ_s is the permittivity of the semiconducting active layer. kT is the thermal energy.

In this model [44], the mobility is thermally activated following the relationship:

$$\mu = \mu_0 \exp(-E_b/kT) \quad (7)$$

where E_b is the barrier energy at the grain boundary.

The relation (6) is valid when the electron concentration in the channel (in the case of N-type transistor) is larger than a critical concentration $N^* = N_T/G$ in which G is the size of the grains. Using this relation (6), the semi-logarithmic plot of $I_D/(V_G-V_{\min})$ versus $1/(V_G-V_{\min})$ may be fitted with a linear function. The slope of the function is proportional to N_T^2 .

As shown in Fig.3-10d, semi-logarithmic plot for OFETs annealed at 160°C and 200°C. Both plots have a linear range. The departure from the linearity occurs at larger

$1/(V_G - V_{\min})$ and the slope of the linear functions is lower for 200°C annealed OFET than for 160°C annealed OFET, meaning lower slope for largest grain size OFET. Larger $1/(V_G - V_{\min})$, corresponding then to larger $N^* = N_T/G$, means larger grains in 200°C annealed OFET.

The slope of the linear function can lead us to calculate N_T . Besides the physical constant q , ϵ_0 and k , the relative dielectric constants are taken 2.7 for SU8 gate insulator [45] and 5 for C₆₀ film [46]. The thickness of the gate insulator is 1.2 μm . The actual unknown is the thickness t of the channel. To jump this difficulty, we can take the channel extending into the full thickness of the active layer that is not realistic, but can give an order of the minimum defect density in the grain boundaries. An order of the maximum defect density can be obtained considering very thin channel, 3 nm for example.

Taking then $t=125$ nm, the calculated superficial defect density N_T at the grain boundaries is $3 \times 10^{11}/\text{cm}^2$ and $2.5 \times 10^{11}/\text{cm}^2$ for 160°C and 200°C annealed OFETs. N_T increases to $1.9 \times 10^{12}/\text{cm}^2$ and $1.6 \times 10^{12}/\text{cm}^2$ for 160°C and 200°C annealed OFETs if we consider a channel thickness of 3 nm (~2-unit cells of C₆₀ crystalline network).

The first observation is the low defect density in the grain boundaries of such organic material. For comparison, the same model gives an order of $10^{12}/\text{cm}^2$ for N_T in polycrystalline silicon transistors considering a channel thickness of 30 nm [47].

The second observation is the slight difference between the values of N_T in both OFETs, even if N_T is lower in 200°C annealed OFETs. The large difference between the mobility values in these OFETs is mainly due to the large increase of the grain size and not to a decrease of the defect density inside the grain boundaries, leading to much lower $N^* = N_T/G$ ratio in 200°C annealed OFET. In conclusion, the mobility is primarily governed by the grain size (or the number of grains in the channel) than by the defect density in the grain boundaries. Importantly, this direct quantitative link between the

physical structure of the active layer and the electrical parameters of organic transistor was never encountered in the literature in our knowledge.

In a summary of this section, the effect of the annealing temperature on printed C₆₀ OFET's properties has been studied. Optimum parameters are obtained for 200°C annealing temperature. Furthermore, compare to OFET annealed at 250°C, OFET annealed at 200°C show similar mobility, lower subthreshold slope and higher on-current to off-current ratio.

- *The research of the thickness influence*

Another experimental parameter that can influence the properties of the OFETs is the thickness of the C₆₀ active layer. Following the previous study, the effect of this thickness on the properties of the OFETs, annealed at 200°C after their fabrication, is presented hereafter.

Fig. 3-11 shows the mean transfer and output characteristics of 4 OFETs having a C₆₀ active layer with a thickness of 60nm, 90 nm, 125 nm or 250nm. All the OFETs have the same size, with a channel width W=4000 μm and a channel length L=150 μm. The best characteristics are obtained for an active layer of 90nm thick.

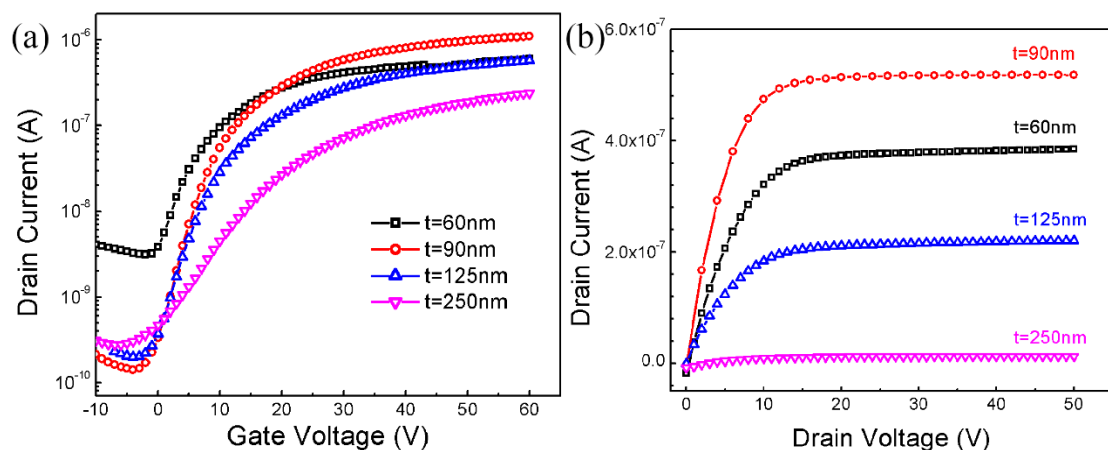


Figure 3-11: (a), (b): Mean transfer and output characteristics of several OFETs

having the same size (channel width $W=4000 \mu\text{m}$, channel length $L=150 \mu\text{m}$) and a C_{60} active layer with a thickness of 60nm, 90 nm, 125 nm or 250nm.

As illustrated in Fig 3-11a, with the thickness increasing, the on-state current of the 90nm C_{60} layer OFETs is the best one. Besides, the leakage current of the 90nm thickness layer C_{60} OFETs is the lowest one. These two parameters are very important for the OFETs. Then, for the on-state current of the 60nm OFET is similar with the 125nm OFET. And with the thickness increasing to 250nm, the on-state current of the device is decreasing. With the 60nm thickness, the C_{60} layer can't cover the thickness of the electrodes. But from 90nm to 250nm, the most important influence factor is the defect density. The thicker layer the more defect density lead to the worst transfer characteristic of the OFET.

Besides, comparing the subthreshold slope, 90nm OFET exhibits the best performance of the subthreshold slope. For the circuit, 90nm device can provide the faster transition from the off state to the on state and the smaller the change in gate voltage. And, the subthreshold voltage is related to the capacitance per unit area of the insulating layer and the performance of the interface between the organic semiconductor layer and the insulating layer. For these, with the thickness changing, the interface between the C_{60} layer and Su8 layer of the 90nm OFETs with the best annealing condition is modified to better performance.

With the defect influence, we also can find this in the output characteristic in Fig 3-11b. With the thickness increasing, the saturation currents of these OFETs emerge the influence of the defect density. For circuit design, output characteristic is one of the most important characteristics.

t_{C60} (nm)	V_{TH} (V)	SS (V/dec)	μ ($cm^2/V.s$)	R_c (Ω)	μ after R_c ($cm^2/V.s$)	I_{off} (A)	I_{on}/I_{off}
60	5,7	5,2	1.8×10^{-2}	2.7×10^6	1.9×10^{-2}	3×10^{-9}	180
90	10,8	3,6	2.9×10^{-2}	7.5×10^5	2.95×10^{-2}	1.4×10^{-10}	7.8×10^3
125	10,8	4	1.4×10^{-2}	1.2×10^7	1.7×10^{-2}	2×10^{-10}	2.85×10^3
250	11	9,2	6.1×10^{-3}	1×10^7	6.5×10^{-3}	2.7×10^{-10}	870

Table 3-3 Main mean electrical parameters of several OFETs having the same size (channel width $W=4000 \mu m$, channel length $L=150 \mu m$) and a C_{60} active layer with a thickness t_{C60} of 60nm, 90 nm, 125 nm or 250nm, all annealed at 200°C. V_{TH} is the threshold voltage, SS the subthreshold slope, μ the field effect mobility, R_c the contact resistance, μ after R_c the mobility after correction by R_c , I_{off} is the minimum current and I_{on}/I_{off} is the ratio between the maximum current and the minimum current.

The behavior of the electrical parameters as a function of the thickness is shown also in Fig. 3-12 and their values are presented in Table 3-3. It seems that the low performance of the 60 nm thick active layer OFETs is probably due to low coverage between the active layer and the 205 nm thick source and drain contacts. The performance of 90 nm thick and 125 nm thick active layer OFETs are more or less similar with higher mobility for 90 nm thick OFET. The bad subthreshold slope of 250 nm thick active layer OFET can be mainly due to the high roughness of the surface.

From the change in threshold voltage, we can find that the defect density increases with the thickness increases. Meanwhile, with the thickness increasing above the 90nm, the leakage currents of the 90nm, 125nm and 250nm exhibits no big difference. But for the on-off ratio, the 90nm device shows the best performance.

In practical applications, the larger the value of the current switching ratio, the better, especially in the active matrix display and logic circuits. To achieve better stability, immunity to interference, and greater load drive capability, higher current switching ratios are required. The highest on-state current depends on the intrinsic mobility of the organic semiconductor and the capacitance per unit area of the insulating layer. With the experiment result, we can find that for the circuit design, the 90nm OFETs exhibits higher compatibility.

The magnitude of the off-state current is determined by the gate leakage current, the conduction path of the interface of the insulating layer, and the body conductance of the organic semiconductor. Usually, the unintentional miscellaneous organic semiconductor, or oblique incidence during the evaporation of the source and drain electrodes, causes the value of the off-state current to become large. With the thickness increasing from 90nm to 250nm, the off-state current is decreasing. Besides, the contact resistance decreasing with the thickness increasing refers to the contact area increases. By this way, we can get a calculation that the influence of the defect density is more important than the others.

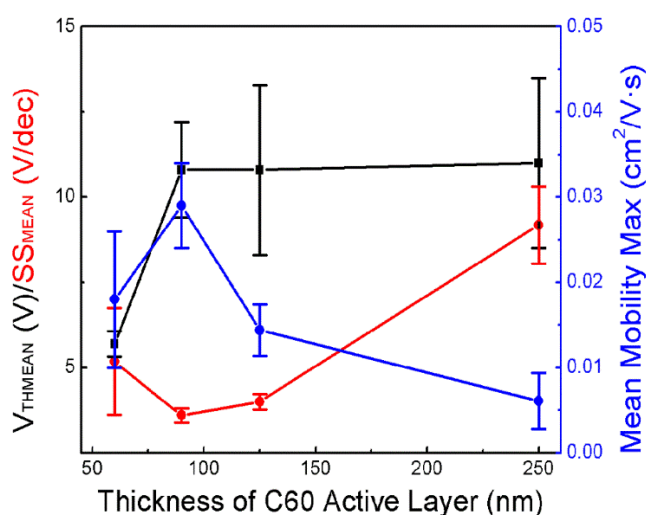


Figure 3-12 The behavior of their mean electrical parameters (Threshold voltage, subthreshold slope and mobility)

As comparison in Fig 3-12, we can find that as function of the thickness, the 90nm exhibits the highest mobility, the lowest subthreshold slope. Besides, with similar threshold voltage, 90nm should be chosen as the most suitable thickness for the OFETs. And for the carrier mobility, there are many factors affecting the mobility, such as the type and purity of semiconductors, the size of semiconductor grains, the difference in crystal quality, the difference in device configuration, the contact between electrodes and semiconductors, and the trench of devices, length to width ratio and so on. In my experiment, we can find that the carrier mobility relates to the purity of semiconductor. With the thickness increasing from 90nm to 250nm, the carrier mobility decreases due to the defect density increasing. Even for 60nm C₆₀ which can't cover the electrodes, the mobility is better than 125nm and 250nm. By this way, we can find a trend that the defect density increases with the thickness increases. And then, the defect density is a huge impact of the performance of the OFETs.

In conclusion, the best conditions to prepare the evaporated C₆₀ active layer of printed bottom-gate/bottom-contacts OFETs, are obtained with a thickness of 90 nm and a post-thermal annealing equal 200°C.

3.2.3 Dynamic behavior of the optimized printed C₆₀ based OFET

Based on the previous experiment results, we can find that the best post-thermal annealing process of C₆₀ OFETs is: (1) temperature increasing from room temperature to ideal degree and sustaining for 10mins; (2) considering the annealing temperature, 200°C OFETs exhibits the best performance than the other degrees; (3) with the compression of the thickness, 90nm C₆₀ OFETs emerges best transfer and output characteristics. By this way, 90nm C₆₀ OFETs with the 200°C through the selected annealing process, can be chosen as the best device for circuit. Generally, the output characteristic of the OFETs is very important for circuit design. But, in order to improve

the circuit stability, the constant polarization of the OFET should be considered. Above all, the output characteristic and constant polarization of the 90nm OFETs with different annealing temperature degrees should be investigated.

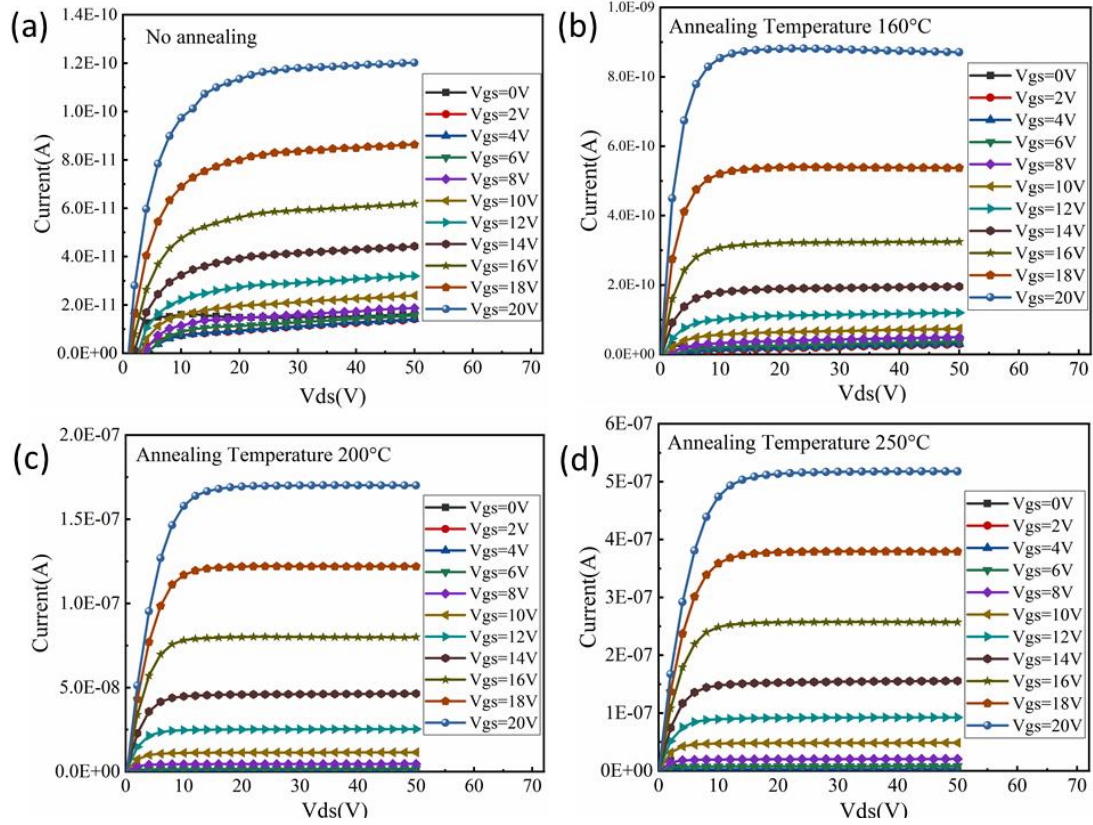


Figure 3-13 the output characteristic of the 90nm C60 OFETs with different annealing temperature.

As illustrated in Fig 3-13, with the as-deposited device, annealing temperature 160°C, 200°C and 250°C, the output characteristics of the 200°C and 250°C are better than others. By this way, annealing temperature 200°C and 250°C OFETs are the better choices for circuit design.

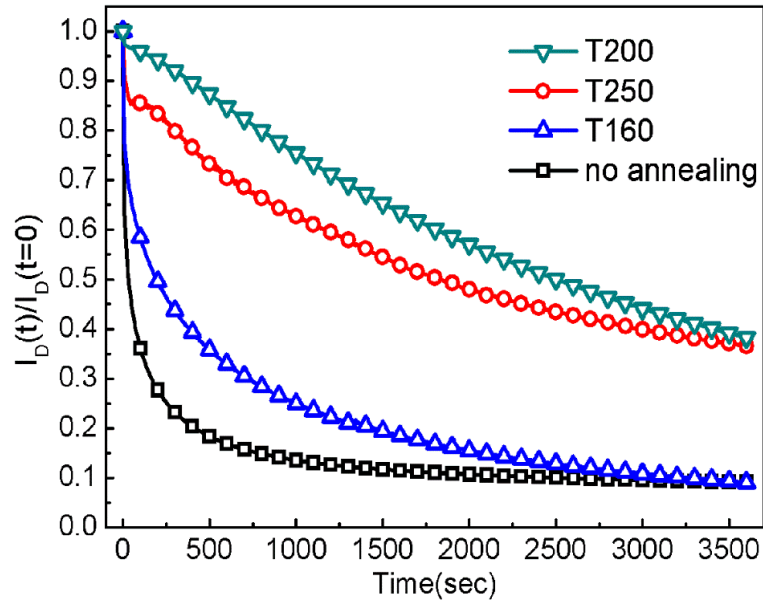


Figure 3-14 Drain-current of OFETs using 90 nm thick C₆₀ active layer un-annealed and annealed at different temperatures, 160°C, 200°C, 250°C as a function of the time under 40V gate-source voltage and 20V drain-source voltage

As shown in Fig 3-14, the drain-current of OFETs using 90 nm thick C₆₀ active layer and annealed at different temperatures, was plotted as a function of the time when constant gate voltage V_{GS} and drain voltage V_{DS} are applied. Under $V_{GS}=40V$ and $V_{DS}=20V$, the drain current decreases with the time (Fig. 3-14). In these conditions, the 200°C annealed OFETs have the slowest decrease leading to more reliable value of the current under constant biasing.

Defining then the best conditions to prepare the evaporated C₆₀ active layer of printed bottom-gate/bottom-contacts OFETs and knowing their static performances, is a prerequisite step to evaluate their optimum dynamic performance. The dynamic performance is studied through the behavior of resistive loaded OFET under square pulsed voltage applied to its gate.

Static output characteristic of the OFET as an inverter is presented in Fig 3-14a. The load resistance R is fixed to 500M Ω and the circuit is biased by $V_{DD}=20V$. With

the V_{IN} increasing from 0V to 20V, the V_{OUT} of the inverter decreases from the 20V to 2.2V. From this phenomenon, with the gate voltage increasing, the transistor works well. And the field effect of the transistor is obviously for the voltage increasing slowly with the input voltage increasing from 0V to 11V. Then, the voltage decreases fast with the voltage ranging from 11V to 16V. At the end of the voltage changing, the output voltage trends to be stable.

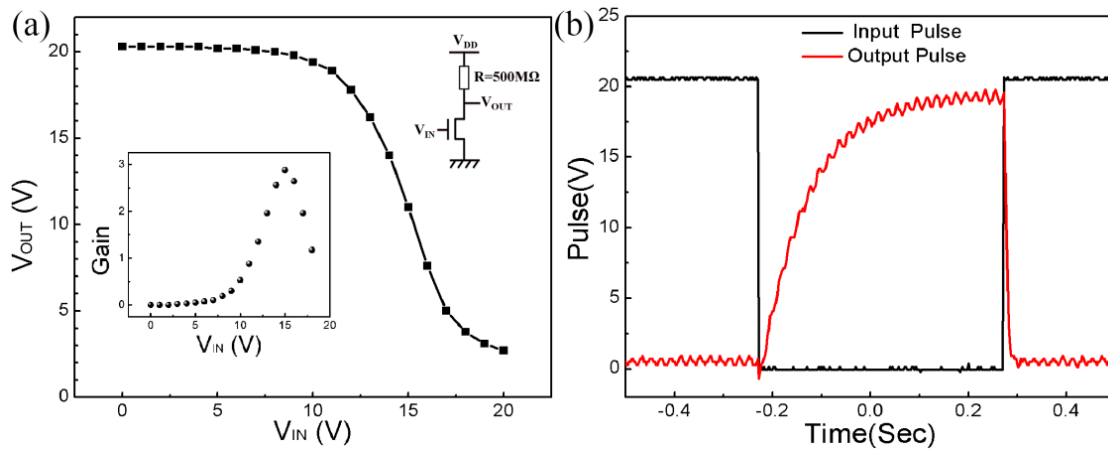


Figure 3-15: (a) Static output characteristic of printed C_{60} based OFET loaded by $500M\Omega$ resistance and (b) its response to 1Hz pulse. The inset shows the gain of the inverter with a maximum value of 3.

In these polarization conditions, the inverter has a gain (maximum of the differentiation dV_{OUT}/dV_{IN} of 3 (Fig 3-15a). This value depends on the load resistance of course. But it is in the order of the gain of organic based OFETs inverters [48]. The minimum output voltage V_{OL} with the maximum input voltage V_{IN} is explained by the resistance value of the channel in on-state compared to the load resistance.

More interestingly than the static characteristic, the dynamic response of the OFET to a voltage pulse gives a better idea of its performance. When applying 20V pulse of 0.5 second duration (1 Hz frequency) to the gate of the OFET, the behavior of the output voltage gives its time response (as shown in fig.3-14b). When the gate-source voltage

switches from 20V to 0V, the OFET status switches from the on-state to the off-state and then the output voltage has to switch from nearly 0V to nearly 20V. The switch time is defined usually by the time from 10% to 90% of the maximum voltage. In the case of the present OFET, the switching time is 220 ms. This time is due to the load resistance as its value is much lower than the resistance of the channel in off-regime, 500M Ω compared to some hundreds G Ω .

The more significant time is the switching time between the off-state and the on-state that depends nearly only on the transistor. This time corresponds to the decrease of the output voltage from the maximum to the minimum value. The switching time from 90% to 10% of the maximum voltage is 13 ms here. Present OFET can answer to more than 10Hz frequency. However, the frequency can be increased more by optimizing the overlap between the gate contacts and source and drain contacts and by chemically modifying the surface of drain and source electrodes before the deposition of C₆₀ active layer as we have done previously for photolithography processed C₆₀ OFETs where 1.5 cm²/V. s was obtained [49]. In fact, the frequency can be considered depending on the applications. For example, more than 10Hz frequency is enough if OFETs are integrated into a treatment electronic circuit of signals coming from human body activities. Such frequency can be reached with such process improvement.

Conclusion

The main purpose of present work was devoted to the optimization of the last deposited layer in bottom-gate bottom contacts printed C₆₀ based OFET. This last deposited layer is a film of C₆₀. The first steps of the process were the printing of the silver gate contact, the photoresist SU8 gate insulator, the drain and source silver contacts. All these steps were previously optimized and the results were published in different papers.

The effect of the post-annealing temperature of the fabricated OFET was studied

firstly. Direct correlation between the structure of the C₆₀ film (grain size, surface roughness) as analyzed from AFM observation and electrical parameters of the OFET was highlighted. More than the correlation, proportionality between the grain size and the field effect mobility was evidenced. The surface roughness is effective only when the grain size does not change a lot. The proportionality between the grain size and the mobility led us to involve the usual Seto model and its derivatives established for polycrystalline films and thin film transistors based on. Treatment of the experimental curves fit well with this model leading us to the calculation of the defect density in the grain boundaries. In our knowledge, such detailed analysis was never made before on the effect of the post-annealing temperature on organic transistors. Determining the 200°C optimum post-annealing temperature, the thickness of the C₆₀ active layer was optimized at 90 nm and confirmed by electrical stability study of the drain current during continuous polarization of the transistor. Considering the potential main application of such transistors in electronic circuits for the treatment of analog signals coming from the human body activities, the response of present OFETs to a voltage pulse applied to the gate was measured. A switching time of 13ms was obtained, leading to application frequency of some 10Hz.

References:

- [1] Rogers, J. A. & Bao, Z. Printed plastic electronics and paper like displays. *J. Polym. Sci., Part A: Polym. Chem.* 40, 3327 – 3334 (2002).
- [2]. Gelinck, G. H. et al. Flexible active-matrix displays and shift registers based on solution-processed organic transistors. *Nat. Mater.* 3, 106 – 110 (2004).
- [3]. Subramanian, V. et al. Progress toward development of all-printed RFID tags: materials, processes, and devices. *Proc. IEEE* 93, 1330 – 1338 (2005).
- [4]. Baude, P. et al. Pentacene-based radio-frequency identification circuitry. *Appl. Phys. Lett.* 82, 3964 – 3966 (2003).
- [5]. Klauk, H., Zschieschang, U., Pflaum, J. & Halik, M. Ultralow-power organic complementary circuits. *Nature* 445, 745 – 748 (2007).
- [6]. Sirringhaus, H. et al. High-resolution inkjet printing of all-polymer transistor circuits. *Science* 290, 2123 – 2126 (2000).
- [7]. Crone, B. et al. Large-scale complementary integrated circuits based on organic transistors. *Nature* 403, 521 – 523 (2000).
- [8]. Someya, T., Dodabalapur, A., Huang, J., See, K. C. & Katz, H. E. Chemical and physical sensing by organic field-effect transistors and related devices. *Adv. Mater.* 22, 3799 – 3811 (2010).
- [9]. Lipomi, D. J. et al. Skin-like pressure and strain sensors based on transparent elastic films of carbon nanotubes. *Nat. Nanotech.* 6, 788 – 792 (2011).
- [10]. Mannsfeld, S. C. et al. Highly sensitive flexible pressure sensors with microstructured rubber dielectric layers. *Nat. Mater.* 9, 859 – 864 (2010).
- [11]. Kuribara, K. et al. Organic transistors with high thermal stability for medical applications. *Nat. Commun.* 3, 723 (2012).

- [12]. Roberts, M. E. et al. Water-stable organic transistors and their application in chemical and biological sensors. *Proc. Natl Acad. Sci. USA* 105, 12134 – 12139 (2008).
- [13]. Berggren, M. & Richter-Dahlfors, A. Organic bioelectronics. *Adv. Mater.* 19, 3201 – 3213 (2007).
- [14] Tsao, H. N.; Cho, D. M.; Park, I.; Hansen, M. R.; Mavrinskiy, A.; Yoon, D. Y.; Graf, R.; Pisula, W.; Spiess, H. W.; Müllen, K. J. *Am. Chem. Soc.* 2011, 133, 2605.
- [15] Payne, M. M.; Parkin, S. R.; Anthony, J. E.; Kuo, C. C.; Jackson, T. N. J. *Am. Chem. Soc.* 2005, 127, 4986.
- [16] Wang, C.-H.; Hsieh, C.-Y.; Hwang, J.-C. *Adv. Mater.* 2011, 23, 1630.
- [17] Wang, Y.; Acton, O.; Ting, G.; Weidner, T.; Shamberge, P. J.; Ma, H.; Ohuchi, F. S.; Castner, D. G.; Jen, A. K. Y. *Org. Electron.* 2010, 11, 1066.
- [18] Virkar, A.; Mannsfeld, S.; Oh, J. H.; Toney, M. F.; Tan, Y. H.; Liu, G. Y.; Scott, J. C.; Miller, R.; Bao, Z. *Adv. Funct. Mater.* 2009, 19, 1962.
- [19] Anthopoulos, T. D.; Singh, B.; Marjanovic, N.; Sariciftci, N. S.; Ramil, A. M.; Sitter, H.; Colle, M.; de Leeuw, D. M. *Appl. Phys. Lett.* 2006, 89, 213504.
- [20] Shukla, D.; Nelson, S. F.; Freeman, D. C.; Rajeswaran, M.; Ahearn, W. G.; Meyer, D. M.; Carey, J. T. *Chem. Mater.* 2008, 20, 7486.
- [21] Polander, L. E.; Tiwari, S. P.; Pandey, L.; Seifried, B. M.; Zhang, Q.; Barlow, S.; Risko, C.; Bredas, J. L.; Kippelen, B.; Marder, S. R. *Chem. Mater.* 2011, 23, 3408.
- [22] Soeda, J.; Uemura, T.; Mizuno, Y.; Nakao, A.; Nakazawa, Y.; Facchetti, A.; Takeya, J. *Adv. Mater.* 2011, 23, 3681.

[24] S. Kobayashi, T. Takenobu, S. Mori, A. Fujiwara, Y. Iwasa, Fabrication and characterization of C60 thin-film transistors with high field-effect mobility, *Appl. Phys. Lett.* 82 (2003) 4581e4583.

[25] Haddon R C, Perel A S, Morris R C, et al. C60 thin film transistors[J]. *Applied Physics Letters*, 1995, 67(1): 121-123.

[26] Anthopoulos T D, Singh B, Marjanovic N, et al. High performance n-channel organic field-effect transistors and ring oscillators based on C 60 fullerene films[J]. *Applied Physics Letters*, 2006, 89(21): 213504.

[27] Itaka K, Yamashiro M, Yamaguchi J, et al. High - mobility C60 field - effect transistors fabricated on molecular - wetting controlled substrates[J]. *Advanced Materials*, 2006, 18(13): 1713-1716.

[28] Vogel R, Hoyer P, Weller H. Quantum-sized PbS, CdS, Ag₂S, Sb₂S₃, and Bi₂S₃ particles as sensitizers for various nanoporous wide-bandgap semiconductors[J]. *The Journal of Physical Chemistry*, 1994, 98(12): 3183-3188.

[29] Vennstra S.C., Heeres A., Hozhoannou G., Sawatzky G.A., Jonkman H.T. On interface dipole layers between C60 and Ag or Au. *Appl. Phys. A*, 2002, 75: 661-666.

[30] Biebersdorf A., Dietmuller A. , Susha A.S., Rogach A.L., Poznyak S.K., Talapin D.V., Weller H. , Klar T.A., and Feldmann J., Semiconductor Nanocrystals Photosensitize C60 Crystals, *NanoLetters* 2006, 6 (7), 1559-1563

[31] Fukuda K, Hikichi K, Sekine T, et al. Strain sensitivity and durability in p-type and n-type organic thin-film transistors with printed silver electrodes[J]. *Scientific reports*, 2013, 3.

[32] Bredas, J.-L., Beljonne, D., Coropceanu, V. & Cornil, J. Charge-transfer and

energy-transfer processes in p-conjugated oligomers and polymers: a molecular picture. *Chem. Rev.* 104, 4971 – 5004 (2004).

[33] Sokolov, A. N. et al. From computational discovery to experimental characterization of a high hole mobility organic crystal. *Nat. Commun.* 2, 437 (2011).

[34] D.K. Hwang, C. Fuentes-Hernandez, J. Kim, W.J. Potscavage, S.-J. Kim, B. Kippelen, Top-gate organic field-effect transistors with high environmental and operational stability, *Adv. Mater.* 23 (2011) 1293e1298.

[35] T. Richards, H. Sirringhaus, Bias-stress induced contact and channel degradation in staggered and coplanar organic field-effect transistors, *Appl. Phys. Lett.* 92 (2008) 23512.

[36] R. Ahmed, C. Simbrunner, M.A. Baig, H. Sitter, Grain size and interface dependence of bias stress stability of N-Type organic field effect transistors, *ACS Appl. Mater. Interfaces* 7 (2015) 22380e22384.

[37] H.L. Cheng, W.Y. Chou, C.W. Kuo, Y.W. Wang, Y.S. Mai, F.C. Tang, S.W. Chu, Influence of electric field on microstructures of pentacene thin-films in field-effect transistors, *Adv. Funct. Mater.* 18 (2008) 285e293.

[38] T.N. Ng, J.H. Daniel, S. Sambandan, A.-C. Arias, M.L. Chabinyc, R.A. Street, Gate bias stress effects due to polymer gate dielectrics in organic thin-film transistors, *J. Appl. Phys.* 103 (2008) 44506.

[39] R. Ahmed, C. Simbrunner, G. Schwabegger, M.A. Baig, H. Sitter, The role of metal contacts in the stability of N-Type organic field effect transistors, *Appl. Phys. A* 117 (2014) 2235e2240

[40] Senthilkumar, M., et al. "Characterization of microroughness parameters in gadolinium oxide thin films: A study based on extended power spectral density

analyses." *Applied surface science* 252.5 (2005): 1608-1619.

[41] Rolland A, Richard J, Kleider J P, et al. Electrical properties of amorphous silicon transistors and MIS - devices: comparative study of top nitride and bottom nitride configurations[J]. *Journal of the Electrochemical Society*, 1993, 140(12): 3679-3683.

[42] Levinson J, Shepherd F, Scanlon P, Westwood W, Este G, Rider M. Conductivity behavior in polycrystalline semiconductor thin film transistors. *Journal of Applied Physics*. 1982;53:1193-202.

[43] Bonnaud O, Mohammed-Brahim T, Ast DG. Poly-Si Thin Film and Substrate Materials. *Thin Film Transistors: Polycrystalline Silicon Thin Film Transistors Bd.* 2004;2:8-94.

[44] Seto JY. The electrical properties of polycrystalline silicon films. *Journal of Applied Physics*. 1975;46:5247-54.

[45] Bebiche S. OTFTs de type N à base de semiconducteurs π -conjugués: fabrication, performance et stabilité: Rennes 1; 2015.

[46] Chern G, Mathias H, Testardi L, Seger L, Schlenoff J. Low-frequency dielectric permittivity of C 60. *Journal of superconductivity*. 1995;8:207-10.

[47] Mourgues K, Rahal A, Mohammed-Brahim T, Sarret M, Kleider J, Longeaud C, Bachrouri A & Romano-Rodriguez A. Density of states in the channel material of low temperature polycrystalline silicon thin film transistors. *Journal of Non-Crystalline Solids*. 2000;266:1279-83.

[48] Chang JS, Facchetti AF, Reuss R. A Circuits and Systems Perspective of Organic/Printed Electronics: Review, Challenges, and Contemporary and Emerging Design Approaches. *IEEE Journal on Emerging and Selected Topics in Circuits and*

Systems. 2017;7:7-26.

[49] Robin M, Harnois M, Molard Y, Jacques E. Improvement of n-type OTFT electrical stability by gold electrode modification. *Organic Electronics*. 2016;39:214-21.

4. The near infrared photodetector system based on the PbS quantum dots and Organic Thin-film Transistor

After optimizing the process of the fabrication of nearly all-printed N-type OTFT, it is the time now to focus on the main goal of the present work that is the fabrication of near-infrared phototransistor. As announced in the general introduction, the goal is to fabricate NIR phototransistor at the lowest cost possible using solution-based process. Previous optimized N-type OTFT can be the basic device of this phototransistor. Indeed, as previously demonstrated in the PhD work of Liu Xiang [1], mixing PbS quantum dots with usual field effect transistor can lead to NIR phototransistor thanks to the light absorption of PbS quantum dots with proper size. This idea is used in the present work

4.1 PbS Quantum Dots

PbS quantum dots have a typical face-centered cubic structure. It is a new IV-VI semiconductor material with a band gap of 0.91eV, which is a direct bandgap semiconductor material with a narrow band gap [2,3]. Since its exciton Bohr radius is only 18 nm, it has a strong quantum confinement effect, and by adjusting its size, quantum dots of different sizes can be obtained for use in a semiconductor device. It is particularly noteworthy that PbS quantum dots have strong multiplex exciton effects and therefore have good application prospects in high efficiency photoelectric conversion devices and other semiconductor devices. [4-6]

PbS quantum dots are usually prepared by liquid colloidal chemistry. Generally, high-quality PbS quantum dots with controlled morphology size are synthesized by adding long-chain organic ligands to the solvent and controlling the temperature and reaction time. [7-10] If the size distribution of the quantum dots is narrow and the morphology is close to a spherical shape, the quantum dots can form a dense and uniform high-quality quantum dot film. Among various devices, field effect devices (FETs) are capable of reflecting transmission performance between quantum dots,

semiconductor layer.

Based on the mature technology from the XingShuo Nano-technology Company (in SuZhou, China), I brought the PbS QDs for fabricating the photo-transistor. However, in order to cover the waveband for medical examination, the PbS QDs with absorption waveband more than 1300nm are required [10]. Due to the size effect, we measured the absorption waveband from the company with various diameter.

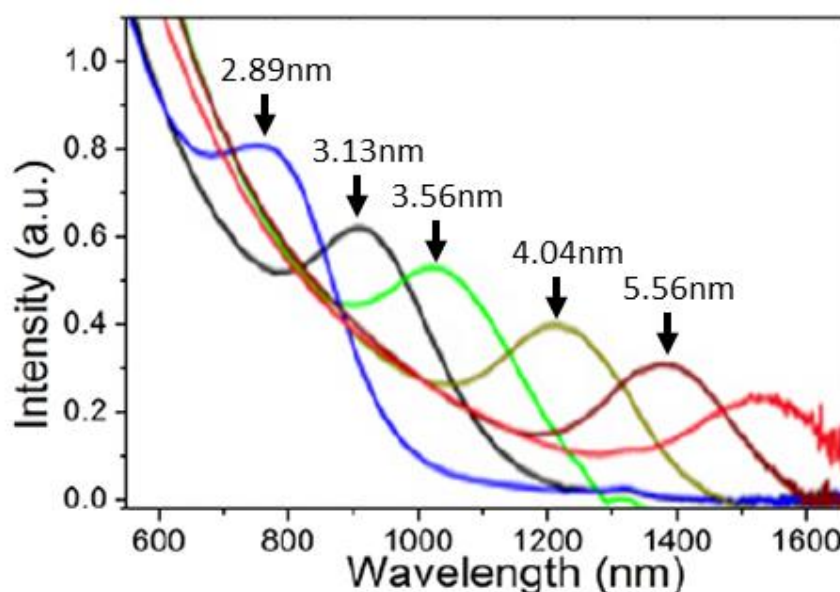


Figure 4-1 the connection between the PbS QDs' size and absorption waveband

With the size of the PbS increasing, the absorption wavelength increases. For covering the medical examination, the 5.56nm PbS QDs are utilized in my devices.

With the purpose to investigate the PbS QDs morphology, tunneling electron microscope (TEM) was utilized for observing. The collected PbS QDs was dissolved in n-Hexane solvent. Then the solvent will be dispersed by sonic and dropped on the copper net. After drying, the sample was set in TEM. With the high-resolution TEM, the size of PbS QDs is the nanoparticles spherical similar with approximately 5nm diameter. Besides, the PbS QDs are well dispersed in the solution as illustrated in Fig

4-2a.

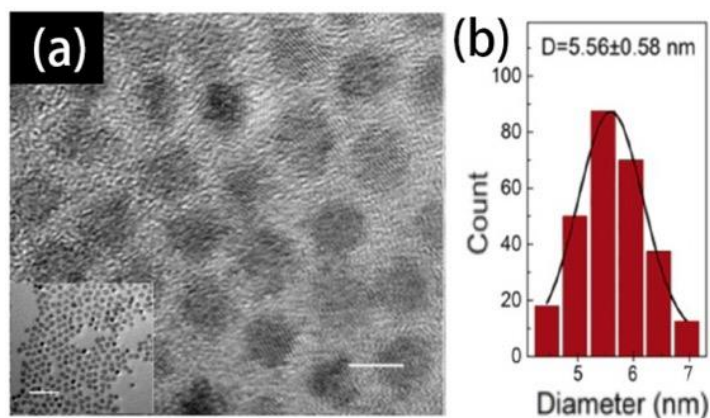


Figure 4-2 (a) HRTEM image of the PbS QDs scale bar: 5nm and overall image (inset), scale bar: 20nm. (b) The statistic size of the 240 PbS QDs.

Besides, from the statistics of the 240 PbS QDs, the distribution of the size follows the normal distribution. This PbS QDs meet the requirement of our devices.

The PbS QDs are well dispersed in the toluene solution and can be spin-coated into the substrate through solution-process. Through this experiment, the compound of PbS QDs can be revealed and the morphology of the QDs' layer can also be investigated. The spin-coating parameters are: 1000 rpm speed, 1000 rpm accelerated rate and 30s duration. The thickness of the QDs layer is around 30nm.

Figure 4-3 shows the infrared absorbance and PL emission spectrum for the as-prepared PbS QDs. From the absorbance spectrum, the peak of the absorbance is in 1380nm, while the emission peak is 1400nm due to a red shift for the PL spectrum. This characterization shows a narrow bandgap (0.91eV) which has a wide potential in the application of the IR detection.

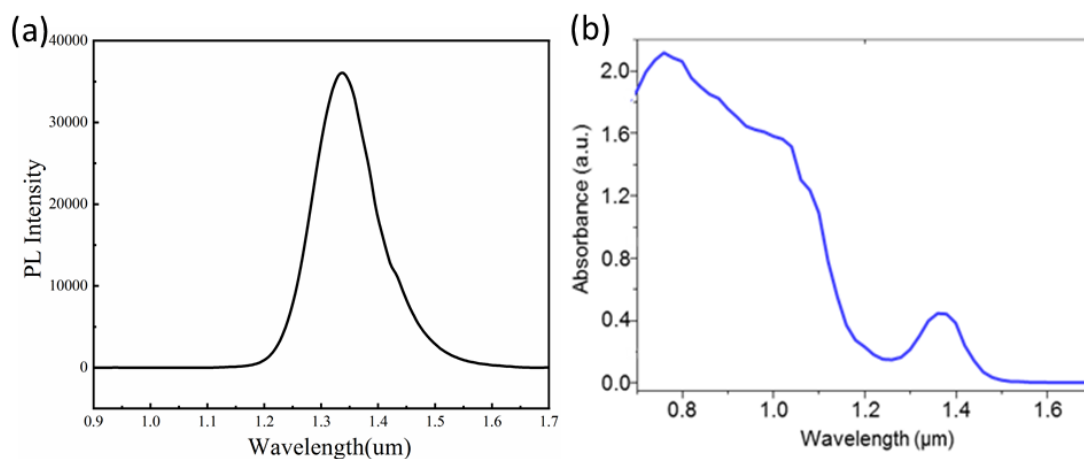


Figure 4-3 IR absorbance and PL emission intensity of the PbS QDs

Therefore, the basic performance of FETs for studying PbS quantum dots has become a necessary condition for understanding the performance of semiconductors. With the combination of the PbS QDs and printed organic thin-film transistors, the low cost and large scale NIR (near infrared) photo-detectors will be our target.

Based on the fabrication process of the C60 OTFT, the incident light will go through the 3 layers as QDs layer, C60 layer and Su8 layer. By this analyze, the absorption of the incident near infrared light should be considered.

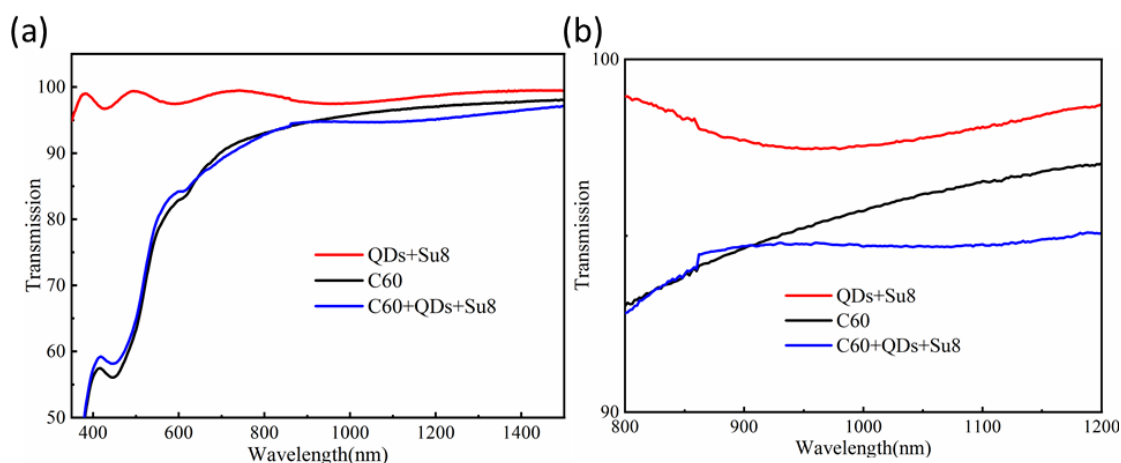


Figure 4-4 the transmission of the samples: C60, C60+QDs and C60+QDs+Su8. The incident light wavelength increases from 380nm-1500nm.

As illustrated in Fig 4-4, comparing the transmission with the incident light wavelength from 380nm to 700nm, the C60 layer play an important role in the absorption of the incident light. By this way, the C60 is more sensitive in visible light waveband. With the incident light wavelength increasing, the PbS QDs absorption is more obviously. The main absorption wavelength of the PbS QDs is fasten on the range from 850nm to 1200nm. In order to fabricating the near infrared detectors, the PbS QDs provide the obviously absorption in the near infrared waveband. Meanwhile, there is little influence from the C60 layer and Su8 layer.

Besides, for concentration selecting, the performance of the typical photo-transistor will be influenced by the PbS QDs concentration. The assumption was provided that if we increased the concentration of the photo-sensitive layer, the photocurrent of the transistor would increase with the concentration. With this purpose, five concentrations were utilized for fabricating the photo-transistor which is 5mg/mL, 7.5mg/mL, 10mg/mL, 12.5mg/mL and 15mg/mL.

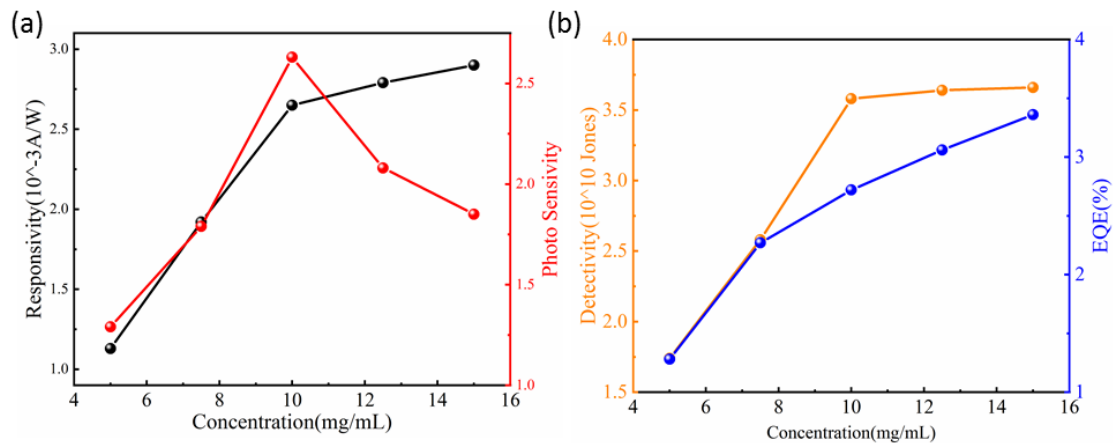


Figure 4-5 (a) the Responsivity and photo sensitivity of the photo-transistors with different concentrations. (b) the detectivity and EQE of the photo-transistors with different concentrations.

As illustrated in Fig 4-5a, with the concentration increasing, the responsivity

increases. For this phenomenon, due to the quantity of electron-hole pair increasing, the photo-current increases. However, the photo-sensitivity decreases at the same time. From the Eq.3, with the photo-current increasing, the increasing of the dark current lead to the decreasing of the photo-sensitivity.

Besides, as shown in Fig 4-5b, the detectivity increases fast with the concentration increasing from 5mg/mL to 10mg/mL. It's similar with the trend of the responsivity. This trend also can be acquired from the detectivity equation. However, the detectivity is much similar with the concentration more than 10mg/mL. Finally, the EQE increases with the concentration increasing for the electron-hole pair increasing.

Above all, for the circuit design, the lower dark current is the more important for photo-transistor. Besides, there is no big difference in the photo-sensitivity and detectivity for 10mg/mL, 12.5mg/mL and 15mg/mL. In a summary, the 10mg/mL concentration is still the best choice for the photo-transistor with separated structure.

4.2 Printed C60 & PbS Photo-transistor

Based on the graduated PhD. Liu Xiang's work [1], our group have already succeeded in fabricating the near infrared detectors with the traditional silicon transistor structure. For detecting the near infrared incident light, PhD. Liu replaced the SiO₂ insulator layer with the mixing layer of Su8 and PbS QDs. The photocurrent of the device in the near infrared waveband is more obviously. And the structure is convenient to design the circuit and to be integrated in the complex circuit.

4.2.1 Mixed PbS QDs / SU8 layer as gate insulator of the photo-OTFT

Based on the result of the PhD. Liu, the present work uses the mixing layer of the Su8 and PbS QDs as the insulator layer in the printed OTFT firstly. Due to the continuity, the near infrared source with 1050nm covering the medical examination wavelength was utilized and the intensity was set as 250 μ W/cm².

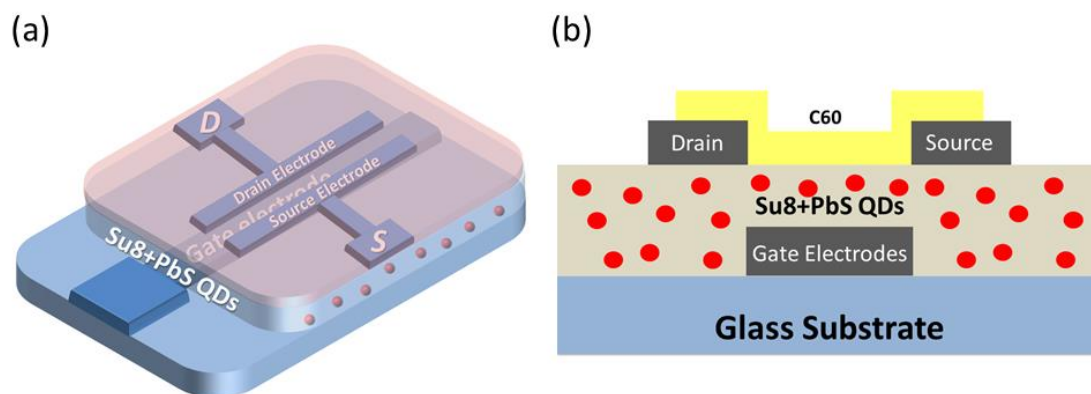


Figure 4-6 (a) the 3D structure of the printed near infrared photo-detector. (b) the cross-sectional image of the printed near infrared photo-detector.

Based on the printed OTFTs, the fabricating process of the organic photo-transistor is similar with the OTFTs. The insulator layer Su8 is replaced by the mixing layer of Su8&PbS QDs. For the concentration of the PbS QDs, 10mg/mL was utilized.

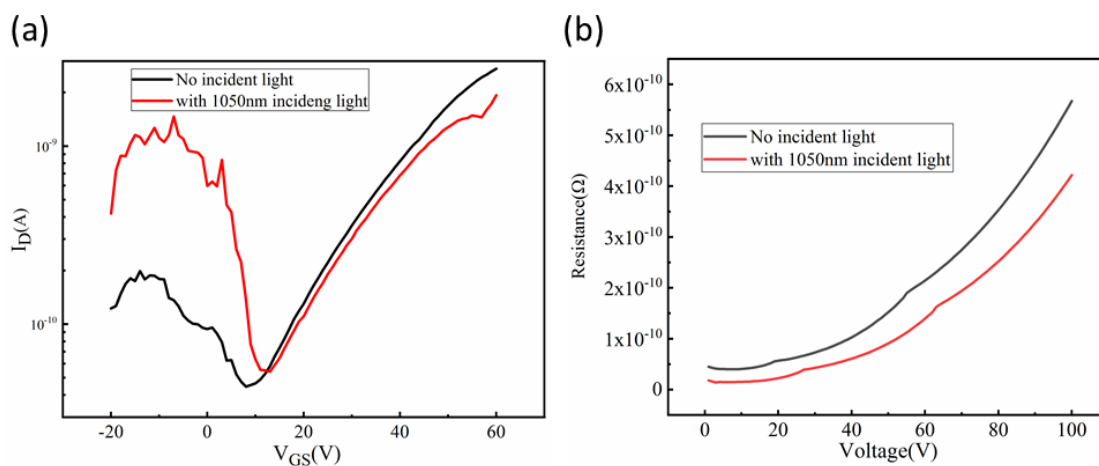


Figure 4-7 (a) the transfer characteristic of the printed organic photo-transistor. ($V_{ds}=20V$) (b) the resistance characteristic of the printed organic photo-transistor.

In order to analyze the photo-response characteristic of the printed organic photo-transistor, the transfer characteristic of the transistor was measured with the comparison of the incident light. As illustrated in Fig 4-7a, with the reverse bias, the photo-current is much higher around 1nA. But, with the mixing layer, there is no obviously typical

thin-film transistor characteristics. The transistor with this performance can't meet our requirement of the photo-detector.

But, in order to find the influence of PbS QDs, we measure the resistance without gate electrodes. With the data in Fig 4-7b, with the incident light, the resistance is lower. Based on the electric field of the source and drain electrodes, it means that the Su8 layer with PbS QDs provide some leakage current which will be influenced by the incident light switching. By this comparison, PbS QDs provide the photo-current and decrease the resistance.

Besides, in this fabricating process, we find that the printing electrodes in the surface of the mixing layer exhibit nonuniform patterns. Based on these, we modify the structure of the devices.

4.2.2 Sandwich of mixed PbS QDs / SU8 layer and SU8 layer as gate insulator of the photo-OTFT

Considering the printing patterns uniformity, the mixing layer is divided into two layers. For the top layer, the Su8 was utilized with the suited parameters for printing. Then, the mixing layer was utilized as the bottom layer for photo-sensitive as illustrated in Fig 4-8. In addition, improving the insulating layer performance is another important target.

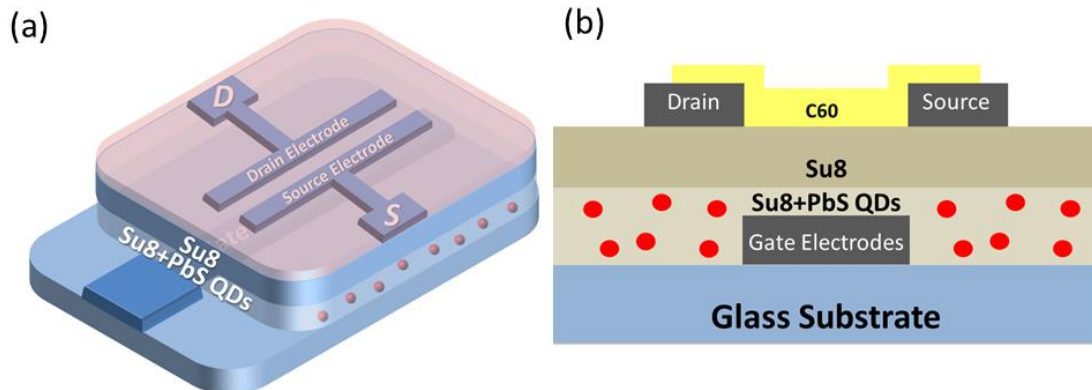


Figure 4-8 (a) the 3D structure of this double layer printed near infrared photo-detector. (b) the cross-sectional image of this device.

By this structure, the printing electrodes patterns of source and drain are similar with the initial device. In our opinion, the interface between the Su8 and C60 becomes better for the transfer characteristic as illustrated in Fig 4-9. In order to find the photocurrent of the transistor, the constant polarization was utilized to observe the photocurrent with the 1050nm incident light switching on and off.

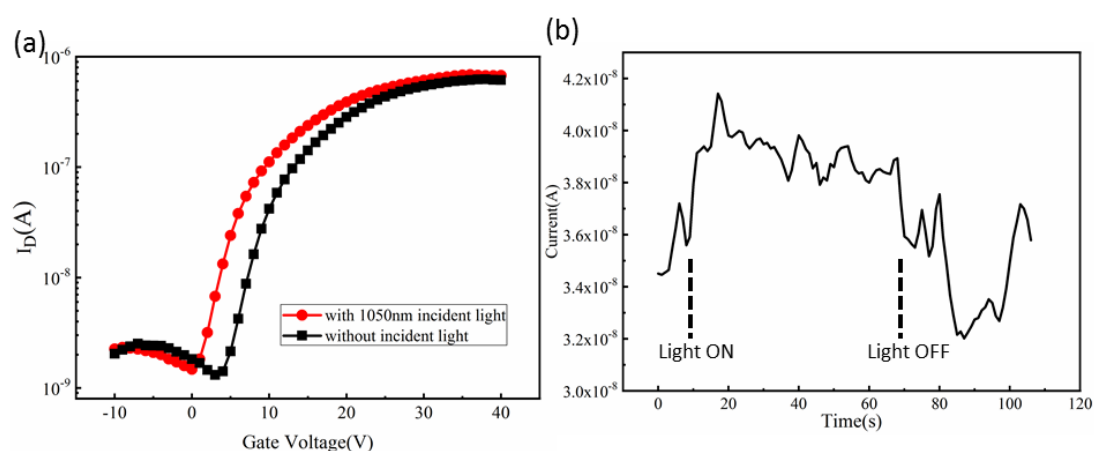


Figure 4-9 (a) the transfer characteristic of the transistor with the switching of the 1050nm incident light. ($V_{ds}=20V$) (b) With the $V_{ds}=20V$ and $V_{gs}=10V$, the constant polarization of the transistor by switching the incident light.

As shown in Fig 4-9a, the transfer characteristic of the sandwich structure is similar with the better performance OTFT. From the transfer characteristic, we can find that the photocurrent is more obvious with the 10V gate voltage. Then, the constant polarization was utilized with the 20V drain-source voltage and 10V gate voltage. As illustrated in Fig 4-9b, the obvious switching of the photo-current can be observed. Besides, the photo-current is approximately 3nA. However, the photocurrent is still difficult for utilized in the simple circuit. And as shown in fig 4-9b, there is some noise signal in the constant polarization.

4.2.3 PbS QDs at the interface between SU8 layer as gate insulator and C60 active layer of the photo-OTFT

Considering the circuit design, we should decrease the noise and increase the photo-current of previous photo-OTFT. Besides, the better the surface of the Su8, the better the performance of the OTFTs. The mixing layer was divided to Su8 layer and QDs layer. Normally, the QDs photo-sensitive mechanism is the electron hole pair divided by the exciton with the incident light. Based on this mechanism, the new structure is designed as the QDs layer directly connecting to the C60 layer. Meanwhile, with the field effect of the transistor, the photo-current will be influenced by the electron-hole pair.

Besides, with the new structure, the fabrication process was changed to fit the structure. As previous fabricating process, it's the same process until the source and drain electrodes printing. Then, we spin-coating the PbS QDs which dissolve in methylbenzene with the concentration 10mg/ml. With the rotate speed 3000r/min and acceleration 3000r/rpm, the device will be baked at the temperature 100°C for 10mins.

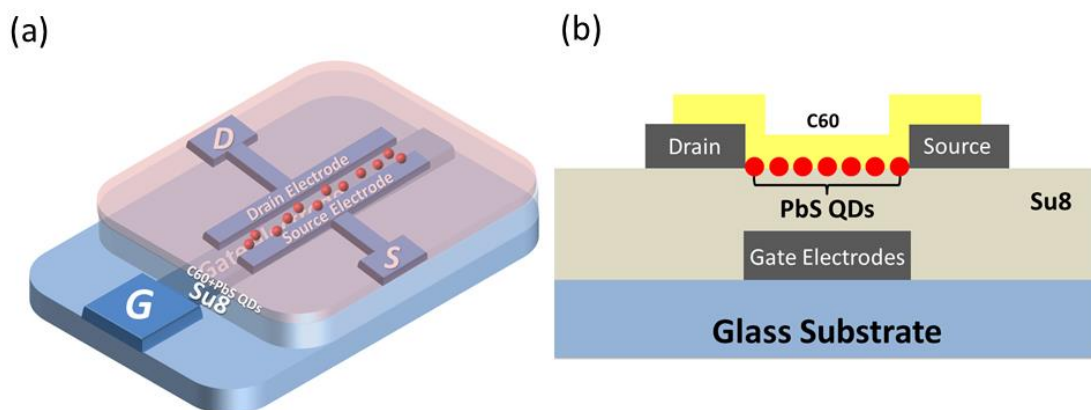


Figure 4-10 (a) the 3D structure of this separated layer structure printed near infrared photo-detector. (b) the cross-sectional image of this device.

As illustrated in Fig 4-10a, even with the spin-coating method, the active PbS QDs were distributed in the channel of the transistor for the field effect of the transistor.

From the Fig 4-10b, the PbS QDs layer was distributed at the interface of the Su8 and C60. As the organic solvent, the PbS QDs layer was spin-coated first before depositing C60.

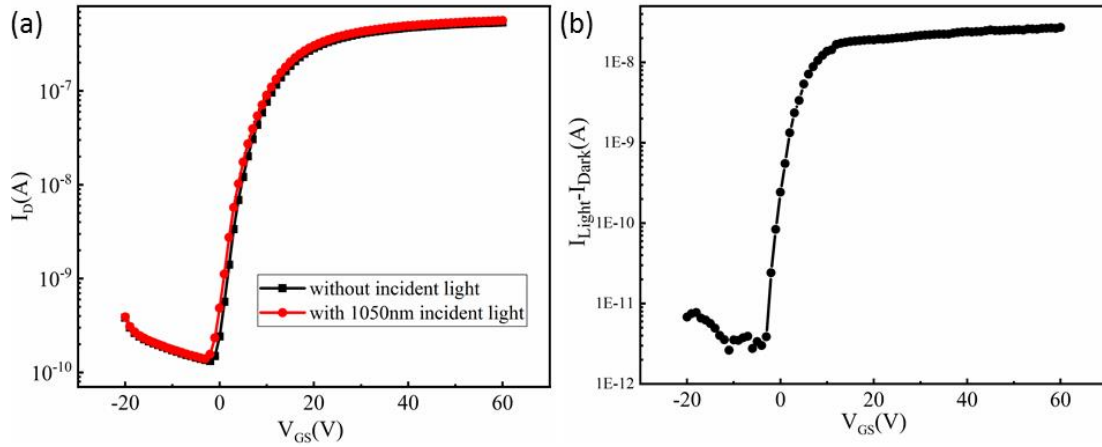


Figure 4-11 (a) transfer characteristic of the photo-transistor. ($V_{DS}=10V$) (b) the photo-current of the photo-transistor.

At first, with the new structure, the transfer characteristic of the photo-transistor was measured. As illustrated in Fig 4-11a, the transfer characteristic of the transistor is similar to the typical transistor. With the electric parameters of the photo-transistor, the on/off ratio is approximately 10^3 , on state current is 5×10^{-7} A and the sub-threshold slope is 3.96V with the 10V V_{DS} . As shown in fig 4-11b, with the gate voltage increasing, the photo-current increase from 1×10^{-11} A to 2.7×10^{-8} A. Based on this performance, the gate field effect was verified for modifying the photo-sensitivity of the photo-transistor. After $V_{GS}=10V$, the photo-current tends to be stable.

4.2.4 Photo-sensitive circuit (Inverter)

Based on the new structure of separated C60 and PbS QDs layers, the transfer characteristic and photo-current have been illustrated in Fig 4-10. In order to design the circuit and research the photo-current, the output characteristic of the photo-transistor is shown in Fig 4-12a, with a channel width $W=4000 \mu m$ and a channel length $L=150$

μm .

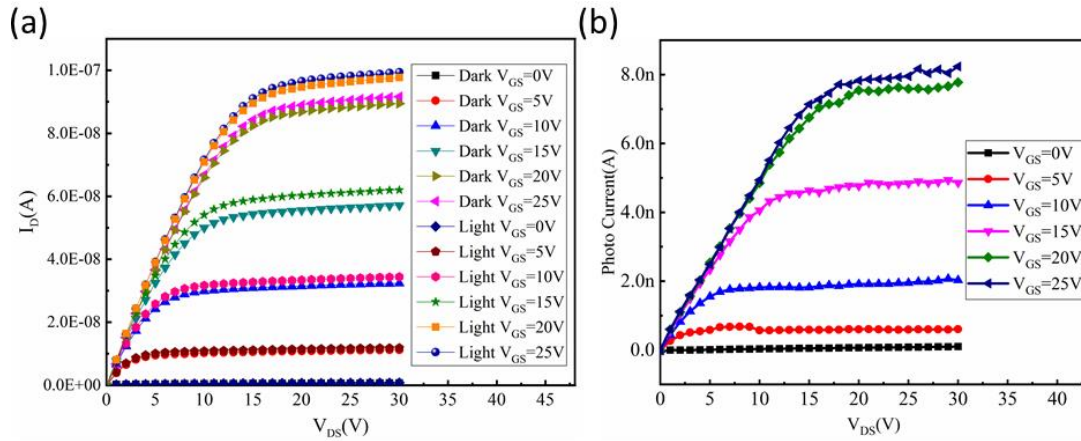


Figure 4-12 (a) the output characteristic of the photo-transistor with the switching of the incident light ($\lambda=1050\text{nm}$) (b) the photo-current of the transistor calculated from the output characteristic

From the Fig 4-12a, with the gate voltage increasing, the photo-current becomes more evident. When the gate voltage is more than 20V, there is no obviously change of the photo-current. For observing the phot-current clearly, the photo-current calculated from the output characteristic is illustrated in Fig 4-12b. With the gate increasing, the highest photo-current is approximately 8nA.

Above all, with the parameters from the output characteristic and photo-current, the $500\text{M}\Omega$ was chosen as the connect resistance. With this connect resistance, the photo inverter was designed.

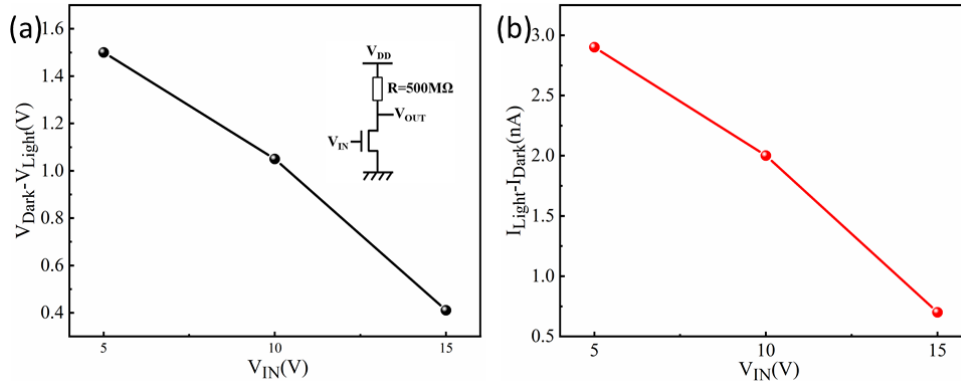


Figure 4-13 With the input voltage increasing, the photo-inverter parameters decrease with the 1050nm incident light and $V_{DD}=20V$ (a) the output voltage change, (b) the current change

Based on the simple inverter circuit, the photo-transistor works as the typical transistor in the inverter circuit. With the input voltage increasing, the resistance of the transistor decreases and the output voltage decreases. Meanwhile, the change of the voltage with the switching of the incident light becomes less obvious as illustrated in Fig 4-13a.

Besides, with the input voltage increasing, the current of the transistor increases. However, the photo-current decreases at the same time as illustrated in Fig 4-13b. Based on this phenomenon, the performance of the photo-inverter doesn't fix the characteristics of the photo-transistor. Because the resistance of the photo-transistor decreases, the voltage of the photo-transistor decreases. It means that the field effect of the photo-transistor influence the electron-hole pair less. And these lead to the photo-voltage and photo-current decrease with the input voltage increasing.

In order to observe the field effect influencing the photo-voltage and photo-current, the V_{DD} as another parameter was considered as shown in Fig 4-14. Concluded from the transfer characteristic and output characteristic of the transistor, the 10V gate voltage was chosen as the input voltage. And the 1050nm wavelength was chosen as

the incident light wavelength as previous one.

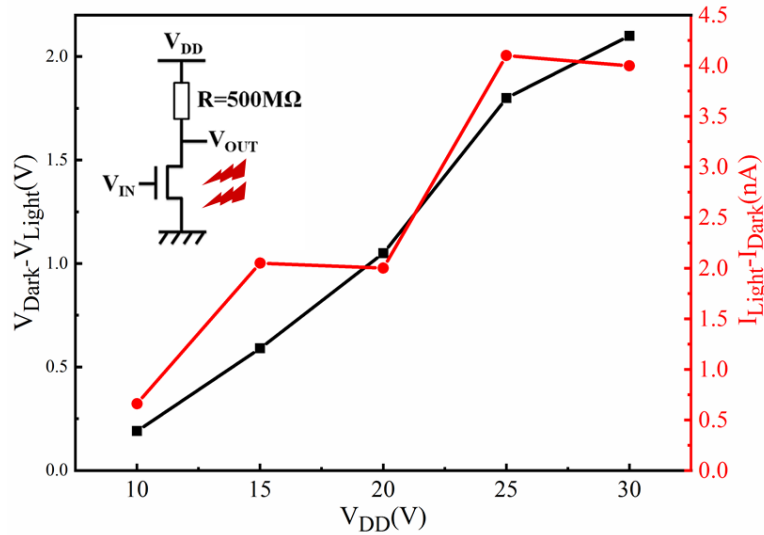


Figure 4-14 the comparison of the photo-inverter with the switching of the incident light ($\lambda=1050\text{nm}$, $V_{GS}=10\text{V}$), the black line is the change of the output voltage and the red line is the change of the current

As illustrated in Fig 4-14, with the V_{DD} increasing, the voltage of the transistor increases. Meanwhile, with the switching of the near infrared light source, the photo-voltage increases due to the enhancement of the field effect of the photo-transistor. The photo-voltage increases from 0.2V to 2.1V.

Besides, from the red line of the fig 4-14, the photo-current increases to 4nA. The highest photo-current of the transistor is approximately 8nA from the output characteristic. In consequence, compared with the photo-current, the signal of the photo-voltage is more obvious. For the circuit design, the photo-voltage of this photo-transistor is easier to be utilized in the circuit design.

4.2.5 Photo-Inverter using OTFT with cross-finger drain and source electrodes (Large Channel area)

Previous inverter was shown as a good photo-detector. However, higher photo-

current is required for the circuit design. Based on the previous printed electronic, the cross-finger electrodes photo-transistor was designed and analyzed. The structure and the optical image of the photo-transistor can be found in fig 4-15.

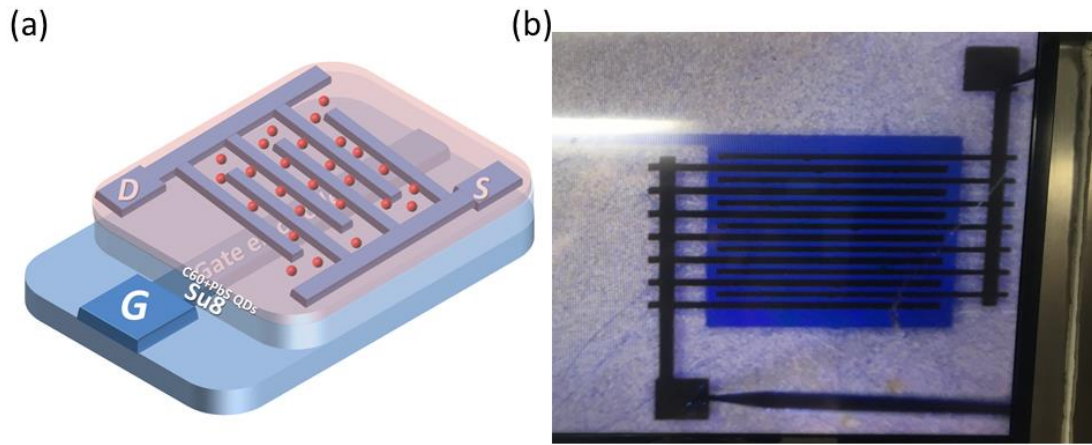


Figure 4-15 (a) the structure of the cross-finger photo-transistor. (b) the optical image of the cross-finger photo-transistor.

With the channel area increasing till $52000 \mu\text{m}^2$ ($13 \times 4200 \mu\text{m}^2$), the electron-hole pair increases. It means that with the photo-current will increase with the modifying of the field effect.

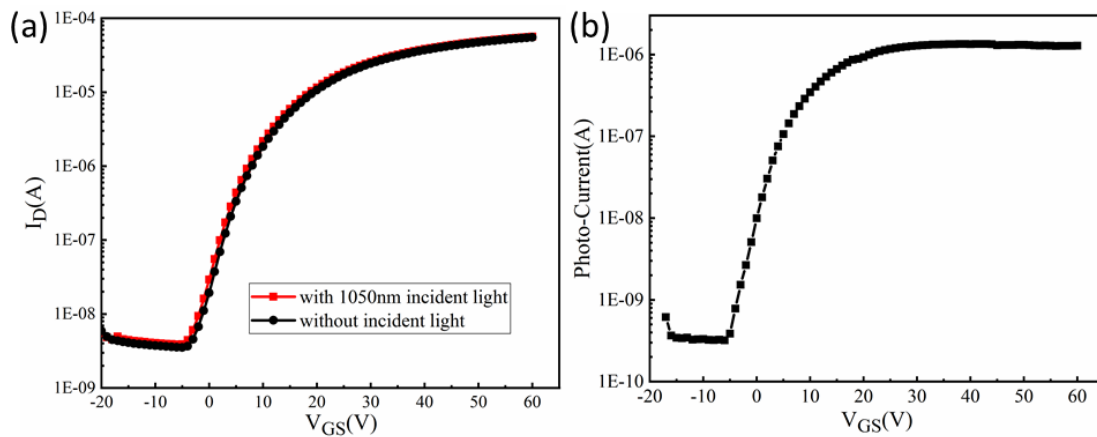


Figure 4-16 (a) transfer characteristic of the photo-transistor with switching of the incident light ($V_{DS}=10\text{V}$). (b) the photo-current of the cross-finger transistor calculated from the transfer characteristic

Due to the channel length increasing, the current of the photo-transistor is much higher than the typical transistor as illustrated in fig 4-16a. At the same time, the photo-current of the transistor increases due to the channel area increasing in fig 4-16b. The photo-current of the transistor increases from the 1nA to 1 μ A. Compared with the typical photo-transistor, the photo-current has increased by two orders.

With the requirement of the circuit design, the output characteristic of the transistor is shown in Fig 4-17.

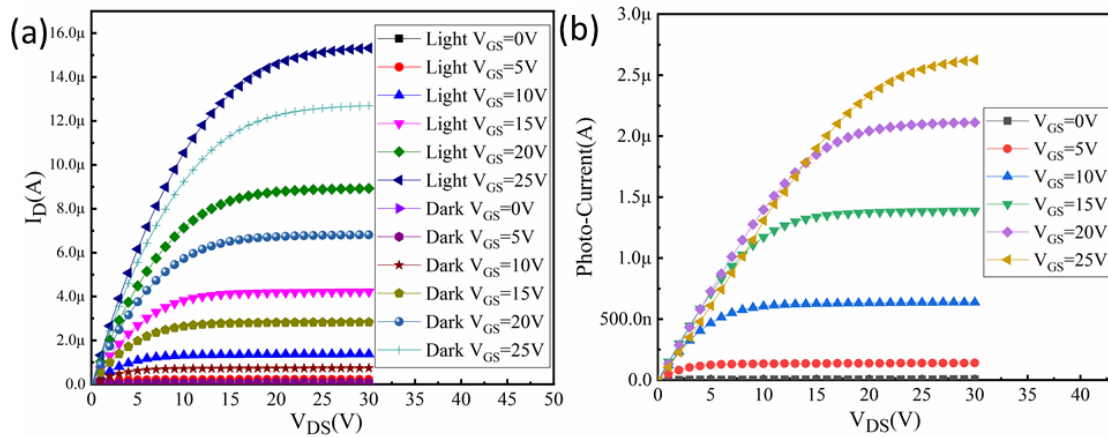


Figure 4-17 (a) the output characteristic of the cross-finger photo-transistor with the switching of the incident light ($\lambda=1050\text{nm}$) (b) the photo-current of the cross-finger transistor calculated from the output characteristic

As shown in output characteristic of the cross-finger transistor, the connect resistance of the inverter circuit should be less than the typical transistor. Besides, from the Fig 4-17b, the photo-current of the transistor increases to 2.6 μ A. The signal of the photo-current of the cross-finger photo-transistor is more obvious than the typical transistor. Therefore, the field effect of the cross-finger photo-transistor is the most important influence factor. The connect resistance was modifying to insure the voltage

of the transistor for observe the photo-current signal.

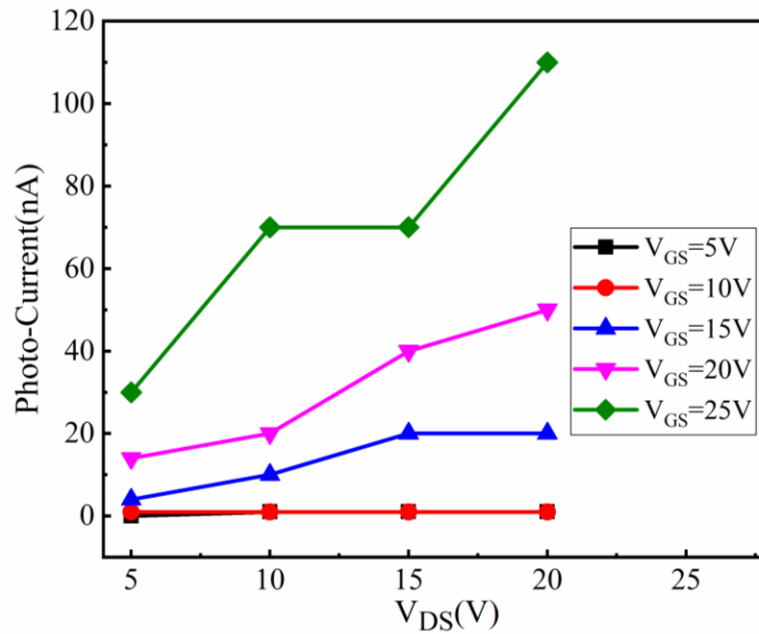


Figure 4-18 the photocurrent from the inverter based on the cross finger photo-transistor

As illustrated in Fig 4-18, with the gate voltage of the transistor increasing, the photo-current of the cross-finger transistor increases. By this phenomenon, the field effect of the cross-finger transistor can be observed. Besides, the photo-current of the inverter increases to the 110nA as the highest current signal which is more obvious than the typical photo-transistor photo-current signal.

Conclusion

We modified the structure of the photo-transistor from mixing to double layer. Finally, the separated layers structure exhibits the best performance of the photo-transistor. For further step, the simple photo-inverter circuit was designed with the photo-transistor. With the typical photo-transistor, the photo-inverter we designed provided the better photo-voltage signal. The photo-voltage increased from 0.2V to 2.1V, which can be utilized for photo-signal readout circuit. Based on the cross-finger photo-transistor, the device provides the choice of the photo-current signal with 2.6 μ A

for next step circuit design. With the simple circuit design, higher photo-current around 100nA was obtained for photo-current signal which was much higher than the typical photo-transistor structure.

References:

[1] Liu Xian, Transistor silicium en couche mince à base de nano-particules de PbS: Un efficace phototransistor pour la détection de lumière infrarouge, PhD Thesis, Rennes 1 University, France, 2017

[2] Zhang J, Gao J, Miller E M, et al. Diffusion-controlled synthesis of PbS and PbSe quantum dots with in situ halide passivation for quantum dot solar cells[J]. ACS nano, 2013, 8(1): 614-622.

[3] Andreakou P, Brossard M, Li C, et al. Size -and temperature-dependent carrier dynamics in oleic acid capped PbS quantum dots[J]. The Journal of Physical Chemistry C, 2013, 117(4): 1887-1892.

[4] Talapin D V, Murray C B. PbSe nanocrystal solids for n-and p-channel thin film field-effect transistors[J]. Science, 2005, 310(5745): 86-89.

[5] Oh S J, Berry N E, Choi J H, et al. Stoichiometric control of lead chalcogenide nanocrystal solids to enhance their electronic and optoelectronic device performance[J]. ACS nano, 2013, 7(3): 2413-2421.

[6] Koh W, Saudari S R, Fafarman A T, et al. Thiocyanate-capped PbS nanocubes: ambipolar transport enables quantum dot based circuits on a flexible substrate[J]. Nano letters, 2011, 11(11): 4764-4767.

[7] Hines M A, Scholes G D. Colloidal PbS nanocrystals with size - tunable near - infrared emission: observation of post - synthesis self - narrowing of the particle size distribution[J]. Advanced Materials, 2003, 15(21): 1844-1849.

[8] Lin W, Fritz K, Guerin G, et al. Highly luminescent lead sulfide nanocrystals in organic solvents and water through ligand exchange with poly (acrylic acid)[J].

Langmuir, 2008, 24(15): 8215-8219.

[9] McDonald S A, Cyr P W, Levina L, et al. Photoconductivity from PbS-nanocrystal/ semiconducting polymer composites for solution-processible, quantum-size tunableinfrared photodetectors[J]. Applied physics letters, 2004, 85(11): 2089-2091.

[10] Rossel R A V, Walvoort D J J, McBratney A B, et al. Visible, near infrared, mid infrared or combined diffuse reflectance spectroscopy for simultaneous assessment of various soil properties[J]. Geoderma, 2006, 131(1-2): 59-75.

General Conclusion

Based on the thin-film transistor's self-amplifying and field effect, the photo-generated carriers' injection into the channel improves. Besides, with the quantum dots' (QDs) unique optical-electrical properties such as quantum confinement, size-tunable and photo-conductivity effects, the combination of the thin-film transistor and QDs is recognized as new photo-detectors. Especially in the near-infrared (NIR) waveband, traditional HgCdTe NIR photo-detectors is restricted to the complex fabrication process and readout circuit design. With the purpose of low cost, large area and flexible electronics, the photo-transistor was fabricated by inkjet printing process. Meanwhile, fullerene (C60) was utilized as the semiconductor layer of the transistor. Therefore, in this thesis, we focus on printing process, C60 organic thin-film transistor and simple photo-sensitive circuit.

Firstly, based on the normally commercial printing silver ink, we research the phase separation which influence the pattern formation. Our work highlights that this phenomenon can occur when PVP is used as stabilizer in colloidal based ink. After drop drying, an inner colloidal rich region and an outer polymer rich region can be distinguished independently of deposition techniques. In addition, with modifying the inkjet printing parameters (i.e., surface energy, working frequency, overlap distance), best performance printing pattern was observed. And this work gives more information for ink designer and experiment involved in the field of printed electronics. It could help to fully understand the phase separation that occurs during inkjet printing of colloids droplets with a systematical study of other experimental conditions such as: ligand kind of material, surface materials and roughness.

With the adjustment of the printing parameters, uniform and smooth electrodes patterns was obtained for the organic thin-film transistors' fabrication. Based on previous PhD. Malo Robin's work, the research focused on the modifying the connect area between electrodes and C60 semiconductor layer that the performance of the

transistor improved by this way. However, it's difficult to follow the same methods to improve the transistor performance. Because the requirement of the substrate surface and the roughness of the electrodes couldn't be modifying by the same way. Therefore, the characteristic of the semiconductor layer was focused on by us. At the beginning, we modified the annealing temperature of the printed C60 thin-film transistors. With the annealing temperature increasing, the grain size and the roughness of the C60 layer increase from the AFM measurement. When annealing temperature is 200°C, the grain size is large enough to increases the transistor electric performance. And there is no obvious change in the surface roughness. In addition, the surface roughness is effective only when the grain size does not change a lot. Through Seto model and its derivatives established for polycrystalline films and thin film transistors, the calculation of the defect density in the grain boundaries exhibits the defect density decreasing. Then, due to the best annealing temperature 200°C obtained, the thickness of the C60 active layer was optimized at 90nm and confirmed by electrical stability study of the drain current during continuous polarization of the transistor. On account of the potential application in electronic circuits for the treatment of analog signals of medical examination, the switching time of 13ms was obtained from the response to a voltage pulse applied to the gate. And the application frequency could approach 10Hz which could cover some normal medical examination measurement.

Finally, considering the size influence of the PbS QDs, the PbS QDs with 5.56nm diameter was selected as the photo-sensitive material. Through the comparison of various concentration from 5mg/mL to 15mg/mL, the device utilizing 10mg/mL concentration exhibited high photo-sensitivity. And there is no obvious difference of the responsivity, EQE and detectivity when the concentration is more than 10mg/mL. Therefore, 10mg/mL concentration was utilized in our device. Then, the structure of the photo-transistor transformed from the mixing layer to sandwich structure. And then PbS QDs at the insulator layer interface structure was selected, which provide evident

photo-signal response. For further step, the simple photo-inverter circuit was designed for obtaining photo-response signal. Connected with $500\text{M}\Omega$ resistance, the simple inverter provided the photo-voltage from 0.2V to 2.1V, and the photo-current from 0.8nA to 4nA. In order to improving the photo-current, cross-finger structure was utilized in the new devices. From the cross-finger electrodes, approximately $2.6\mu\text{A}$ photo-current was obtained. In the simple inverter circuit, more than 110nA photo-current was obtained, which can be used in medical examination field.

Moreover, due to the requirement of the low cost, large area and flexible electronics, all solution processed devices will be optimized for next step. Besides, combining with the P-type organic transistor, photo-sensitive printed organic CMOS circuit could be available.

Résumé en Français

Introduction

Dans la vie courante, le besoin d'information en temps réel nécessite le plus souvent la capture d'images dans une grande gamme de longueur d'onde. Les photodétecteurs jouent un rôle important dans cette capture d'informations.

Les photodétecteurs actuels sont fabriqués avec des techniques coûteuses telles que l'épaxie et des procédés micro-nano pour la couche photosensible et le circuit électronique de lecture.

Avec la démocratisation des équipements et l'extension de l'informatisation, le besoin de procédés de fabrication plus simples et sur grande surface se fait croissant.

Dans ce but, les photodétecteurs associant des nanoparticules ont attiré et attirent l'attention de la communauté scientifique eu égard aux propriétés particulières de ces nanoparticules en efficacité photo-électrique et en modulation de la longueur d'onde d'absorption. Des photodétecteurs associant l'efficacité de ces nanoparticules et l'effet d'amplification propre des transistors attirent particulièrement l'attention.

Si en plus, on peut fabriquer ces phototransistors à très faible coût par des moyens propres sur grande surface, la démocratisation des photodétecteurs pour des applications diverses sera assurée.

Le but principal de ce travail de thèse est de développer des photodétecteurs sur une grande gamme de longueur d'onde par des moyens peu onéreux en utilisant de l'impression par jet d'encre pour certaines étapes

Après un premier chapitre introductif décrivant l'état de l'art des photodétecteurs et des techniques expérimentales de fabrication, le document de thèse est divisé en une

première partie A sur les photodétecteurs dans la gamme UV-Vis et une seconde partie B sur les photodétecteurs dans la gamme du proche infrarouge. Cette dernière partie est particulièrement étendue car elle présente tout d'abord les résultats de l'optimisation de la technique d'impression par jet d'encre utilisée pour fabriquer le phototransistor organique, puis les résultats de l'optimisation du transistor organique servant comme base du phototransistor. Elle s'intéresse enfin dans une dernière partie à la jonction des nanoparticules avec le transistor donnant naissance au phototransistor. Les performances du phototransistor en détection de lumière infrarouge y sont présentées.

Partie A: Photodétecteurs UV-Visible

Une structure de transistor en couche mince dit TFT est utilisée pour fabriquer un phototransistor sensible dans le domaine UV-Visible (Fig.1). La couche active de ce transistor constitue l'élément photosensible. Elle est composée de nanofils de ZnO décorés par des fragments de nanoparticules de CdSe (QDs CdSe) et d'oxyde de graphène réduit (RGO).

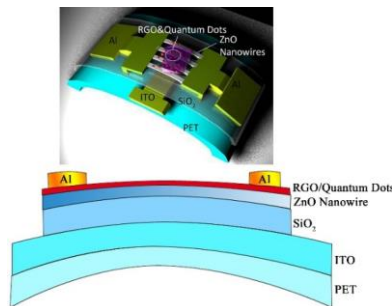


Fig. 1 : Structure du phototransistor UV-Vis

4. Fabrication

Les nanofils de ZnO sont déposés à 800°C par pulvérisation radiofréquence d'une cible de zinc dans un mélange argon/oxygène. Les nanofils obtenus ont une longueur de 25 μm et un diamètre de 150 nm.

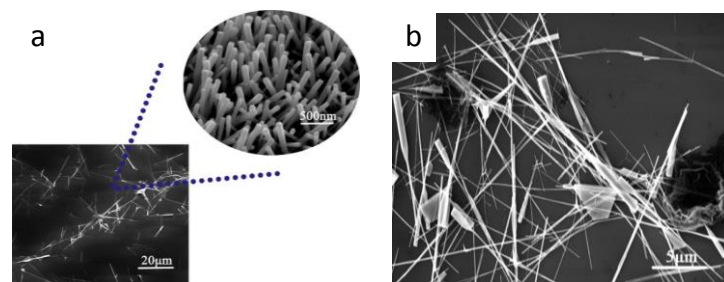


Fig. 2 : Images obtenues au Microscopie électronique à balayage de nanofils de ZnO (a) et du matériau hybride (b).

La synthèse des fragments de nanoparticules de CdSe et de RGO se fait en solution à partir d'oxyde de graphène acheté puis réduit pour obtenir des fragments de RGO de 5 μm de diamètre et de nanoparticules de CdSe de type N de 7nm de diamètre

modifiées par de l'oxyde tri-n-octylphosphine (TOPO).

La fabrication du phototransistor commence par les dépôts successifs d'une couche de ITO et d'une couche de SiO₂ par pulvérisation radiofréquence sur un substrat plastique de type PET. Les nanofils de ZnO dispersés dans l'éthanol sont déposés ensuite par spin-coating sur la surface de SiO₂. La succession de dépôt de couches se termine par le dépôt par spin-coating de la solution hybride QDs de CdSe/RGO.

La structure entière est ensuite recuite à 180°C. Finalement, les électrodes de source et drain (W:L=100 µm:20 µm) sont déposées par électrolyse.

5. Résultats

La figure 3 montre des caractéristiques de transfert sous une tension drain-source de 5V de 2 types de phototransistors en l'absence et en présence de lumière de longueur d'onde 580 nm. La couche active du premier transistor est composée uniquement de nanofils de ZnO décorés par des nanoparticules de CdSe. La couche active du second est composée de nanofils de ZnO décorés par les fragments de QD CdSe et de RGO. La comparaison permet de déterminer l'importance d'utiliser le RGO pour faire la transition des porteurs de charges créés par la lumière dans les QD CdSe vers le ZnO. Visiblement la différence entre les courbes sous obscurités et les courbes sous lumière est plus importante quand on utilise le RGO, démontrant une meilleure sensibilité à la lumière. La photo-réponse calculée du second phototransistor (avec RGO) est de ~2000 A W⁻¹, soit approximativement 2 ordres de grandeur supérieure à celle du premier transistor (sans RGO). Ceci démontre l'importance du RGO dans le transfert des électrons excités par la lumière dans les QD CdSe vers les nanofils de ZnO où ils participeront au courant du transistor.

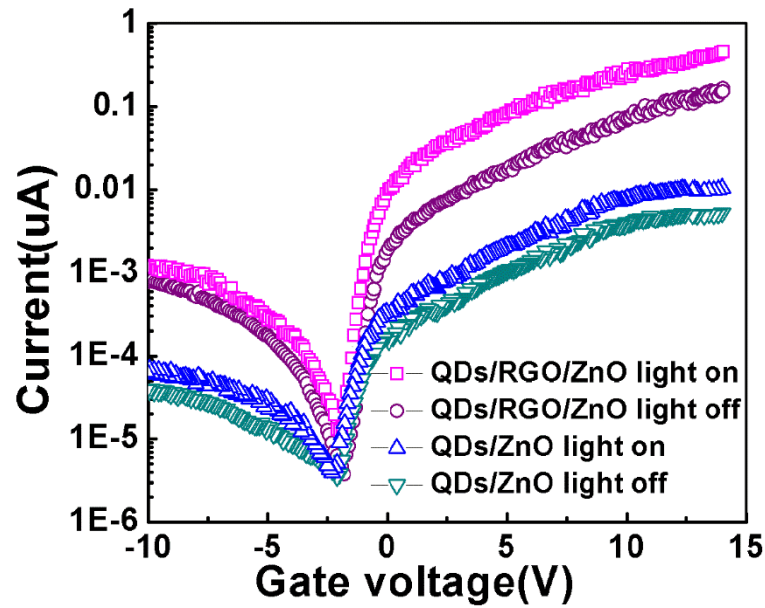


Fig. 3 Caractéristiques de transfert de 2 transistors avec des couches actives de QD CdSe et nanofils de ZnO seulement et de QD CdSe, RGO et nanofils de ZnO sous obscurité (light off) et sous lumière de longueur d'onde 580 nm (light on). La tension drain-source V_{DS} est égale à 5V.

L'explication de cette meilleure photoréponse peut être trouvée dans le schéma de bande d'énergie représenté dans la figure 4.

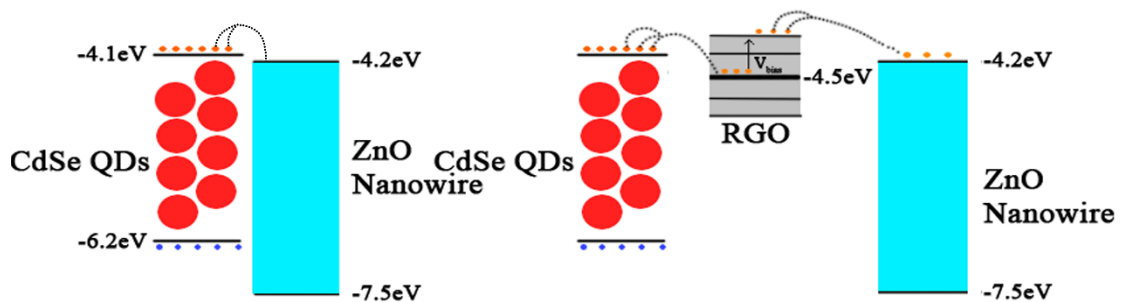


Fig. 4 schéma de bandes d'énergie du système QD CdSe/ZnO et du système QD CdSe/RGO/ZnO.

La position du niveau de Fermi du RGO favorise le passage des électrons de la bande de conduction des QD CdSe vers le RGO. Ces électrons peuvent être excités vers les niveaux de défauts du RGO et transférés vers le ZnO grâce à la polarisation positive du contact de grille.

Afin d'apprécier la gamme de longueur d'onde détectée par le phototransistor, la figure 5 montre les caractéristiques de transfert de ce transistor à l'obscurité et soumis à des lumières de longueur d'onde différentes allant de l'UV au Visible.

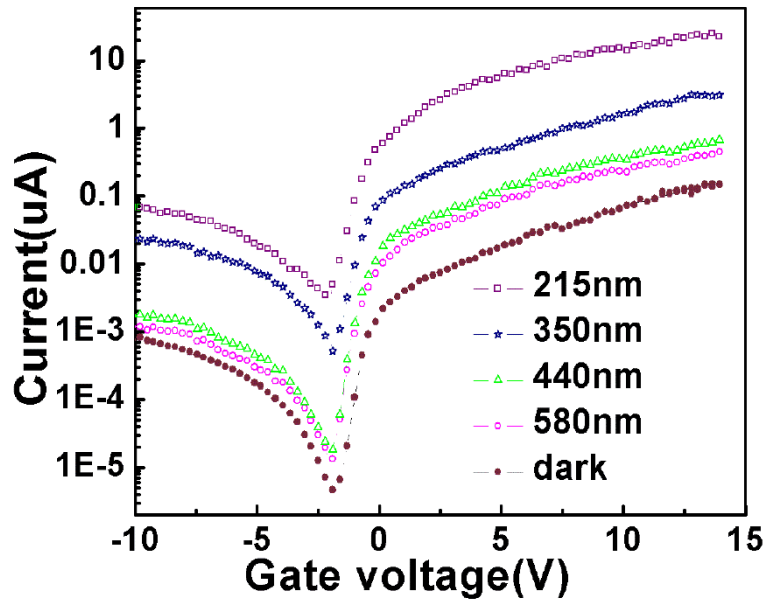


Fig. 5 Caractéristiques de transfert du phototransistor QD CdSe/RGO/nanofils de ZnO sous obscurité (dark) et sous une lumière de longueur d'onde variant du lointain UV (215 nm) au visible (580 nm).

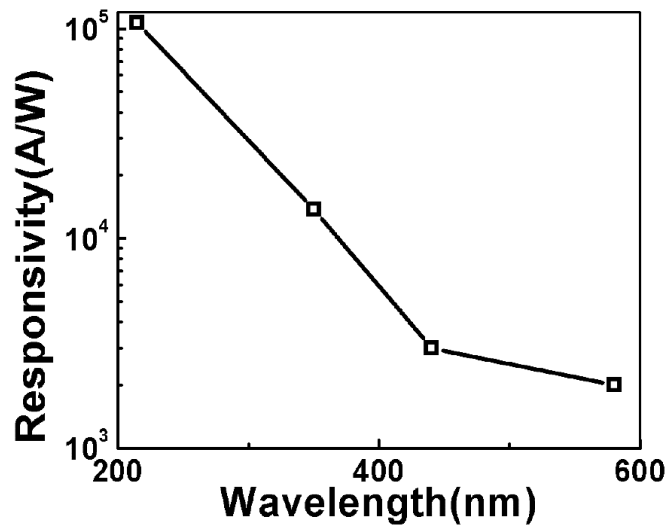


Fig. 6 Variation de la photo-réponse (responsivity) en fonction de la longueur d'onde.

Le phototransistor détecte ainsi dans toute la gamme de longueur d'onde UV-Vis. Cependant la réponse est plus importante dans l'UV que dans le visible.

La photo-réponse peut être modulée par la tension appliquée sur la grille comme l'explique le schéma de bande de la structure en présence et en l'absence de tension de grille positive (Fig.7).

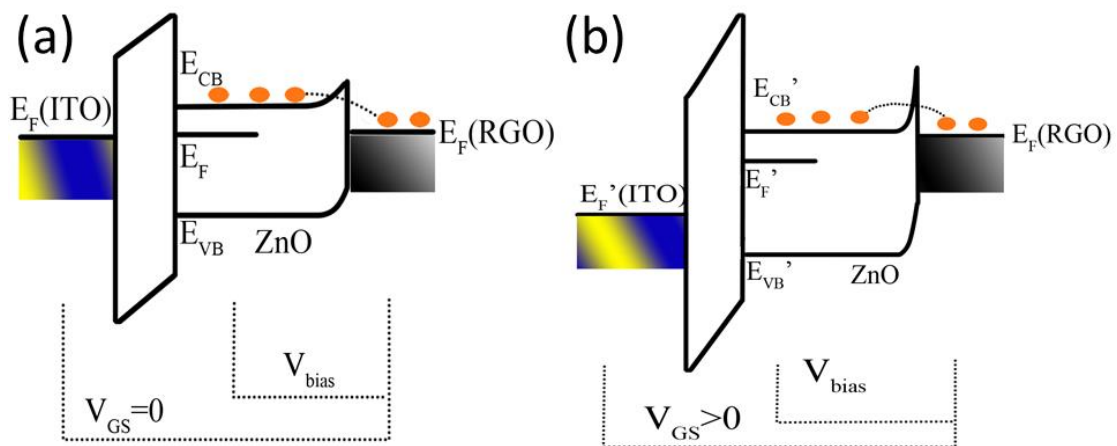


Fig. 7. Schéma de bandes du système sans tension de grille et avec une tension de grille positive.

L'effet direct de la tension de grille positive sur la valeur du courant en présence de lumière peut être constaté dans la figure 8, représentant le courant sous une impulsion de lumière de 580 nm de longueur d'onde. Une proportionnalité peut être remarquée entre le courant et la tension de grille.

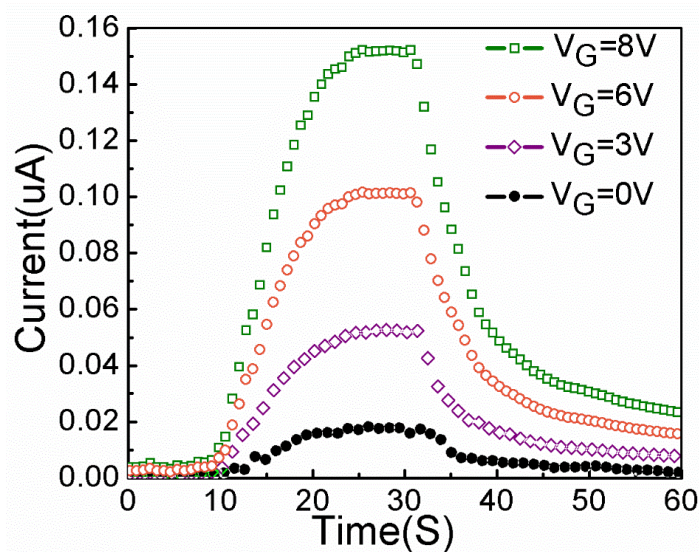


Fig. 8 Réponse du phototransistor à une impulsion de lumière de 580 nm de longueur d'onde lorsqu'une tension positive de différentes valeurs est appliquée. ($V_{DS}=5V$)

6. Conclusion

En conclusion un nouveau phototransistor de couche active composée d'un matériau hybride nanoparticules de CdSe, oxyde de graphène réduit, nanofils de ZnO,

déTECTANT dans l'UV et le visible a été démontré et fabriqué. L'interface QD CdSe/ZnO a été grandement améliorée par l'incorporation de l'oxyde de graphène réduit comme matériau intermédiaire. La photo-réponse a été améliorée par un facteur 100. De plus le photocourant peut encore être amélioré par un facteur 10 en augmentant la tension positive appliquée sur la grille.

Enfin, le procédé de fabrication de ce dispositif réalisé à température ambiante sur un substrat flexible rend ce phototransistor très attractif pour la photo-électronique flexible transparente en grande surface.

Partie B: Phototransistors organiques dans la gamme du proche-infrarouge

Cette partie B fait appel à la nouvelle électronique organique et spécialement aux nouveaux procédés de fabrication de cette électronique par impression à jet d'encre. Une description poussée de ce procédé accompagnée des résultats de notre optimisation sera tout d'abord donnée. L'optimisation du procédé de fabrication du transistor organique sera ensuite présentée. Enfin la technique de fabrication du phototransistor associant les nanoparticules de PbS (QD PbS) et le transistor organique et les résultats en détection de lumière proche infrarouge termineront l'exposé de cette partie B.

3. Impression par jet d'encre

L'impression continue de jet d'encre fait de plus en plus place à l'impression par jet à la demande ou drop-on-demand (DoD) en anglais. La formation d'un motif par impression à jet d'encre fait appel à 3 phénomènes : l'extension, le mouillage et le séchage. Le procédé comporte 3 étapes : i) génération d'une gouttelette, ii) l'extension de la gouttelette sur un substrat quelconque iii) le séchage de la gouttelette.

Pour notre étude de l'impression nous avons utilisé une machine de l'entreprise CERADROP appelée Ceraprinter X-series



Figure 1: Machine Ceraprinter X-series

Elle est équipée d'une tête d'impression de 256 embouts. Nous l'avons utilisée pour imprimer de l'encre d'argent directement sur substrat de verre (pour le contact de grille du transistor « bottom gate ») et sur couche de photorésine SU8 (pour les contacts de drain source en configuration « bottom contacts » pour le transistor). Les caractéristiques de mouillage des surfaces de ces 2 substrats très différentes ont amené à la mise au point de paramètres de dépôt différents pour la même encre d'argent.

Le travail a consisté en la détermination des paramètres de dépôt d'une goutte, puis du dépôt de gouttes successives pour former une ligne d'argent et enfin d'un carré ou rectangle d'argent pour former un contact.

Les figures suivantes donnent quelques exemples de ce long travail d'optimisation et de compréhension des phénomènes.

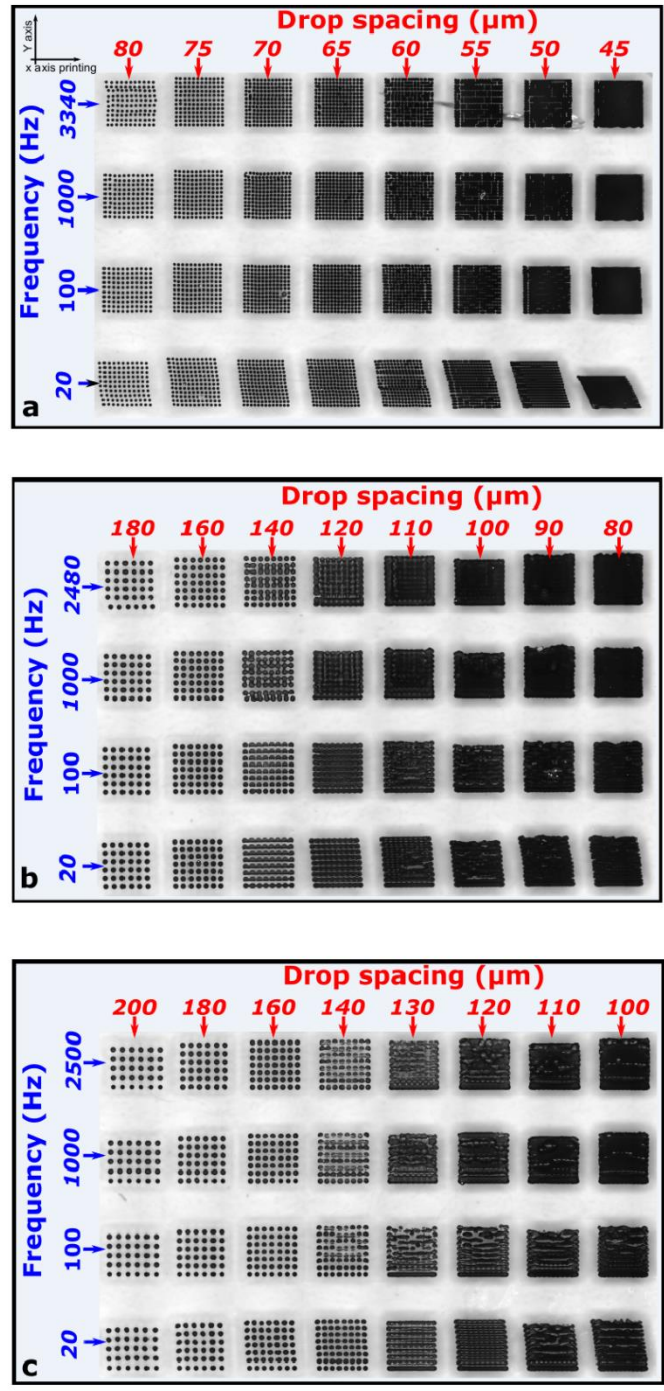


Fig. 2 Motifs carrés (1mmx1mm approximativement) obtenus en variant la distance entre gouttelettes, la fréquence du jet et le temps du traitement UV ozone de la surface avant le jet: a) temps UV ozone 2 minutes; distance entre gouttelettes variant de 80 à 45 μm et fréquence de jet variant de 3340 à 20Hz; b) temps UV ozone 6 minutes; distance entre gouttelettes variant de 180 à 80 μm et fréquence de jet variant de 2480 à 20Hz; c) temps UV ozone 10 minutes; distance entre gouttelettes variant de 200 à 100 μm et fréquence de jet variant de 2500 à 20Hz

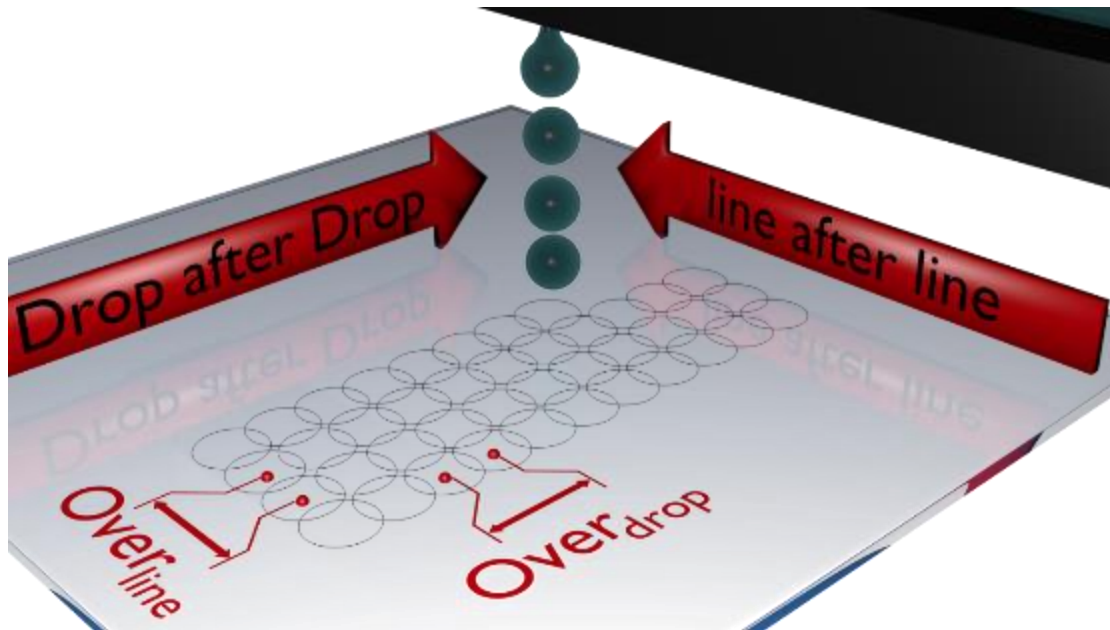


Figure 3: schéma montrant le principe de l'impression par jet à la demande (DoD) pour la formation d'un motif carré. $Over_{drop}$ concerne l'espace entre gouttelettes qui doivent coalescer pour former une ligne. $Over_{line}$ concerne l'espace entre lignes pour former des lignes jointives et ainsi un carré.

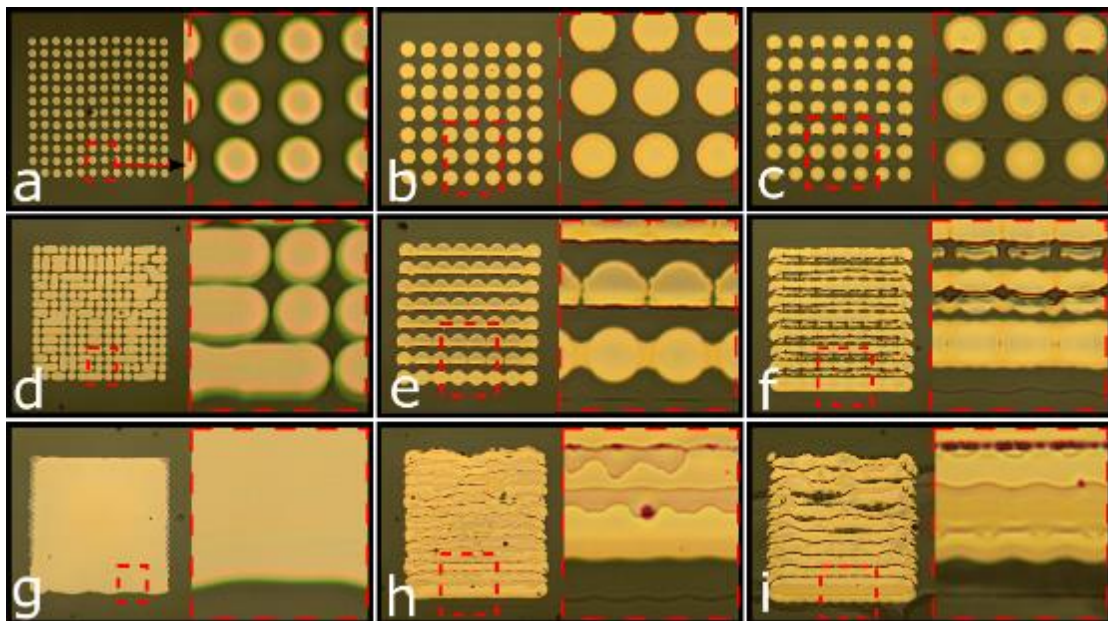


Fig. 4 Images de motifs carrés (1mmx1mm) imprimés à fréquence de jet fixée à 100Hz en faisant varier: i) le temps d'exposition à l'UV ozone, 2, 6 et 10 minutes (colonnes 1, 2 et 3 respectivement); ii) espace entre gouttelettes afin d'imprimer des matrices de gouttelettes isolées, gouttelettes partiellement fusionnées, motifs continus (lignes 1, 2 et 3 respectivement). L'espace entre gouttelettes est égal à: a) 75 μ m; b) 160 μ m; c) 160 μ m; d) 60 μ m; e) 140 μ m; f) 130 μ m; g) 45 μ m; h) 80 μ m; i) 100 μ m.

En complément de l'étude précédente de variation de différents paramètres à fréquence de jet fixée, l'étude suivante (Figure 5) montre l'effet de la fréquence à temps d'exposition à l'UV-ozone fixé à 10 minutes.

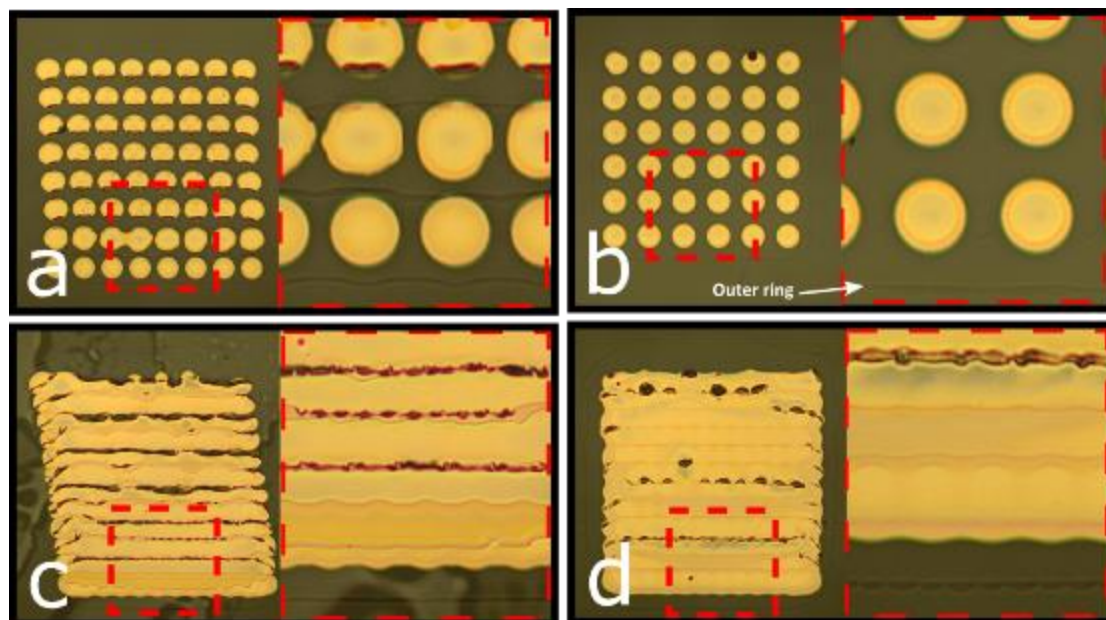


Fig. 5 Images de motifs carrés (1mmx1mm) imprimés à temps d'exposition à l'UV-ozone fixé à 10 minutes en faisant varier: i) la fréquence de jet, 20Hz et 3340Hz (colonnes 1 et 2 respectivement); il faut remarquer que ces valeurs correspondent aux plus faible et plus grande vitesses d'impression disponibles. ii) l'espace entre gouttelettes afin d'imprimer des matrices de gouttelettes isolées et des motifs continus (lignes 1 et 2 respectivement). L'espace entre gouttelettes est égal à: a) 180µm; b) 180µm; c) 100µm; d) 100µm.

4. Transistors en Couche Mince Organiques (OTFT) de type N à base de C60

Le travail d'optimisation des performances mené dans cette thèse concerne particulièrement l'étude d'obtention de la couche active de C60 ayant les meilleures qualités électriques. Les interfaces entre contacts de source et drain et la couche active ont été auparavant optimisées lors du travail de thèse de Malo Robin au laboratoire [Thèse Université de Rennes 1, 19 décembre 2017].

La structure de transistor choisie est de type Grille en dessous « Bottom Gate » –

Contacts de drain et source en dessous « Bottom Contacts ». Elle est représentée dans la figure 6.

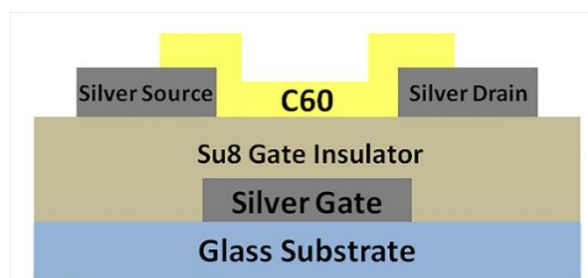


Fig. 6: Schéma en coupe montrant la structure du transistor fabriqué

La fabrication commence par l'impression du contact de grille en argent sur un substrat de verre. Ensuite une couche de photorésine SU8 2000 (Bisphenol A Novolak epoxy; MicroChem) est déposée par spin-coating et recuite. Elle sera utilisée comme isolant de grille et a une épaisseur de 1,2 μm . Après un traitement UV-ozone de la surface de cette couche de SU8, les contacts de source et de drain en argent sont imprimés. Finalement, une couche de C60 est évaporée à température ambiante.

L'optimisation du transistor a consisté en l'étude de l'effet de la température de recuit tout d'abord suivie ensuite de l'étude de l'effet de l'épaisseur de la couche de C60. En effet considérant l'épaisseur des contacts de source et de drain, un problème de marche peut se poser pour la continuité de la couche C60.

- *Effet de la température de recuit*

La surface de la couche de C60 a été observée par Microscope à Force Atomique (AFM) juste après la fabrication du transistor et après des recuits à 160°C, 200°C et 250°C. L'observation a permis de déduire la rugosité de la surface, exprimée en RMS, et la taille des grains ; la couche de C60 est en effet polycristalline.

La figure 7 montre des images de cette surface pour les différentes températures.

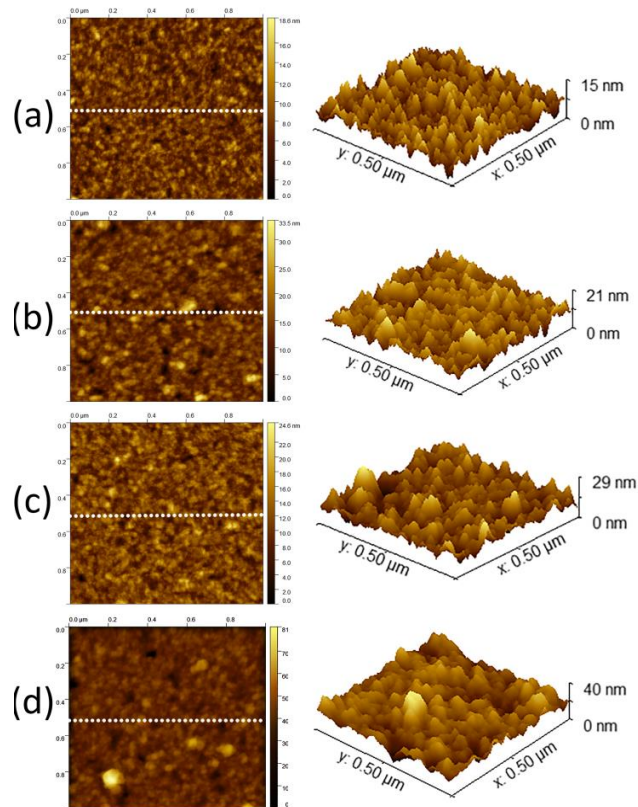


Fig. 7: Images AFM en 2D et 3D de la surface de la couche de C60 juste après la fabrication du transistor (a) et après des recuits à 160°C (b), 200°C (c) et 250°C (d) montrant l'augmentation de la taille des grains et de la rugosité avec la température.

Les valeurs RMS de la rugosité de surface σ et de la taille des grains τ sont données dans le tableau 1.

Température de recuit (°C)	Rugosité σ (nm)	Taille des Grains τ (nm)
Après dépôt	1.42	4.72
160	1.75	7.70
200	1.91	13.46
250	2.72	14.16

Tableau 1: rugosité de surface σ et de la taille des grains τ

Les 4 types de transistors (juste après fabrication, et après des recuits à 160°C, 200°C et 250°C) sont ensuite électriquement caractérisés. La figure 8 donne leurs caractéristiques de transfert et de sortie (les transistors ont la même largeur de canal 4000µm et la même longueur de canal 150µm).

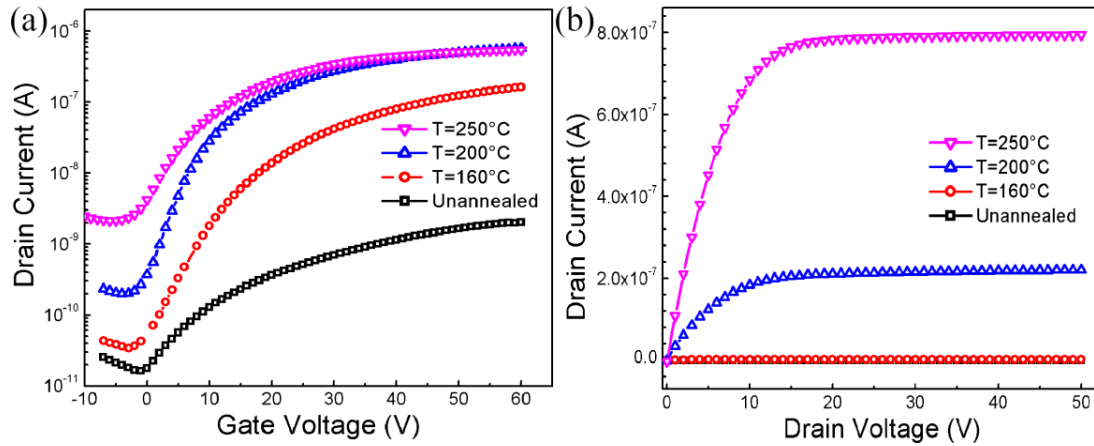


Fig.8: (a) Caractéristiques de transfert moyennes ($V_D=20V$) et (b) Caractéristiques de sortie ($V_G=20V$) de OTFTs ayant la même taille (Largeur de canal $W=4000\ \mu m$, Longueur de canal $L=150\ \mu m$) et 125 nm d'épaisseur de couche active C60 mesurées juste après fabrication, et après des recuits à 160°C, 200°C et 250°C.

Tous les paramètres électriques (tension de seuil, pente sous le seuil, mobilité d'effet de champ, courant direct) s'améliorent avec la température. Le tableau 2 donne leurs valeurs.

T_A (°C)	V_{TH} (V)	SS (V/dec)	μ ($cm^2/V.s$)	R_c (Ω)	μ après R_c ($cm^2/V.s$)	I_{off} (A)	I_{on}/I_{off}
Non-recuit	19.3	9.3	5.3×10^{-5}	8×10^6	5.8×10^{-5}	1.6×10^{-11}	125
160°C	20	7	4.2×10^{-3}	2×10^6	4.47×10^{-3}	3.4×10^{-11}	4.7×10^3
200°C	11.2	4	1.44×10^{-2}	1.7×10^6	1.46×10^{-2}	2×10^{-10}	2.85×10^3
250°C	6.2	6.2	1.46×10^{-2}	2×10^6	1.5×10^{-2}	2×10^{-9}	270

Tableau 2 Principaux paramètres électriques moyens de plusieurs transistors de même taille

(Largeur de canal $W=4000 \mu\text{m}$, Longueur de canal $L=150 \mu\text{m}$. V_{TH} est la tension de seuil, SS la pente sous le seuil, μ la mobilité, R_C la résistance de contact, μ après R_C la mobilité après correction par R_C , I_{off} est le courant minimum et I_{on}/I_{off} est la rapport du courant maximum sur le courant minimum

La figure 9 montre la très bonne corrélation entre la mobilité d'effet de champ du transistor et la taille des grains de la couche active C60. Cette proportionnalité montre que la couche de C60 polycrystalline obéit parfaitement au modèle classique de Seto établi pour les matériaux polycrystallins.

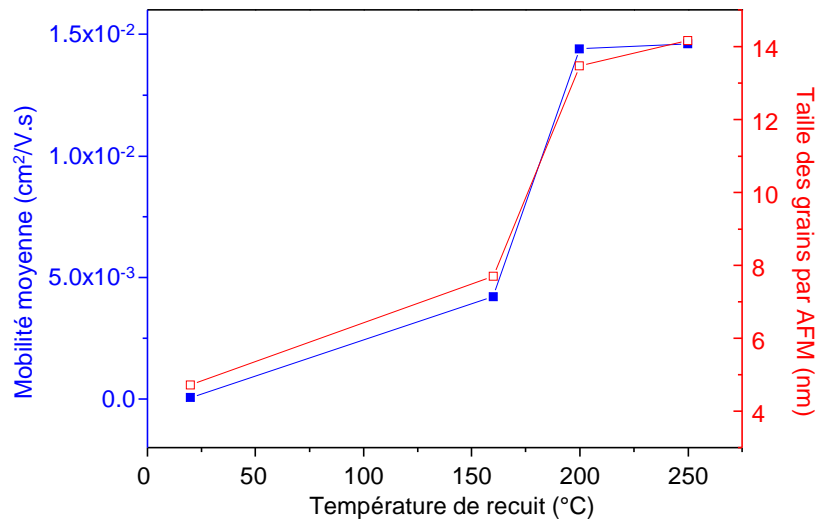


Fig. 9: Corrélation entre la mobilité d'effet de champ et la taille des grains de la couche de C60

- *Effet de l'épaisseur de la couche active C60*

L'effet de l'épaisseur de la couche active C60 a été étudié sur des transistors recuits à 200°C, résultat de l'étude précédente sur l'effet de la température de recuit.

La figure 10 donne les caractéristiques de transfert et de sortie de 4 OTFTS ayant des épaisseurs de couche active C60, 60nm, 90 nm, 125 nm et 250nm (les transistors ont la même largeur de canal 4000μm et la même longueur de canal 150μm) .

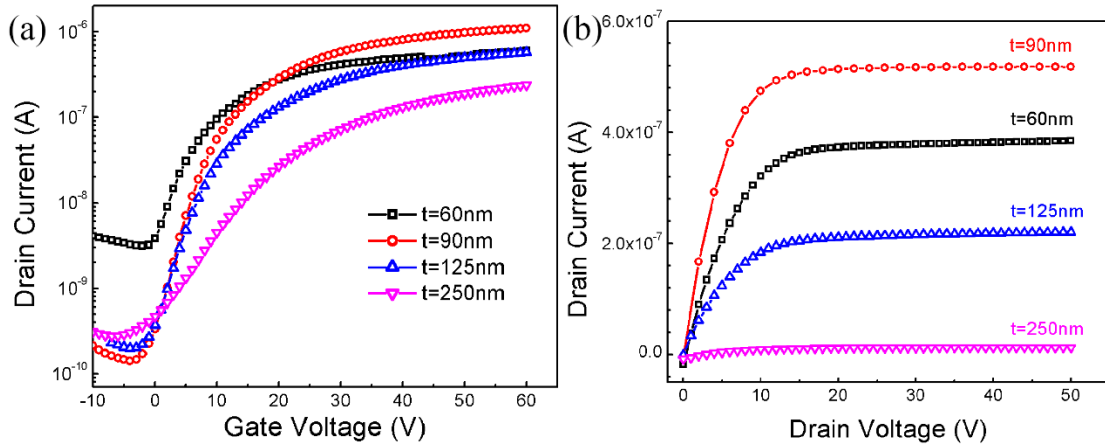


Fig.10: (a) Caractéristiques de transfert moyennes ($V_D=20V$) et (b) Caractéristiques de sortie ($V_G=20V$) de OTFTs ayant la même taille (Largeur de canal $W=4000 \mu m$, Longueur de canal $L=150 \mu m$) et des épaisseurs de couche active C60, 60nm, 90 nm, 125 nm et 250nm.

La figure 10 montre que le plus grand courant est obtenu avec l'épaisseur de 90 nm. Le minimum de courant est aussi le plus faible à 90 nm. Enfin, le transistor à 90 nm d'épaisseur de C60 présente la pente sous le seuil la plus abrupte. Le tableau 3 donne les valeurs de ces paramètres.

t_{C60} (nm)	V_{TH} (V)	SS (V/dec)	μ ($cm^2/V.s$)	R_c (Ω)	μ après R_c ($cm^2/V.s$)	I_{off} (A)	I_{on}/I_{off}
60	5,7	5,2	1.8×10^{-2}	2.7×10^6	1.9×10^{-2}	3×10^{-9}	180
90	10,8	3,6	2.9×10^{-2}	7.5×10^5	2.95×10^{-2}	1.4×10^{-10}	7.8×10^3
125	10,8	4	1.4×10^{-2}	1.2×10^7	1.7×10^{-2}	2×10^{-10}	2.85×10^3
250	11	9,2	6.1×10^{-3}	1×10^7	6.5×10^{-3}	2.7×10^{-10}	870

Tableau 3 Principaux paramètres électriques moyens de plusieurs transistors ayant des épaisseurs de couche active C60 de 60nm, 90nm, 125nm et 250nm et de même taille (Largeur de canal $W=4000 \mu m$, Longueur de canal $L=150 \mu m$). V_{TH} est la tension de seuil, SS la pente sous le seuil, μ la mobilité, R_c la résistance de contact, μ après R_c la mobilité après correction par R_c , I_{off} est le courant minimum et I_{on}/I_{off} est la rapport du courant maximum sur le courant minimum

En conclusion de ces études, les meilleures conditions de préparation de OTFT performant consistent en l'utilisation d'une couche active de 90 nm d'épaisseur et en un recuit postérieur de 200°C.

- *Etude dynamique des OTFTs C60*

L'étude des OTFTs par des polarisations statiques est intéressante pour déterminer leurs qualités électriques. Cependant, dans beaucoup d'utilisations, les OTFTs sont soumis à des signaux dynamiques. L'analyse de leur réponse à une excitation dynamique s'avère importante. Le comportement dynamique de transistors est beaucoup plus lié à leurs caractéristiques de sortie statiques qu'aux caractéristiques de transfert. Nous présentons ainsi dans la figure 11, les caractéristiques de sortie de OTFTs ayant une couche active C60 de 90 nm d'épaisseur après différents recuits.

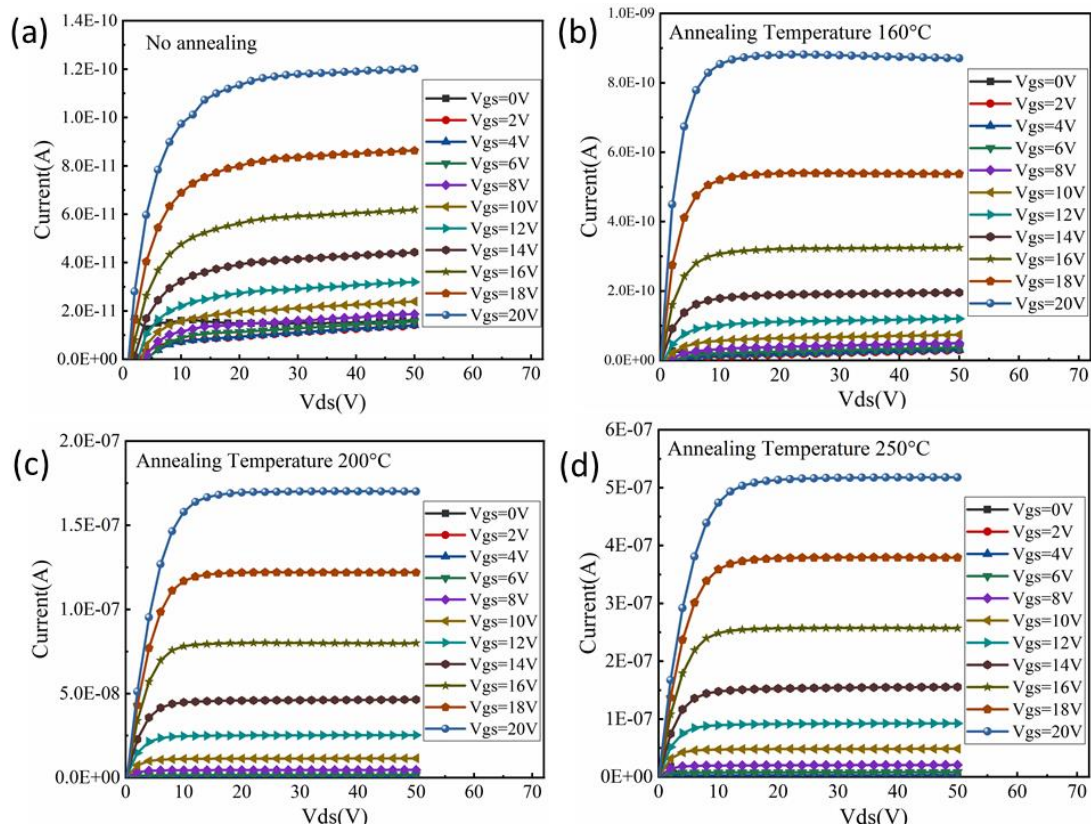


Fig. 11 Caractéristiques de sortie de OTFTs ayant une couche active C60 de 90 nm d'épaisseur après différentes température de recuit.

Les caractéristiques des OTFTs recuits à 200°C et 250°C présentent les meilleures allures avec une très bonne saturation du courant.

Le comportement dynamique de ces OTFTs est étudié à travers une résistance de charge de 500MΩ. Ces OTFTs sont ainsi montés en inverseurs. La réponse statique de l'inverseur polarisé par $V_{DD}=20V$ est montrée dans la figure 12. Quand la tension d'entrée augmente de 0V à 20V, la tension de sortie diminue de 20V à 0,2V

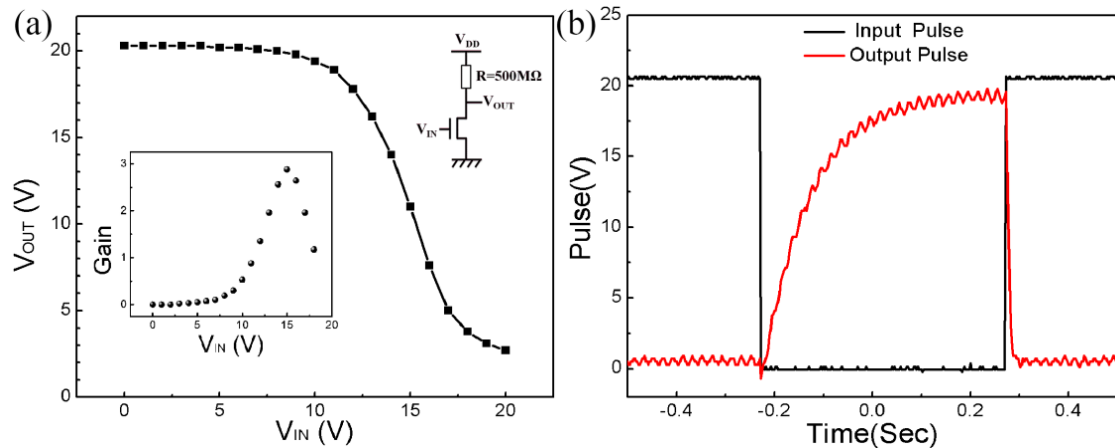


Fig. 12: (a) Caractéristique statique du OTFT chargé par une résistance de 500MΩ et (b) sa réponse à une impulsion de 0,5 sec. Le gain de l'inverseur est de 3.

Dans ces conditions de polarisation l'inverseur a un gain (maximum de la dérivée dV_{OUT}/dV_{IN}) de 3. Cette valeur dépend de la résistance de charge mais elle est dans l'ordre de grandeur des inverseurs organiques.

La réponse dynamique du transistor à une impulsion de tension d'entrée de 20V et de durée 0,5 seconde est montrée dans la figure 12. Le temps de basculement entre l'état off et l'état on du transistor, représentatif du comportement du transistor, est de 13 ms entre 90% et 10% de la tension maximum. Les OTFTs répondent ainsi à un signal de fréquence supérieure à 10Hz.

5. Photodétecteur Proche Infrarouge composé de nanoparticules de PbS et de OTFT

Après l'optimisation du procédé de fabrication du transistor organique de type N, on peut maintenant se focaliser sur le principal objectif de ce travail à savoir la fabrication d'un phototransistor dans le proche infrarouge au plus faible coût possible en utilisant des procédés en solution et entièrement additifs sans étape de lithographie.

- *Nanoparticules de PbS (QD PbS)*

QD PbS a une structure cubique faces centrées avec une largeur de bande interdite directe de 0,91 eV. Avec un rayon de Bohr de l'exciton de 18 nm seulement, il a un très fort effet de confinement et par ajustement de la taille des nanoparticules, différents spectres d'absorption de lumière peuvent être obtenus. La figure 13 montre les différents spectres obtenus en variant les tailles des nanoparticules.

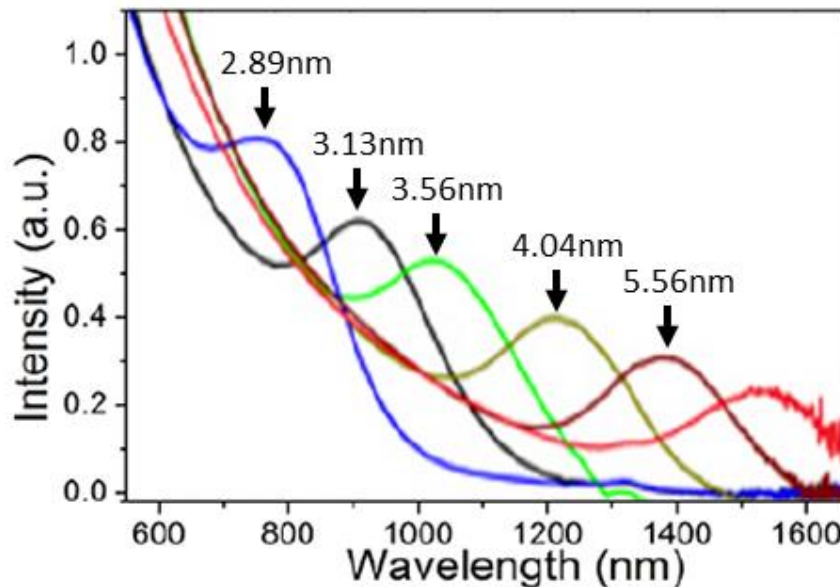


Fig. 13 Spectres d'absorption de nanoparticules de PbS pour différentes tailles de nanoparticules.

Pour couvrir le domaine des applications médicales, nécessitant des longueurs d'onde supérieures à 1300 nm, nous avons choisi dans ce travail des particules de taille

5,56 nm. La figure 14 montre la morphologie des QD PbS choisis observée par microscope à transmission et la taille homogène de 64 QD PbS centrée autour de 5,56 nm..

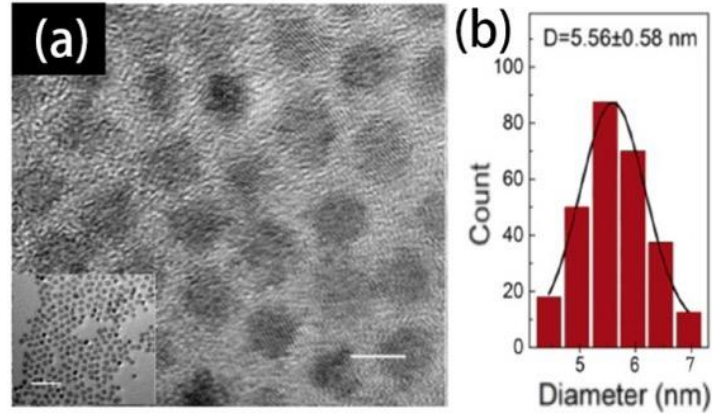


Fig. 14 (a) Image obtenue au microscope à transmission à haute résolution des nanoparticules de PbS. La barre d'échelle est 5nm. (b) Distribution statistique des tailles de 240 nanoparticules.

Pour déterminer la bonne concentration de nanoparticules à utiliser pour une bonne détection, des phototransistors ont été fabriqués avec différentes concentrations. 5mg/mL, 7.5mg/mL, 10mg/mL, 12.5mg/mL and 15mg/mL. Le photo-réponse (responsivity), la photo-sensitivité, la détectivité et l'efficacité EQE de ces transistors sont donnés dans la figure 15 en fonction de la concentration.

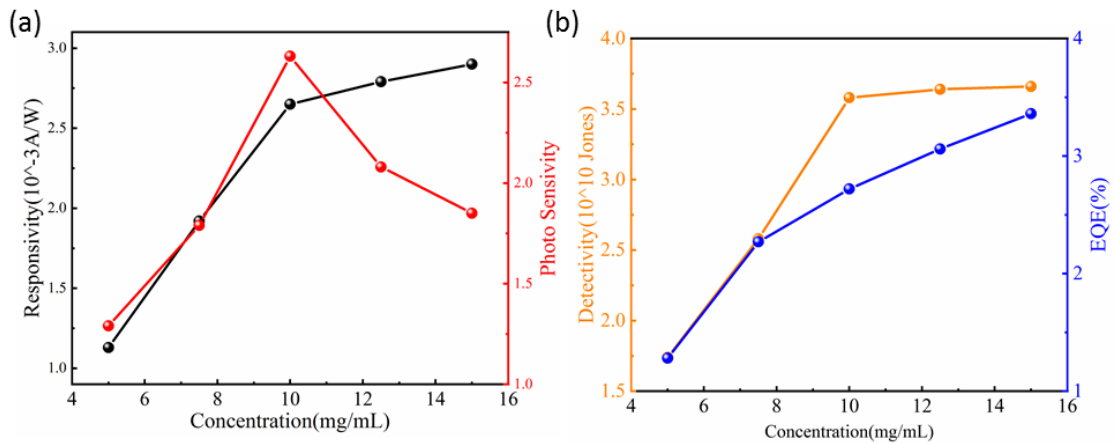


Fig. 15 (a) Photo-Réponse et photo-sensitivité des phototransistors avec différentes concentrations de nanoparticules. (b) Leur détectivité et leur efficacité EQE.

Comme le courant sous obscurité est très important pour un photodétecteur et que ce courant augmente avec la concentration de nanoparticules et considérant la très faible différence de photo-sensitivité et détectivité entre les concentrations 10mg/mL, 12.5mg/mL et 15mg/mL, la concentration de 10mg/mL est choisie pour la suite de l'étude.

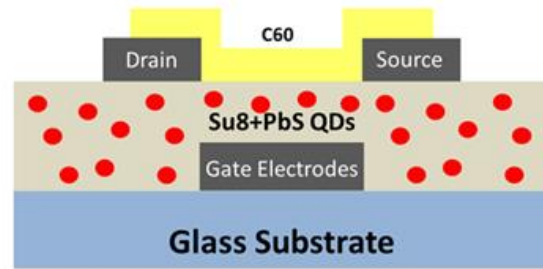
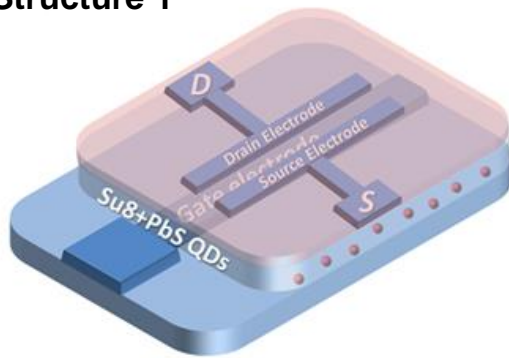
- *Phototransistor utilisant les nanoparticules de PbS comme éléments photosensibles et le transistor organique de type N comme amplificateur propre.*

3 structures de phototransistor variant par le positionnement des nanoparticules dans le transistor ont été testées. Dans la première, les nanoparticules ont été dispersées dans tout le volume de l'isolant de grille SU8. La pente sous le seuil des transistors a été beaucoup dégradée probablement par la mauvaise interface introduite par les nanoparticules. Par ailleurs le courant de fuite, particulièrement sous lumière, a beaucoup augmenté. Pour remédier à ceci, l'isolant de grille a consisté en une double couche SU8 seule au contact de la couche active et SU8 mélangée avec les nanoparticules au contact avec la grille, dans la deuxième structure étudiée. Les caractéristiques du transistor se sont beaucoup améliorées mais le photocourant obtenu est faible du fait probablement de l'éloignement des nanoparticules de la couche active.

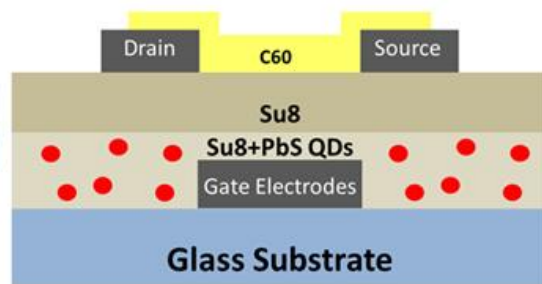
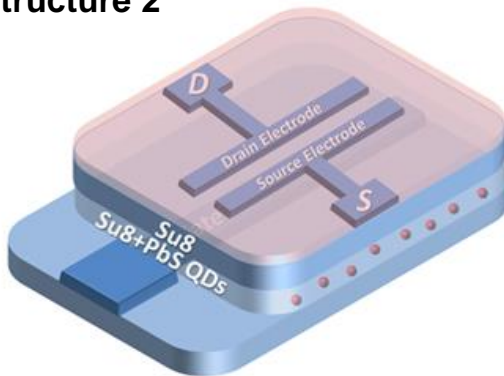
La troisième structure a consisté en un dépôt d'une couche de nanoparticules par spin coating sur la surface de l'isolant de grille SU8 avant le dépôt de la couche active C60. Les nanoparticules se trouvent ainsi à l'interface isolant de grille / couche active.

Les 3 types de structures sont représentés dans la figure 16.

Structure 1



Structure 2



Structure 3

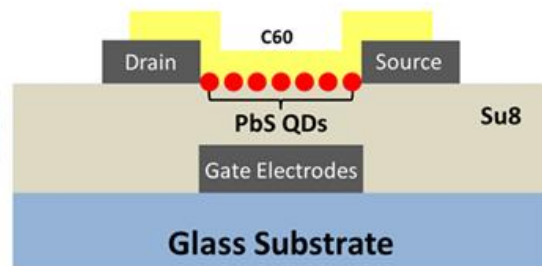
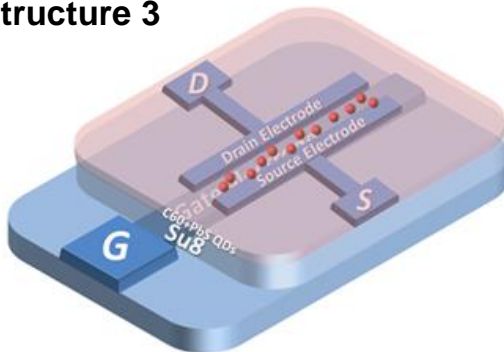


Fig.16 les 3 types de structures de phototransistors testés, variant par l'emplacement des nanoparticules.

La figure 17 présente les caractéristiques de transfert du phototransistor sous obscurité et sous lumière infrarouge de 1050 nm de longueur d'onde et de 250 $\mu\text{W}/\text{cm}^2$ de puissance, et le photocourant net (courant sous lumière – courant sous obscurité).

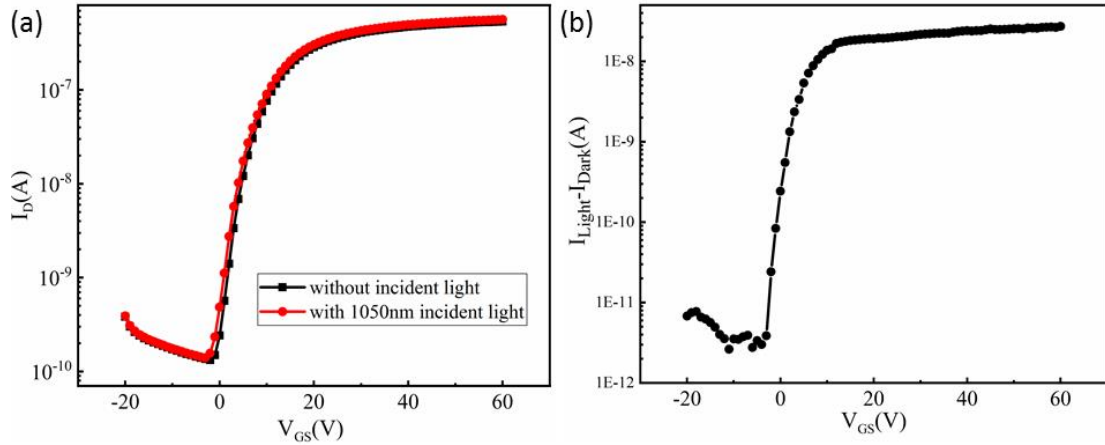


Fig.17 (a) Caractéristiques de transfert du phototransistor sous obscurité et sous lumière infrarouge de 1050 nm de longueur d’onde et de $250 \mu\text{W}/\text{cm}^2$ de puissance ($V_{DS}=10\text{V}$) (b) Photocourant net (courant sous lumière – courant sous obscurité).

Le photocourant net augmente de $1 \times 10^{-11}\text{A}$ à $2,7 \times 10^{-8}\text{A}$ quand la tension de grille augmente. Il devient stable après $V_{GS}=10\text{V}$.

La figure 18 donne les caractéristiques de sortie dans les mêmes conditions. Le photocourant net devient de plus en plus important quand la tension de grille augmente jusqu’à $V_{GS}=20\text{V}$. Le photocourant net maximum est de 8nA .

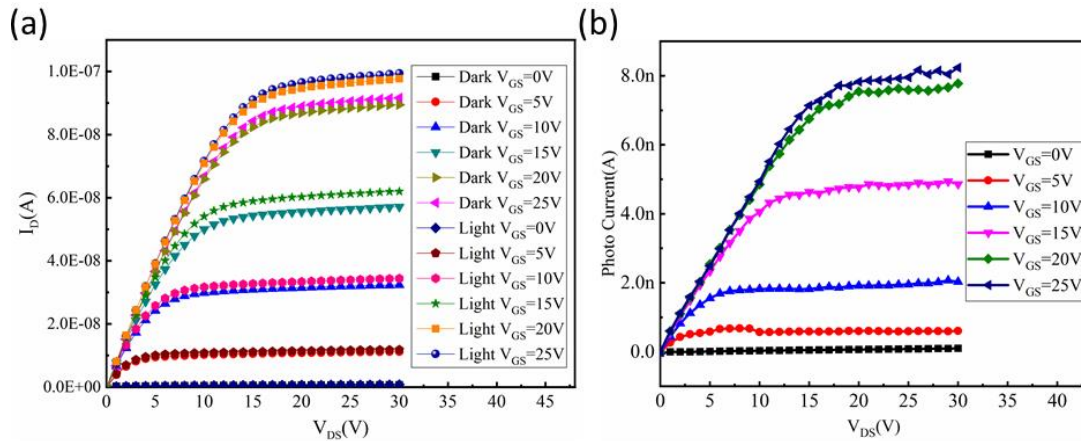


Fig.18 (a) Caractéristiques de sortie du phototransistor sous obscurité et sous lumière infrarouge de 1050 nm de longueur d’onde et de $250 \mu\text{W}/\text{cm}^2$ de puissance ($V_{DS}=10\text{V}$) (b) Photocourant net (courant sous lumière – courant sous obscurité).

Le phototransistor est monté en inverseur avec une résistance de charge de $500\text{M}\Omega$.

La figure 19 montre la variation de la tension de sortie de l'inverseur et celle du courant entre l'obscurité et la même lumière infrarouge.

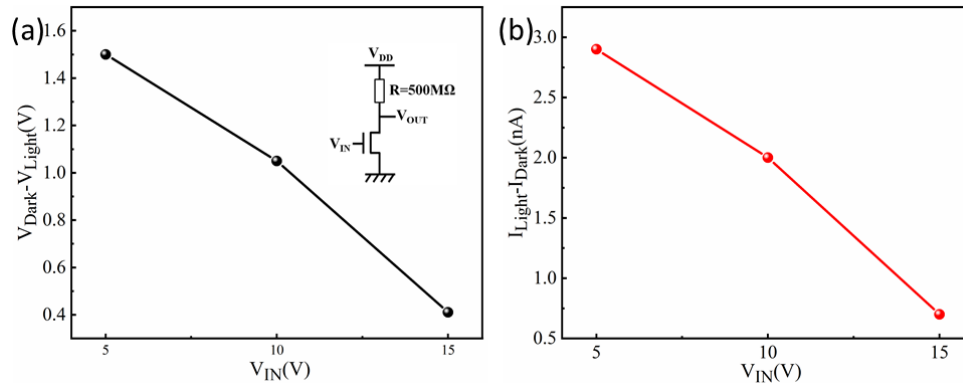


Fig. 19 Variation de la tension de sortie de l'inverseur et celle du courant entre l'obscurité et la lumière infrarouge de 1050 nm de longueur d'onde et de $250 \mu\text{W}/\text{cm}^2$ de puissance. ($V_{\text{DD}}=20\text{V}$)

La figure 20 montre les mêmes variations de la tension de sortie de l'inverseur et celle du courant entre l'obscurité et la même lumière infrarouge en fonction de la polarisation V_{DD} pour une tension d'entrée de 10V. La photo-tension de sortie augmente de 0.2V à 2.1V quand V_{DD} augmente de 10V à 30V.

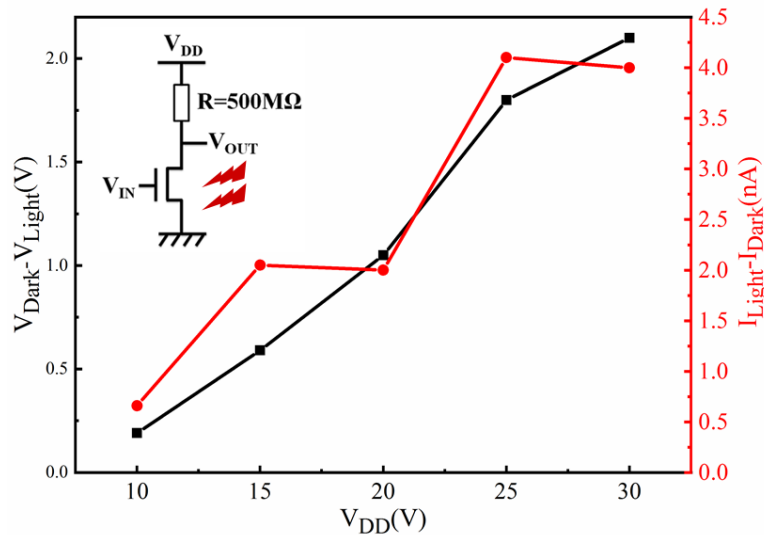


Fig.20 Variation de la tension de sortie de l'inverseur et celle du courant entre l'obscurité et la lumière infrarouge de 1050 nm de longueur d'onde et de $250 \mu\text{W}/\text{cm}^2$ de puissance. ($V_{\text{IN}}=10\text{V}$) en fonction de la polarisation V_{DD}

Une variation de l'ordre du volt de la tension de sortie donne un signal de détection aisément mesurable. Pour augmenter encore plus le signal de sortie, un phototransistor avec un canal en forme de peigne afin d'augmenter la largeur jusqu'à $52000 \mu\text{m}$ ($13 \times 4200 \mu\text{m}$) et donc le courant a été fabriqué. La figure 21 montre un dessin et une photo de ce transistor en forme de peigne

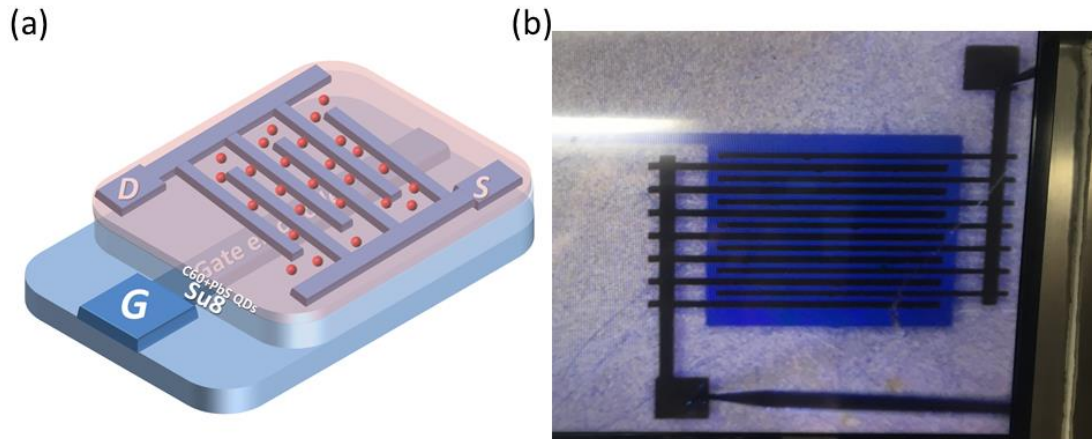


Fig. 21 (a) Structure du phototransistor en forme de peigne. (b) Photo de ce transistor.

La figure 22 présente les caractéristiques de transfert de ce phototransistor sous obscurité et sous lumière infrarouge de 1050 nm de longueur d'onde et de $250 \mu\text{W}/\text{cm}^2$ de puissance, et le photocourant net (courant sous lumière – courant sous obscurité). Le photocourant net maximum est beaucoup augmenté de presque 2 ordres de grandeur.

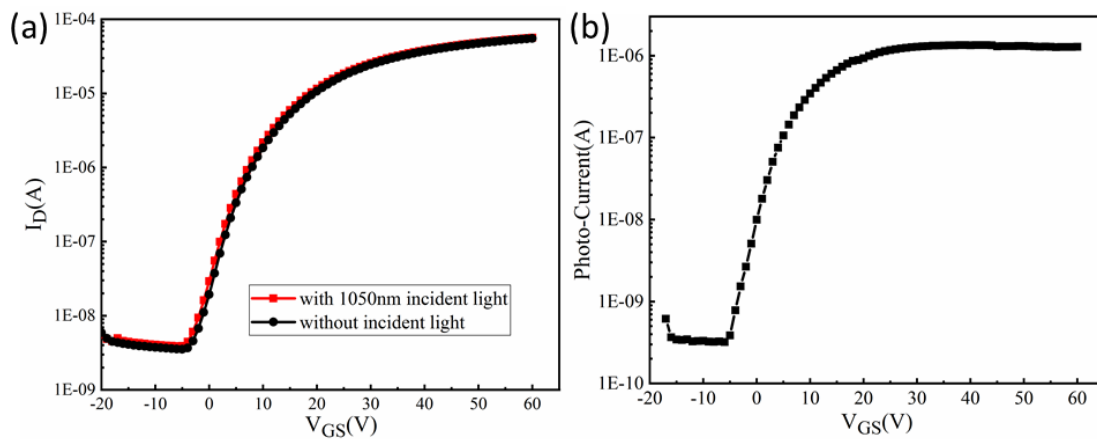


Fig.22 (a) Caractéristiques de transfert du phototransistor en forme de peigne sous obscurité et sous lumière infrarouge de 1050 nm de longueur d'onde et de $250 \mu\text{W}/\text{cm}^2$ de puissance ($V_{DS}=10\text{V}$) (b) Photocourant net (courant sous lumière – courant sous obscurité).

Ce phototransistor monté en inverseur donne un photocourant nettement augmenté comme le montre la figure 23 où une valeur supérieure à 100 nA est observée...

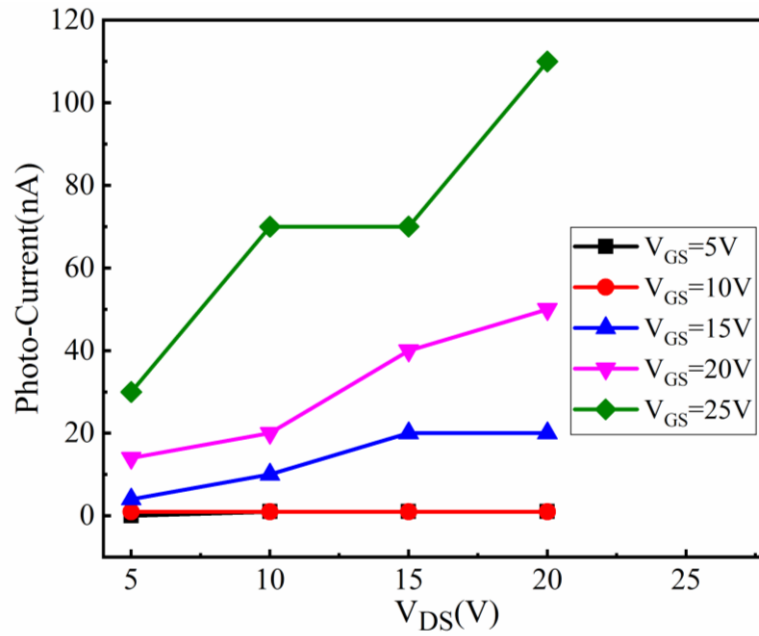


Fig. 23 Photocourant du phototransistor en forme de peigne monté en inverseur pour différentes tensions de grille

Titre : Photodetection dans une large gamme de longueur d'onde :
Phototransistor CdSe QDs/RGO sur des Nanofils de ZnO dans la gamme UV-Vis,
PbS QDs avec un transistor organique C₆₀ de type N imprimé dans la gamme proche IR

Mots clés : Phototransistor, UV-Vis-IR, FET, Organique, Nanoparticules, Nanofils, Printing

Résumé : la détection de lumière dans une large gamme de longueur d'onde allant de l'UV au proche infrarouge est réalisée avec une sensibilité importante en utilisant l'effet d'amplification amené par un transistor à effet de champ et la capacité de détection dans une grande gamme de longueur d'onde amenée par des nanoparticules de CdSe et de PbS de diamètres différents. Dans une première partie, un FET utilisant une couche active de nanofils de ZnO est fabriqué. La détection de lumière UV-Vis est assurée en enrobant ces nanofils par un mélange de nanoparticules de CdSe et d'oxyde de graphène. L'oxyde de graphène assure une bonne transition des électrons créés par la lumière dans le CdSe vers le ZnO. La photo-réponse obtenue, supérieure à 10⁴ A/W à 350 nm, a été multipliée par un facteur 100 dans la gamme 200-500nm en utilisant l'oxyde de graphène.

Dans une seconde partie, la détection de lumière infrarouge a été assurée par des nanoparticules de PbS incorporées dans un transistor organique de type N utilisant du C₆₀ comme couche active. Les électrodes en argent de ce transistor et son isolant de grille en photorésine SU8 sont déposés par impression. Les nanoparticules sont déposées en solution à l'interface entre le semiconducteur et l'isolant de grille. Ce phototransistor incorporé dans un inverseur a montré l'apparition d'un signal de sortie de 2V dû à l'application d'une lumière de 1050 nm de longueur d'onde et de 250 μW/cm² de puissance.

Title : Large Wavelength Range Photodetection:
CdSe QDs/RGO on ZnO Nanowires Transistor in UV-Vis range,
PbS QDs with Nearly Fully Printed C₆₀ based N-type Organic transistor in NIR range

Keywords : Phototransistor, UV-Vis-IR, FET, Organic, Quantum Dots, Nanowires, Printing

Abstract : Detection of light in large wavelength range, from the UV to NIR, is got with high sensitivity by using the amplification of a field effect transistor and the ability of light detection in large range by CdSe and PbS quantum dots with different diameters. In the first part, a FET with ZnO nanowires active layer is fabricated. The light detection in UV-Vis range is insured thanks to CdSe QDs/RGO (Reduced Graphene Oxide) fragments decorating the surface of the ZnO nanowires RGO insures good transfer of photo-electrons induced by the light into the CdSe QDs towards ZnO. The responsivity, higher than 10⁴ A/W at 350 nm, has been improved by 100 in 200-500 nm range by using RGO.

In the second part, IR light detection has been insured by using PbS QDs embedded in N-type Organic FET using C₆₀ film as active layer. Silver electrodes of this transistor and its SU8 photoresist gate insulator have been printed. QDs have been deposited in solution at the interface between the semiconducting layer and the gate insulator. This phototransistor has been used in an inverter. The output voltage of the inverter change by 2V under lighting with 1050 nm wavelength and 250 μW/cm² power.